INVESTIGATION OF MIX DESIGN PARAMETERS AFFECTING THE THERMAL PROPERTIES OF ASPHALT CONCRETE UNDER TRANSIENT AND STEADY-STATE HEAT TRANSFER CONDITIONS

A THESIS SUBMITTED TO
THE GRADUATE SCHOOL OF NATURAL AND APPLIED SCIENCES
OF
MIDDLE EAST TECHNICAL UNIVERSITY

BY

DUYGU DEMİRTÜRK

IN PARTIAL FULFILLMENT OF THE REQUIREMENTS
FOR
THE DEGREE OF DOCTOR OF PHILOSOPHY
IN
CIVIL ENGINEERING

JANUARY 2024

Approval of the thesis:

INVESTIGATION OF MIX DESIGN PARAMETERS AFFECTING THE THERMAL PROPERTIES OF ASPHALT CONCRETE UNDER TRANSIENT AND STEADY-STATE HEAT TRANSFER CONDITIONS

submitted by **DUYGU DEMİRTÜRK** in partial fulfillment of the requirements for the degree of **Doctor of Philosophy in Civil Engineering, Middle East Technical University** by,

Prof. Dr. Halil Kalıpçılar
Dean, Graduate School of **Natural and Applied Sciences** _____

Prof. Dr. Erdem Canbay
Head of the Department, **Civil Engineering** _____

Prof. Dr. Murat Güler
Supervisor, **Civil Engineering, METU** _____

Assoc. Prof. Dr. Hande Işık Öztürk
Co-Supervisor, **Civil Engineering, METU** _____

Examining Committee Members:

Prof. Dr. İsmail Özgür Yaman
Civil Engineering, METU _____

Prof. Dr. Murat Güler
Civil Engineering, METU _____

Prof. Dr. Mustafa Şahmaran
Civil Engineering, Hacettepe University _____

Assoc. Prof. Dr. Çağla Meral Akgül
Civil Engineering, METU _____

Asst. Prof. Dr. Reza Shabani
Civil Engineering, Atılım University _____

Date: 24.01.2024

I hereby declare that all information in this document has been obtained and presented in accordance with academic rules and ethical conduct. I also declare that, as required by these rules and conduct, I have fully cited and referenced all material and results that are not original to this work.

Name Last name : Duygu Demirtürk

Signature :

ABSTRACT

INVESTIGATION OF MIX DESIGN PARAMETERS AFFECTING THE THERMAL PROPERTIES OF ASPHALT CONCRETE UNDER TRANSIENT AND STEADY-STATE HEAT TRANSFER CONDITIONS

Demirtürk, Duygu
Doctor of Philosophy, Civil Engineering
Supervisor : Prof. Dr. Murat Güler
Co-Supervisor: Assoc. Prof. Dr. Hande Işık Öztürk

January 2024, 219 pages

The reliability of the measurement methods and the thermal properties of the mix components play a crucial role in determining the thermal properties of asphalt concrete. In this thesis, a study plan is proposed to analyze the effect of mix design parameters on the thermal properties of asphalt concrete under both transient and steady-state heat transfer conditions. The laboratory samples are prepared using the Superpave Gyratory Compactor and cut into appropriate sizes for testing under steady-state and transient conditions. The measurement of thermal conductivity under transient conditions is conducted using a Transient Plane Source (TPS) device. While a steady-state test setup is developed in the laboratory to measure thermal conductivity, a separate calorimetry-based setup is used to measure the specific heat capacity of the samples. The results obtained with the TPS device show that not only the microstructural properties of the mixture but also the mix design parameters, i.e., the aggregate type, the air void content, and the maximum aggregate size, are important for the thermal conductivity of the samples. The measurements with the calorimetry-based setup show that all mixture components, i.e., aggregates, bitumen, and air voids, as well as the initial conditioning temperature, influence the specific heat capacity of the samples. Under steady-state conditions, only the aggregate type

appears to be an influential factor, while the other properties of the mixture are all insignificant. Given the measured thermal properties, it appears that the aggregate type is by far the most influential mixture component affecting the thermal properties of the mixtures.

Keywords: Thermal Conductivity, Specific Heat Capacity, Heat Transfer, Transient Plane Source, Asphalt Concrete

ÖZ

GEÇİCİ VE SÜREKLİ DURUM ISI TRANSFER KOŞULLARI ALTINDA ASFALT BETONUNUN ISIL ÖZELLİKLERİNİ ETKİLEYEN KARIŞIM TASARIM PARAMETRELERİNİN İNCELENMESİ

Demirtürk, Duygu
Doktora, İnşaat Mühendisliği
Tez Yöneticisi: Prof. Dr. Murat Güler
Ortak Tez Yöneticisi: Doç. Dr. Hande Işık Öztürk

Ocak 2024, 219 sayfa

Ölçüm yöntemlerinin güvenilirliği ve karışım bileşenlerinin ısıl özellikleri, asfalt betonunun ısıl özelliklerini belirlemede önemli bir rol üstlenir. Bu tezde, geçici ve kararlı durum ısı transfer koşulları altında asfalt betonunun ısıl özelliklerini etkileyen karışım tasarım parametrelerini incelemek üzere bir çalışma planı önerilmektedir. Çalışmada, Superpave yoğurmalı pres cihazı kullanılarak sıkıştırılan deney numuneleri, kararlı ve geçici ısı transfer koşulları altında yapılacak testler için uygun boyutlarda hazırlanmaktadır. Geçici ısı transfer koşulları altında ısıl iletkenlik, Geçici Düzlem Kaynak (TPS) cihazı ile ölçülmektedir. Laboratuvarda, numunelerin ısıl iletkenliğini ölçmek için kararlı durum test yöntemleri esas alınarak bir test düzeneği geliştirilirken numunelerin özgül ısı kapasitelerinin ölçümü için ise kalorimetri yaklaşımına dayalı ayrı bir test düzeneği kullanılmaktadır. TPS cihazı kullanılarak elde edilen sonuçlar, karışımın mikroyapısal özelliklerinin yanı sıra, karışım tasarım parametrelerinin de (agrega tipi, hava boşluğu içeriği ve maksimum agrega boyutu gibi) numunelerin ısıl iletkenliği üzerinde önemli bir rol oynadığını göstermektedir. Kalorimetri test düzeneğinde yapılan ölçümler, tüm karışım bileşenlerinin (agrega, bitüm ve hava boşluklarının) yanı sıra başlangıç

koşullandırma sıcaklığının numunelerin özgül ısı kapasitesini etkilediğini ortaya koymaktadır. Kararlı durum koşullarında yapılan ısıl iletkenlik ölçümlerinde ise karışımın diğer özelliklerinin hemen hemen hiç etkisi görülmezken, agrega tipinin etkili bir faktör olduğu dikkat çekmektedir. Ölçülen ısıl özellikler dikkate alındığında, karışımların ısıl özellikleri üzerinde agrega tipinin en belirgin etkiye sahip karışım bileşeni olduğu anlaşılmaktadır.

Anahtar Kelimeler: Isıl İletkenlik, Özgül Isı Kapasitesi, Isı Transferi, Geçici Düzlem Kaynak, Asfalt Beton.

To my grandfather

ACKNOWLEDGMENTS

Foremost, I would like to express my sincere gratitude to my supervisor, Prof. Dr. Murat Güler, for his guidance, advice, endless patience, and support throughout my thesis. Additionally, I wish to extend my deep gratitude to my co-supervisor, Assoc. Prof. Dr. Hande Işık Öztürk, for her valuable contributions, endless patience, and guidance throughout my research journey.

I would like to thank my thesis committee: Prof. Dr. İsmail Özgür Yaman, Prof. Dr. Mustafa Şahmaran, Assoc. Prof. Dr. Çağla Meral Akgül, and Asst. Prof. Dr. Reza Shabani, for their valuable advice and comments.

I want to express my profound gratitude to Prof. Dr. Eray Baran, Prof. Dr. Tolga Akış, Asst. Prof. Dr. Halit Cenan Mertol, Asst. Prof. Dr. Gökhan Tunç, Assoc. Prof. Dr. Burcu Güneş and Asst. Prof. Dr. Oğuz Güneş. The professors at Atılım University inspired me throughout my academic journey, both as a student and a graduate.

I also extend my gratitude to the transportation lab team for their support, particularly to Ahmet Sağlam for his invaluable assistance during my experiments. I also sincerely appreciate Dr. Yalçın Karakaya and Dr. Ayhan Öner Yücel for their valuable contributions.

I would like to extend special thanks to Semiha Uhde Yıldırım for her support throughout my thesis. I am also grateful to my friends Can Atakan Öztürk and Ufuk Duygu for their support. Furthermore, I will always remember the moral support of my dear friends Tuğba Öçalan, Nurgül Baldemir, Elif Şanlıalp, and İffet Gamze Mütevelli Özkan.

I want to express my deepest gratitude to my family, who have always accompanied and supported me throughout my educational journey. This learning experience was more meaningful with their endless patience and encouragement.

Finally, I am grateful to the Middle East Technical University Scientific Research Projects (METU-BAP) for their financial support under the research project GAP-303-2021-10743.

TABLE OF CONTENTS

ABSTRACT v

ÖZ vii

ACKNOWLEDGMENTS xi

TABLE OF CONTENTS xiii

LIST OF TABLES xix

LIST OF FIGURES xxiii

LIST OF ABBREVIATIONS xxxi

CHAPTERS

1 INTRODUCTION 1

1.1 Background 1

1.2 Problem Statement 3

1.3 Research Objectives 4

1.4 Scope 5

1.5 Outline of Research 6

2 LITERATURE REVIEW 9

2.1 Heat Transfer Overview 9

2.1.1 Heat Transfer Modes and Definitions 10

2.1.2 The Role of Thermal Properties in Heat Transfer 12

2.2 Heat Transfer in Asphalt Concrete 14

2.2.1 The Role of Thermal Properties in Heat Transfer 15

2.3 Experimental Methods for Measuring the Thermal Properties of Asphalt Concrete 18

2.3.1 Steady-State Methods 20
2.3.1.1 Thermal Conductivity Measurements Using Steady-State Methods in Previous Studies 23
2.3.1.2 Specific Heat Capacity Measurements Using Steady-State Methods in Previous Studies 28
2.3.2 Transient Methods 30
2.3.2.1 Thermal Conductivity Measurements Using Transient Methods in Previous Studies 38
2.3.2.2 Specific Heat Capacity Measurements Using Transient Methods in Previous Studies 42
2.4 Determination of Thermal Properties of Asphalt Concrete with Numerical Approaches 43
2.4.1 Determination of Thermal Properties of Asphalt Concrete Using Numerical Approaches in Previous Studies 44
2.5 Effects of Mixture Components on Thermal Properties of Asphalt Concrete 48
2.5.1 Effects of Aggregate on Thermal Properties of Asphalt Concrete 49
2.5.2 Effects of Bitumen on Thermal Properties of Asphalt Concrete 52
2.5.3 Effects of Air Voids on Thermal Properties of Asphalt Concrete 53
3 METHODOLOGY 57
3.1 Introduction 57
3.1.1 Classification of Experimental Groups 57
3.2 Materials 58
3.2.1 Aggregates 59
3.2.2 Bitumen 60

3.2.2.1 Mixing and Compaction Temperature 61
3.3 Superpave Mix Design 62
3.3.1 Superpave Gyratory Compactor 63
3.3.2 Control Points in the Selection of Aggregate Blends 64
3.3.3 Design Requirements in Volumetric Properties 66
3.3.4 Sample Preparation Procedure with Superpave Gyratory 68
3.3.5 Design Gradation 69
3.3.6 Optimum Bitumen Content of the Design Gradation 71
3.4 Volumetric Properties of the Compacted Samples 75
3.5 Measurement of Thermal Properties for Asphalt Concrete Samples 76
3.5.1 Measurement of Specific Heat Capacity in Asphalt Concrete Using a Calorimetry-Based Approach 77
3.5.1.1 Sample Preparation 77
3.5.1.2 Test Setup 78
3.5.1.3 Test Procedure 81
3.5.1.4 Details of Specific Heat Capacity Calculation 83
3.5.2 Measurement of Thermal Conductivity in Asphalt Concrete Using a Steady-State Approach 83
3.5.2.1 Sample Preparation 84
3.5.2.2 Test Setup 85
3.5.2.3 Test Procedure 93
3.5.2.4 Details of Thermal Conductivity Calculation 95
3.5.3 Measurement of Thermal Conductivity in Asphalt Concrete Using Transient Approach 97
3.5.3.1 Hot Disk TPS 2500S 97

3.5.3.2 Sample Preparation 98
3.5.3.3 Test Procedure 99
3.5.3.4 Thermal Conductivity Determination in the Hot Disk Constant Analyzer 103
3.6 Investigation of Microstructural Properties of Asphalt Concrete Samples 104
3.6.1 Image Processing-Based Analysis of Aggregate Distribution 105
4 RESULTS AND DISCUSSIONS 109
4.1 Evaluation of Specific Heat Capacity Results Using the Calorimetry-Based Test Method 109
4.1.1 Effect of Optimum Bitumen Content on Specific Heat Capacity 110
4.1.2 Effect of Aggregate Type on Specific Heat Capacity 111
4.1.3 Effect of Air Void Content on Specific Heat Capacity 115
4.1.4 Effect of Maximum Aggregate Size on Specific Heat Capacity 117
4.1.5 Effect of Conditioning Temperature on Specific Heat Capacity 119
4.2 Evaluation of Thermal Conductivity Results Using the Transient Plane Source Method 126
4.2.1 Effect of Aggregate Type on Thermal Conductivity 128
4.2.2 Effect of Air Void Content on Thermal Conductivity 130
4.2.3 Effect of Volumetric Properties on Thermal Conductivity 133
4.2.4 Effect of Maximum Aggregate Size on Thermal Conductivity 136
4.2.5 Effect of Microstructural Properties of the Contact Zone on Thermal Conductivity 138
4.3 Evaluation of Thermal Conductivity Results Using the Developed Steady-State Test Method 143

4.3.1 Effect of Mix Properties on Thermal Conductivity 148
4.3.2 Relationship Between Heat Flux and Temperature Difference 150
4.3.3 Parameters to Enhance the Reliability of the Developed Steady-State Test Setup 157
4.4 Comparison of Steady-State and Transient Methods 158
5 CONCLUSION AND RECOMMENDATION 163
5.1 Conclusion 163
5.2 Recommendations For Future Studies 171
REFERENCE 173
APPENDICES 193
A. Optimum Bitumen Content and Volumetric Properties 193
B. Volumetric Properties of Mix Designs 197
C. Sliced Samples Properties for The Calorimetry-Based Test Setup 201
D. Temperature & Time Curves Obtained in the Developed Steady State Method 203
E. Thermal Conductivity and Heat Flux Values in The Developed Steady-State Method 207
F. Heat Flux and Thermal Conductivity & Temperature Difference Curves 211
CURRICULUM VITAE 219

LIST OF TABLES

TABLES

Table 2.1 Three modes in heat transfer mechanism (Mahan, 2002). 10
Table 2.2 Thermal properties of asphalt mixtures in previous studies (Yu et al., 2021). 19
Table 2.3 Measurement details of asphalt concrete samples using the different TPS sensor sizes (Mirzanamadi et al., 2018). 40
Table 2.4 Thermal conductivity results obtained by the studies of Chen et al. (2015a) and Mrawira & Luca (2006). 46
Table 2.5 Thermal conductivity values of different rocks in the Sichuan Basin (Tang et al., 2019) 50
Table 2.6 Thermal conductivity of different bitumen types measured by Côté & Konrad (2013). 52
Table 3.1 Nomenclature of the samples. 58
Table 3.2 Physical properties of aggregates used in this study. 59
Table 3.3 Bitumen properties used in this study. 61
Table 3.4 The number of gyrations according to different design ESALs (specified in AASHTO R35). 64
Table 3.5 Gradation limits according to TGDH specifications for the wearing course. 65
Table 3.6 The control points and restricted zone boundary (AASHTO M 323). ... 66
Table 3.7 Volumetric design requirements according to TGDH. 67
Table 3.8 Volumetric design requirements according to AASHTO M323. 67
Table 3.9 Selected design parameters. 68
Table 3.10 Mix design classifications. 69
Table 3.11 The design gradations used in this study. 69
Table 3.12 The bulk specific gravity values of aggregate blends in mix designs. . 71
Table 3.13 Volumetric properties of each mix design in this study. 75
Table 3.14 Average volumetric properties of five replicate samples. 76

Table 3.15 Technical specifications of the FluxTeq-Heat Flux sensor. 91
Table 3.16 Summary of the experimental parameters for different materials. 102
Table 4.1 Optimum bitumen contents of the design mixtures and the average specific heat capacities of the compacted samples. 110
Table 4.2 Measured air void contents of the sliced samples. 115
Table 4.3 Comparison of specific heat capacities according to maximum aggregate sizes. 118
Table 4.4 The temperature gradients of the samples prepared with basalt and dolomite at a conditioning temperature of -2°C. 125
Table 4.5 The temperature gradients of the samples prepared with basalt and dolomite at a conditioning temperature of 20°C. 125
Table 4.6 The temperature gradients of the samples prepared with basalt and dolomite at a conditioning temperature of 40°C. 126
Table 4.7 According to the ANOVA results, the mix components effects. 127
Table 4.8 The bulk specific gravity, air void content, and thermal conductivity results of the basalt samples. 131
Table 4.9 The bulk specific gravity, air void content, and thermal conductivity results of the dolomite samples. 132
Table 4.10 The average thermal conductivity results of the samples with their volumetric properties. 134
Table 4.11 The microstructural properties of the samples prepared with basalt. 140
Table 4.12 The microstructural properties of the samples prepared with dolomite. 141
Table 4.13 Calibration coefficient of the test setup based on thermal conductivity results from Izocam Foam Board and Autoclaved Aerated Concrete samples. 143
Table 4.14 Thermal conductivity results of the samples prepared with basalt (Replicate No: 1). 145
Table 4.15 Thermal conductivity results of the samples prepared with basalt (Replicate No: 2). 146

Table 4.16 Thermal conductivity results of the samples prepared with dolomite (Replicate No: 1). 147
Table 4.17 Thermal conductivity results of the samples prepared with dolomite (Replicate No: 2). 148
Table 4.18 The relationship between mix components and thermal conductivity in the steady state using ANOVA analysis. 150
Table 4.19 Comparison of test setups prepared based on selected test methods. . 160
Table 4.20 Comparison of thermal conductivity results taken from the Hot Disk TPS 2500S test device and the developed steady-state test setup. 161
Table B. 1 Volumetric properties of Mix Design 1 with different air void contents and MAS: 19 mm. ……..... 197
Table B. 2 Volumetric properties of Mix Design 2 with different air void contents and MAS: 12.5 mm. 198
Table B. 3 Volumetric properties of Mix Design 3 with different air void contents and MAS: 19 mm. 199
Table B. 4 Volumetric properties of Mix Design 4 with different air void contents and MAS: 12.5 mm. 200
Table C. 1 For the calorimetry-based test setup, the physical properties of the sliced samples prepared with basalt……..... 201
Table C. 2 For the calorimetry-based test setup, the physical properties of the sliced samples prepared with dolomite. 202
Table E. 1 For the developed steady-state test setup, all thermal conductivity results and properties of the slices prepared with basalt (Replicate No.1)..... 207
Table E. 2 For the developed steady-state test setup, all thermal conductivity results and properties of the slices prepared with basalt (Replicate No.2). 208
Table E. 3 For the developed steady-state test setup, all thermal conductivity results and properties of the slices prepared with dolomite (Replicate No.1). 209
Table E. 4 For the developed steady-state test setup, all thermal conductivity results and properties of the slices prepared with dolomite (Replicate No.2). 210

LIST OF FIGURES

FIGURES

Figure 2.1 Radiation between a surface and the surfaces surrounding it (Cengel, 2003). 12
Figure 2.2 The approximate ranges of thermal conductivity for various materials (Lienhard & Lienhard, 2019). 13
Figure 2.3 Heat transfer modes in asphalt pavements (Basheer Sheeba & Krishnan Rohini, 2014) 15
Figure 2.4 Mechanistic Empirical Design Flow Chart (Ceylan et al., 2009; Ksaibati & Kasperick, 2015). 17
Figure 2.5 Pavement cooling curve and timescale for compaction (Timm et al., 2001). 18
Figure 2.6 Methods for measuring thermal properties (Kuvandykova & Bateman, 2013; Palacios et al., 2019). 20
Figure 2.7 Schematic diagrams of (a) Guarded Hot Plate and (b) Heat Flow Meter methods (Kim et al., 2021)..... 22
Figure 2.8 Schematic view of UNB k-alpha tester (Mrawira & Luca, 2002)..... 24
Figure 2.9 Schematic view of heat transfer diagram (Carlson et al., 2010)..... 25
Figure 2.10 Temperature values measured at different points on the sample (Xu & Solaimanian, 2010). 26
Figure 2.11 Heat transfer cell (Côté et al., 2013). 27
Figure 2.12 Schematic view of the experimental setup (Hassn et al., 2016a & 2016b). 28
Figure 2.13 Test setup for specific heat capacity measurement in asphalt concrete (Islam & Tarefder, 2014). 29
Figure 2.14 Thermal conductivity and temperature measurement ranges for steady-state and transient methods (Palacios et al., 2019). 31
Figure 2.15 Schematic view of the hot wire method (Dos Santos & Gregório, 2003). 32

Figure 2.16 Test set-up of the TPS method and side view of TPS sensor (Log & Gustafsson, 1995). 33
Figure 2.17 A modified transient plane source (Martínez-Ibáñez et al., 2021). 34
Figure 2.18 A Thermtest Inc. thermal needle (Internet source: https://www.wetec.com.sg) 34
Figure 2.19 (a) (a) A Basic LFA setup (b) the representation of the sample configuration (Philipp et al., 2020). 35
Figure 2.20 The illustration of MDSC device (Palacios et al., 2019). 37
Figure 2.21 Use of the TLS method in asphalt concrete sample (Byzyka et al., 2021). 38
Figure 2.22 The test setup of TPS device (Chen et al., 2022b). 40
Figure 2.23 Testing different samples with the MTPS (Petkova-Slipets & Zlateva, 2018). 41
Figure 2.24 Illustration of steady heat transfer in FEA (Chen et al., 2015b) 45
Figure 2.25 Generating the microstructure of aggregates using a hierarchical multiscale method (Chen et al., 2015a). 46
Figure 2.26 2D row-column representation of asphalt mixture (Chu et al., 2020). 47
Figure 2.27 Image-based model development steps (Zhao et al. 2020). 48
Figure 2.28 Endothermic and exothermic stages of aggregates (Jamshidi et al., 2017). 49
Figure 2.29 Change in thermal conductivity with coarse aggregate content (Chen et al., 2022a). 51
Figure 2.30 Effects of air voids on six sets of three-dimensional digital asphalt concrete specimens (Chen et al., 2022a). 54
Figure 2.31 Thermal conductivity of dry and water-saturated asphalt mixtures (Pan et al., 2017). 55
Figure 3.1 Variables in the experimental matrix. 58
Figure 3.2 X-ray diffraction intensity vs. diffraction angle of basalt and dolomite. 60
Figure 3.3 Temperature-viscosity curve of Pen 50/70 bitumen. 62

Figure 3.4 Superpave gyratory compactor. 63
Figure 3.5 The gradation curves of aggregate blends for Type 1 basalt and dolomite. 70
Figure 3.6 The gradation curves of aggregate blends for Type 2 basalt and dolomite. 70
Figure 3.7 Plots for determination of optimum bitumen content (Roberts et al., 1996). 72
Figure 3.8 Components in volume and mass of asphalt mixtures (Coree & Hislop, 2000). 74
Figure 3.9 Samples with sensors attached prior to testing. 78
Figure 3.10 a) Izocam foam boards, b) Insulated cabinet, c) Insulated environmental chamber, d) Samples inside the insulated cabinet. 79
Figure 3.11 A detailed illustration of the test setup. 80
Figure 3.12 The main parts of the test setup. 81
Figure 3.13 Change in temperature of water over time. 82
Figure 3.14 Samples used in the thermal conductivity measurements. 85
Figure 3.15 a) The control of the sample surface before the test and b) A thermal silicone paste. 85
Figure 3.16 The basic test configuration (specified in ASTM C518-21). 86
Figure 3.17 General view of the test setup. 87
Figure 3.18 Interior design of the insulated chamber. 88
Figure 3.19 a) The assembly of interior parts in the insulated hollow cylinder, b) temperature sensor under the cold plate, c) a heat flow meter on the hot plate, and d) a silicone heating pad under the hot plate. 89
Figure 3.20 a) Heat flux sensor positioned on the hot plate and b) schematic view of the sensor. 90
Figure 3.21 Sensitivity multiplication factor and sensor temperature chart. 91
Figure 3.22 Side insulation of the hot and cold plates in the insulated hollow cylinder. 92
Figure 3.23 The flow diagram of the test procedure. 93

Figure 3.24 Heat flux at steady state. 95
Figure 3.25 a) Izocam foam board, b) autoclaved aerated concrete, and c) asphalt concrete for the test setup calibration. 96
Figure 3.26 Hot Disk TPS 2500S Test Device and parts. 98
Figure 3.27 Schematic view of the TPS sensor and probing depth from the side... 98
Figure 3.28 The measurement areas of the TPS sensor and the placement of two identical samples in the sensor holder. 99
Figure 3.29 Contact zones on the plane surface of the sample. 101
Figure 3.30 Example of a scatter plot taken during a thermal conductivity measurement (Gunasekara et al., 2019). 103
Figure 3.31 Steps of image processing (Coenen et al., 2012). 106
Figure 3.32 Rectangular area extracted from the sample surface..... 107
Figure 3.33 Image processing steps: (a) Original image, (b) Grayscale image, (c) Median filtered, (d) H_{max} filtered, (e) After watershed transform, (f) After thresholding. 108
Figure 3.34 Detection of aggregate distribution in iPas image analysis. 108
Figure 4.1 Specific heat capacity of basalt and dolomite samples with 2% air voids, maximum aggregate size of 19 mm, and varying initial temperatures..... 112
Figure 4.2 Specific heat capacity of basalt and dolomite samples with 4% air voids, maximum aggregate size of 19 mm, and varying initial temperatures..... 112
Figure 4.3 Specific heat capacity of basalt and dolomite samples with 6% air voids, maximum aggregate size of 19 mm, and varying initial temperatures..... 113
Figure 4.4 Specific heat capacity of basalt and dolomite samples with 2% air voids, maximum aggregate size of 12.5 mm, and varying initial temperatures..... 113
Figure 4.5 Specific heat capacity of basalt and dolomite samples with 4% air voids, maximum aggregate size of 12.5 mm, and varying initial temperatures..... 114
Figure 4.6 Specific heat capacity of basalt and dolomite samples with 6% air voids, maximum aggregate size of 12.5 mm, and varying initial temperatures..... 114
Figure 4.7 Average specific heat capacities of basalt samples at three air void contents and conditioning temperatures. 116

Figure 4.8 Average specific heat capacities of dolomite samples at three air void contents and conditioning temperatures. 117
Figure 4.9 Temperature and time curves for B4T1 under three different conditioning temperatures. 120
Figure 4.10 Temperature and time curves for B4T2 under three different conditioning temperatures. 121
Figure 4.11 Temperature and time curves for D4T1 under three different conditioning temperatures. 121
Figure 4.12 Temperature and time curves for D4T2 under three different conditioning temperatures. 122
Figure 4.13 Temperature behavior characteristic of B2T1 at three conditioning temperatures. 123
Figure 4.14 Temperature behavior characteristic of D2T1 at three conditioning temperatures. 123
Figure 4.15 Preparation of the aggregate particle for the TPS measurements in this study. 128
Figure 4.16 Thermal conductivity values of the samples prepared with basalt and dolomite aggregates. 129
Figure 4.17 Distribution of thermal conductivity in the upper part (a) and bottom part (b) of the sliced samples prepared with basalt. 133
Figure 4.18 Distribution of thermal conductivity in the upper part (a) and bottom part (b) of the sliced samples prepared with dolomite. 133
Figure 4.19 The relationship between the average thermal conductivities of the entire samples and the density of the mixtures prepared with basalt and Type 1 and Type 2 gradations. 135
Figure 4.20 The relationship between the average thermal conductivities of the entire samples and the density of the mixtures prepared with dolomite and Type 1 and Type 2 gradations. 135
Figure 4.21 Change in thermal conductivity of basalt samples at different air void contents and maximum aggregate sizes. 137

Figure 4.22 Change in thermal conductivity of dolomite samples at different air void contents and maximum aggregate sizes. 137
Figure 4.23 a) Top view of the TPS sensor, b) Schematic view of TPS sensor from the side, and c) TPS sensor contact zones on the section surface. 139
Figure 4.24 Relationship between thermal conductivity values and total aggregate area values of the samples prepared with basalt. 142
Figure 4.25 Relationship between thermal conductivity values and total aggregate area values of the samples prepared with dolomite. 142
Figure 4.26 The change in heat flux and thermal conductivity values of the first slice of B4T1. 153
Figure 4.27 The change in heat flux and thermal conductivity values of the second slice of B4T1. 153
Figure 4.28 The change in heat flux and thermal conductivity values of the first slice of B4T2. 154
Figure 4.29 The change in heat flux and thermal conductivity values of the second slice of B4T2. 154
Figure 4.30 The change in heat flux and thermal conductivity values of the first slice of D4T1. 155
Figure 4.31 The change in heat flux and thermal conductivity values of the second slice of D4T1. 155
Figure 4.32 The change in heat flux and thermal conductivity values of the first slice of D4T2. 156
Figure 4.33 The change in heat flux and thermal conductivity values of the second slice of D4T2. 156
Figure A. 1 Optimum bitumen content and volumetric properties for Mix Design 1. 193
Figure A. 2 Optimum bitumen content and volumetric properties for Mix Design 2. 194
Figure A. 3 Optimum bitumen content and volumetric properties for Mix Design 3. 195

Figure A. 4 Optimum bitumen content and volumetric properties for Mix Design 4. 196
Figure D. 1 The temperature & time curves of B2T1 under three different conditioning temperatures..... 203
Figure D. 2 The temperature & time curves of B2T2 under three different conditioning temperatures..... 203
Figure D. 3 The temperature & time curves of B6T1 under three different conditioning temperatures..... 204
Figure D. 4 The temperature & time curves of B6T2 under three different conditioning temperatures..... 204
Figure D. 5 The temperature & time curves of D2T1 under three different conditioning temperatures..... 205
Figure D. 6 The temperature & time curves of D2T2 under three different conditioning temperatures..... 205
Figure D. 7 The temperature & time curves of D6T1 under three different conditioning temperatures..... 206
Figure D. 8 The temperature & time curves of D6T2 under three different conditioning temperatures..... 206
Figure F. 1 The change in heat flux and thermal conductivity values of first slice made with basalt, 2% air void content and Type 1 gradation..... 211
Figure F. 2 The change in heat flux and thermal conductivity values of second slice made with basalt, 2% air void content and Type 1 gradation..... 211
Figure F. 3 The change in heat flux and thermal conductivity values of first slice made with basalt, 6% air void content and Type 1 gradation..... 212
Figure F. 4 The change in heat flux and thermal conductivity values of second slice made with basalt, 6% air void content and Type 1 gradation..... 212
Figure F. 5 The change in heat flux and thermal conductivity values of first slice made with basalt, 2% air void content and Type 2 gradation..... 213
Figure F. 6 The change in heat flux and thermal conductivity values of second slice made with basalt, 2% air void content and Type 2 gradation..... 213

Figure F. 7 The change in heat flux and thermal conductivity values of first slice made with basalt, 6% air void content and Type 2 gradation. 214
Figure F. 8 The change in heat flux and thermal conductivity values of second slice made with basalt, 6% air void content and Type 2 gradation. 214
Figure F. 9 The change in heat flux and thermal conductivity values of first slice made with dolomite, 2% air void content and Type 1 gradation.....215
Figure F. 10 The change in heat flux and thermal conductivity values of second slice made with dolomite, 2% air void content and Type 1 gradation.....215
Figure F. 11 The change in heat flux and thermal conductivity values of first slice made with dolomite, 6% air void content and Type 1 gradation.....216
Figure F. 12 The change in heat flux and thermal conductivity values of second slice made with dolomite, 6% air void content and Type 1 gradation.....216
Figure F. 13 The change in heat flux and thermal conductivity values of first slice made with dolomite, 2% air void content and Type 2 gradation.....217
Figure F. 14 The change in heat flux and thermal conductivity values of second slice made with dolomite, 2% air void content and Type 2 gradation.....217
Figure F. 15 The change in heat flux and thermal conductivity values of first slice made with dolomite, 6% air void content and Type 2 gradation.....218
Figure F. 16 The change in heat flux and thermal conductivity values of second slice made with dolomite, 6% air void content and Type 2 gradation.....218

LIST OF ABBREVIATIONS

2D: 2-dimensional

3D: 3-dimensional

AASHTO: American Association of State Highway and Transportation

ANOVA: Analysis of Variance

ASTM: American Society of Testing and Materials

DSC: Differential Scanning Calorimetry

FE: Finite Element

FEA: Finite Element Analysis

FEM: Finite Element Method

GHP: Guarded Hot Plate

GSHP: Ground Source Heat Pump

HFM: Heat Flow Meter

HMA: Hot Mix Asphalt

LFA: Laser/Flight Flash Analysis

MAS: Maximum Aggregate Size

MDSC: Modulated Differential Scanning Calorimetry

MEPDG: Mechanistic-Empirical (M-E) Pavement Design Guide

MTLS: Modified Transient Line Source

MTPS: Modified Transient Plane Source

NMAS: Nominal Maximum Aggregate Size

PG: Performance Grade

PHFS: Plate Heat Flux Sensor

SDT: Surface Distance Threshold

SHRP: Strategic Highway Research Program

Superpave: Superior Performing Asphalt Pavements

TGDH: Turkish General Directorate of Highways

TLS: Transient Line Source

TPS: Transient Plane Source

V_a: Air Void Content

V_{ba} : Volume of Absorbed Asphalt

VFA: Voids Filled with Asphalt

VMA: Voids in the Mineral Aggregate

CHAPTER 1

INTRODUCTION

1.1 Background

Asphalt mixture is susceptible to temperature changes due to the asphalt binder's viscoelastic nature (Pan et al., 2017; Yu et al., 2021). Therefore, temperature changes in the field determine the thermal behavior of asphalt concrete pavements (Chen et al., 2015a). At high temperatures, it is relatively soft and prone to rutting or permanent deformation (Xu & Mohammad, 2008). At low temperatures, on the other hand, it is relatively brittle and more susceptible to thermal cracking (Xu & Solaimanian, 2010). In asphalt pavements, heat transfer takes place by convection, radiation and conduction, which are site-dependent factors that influence the overall thermal performance of the pavements (Shamsaei et al., 2022). Convection is a heat transfer mode between the pavement surface and the ambient air (Chiarelli et al., 2017). Solar radiation causes radiation in the asphalt pavement, which leads to heat accumulation due to the dark color of the pavement (Gong et al., 2023). Conduction is the heat flow from high to low temperatures within the pavement layers (Jbeili & Zhang, 2021). It is known that the modes of heat transfer in asphalt pavements depend on critical factors such as surface color, surface roughness, thermal properties of asphalt mixtures, wavelength of incident radiation, etc. (Aletba et al., 2021; Shamsaei et al., 2022).

Thermal conductivity and specific heat capacity are the most commonly used thermal properties to determine the ability of asphalt concrete to change its volume due to temperature changes, as well as its ability to conduct and absorb heat (Mamlouk et al., 2005). Therefore, they play a crucial role in evaluating the thermal

performance of asphalt concrete pavements (Dawson et al., 2012; Islam & Tarefder, 2014; Mirzanamadi et al., 2018; Khasawneh et al., 2023). In particular, thermal conductivity is often used in the thermal analysis of pavements exposed to different climatic conditions (Côté et al., 2013). The other thermal properties are also used as input parameters for many recent approaches, self-healing asphalt pavements, solar panel applications and mitigation of urban heat island effects, etc. (Garcia et al., 2013; Han et al., 2021; Abbas & Alhamdo, 2023).

Two main methods are used in the literature to measure the thermal properties of asphalt concrete: steady-state and transient methods (Kuvandykova & Bateman, 2013; Elkholy et al., 2019; Byzyka et al., 2021). Although there have been only a few studies on measuring the specific heat capacity of asphalt concrete, researchers have mainly focused on determining the thermal conductivity using various methods. However, field measurements have so far failed to correlate with the results obtained using these laboratory methods (Islam & Tarefder, 2014). This can be explained by the inherent limitations of the proposed methods (Luca & Mrawira, 2005; Chen et al., 2015a). For the steady-state methods, a long test duration to achieve a constant temperature difference is one of the limitations mentioned (Kuvandykova & Bateman, 2013). Another limitation is that the sample depth should not be more than 1/3 of the largest sample dimension to ensure one-dimensional heat transfer through the measurement section (Luca & Mrawira, 2005). Despite these limitations, it is stated that the steady-state method can still provide more accurate results for heterogeneous materials.

Recently, transient methods have also been proposed as an alternative to steady-state methods. They are defined as fast and new measurement approaches (Elkholy et al., 2019). In particular, the Transient Plane Source (TPS) method is chosen for measuring the thermal properties of asphalt mixtures (Mirzanamadi et al., 2018; Khasawneh et al., 2023). However, in the TPS method, the measurement mainly depends on the thermal resistance of the TPS sensor. The TPS sensor assumes that the sensor diameter determines an infinite medium and the measurement depth (Log & Gustafsson, 1995). Although this approach does not lead to deviations in the

results for homogeneous materials, it is not as reliable for heterogeneous materials and remains controversial when applied to asphalt concrete (Bouguerra et al., 2001).

In the scope of this study, not only the measurement of thermal properties but also their relationship with mixture properties is considered. This is because the changes in the asphalt mixture properties significantly affect its thermal properties thus, its thermal performance. In particular, if appropriate mixture properties are selected and correct mix designs are used, distress due to thermal behavior can be reduced in the field. As a result, the effects of aggregate type, air void content, maximum aggregate size, aggregate gradation, etc., on thermal properties have been investigated by many researchers (Luca & Mrawira, 2005; Mrawira & Luca, 2006; Hassan et al., 2016b; Mirzanamadi et al., 2018; Khasawneh et al., 2023). However, it should be noted that previous studies have ignored the influence of the measurement method used when considering the effects of mixture properties on thermal properties. Therefore, further research is needed to determine the effects of mix properties on thermal properties to obtain more trustworthy results. In this study, a comparative evaluation is conducted to show the effects of mix properties on the thermal properties of asphalt concrete based on the developed test setups.

1.2 Problem Statement

There is currently no standard test method to determine the thermal properties of asphalt concrete pavements. Although some attempts have been made recently using steady-state and transient methods, more research effort is required to highlight the key properties affecting the thermal behavior of asphalt concrete. In particular, new test setups should be developed to eliminate the limitations of test methods identified in the literature. Apart from this, a comparative study has not been conducted yet for the test methods to discuss their suitability and their deficiencies. Thus, the impact of the test method used in obtaining thermal properties is still unknown. On the other hand, it is stated that while some mix properties significantly influence thermal properties in some test methods, they appear insignificant in others. To clarify this

discrepancy, the effects of mix properties on thermal properties should be explained in relation to the measurement method used. In summary, this study acknowledges the need for a comprehensive evaluation of the mix properties affecting the thermal properties, as well as a comparison of the test methods used.

1.3 Research Objectives

The main objective of this study is to investigate the effects of mix properties on thermal properties and show that the steady-state and transient methods used influence the measurement results. The specific objectives of the study can also be summarized as follows:

1. To design an experimental setup based on a calorimetry device for measuring the specific heat capacity of the asphalt mixtures.
2. To develop an experimental setup for measuring the thermal conductivity of asphalt mixtures using the steady-state approach and improve the applicability of this setup in accordance with ASTM C518-21.
3. To apply the Transient Plane Source (TPS) method for measuring the thermal conductivity of asphalt mixtures and show the deficiencies of the transient heat transfer approach in thermal conductivity measurements for asphalt mixtures.
4. To compare the efficiency and applicability of steady-state and transient methods to asphalt mixtures.
5. To determine the effects of the volumetric properties and components of the mixture, particularly aggregate type, air void content, and aggregate gradation, on thermal properties.
6. To monitor the temperature change throughout the measurement at the calorimeter-based test setup and discuss the effects of the conditioning temperature of the samples on the specific heat capacity.

7. To investigate the influence of the distribution of the mix components on the contact zone of the TPS sensor, i.e., the microstructural properties of the measuring surface, on the thermal conductivity.
8. To discuss the effect of internal structural properties varying along the sample depth on the results obtained in the developed steady-state method.

1.4 Scope

This study focuses primarily on achieving three key phases. The first phase involves sample preparation, where four asphalt mix designs with two different aggregates (basalt and dolomite) and two different maximum aggregate sizes (19 and 12.5 mm) are prepared using the same asphalt cement according to the Superpave mix design method. In addition to the samples with optimum air void content (4%), samples with air void content of 2% and 6% are also compacted to further analyze the influence of air void content on thermal properties. Once a sufficient number of samples are prepared, the dimensions and surfaces of the samples are adjusted (trimmed and cored) according to the requirements of the test methods.

The second phase aims to develop test setups for the measurement of thermal properties and to define applicable test principles. Two different test setups are developed based on the steady-state method. Firstly, a newly developed calorimeter cabinet are used to measure the specific heat capacity. Secondly, a test setup is developed to measure thermal conductivity according to the procedures specified in ASTM C177-19 and ASTM C518-21. Finally, the TPS method is chosen to investigate the transient approach in measuring the thermal conductivity of asphalt concrete samples.

The third phase aims to discuss the results of the specific heat capacity and thermal conductivity of asphalt mixtures and the effects of the different mixture properties on the results. In addition, the results of the thermal conductivity measurements obtained with steady-state and transient methods are compared. In this way, it will

be possible to evaluate the applicability and reliability of the methods used. Finally, the results of statistical analyses from both methods are used to evaluate the significance of mixture properties in determining thermal conductivity.

1.5 Outline of Research

This study begins with an introductory section in which the significance and purpose of the research are emphasized. The introduction is followed by a comprehensive review of the existing literature on determining and analyzing the thermal properties of asphalt concrete.

Chapter 2 begins by explaining the phenomena of heat transfer in asphalt concrete. Then, the previous studies on the determination of thermal properties are presented and the importance of these properties for heat transfer is emphasized. Finally, recent studies investigating the effects of mix properties on thermal properties are summarized.

Chapter 3 describes the properties of the materials used and the steps of sample preparation. This chapter also explains the proposed methods, outlines the research methodology and presents the necessary test equipments in detail. The design of the test setups and the test procedures developed are then explained in detail.

In Chapter 4, the results of the measurements for the specific heat capacity using a calorimeter-based setup is presented. Subsequently, the results of the thermal conductivity measurements with the developed steady-state setup and the TPS methods are presented. In this section, the effects of mixture properties on the thermal properties are critically evaluated for each method and supported with the statistical analysis results. In addition, the results of image analysis are presented to clarify the results of the TPS method. Finally, a comparison between steady-state and transient methods is made based on the results.

Chapter 5 presents the results, evaluates the test methods used, analyzes the significance of the results, and makes recommendations for improving future test designs. An outlook for further research is also given.

CHAPTER 2

LITERATURE REVIEW

This section briefly explains the heat transfer phenomena in asphalt concrete. In particular, the advances in research on the thermal properties of asphalt concrete are discussed. It also examines the role of experimental and numerical methods in determining the thermal properties. Finally, the results of previous works investigating the effects of mix constituents on the thermal properties of asphalt concrete are reviewed.

2.1 Heat Transfer Overview

Heat transfer is a fundamental phenomenon of energy transport that is generally triggered by a temperature difference (Chen, 2005). When a system has a temperature gradient, heat energy flows from the high to low-temperature areas (Kreith & Bohn, 2001; Kothandaraman, 2006). Understanding the heat transfer mechanism is crucial for solving many engineering problems as well as global problems such as global warming, urban heat islands (UHI), energy crisis and heating of electronic devices, etc. (Li et al., 2021).

Heat transfer in asphalt concrete is also an essential phenomenon in pavement engineering. Heat transfer and temperature distribution directly affect the thermal performance of asphalt pavements (Aletba et al., 2021). This is because asphalt concrete is a temperature-sensitive material exposed to thermal differences during its service life. Therefore, it is necessary to understand the basic principles of the heat transfer mechanism. In this context, a summary of the general information on heat transfer is given below.

2.1.1 Heat Transfer Modes and Definitions

Heat transfer occurs in three main ways: conduction, radiation, and convection. The basic mechanisms of these modes are summarized in Table 2.1 (Annaratone, 2010).

Table 2.1 Three modes in heat transfer mechanism (Mahan, 2002).

Heat Transfer Modes	**Model or "Law"**	**Coefficient Defined by Model**	**Range of Temperature Exponent**
Conduction	Fourier's Law	Thermal Conductivity	1.0-1.1
Convection	Newton's Law of Cooling	Heat Transfer Coefficient	1.0-2.0
Radiation	The Stefan-Boltzmann Law	Emissivity	4.0-5.0

Conduction occurs when interactions between more energetic and neighboring, less energetic particles of a substance lead to the transfer of energy from one particle to the other (Cengel, 2003). The Fourier equation in Equation 2.1 is the general equation for one-dimensional heat conduction in a material.

$$Q_{cond} = -kA\frac{dT}{dx} \qquad 2.1$$

Q_{cond} (W) refers to the rate of heat flow in one direction. The proportionality constant, k (W/m.°C) is the thermal conductivity of the material. The heat transfer area, A (m^2) is always normal to the direction of heat flux. The dT/dx expression is used to express the thermal gradient.

Convection occurs in situations in which energy in the form of heat is transferred to a flowing fluid at the surface over which the flow takes place (Kothandaraman, 2006). In this mode, the effects of conduction and fluid motion work together. The rate of heat transfer by convection between a surface and a fluid can be calculated

by Newton's law of cooling equation (Solaimanian & Kennedy, 1993; Hermansson, 2001; Cengel 2003), as given in Equation 2.2.

$$Q_{conv} = hA_s(T_s - T_\infty) \quad 2.2$$

In general, h (W/m.°C) depends on the geometry of the surface, the wind velocity, and the physical properties of the fluid. A_s (m^2) refers to the surface area through which convection takes place, T_s (°C) is the surface temperature and T_∞ (°C) is the temperature of the liquid far enough from the surface. Because these parameters are not always fixed on a surface, the convection heat transfer coefficient can vary from one point to the next. As a result, distinguishing between a local and an average convection heat transfer coefficient is required.

When atomic or molecular electronic configurations change, it releases or transmits energy as electromagnetic waves. This phenomenon is known as radiation (Weisstein, 2014). Radiation is different from the heat transfer mechanisms of conduction and convection, since it does not require a material medium or temperature gradient (Kothandaraman, 2006). At temperatures above absolute zero, all objects emit thermal radiation (Cengel, 2003). According to the Stefan–Boltzmann law, the maximum rate of radiation emission from a surface at an absolute temperature T_s (°C) is as follows:

$$Q_{emit,max} = \sigma A_s T_S^4 \quad 2.3$$

where $\sigma = 5.6704 \times 10^{-8}$ $W/m^2.K^4$ is the Stefan–Boltzmann constant. A blackbody is an idealized surface that emits radiation at this maximum rate. The radiation emitted by a blackbody is then referred to as blackbody radiation. Conversely, at a given temperature, real surfaces typically emit and absorb less heat than a blackbody. This is expressed by the following equation.

$$Q_{emit,max} = \varepsilon \sigma A_s T_S^4 \quad 2.4$$

In Equation 2.4, ε is referred to as the surface's emissivity. The emissivity with values between 0 and 1 indicates the extent to which a surface resembles a black

body, with a value of 1 meaning an ideal black body. Absorptivity, symbolized as α, is another radiation coefficient that describes the amount of incident radiant energy that a surface absorbs. Generally, the temperature and wavelength of the radiation affect both Ɛ and α of a surface. Moreover, Kirchhoff's law states that absorbed and incident radiation is in balance, as shown in Figure 2.1 (Cengel, 2003). In this direction, the radiation absorption rate of a surface is given by the following Equation 2.5.

$$Q_{absorbed} = \alpha Q_{incident} \qquad 2.5$$

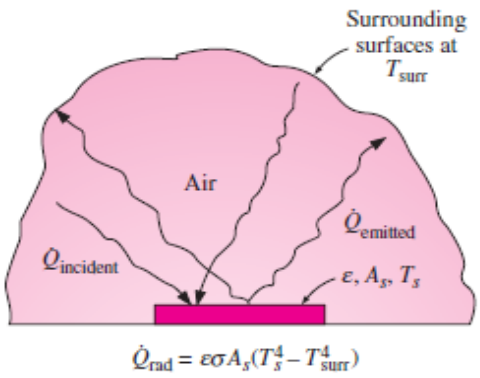


Figure 2.1 Radiation between a surface and the surfaces surrounding it (Cengel, 2003).

2.1.2 The Role of Thermal Properties in Heat Transfer

The kinetic theory of gases is a fundamental model for describing the thermodynamic properties of gases (Kreith & Bohn, 2001). According to this theory, the molecular velocity is temperature dependent, and thus, the thermal properties of materials are also temperature dependent (Lienhard & Lienhard, 2019). Moreover, thermal properties depend on the material's structure (Boháč, 2017). Hence, different materials behave differently when exposed to thermal changes. Understanding heat transfer in a material is synonymous with understanding its thermal properties. In this context, the definitions of thermal properties are briefly explained below.

The thermal conductivity of a material represents its ability to conduct heat. It is a fundamental materials' physical property. At room temperature, k = 0.608 W/m.°C for water and k = 80.2 W/m.°C for iron, indicating that iron conducts heat about 100 times faster than water. Essentially, high thermal conductivity means effective heat conduction, while low conductivity indicates poor heat conduction. This result is mainly about the material structure. In addition, the grain size, temperature, porosity, direction of heat flow and chemical composition have a substantial impact on thermal conductivity (Liu & Chen, 2014). Thus, the thermal conductivity range is enormous and is summarized below in Figure 2.2.

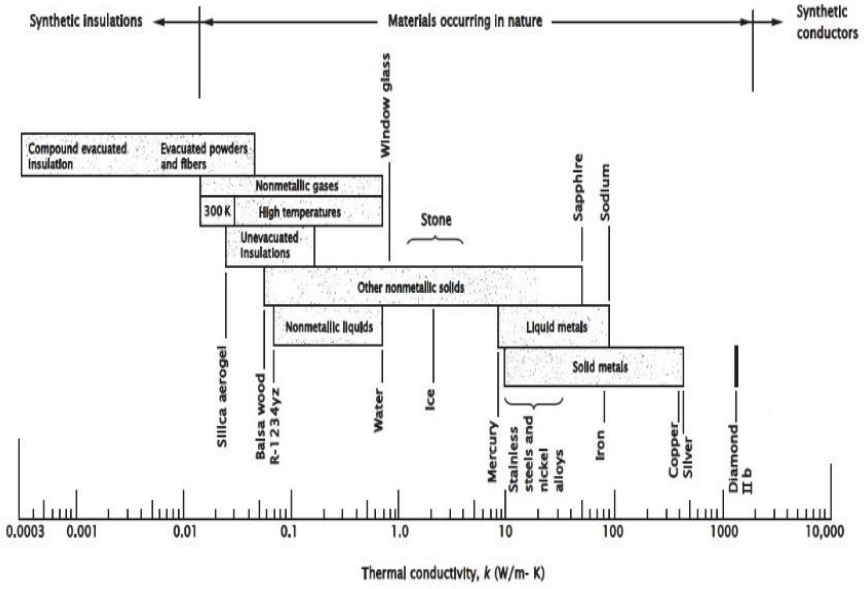


Figure 2.2 The approximate ranges of thermal conductivity for various materials (Lienhard & Lienhard, 2019).

Specific heat capacity refers to the material's ability to store heat (Chen et al., 2019). For instance, at room temperature, C_p = 4.18 kJ/kg.°C for water and C_p = 0.45 kJ/kg.°C for iron, showing that water has a nearly 10 times greater capacity for energy storage than iron. The subsequent formula calculates the specific heat

capacity, C_p (J/kg.°C). According to Equation 2.6, m (kg) indicates the mass, Q (Joule) is the thermal energy and ΔT (°C) represents the temperature difference.

$$Q = mC_p\Delta T \quad 2.6$$

Thermal diffusivity is another thermal property that plays a role in the analysis of transient heat conduction. It is also defined as a representation of the heat propagation rate within a substance. Equation 2.7 is used for the calculation of thermal diffusivity.

$$A = \frac{\text{Heat Conducted}}{\text{Heat Stored}} = \frac{k}{\rho C_p} \quad 2.7$$

In the above equation, the thermal conductivity (k) and the heat storage capacity (ρC_p) of the materials are used. Thus, the thermal diffusivity of a substance can be defined as the proportion of the heat conducted through the substance and the heat absorbed per unit volume. In brief, a material with high thermal conductivity or low specific heat capacity exhibits a high rate of heat conduction (Cengel, 2003; Kreith & Bohn, 2001).

2.2 Heat Transfer in Asphalt Concrete

One of the most popular pavement materials worldwide is asphalt concrete and is defined as a multiphase granular material composed mainly of aggregates, air, and asphalt binder (Chen et al., 2019; Yang et al., 2021; Shamsaei, 2022). The aggregates form the structural framework of the pavement, while the asphalt binder acts as an adhesive that holds the mixture together (Kandhal et al., 1997). The asphalt binder is also defined as a thermoplastic material whose behavior changes with temperature (Chen et al., 2015a). Therefore, heat transfer in asphalt concrete is complex due to the different thermophysical properties of its constituents (Kuvandykova & Bateman, 2013).

Heat transfer in asphalt concrete occurs due to daily and seasonal temperature variations (Mamlouk et al., 2005; Khadrawi et al., 2012; Islam & Tarefder, 2014;

Chen et al., 2015a; Byzyka et al., 2021). In other words, the temperature profile in asphalt concrete is directly affected by the ambient thermal conditions to which it is exposed (Basheer Sheeba & Krishnan Rohini, 2014). Moreover, the change in pavement temperature is essentially a physical process governed by heat transfer theory (Chen et al., 2019). Heat transfer in asphalt concrete occurs through radiation, conduction, and convection (Annaratone, 2010). As shown in Figure 2.3, the predominant mode of heat transfer in pavement is conduction. Heat flux between the pavement surface and the external environment occurs via convection and radiation (Chen et al., 2019). Heat transfer modes in asphalt pavements depend on several factors, such as the surface color, the surface roughness, the thermal properties, environmental conditions, and the wavelength of the incident radiation, etc. (Shamsaei et al., 2022).

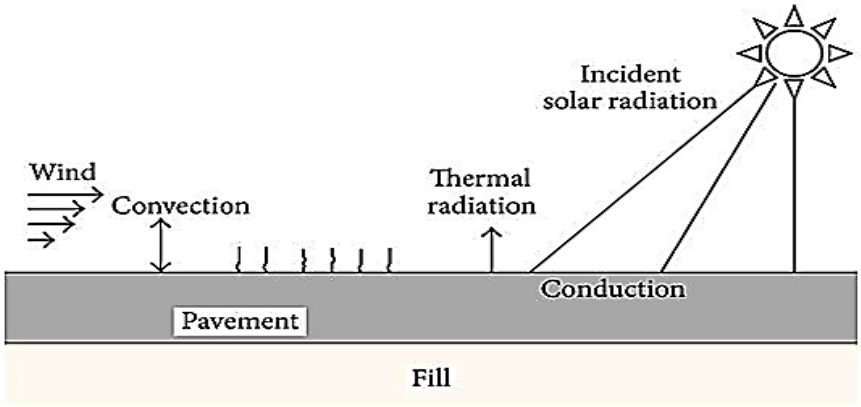


Figure 2.3 Heat transfer modes in asphalt pavements (Basheer Sheeba & Krishnan Rohini, 2014)

2.2.1 The Role of Thermal Properties in Heat Transfer

Principally, the coefficient of thermal expansion, thermal conductivity, specific heat capacity, and thermal diffusivity characterize the thermal properties of asphalt concrete (Luca & Mrawira, 2005; Dawson et al., 2012; Islam & Tarefder, 2014; Mirzanamadi et al., 2018). These characteristics identify the material's capacity to

undergo volumetric changes in response to variations in temperature, as well as its capability to conduct and absorb heat (Mamlouk et al., 2005). Therefore, many researchers have used them as essential inputs for numerous studies on heat transfer in asphalt concrete. The following list contains critical research topics that require thermal properties in pavement engineering.

1. Thermal stresses and strains resulting from changes in temperature in asphalt concrete vary depending on its thermal properties (Zhong & Geng, 2009; Islam & Tarefder, 2014).

2. The amount of heat absorbed and stored in asphalt pavement and its impact on the environment are also determined by the thermal properties of asphalt concrete. For example, the high surface temperature, especially in summer, together with the traffic load, leads to thermal oxidation and plastic deformation, which accelerates the problem of rutting (Abbas & Alhamdo, 2023; Khasawneh et al., 2023).

3. The thermal conductivity of asphalt pavements is low, and asphalt pavements absorb much solar radiation due to their dark color, which results in heat accumulation and a rise in the surface temperature (Gong et al., 2023). Thus, a high surface temperature exacerbates the Urban Heat Island (UHI) effect (Calkins, 2012).

4. Pavement surface temperature affects pavement mechanical performance, frost effect in the subgrade, and winter maintenance. Therefore, heat transfer models have been used to predict pavement surface temperature over the past three decades (Minhoto et al., 2005; Ayasrah et al., 2023). However, the change in pavement surface temperature is complex because internal and external variables influence it (Qin et al., 2022).

5. Heating methods based on the heat transfer mechanism are usually recommended for self-healing microcracks. Therefore, determining the thermal properties is essential for applying these methods (García et al.,

2013; Sun et al., 2017; Grossegger & Garcia, 2019; Concha & Norambuena-Contreras, 2020; Liang et al., 2021).

6. The New Mechanistic Empirical Pavement Design Guide (MEPDG) offers users with an integrated set of models (climate + traffic + materials) that predict future performance using a variety of empirical models, as shown in Figure 2.4. This design guide uses thermal properties as crucial inputs (Ceylan et al., 2009).

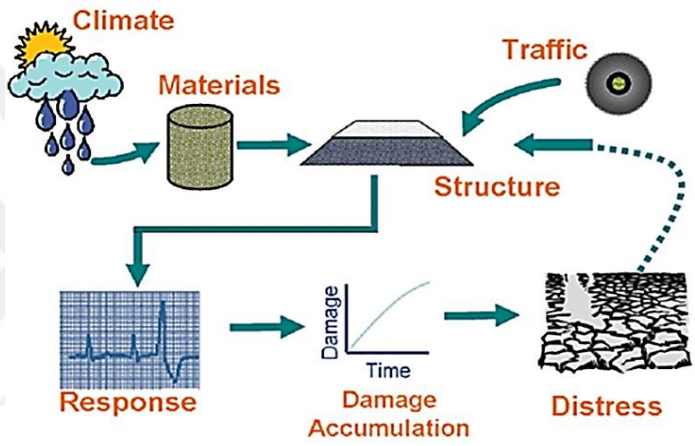


Figure 2.4 Mechanistic Empirical Design Flow Chart (Ceylan et al., 2009; Ksaibati & Kasperick, 2015).

7. According to Timm et al. (2001), overstressed and understressed conditions are two difficulties encountered in the compaction of asphalt mixtures, as shown in Figure 2.5. In both cases, achieving the optimum density is difficult, so the pavement's cooling rate should be considered. To figure out the rate at which pavements cool, thermal properties such as thermal conductivity, specific heat capacity, and thermal diffusivity are presently vital. Various models have recently been developed to monitor the cooling rate of pavements during construction. In this way, it is inevitable to use the thermal properties to adjust the cooling rate and the test cost (Highter & Wall, 1984).

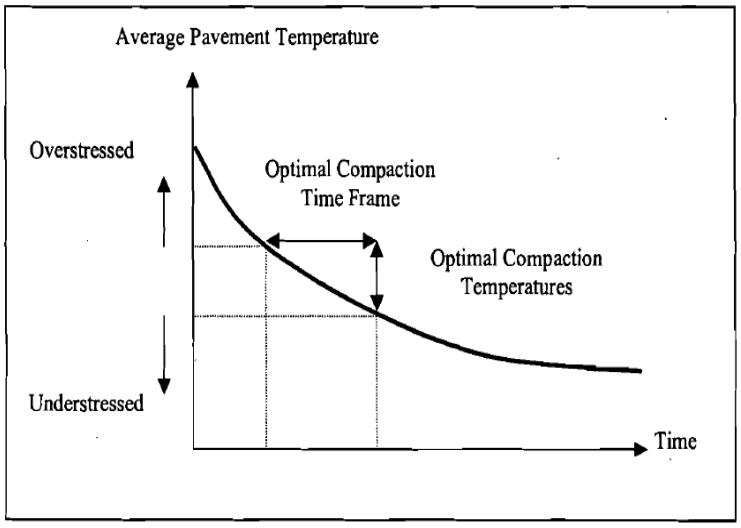


Figure 2.5 Pavement cooling curve and timescale for compaction (Timm et al., 2001).

It is clear from the numerous applications listed above that thermal properties are important considerations when choosing pavement, designing it, using construction techniques, maintaining and restoring it over time, conducting urban climate studies, etc. (Carlson et al., 2010). Therefore, conducting studies to determine the thermal properties of asphalt mixtures is inevitable. The following section presents the proposed experimental methods for determining the thermal properties of asphalt concrete.

2.3 Experimental Methods for Measuring the Thermal Properties of Asphalt Concrete

The determination of thermal properties is becoming increasingly important. Specifically, measuring thermal conductivity is the focus of various experimental studies. Besides thermal conductivity, specific heat capacity is another crucial thermal property central to recent research. If precisely measured, these properties allow direct calculation of thermal diffusivity using Equation 2.7. Although many researchers have been interested in thermal properties in the past, more studies are

still needed (See Table 2.2). Since the thermal properties of bitumen and asphalt mixtures vary considerably due to the limitations of conventional test methods (See Table 2.2). It means that creating a user-friendly and standardized testing procedure to quantify the thermal properties is indispensable (Yu et al., 2021).

Table 2.2 Thermal properties of asphalt mixtures in previous studies (Yu et al., 2021).

Authors (Year)	**Thermal conductivity (W/m.°C)**	**Specific Heat Capacity (J/kg.°C)**
Tegeler and Dempsey (1973)	1.21–1.38	840–1090
Kavianipour and Beck (1977)	2.28–2.88	-
Yan (1984)	0.3–0.95	-
Zhang and Tao (1985)	1.040–1.527	803.68–1021.35
Bing (1992)	1.1–1.5	-
Niu et al. (1998)	0.2659–1.2247	-
Chadbourn et al. (1998)	1.5–2.0	1000–1010
Zi et al. (2006)	1.023–1.581	929–967
Stempihar et al. (2012)	0.8–2.0	520–1835
García et al. (2014)	1.2–1.6	-
Hassn et al. (2016a)	0.82–1.16	946–963
Sreedhar and Biligiri (2016)	0.51–0.96	664–1039
Si et al. (2018)	1.25	324–1310

It should be noted that several researchers have proposed experimental techniques and new equipment to obtain accurate results. These studies point out two primary approaches for determining the thermal properties of asphalt concrete: steady-state and transient methods (Kuvandykova & Bateman, 2013; Côté et al., 2013; Islam & Tarefder, 2014; Elkholy et al., 2019; Byzyka et al., 2021). All measurement methods are summarized in Figure 2.6. Moreover, the working mechanism of these methods and advances in previous studies are detailed in the following sections.

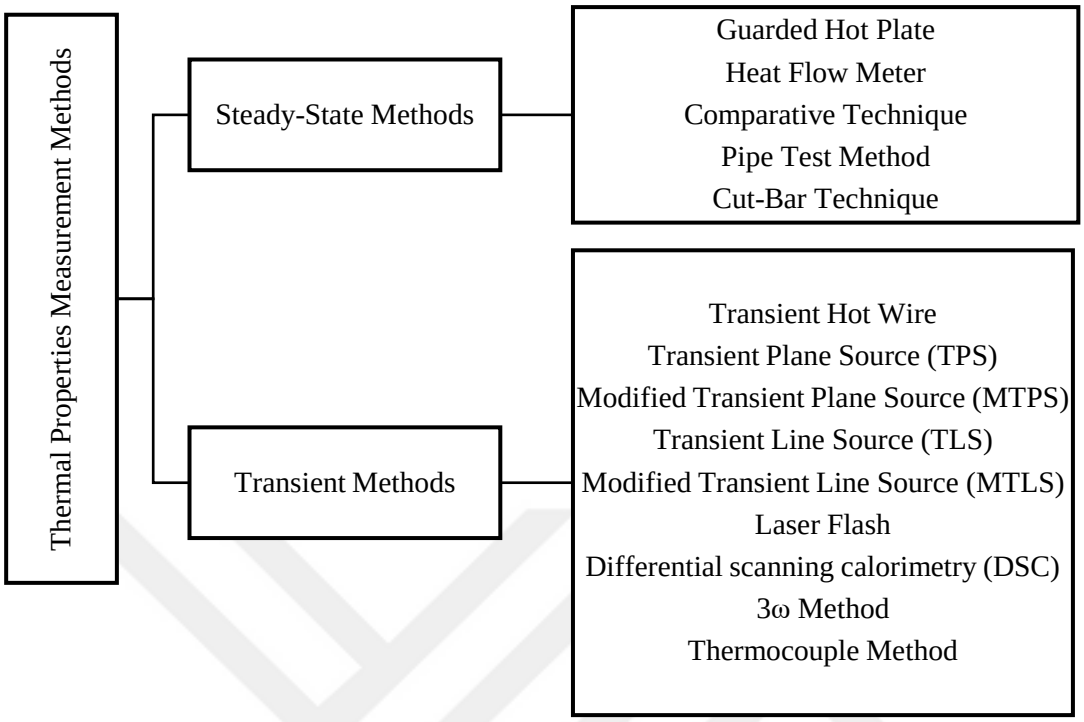


Figure 2.6 Methods for measuring thermal properties (Kuvandykova & Bateman, 2013; Palacios et al., 2019).

2.3.1 Steady-State Methods

Methods based on the steady-state approach aim to achieve a one-dimensional heat flow (Carlson et al., 2010). At a constant temperature difference, the heat flow through the sample is measured in steady state. Therefore, all steady-state methods are fundamentally derived from Fourier's law (Mehling & Cabeza, 2008). According to Fourier's law, the slope of the temperature gradient between both sides of the sample is required to obtain the thermal conductivity (Tritt, 2005; Zhao et al., 2016).

In general, Standard Test Method for Steady-State Heat Flux Measurements and Thermal Transmission Properties by Means of the Guarded-Hot-Plate Apparatus (ASTM C177-19), Standard Test Method for Steady-State Thermal Transmission Properties by Means of the Heat Flow Meter Apparatus (ASTM C518-21), and Standard Practice for Calculating Thermal Transmission Properties Under Steady-

State Conditions (ASTM C1045-19) are highly recommended and contain procedures for steady-state measurement of thermal properties. Among these, the most popular steady-state methods are probably the Guarded Hot Plate and the Heat Flow Meter (HFM) techniques (Kim et al., 2021), as they are more accurate than the other steady-state approaches (Richter et al., 2003; Palacios et al., 2019).

The GHP method determines the thermal conductivity of a material using an electrically heated plate with guided heat conduction. Heat flow happens when the surfaces of homogeneous, flat specimens come into contact with parallel, solid boundaries that are kept at a constant temperature by the hot plate that is guarded. According to ASTM C177-19, a guarded hot plate is designed for this purpose and is a primary method. In this method, the preparation of the sample requires very flat and parallel surfaces. Roughness can cause significant thermal resistance at the interfaces and a temperature drop because of the air gaps between the hot and cold plates and the sample surfaces (Kim et al., 2021).

The HFM method also involves measuring heat transmission through flat slab specimens utilizing a heat flow meter apparatus. According to ASTM C518-21, this method quickly and accurately measures the steady-state heat transfer properties when calibrated correctly. As indicated, calibration is essential to minimize lateral heat losses or gains in all test procedures. The apparatus must be calibrated with materials with the known thermal properties and thickness as the tested materials. This method determines the heat flow through a sample when the two sides of the sample (thickness, d (mm)) are held at a constant temperature difference ΔT (°C). Calibrated heat flux sensor devices are used to measure the heat flux. The output voltage V (Volt) is related to the heat flux across the sensor. Equation 2.8 below can be used to figure out the thermal conductivity from the HFM measurement. In the equation, S is the transducer's sensitivity. For comparison, here are some schematic diagrams of the GHP and HFM methods, as illustrated in Figure 2.7.

$$k = \frac{Vd}{S\Delta T} \qquad 2.8$$

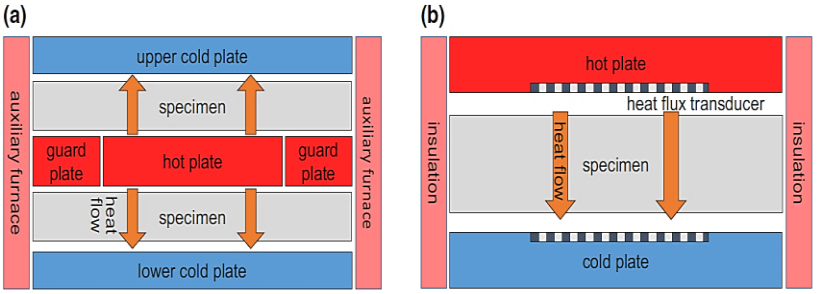


Figure 2.7 Schematic diagrams of (a) Guarded Hot Plate and (b) Heat Flow Meter methods (Kim et al., 2021).

The GHP and HFM methods are not like other steady-state techniques. For example, the Comparative Technique is among the recommended methods for a steady-state approach. It is an alternative method for measuring thermal conductivity in which a stack consisting of a sample sandwiched between two references and protected by a cylindrical heat source produces a steady-state, linear heat flux. Then, the Pipe Test Method is similar to the GHP method. This method involves wrapping a long, cylindrical specimen around a central heater with end guard heaters and radial heat flow to measure thermal conductivity and heat transfer. Lately, the Cut-Bar Technique uses the concept of constant temperature in conjunction with a thick guard ring. A sample disk is placed between two cylindrical metal bars, and one end of the bar is heated while the other is cooled. In summary, regardless of the experimental setup, the fundamental goal of all steady-state methods is to achieve a stable temperature condition (Kuvandykova & Bateman, 2013).

The steady-state methods discussed above have two fundamental limitations (Mrawira & Luca, 2002; Carlson et al., 2010). One of the apparent limitations of steady-state methods is that the thickness of flat slab samples must not exceed one-third of the length of the measurement zone. Preparing a sample with such dimensions from cores of in-situ pavements or asphalt mix briquettes compacted in the laboratory is challenging. Another limitation is that reaching equilibrium takes a long time (Kuvandykova & Bateman, 2013). Despite the drawbacks of steady-state methods for measuring thermal properties mentioned in previous studies, better

accuracy can be obtained for inhomogeneous materials with moderate conductivity if the one-dimensional and steady-state conditions can be adequately controlled (Mrawira & Luca, 2002). Therefore, the following section summarizes the previous studies that use the steady-state method.

2.3.1.1 Thermal Conductivity Measurements Using Steady-State Methods in Previous Studies

This section offers a concise overview of studies focused on the thermal conductivity of asphalt concrete. Several steady-state test procedures for determining asphalt concrete's thermal conductivity are detailed in the section that follows. Before evaluating these studies, it is necessary to emphasize a generally accepted limitation of the steady-state method. Tan et al. (1992 & 1997) stated that the ASTM methods, which are based on the steady-state approach to measuring thermal properties, require a long testing time and may not be suitable for measuring the thermal properties of building materials. In response to this limitation, numerous investigations into the asphalt concrete's thermal properties have been carried out during the last 20 years. However, the need for further studies is still emphasized (Luca & Mrawira, 2005).

Luca & Mrawira (2005) stated that the current methods are not suitable for asphalt concrete samples because of the difficulty in meeting the slab dimensional requirements. Therefore, the University of New Brunswick (UNB) k-alpha tester developed by Mrawira & Luca (2002) was proposed as a new procedure in their study, as shown in Figure 2.8. The key components of the UNB k-alpha tester were a protected hot plate, thermal insulation, a heat sink, and temperature-controlled fluid circulation. In addition, the new device was suitable for small samples made either from cores of current pavements or from 150-mm-diameter briquettes compacted in the laboratory. The thermal conductivity of the samples was determined once the test had stabilized, providing a solution to the previously mentioned sample size limitation.

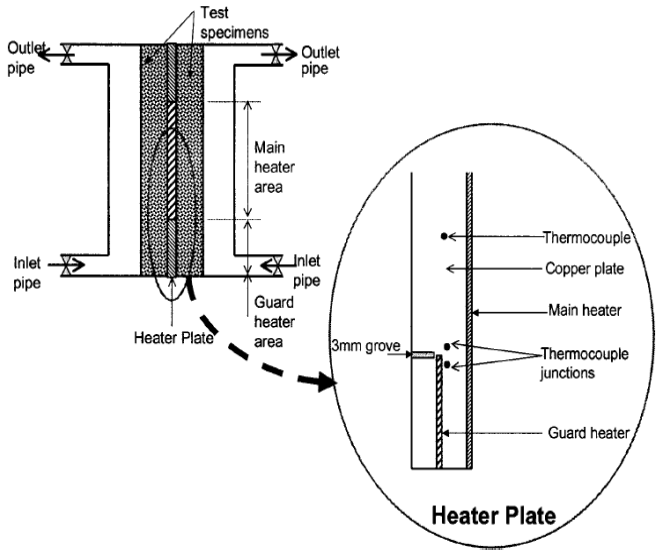


Figure 2.8 Schematic view of UNB k-alpha tester (Mrawira & Luca, 2002).

According to Luca & Mrawira (2005), the thermal conductivity of dense mixtures was determined to be between 1.45 and 1.81 W/m.K. This was observed when the bulk density was between 2.250 and 2.450 kg/m^3 and the air void content is 3-7%. Finally, the study reported that the sample sizes employed in this research for assessing thermal properties were inadequate for evaluating the strength properties of hot mix asphalts.

Carlson et al. (2010) devised a test setup for testing the thermal conductivity of asphalt concrete samples adopting a cylindrical sample geometry. Due to the limitations of sample size in the relevant standards, cylindrical geometry was preferred in their study. This limitation was overcome by inserting a heat source along the axis of a cylinder of material. Then, heat losses were minimized by thermally insulating the top and bottom of the cylinder. In this way, a radial and unidirectional heat flow was generated. In the following, Figure 2.9 illustrates a schematic representation of heat transfer.

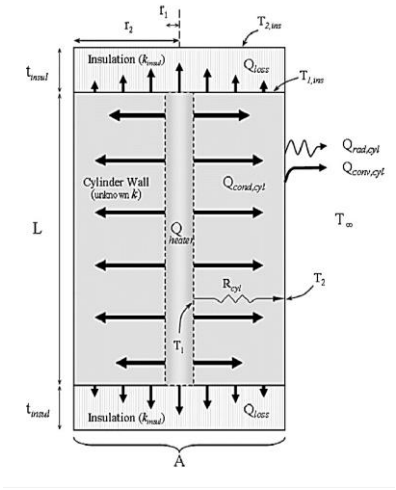


Figure 2.9 Schematic view of heat transfer diagram (Carlson et al., 2010).

Unlike the study by Luca & Mrawira (2005), the outstanding aspect of the study by Carlson et al. (2010) was its dual focus: not only did it propose an experimental method for measuring thermal properties, but it also attempted to measure thermal conductivity using the cylindrical sample geometry generally used in conventional mechanical tests. In other words, this new experimental method facilitates the determination of thermal and mechanical properties within the same material geometry. The asphalt concrete samples had a thermal conductivity value of 0.896 ± 0.023 W/m.°C with a confidence interval of 95%. This result showed that the accuracy and repeatability of the new test method were acceptable because they fell within the range of values reported in the past regarding the thermal conductivity of asphalt concrete.

The analytical model to accurately predict the measured temperatures was the main focus of Xu & Solaimanian (2010). An experimental study was first established to estimate the analytical model for predicting transient temperature distribution. First, a climatic chamber with a steady-state high temperature of 36 °C was used to hold the sample, which had a low temperature of 3.5 °C. Then, the temperature change of the sample over time was measured at different time intervals until the system reached a steady state. During the test, the difference in temperature over time was

also observed at various points in asphalt concrete samples. Figure 2.10 shows the transition to a steady state with temperature values measured at different points on the sample over time. Moreover, the simulation approach and the experimental method were applied in the case of increasing temperatures. Then, the analytical model was validated based on this approach. The investigation concluded that additional testing of the suggested method necessitated combinations with various binders and aggregates because both affect the heat transfer characteristics.

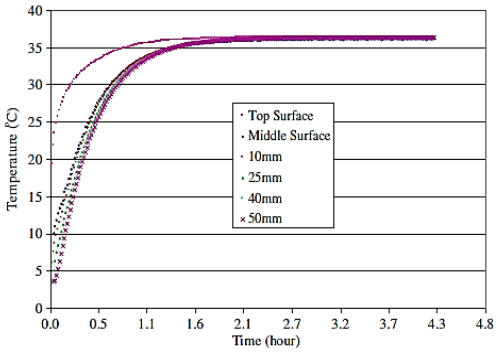


Figure 2.10 Temperature values measured at different points on the sample (Xu & Solaimanian, 2010).

A thermal conductivity cell based on the steady-state approach was created by Côté et al. (2013) to measure the temperature of a cylindrical sample, as shown in Figure 2.11. Two brass disks were placed between the heat flux meters and the heat exchangers to balance the temperature distribution on the two horizontal sides of the sample. In their test setup, the heat flux at each end of a cylindrical sample was measured using thermoelectric heat flux meters. This setup comprised five independent thermocouples that simultaneously measured the temperatures at different points on the two flat ends of the sample. The effects of bitumen type, aggregate size, and air void content were taken into consideration when evaluating the thermal conductivity results of the asphalt mixtures used in this study. At the end of the study, the consistency of the effects of these components with the results in the literature made the study valuable as it confirmed the experimental setup.

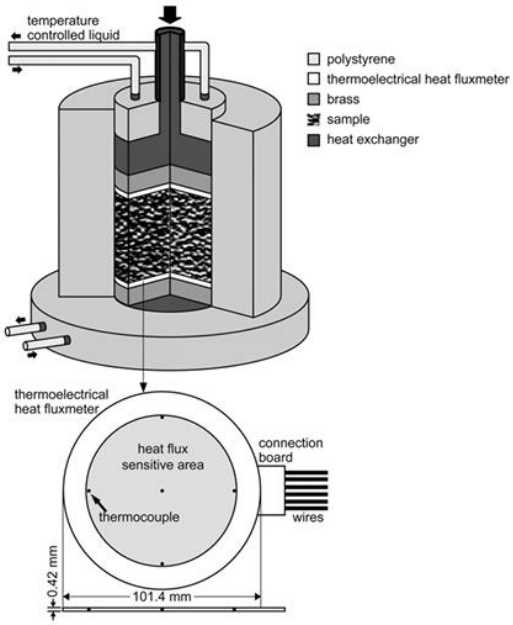


Figure 2.11 Heat transfer cell (Côté et al., 2013).

Hassn et al. (2016a & 2016b) studied the thermal properties of asphalt concrete with a different test setup. Figure 2.12 below gives the test setup used for conducting laboratory tests on asphalt concrete slabs. Using type J thermocouples, the ambient temperature, the top temperature of the asphalt concrete slabs, and the bottom temperature of the slabs were all recorded throughout the test. Then, the thermal conductivity was determined utilizing a computer-controlled P.A. Hilton B480 uniaxial HFM due to its superior precision and suitability for inhomogeneous mixtures. When the test system reached the steady state, as seen in Figure 2.10, the thermal conductivity of the sample was calculated. The impact of air voids was also discussed in the study by Hassn et al. (2016a). Ultimately, the investigation demonstrated that the asphalt mixture transfers heat more slowly through air because the latter has a lower thermal conductivity than the former. Additionally, the valuable contribution of the experimental setup developed by the study of Hassn et al. (2016a) was that the slab specimens (306 x 306 x 50 mm3) can be used for the thermal conductivity measurements. In short, this study presented a solution to the sample size limitation emphasized in the steady-state test methods.

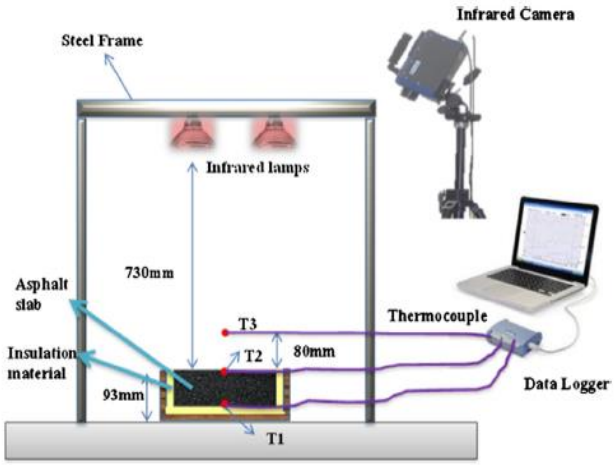


Figure 2.12 Schematic view of the experimental setup (Hassn et al., 2016a & 2016b).

Reviewing previous studies on steady-state approaches found that each study had its unique test setup and limitations. This means that there is no standard test design based on a steady-state approach to determine the thermal conductivity of asphalt concrete. Apart from measuring thermal conductivity using the steady-state approach, it is also highly important to measure and determine the specific heat capacity in order to evaluate the thermal performance of asphalt pavements. Accordingly, the following section deals with the experimental measurement of the specific heat capacity using the steady-state approach.

2.3.1.2 Specific Heat Capacity Measurements Using Steady-State Methods in Previous Studies

A material's specific heat capacity is the amount of heat it can hold. To judge the heat storage capacity of asphalt concrete, it is necessary to determine its specific heat capacity. In past, it was suggested that the specific heat capacity of asphalt mixtures can be determined by adding the weighted specific heat capacities of the mix constituents (Jordan & Thomas 1976; Johnston 1981). However, this method can lead to unreliable results because of the effects of air voids and variations in moisture

content (Luca & Mrawira, 2005). Therefore, Wolfe et al. (1980) attempted to determine the specific heat capacity of materials at steady state using the drop calorimeter method. The basic idea behind the drop calorimeter method is that energy input and output must be equal when a steady state is reached (Schärli & Rybach, 2001). This approach was later developed by Islam & Tarefder (2014) using a thermally insulated foam ice box that serves as a calorimeter, as shown in Figure 2.13.

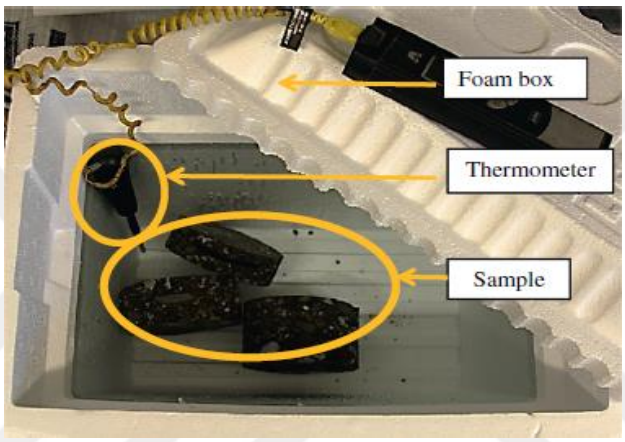


Figure 2.13 Test setup for specific heat capacity measurement in asphalt concrete (Islam & Tarefder, 2014).

In the study of Islam & Tarefder (2014), the hot water provided a heat transfer medium from the high to the low temperature. The temperature drop was recorded to measure the heat loss through the water during the first three hours. According to the study, the temperature dropped 1.9 °C in the first hour, 1.7 °C in the second hour, and 1.6 °C in the third hour. In their test setup, the sample was divided into three pieces. Each piece's weight and body temperature were recorded after checking the heat loss of the water. The samples were then conditioned at room temperature for at least one day. Subsequently, they were quickly immersed in hot water to measure their temperatures. The temperature change of the samples and water was monitored with a thermometer. When the temperature had reached a constant level, the experiment was stopped, and the specific heat capacity of the samples was

determined according to the approach that the energy absorbed is equal to the energy released. In short, this study is a good example of specific heat capacity testing in the laboratory. However, previous studies lack a well-accepted or universal approach to a steady-state test for measuring the specific heat capacity of asphalt concrete.

2.3.2 Transient Methods

The transient methods show temperature changes over time. They employ pulsed or periodic heat sources, which cause the sample's temperature to fluctuate either transiently (amplitude signal output) or periodically (phase signal output) (Zhao et al., 2016). Although the data analysis required for these methods is a challenge, the shortest test time of the methods is their greatest advantage. But first, choosing the right test method is an important step in the transient methods. Indeed, the best method depends on several factors, such as the type of material (insulating or conductive, bulk or thin film), the configuration of the sample, and the temperature (Elkholy et al., 2019). Each transient method can operate within a specific temperature range; thus, proper test method selection is essential, as shown in Figure 2.14. According to the following figure, the TPS method works in a broader range of thermal conductivity, as it measures materials from 0.001 to 1800 W/m.K (Palacios et al., 2019).

Moreover, some relevant standards are recommended for test setups in transient methods. Standard Test Method for Determination of Thermal Conductivity of Soil and Rock by Thermal Needle Probe Procedure (ASTM D5334-22), Standard Test Method for Thermal Conductivity of Plastics by Means of a Transient Line-Source Technique (ASTM D5930-17), Standard Test Method for Measurement of Thermal Effusivity of Fabrics Using a Modified Transient Plane Source (MTPS) Instrument (ASTM D7984-21), and Plastics-Determination of thermal conductivity and thermal diffusivity- Part 2: Transient plane heat source (hot disc) method (ISO 22007-2) are some of them and are generally used to measure thermal conductivity (Harris et al., 2014; Mrawira & Luca, 2002; Jiao et al., 2020; Zheng et al., 2020).

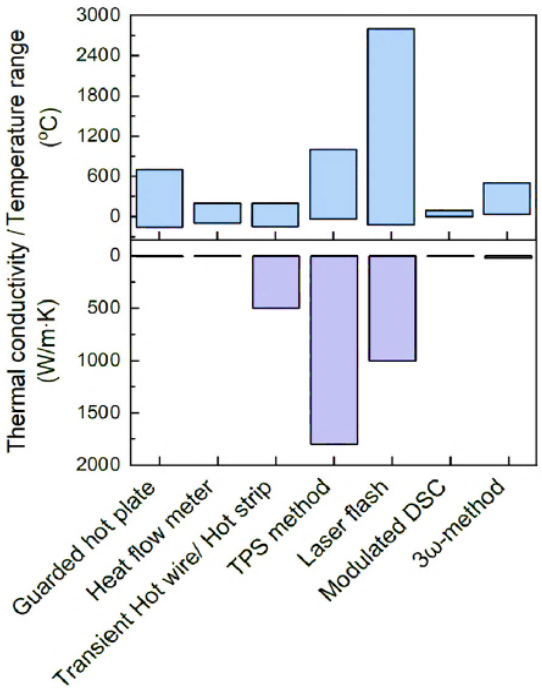


Figure 2.14 Thermal conductivity and temperature measurement ranges for steady-state and transient methods (Palacios et al., 2019).

The Transient Hot Wire Method is employed to precisely determine the thermal conductivity of fluids across a broad spectrum of temperatures and pressures. It relies on recording the instantaneous temperature rise when a step voltage is applied to an infinitely long, thin, and vertical metal wire, as shown in Figure 2.15. The advantage over other methods of measuring thermal conductivity is the fully developed theory and the lack of calibration or one-point calibration. It should be highlighted that there is no convection and an accurate determination of the thermal conductivity of any fluid (Assael et al., 1998). Additionally, the hot wire works as an ideal heat source, exhibiting a consistent output across the depth of the sample. It also measures the temperature of the sample. When radial heat is transferred from the wire to the sample, the thermal conductivity is calculated using Equation 2.9. It is derived from the slope of the wire's temperature increase over a logarithmic time interval (Nagasaka & Nagashima, 1981; Hwang et al., 2006). In Equation 2.9, q (W/m) is the

heating power, k (W/m.K) is the thermal conductivity, and T (K) is the wire's temperature at time t (s) during heating.

$$k = \frac{q}{4\pi(T_2 - T_1)} \ln\left(\frac{t_2}{t_1}\right) \quad 2.9$$

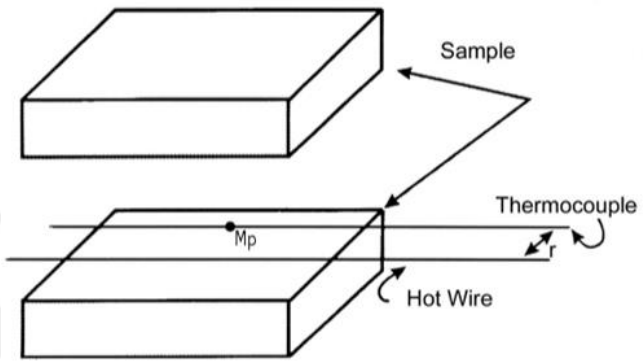


Figure 2.15 Schematic view of the hot wire method (Dos Santos & Gregório, 2003).

The TPS method was initially proposed by Gustafsson in 1991. In this method, a thin, temperature-dependent resistor in the form of a disk is used as both a temperature sensor and a heat source. A planar heater is made up of many concentric rings, which are usually made of nickel, that are strengthened by layers of insulating gaps, as shown in Figure 2.16. Throughout the examination, the sensor is positioned between the two sections of the sample in a sandwich-like manner (Log & Gustafsson, 1995). The temperature and electrical resistance are then used to determine the thermal conductivity according to heating rate using Equation 2.10 (Krupa & Malinaric, 2014). In the given equation, P_0 (W) is the power of the sensor; τ is the non-dimensional time; r (m) is the outer ring heater's radius; $\Delta T(\tau)$ (°C) is the temperature increase at the sample surface; $D_s(\tau)$ is a shape function of τ (Palacios et al., 2019).

$$k = \frac{P_0}{r\Delta T(\tau)\pi^{\frac{3}{2}}} D_s(\tau) \quad 2.10$$

Besides the advantages of the TPS method, there are also some disadvantages related to the working mechanism. The most significant disadvantage is the temperature change generated by the electric power, which depends on the thermal resistance of the sensor. In other words, the reliability of TPS measurements depends on the sensitivity of the sensor. Another limitation is the assumption that the sensor is in an infinite medium (Mirzanamadi et al., 2018). Therefore, correctly determining the probing depth (d), as shown in Figure 2.16, is critical for measurement reliability. Accordingly, it should always be determined as close to or slightly lower than the diameter of the sensor. Moreover, the thickness of the sample in the x-direction must be greater than the probing depth (Log & Gustafsson, 1995). In general, obtaining reliable results with a TPS sensor necessitates significant experience and knowledge of the TPS method (Tang et al., 2014; Pan et al., 2017; Palacios et al., 2019).

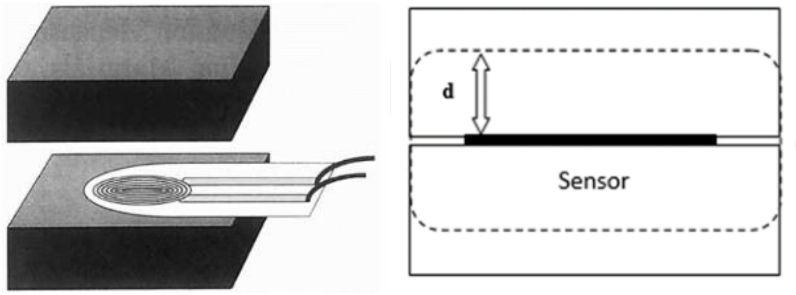


Figure 2.16 Test set-up of the TPS method and side view of TPS sensor (Log & Gustafsson, 1995).

The MTPS method is also proposed and is a new version of the TPS method. In this method, the sample is placed in contact with a heat reflectance sensor, which acts as a steady heat source on one side, as shown in Figure 2.17. The working principle of the MTPS method is almost the same as the TPS method. The heat exchanger is reinforced by a framework offering mechanical stability, electrical insulation, and thermal isolation. This design enhances flexibility for testing liquids, powders, pastes, and solids (Bateman et al., 2016).

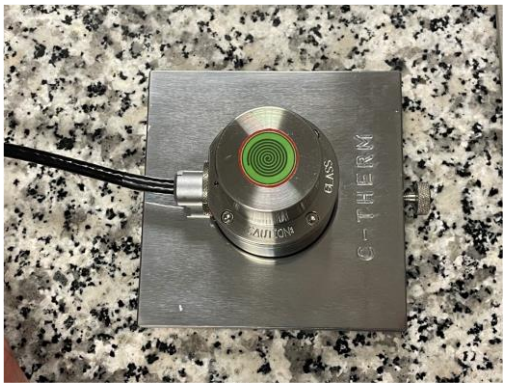


Figure 2.17 A modified transient plane source (Martínez-Ibáñez et al., 2021).

The TLS is another simple, direct, and highly portable method for testing thermal conductivity (see Figure 2.18). In this method, a thermocouple in the center of the heating wire records the temperature rise of the sample under test as a function of time as the heat propagates radially from this line source (Gist, 1971). After the heating process is completed, the temperature is also recorded at the same time intervals during the cooling process. Using the power of the heating wire, the sample temperature variation, and the time, the thermal conductivity of the sample can be calculated. In addition to the TLS method, a modification of the TLS method is also developed and used to measure the thermal conductivity of a large earth mass for ground source heat pump (GSHP) design. This modified method is defined as the Modified Transient Line Source (MTLS).

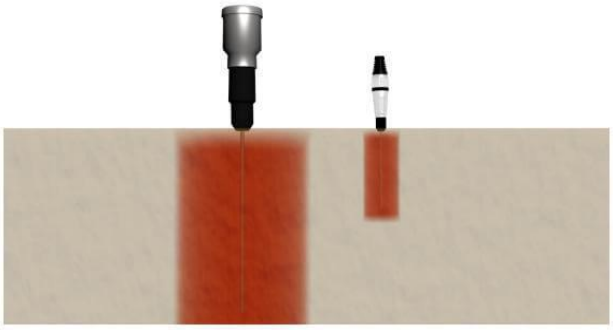


Figure 2.18 A Thermtest Inc. thermal needle (Internet source: https://www.wetec.com.sg)

In addition to the abovementioned methods, non-destructive methods such as Laser/Light Flash Analysis (LFA), Differential Scanning Calorimetry (DSC), and the 3ω method have been developed recently. Parker et al. (1961) presented the first LFA method. It measures temperature quickly and non-destructively using a thermographic technique and optic heating as an instantaneous heat source (Min et al., 2007; Philipp et al., 2020). Solid and planar materials for measuring thermal properties are used in this approach. In the following, Figure 2.19 shows a typical test setup using the laser flash technique. Normally, a graphite coating is sprayed on both sides of the test sample to serve as an absorber on one side and an emitter on the other for temperature detection (Zhao et al., 2016). A laser or flash lamp produces a short light pulse that heats the sample's top surface. On the back surface of the sample, a contactless infrared detector records the temperature increase over time. Then, the thermal diffusivity may be simply determined from the half-rise time $t_{1/2}$ (sec) in a perfect adiabatic case using Equation 2.11.

$$A = \frac{1.38L^2}{\pi^2 t_{\frac{1}{2}}} \qquad 2.11$$

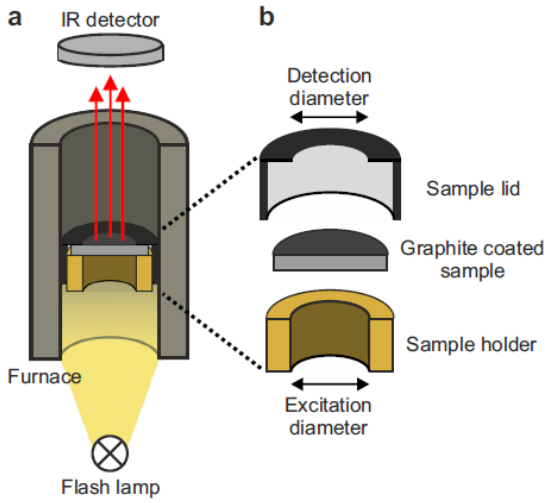


Figure 2.19 (a) (a) A Basic LFA setup (b) the representation of the sample configuration (Philipp et al., 2020).

One other method for measuring the rate of heat transfer into or out of a material with respect to both temperature and time is DSC (Marcus & Blaine, 1994). The DSC method measures heat flows between a substance and a reference material based on temperature, using a precise temperature program between the substances. Indeed, each DSC is a twin calorimeter because it has two chambers, one for the sample and one for the reference. During the test, the temperature difference between them is measured (Danley, 2002). Then, the difference between the heat fluxes measured by each calorimeter is the DSC output. In fact, the main application of DSC is the measurement of transition temperatures and the associated heat of reaction in materials, especially polymers (Gill et al., 1993).

Measuring thermal conductivity using a DSC is a good option, but it does necessitate modifying a commercially available DSC cell (Marcus & Blaine, 1994). Accordingly, temperature modulated or advanced DSC (MDSC) was developed by Reading in 1993 (Gill et al., 1993). This method employs a heating mechanism that follows a linear and periodic oscillation pattern, resulting in the division of heat flow into recoverable and irrevocable components (Isa & Jodeh, 2001). Hence, the MDSC technique provides a greater resolution than DSC and can do quasi-isothermal observations (Hu et al., 2014). According to this approach, two pans in the sample chamber hold the sample and reference, and thermocouples measure the differential heat flow between the sample and reference (see Figure 2.20). Subsequently, a neutral gas is introduced into the furnace chamber to avert undesired reactions or the condensation of gases (Palacios et al., 2019). Materials that are insulators, like polymers, ceramics, and glasses, are typically measured using this device (Marcus & Blaine, 1994).

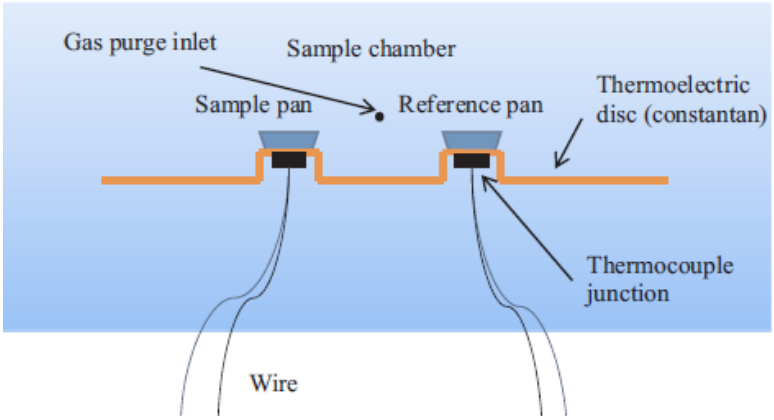


Figure 2.20 The illustration of MDSC device (Palacios et al., 2019).

Lastly, the 3ω method is recommended to measure thermal properties. This technique has been described by Risk et al. (2009) as a sensitive and proven way to measure the thermal conductivity of a thin film. A current that oscillates at a frequency ω is passed through a metal strip that is attached to the surface of the material being tested in order to apply a known amount of heat to its surface. The temperature increase that follows is calculated by taking the voltage across the identical strip at a frequency of 3ω. The thermal conductivity is determined by analyzing the variation of voltage 3ω with driving frequency ω using an appropriate mathematical model. This method can be employed to assess the feasibility of obtaining a consistent and uniform sample using small sample volumes. Furthermore, the spatial variability of the reaction could be employed to observe and analyze aggregation mechanisms (Palacios et al., 2019).

In summary, among the above transient methods, TPS and TLS are the most suitable methods for the asphalt concrete. There are not enough studies on non-destructive methods to measure the thermal properties owing to the limited sample size. Therefore, the success of these new approaches in determining the thermal properties of asphalt concrete is uncertain. The following section briefly presents the most commercially successful experimental setups for measuring the thermal properties of asphalt concrete based on transient methods.

2.3.2.1 Thermal Conductivity Measurements Using Transient Methods in Previous Studies

As detailed in the previous sections, conventional one-dimensional steady-state methods may result in incorrect and inaccurate test outcomes due to certain limitations (Zarr, 2010). Therefore, several researchers have explored the transient approach, which is considered a modern and rapid method. Among the transient methods, thermal conductivity measurements in asphalt concrete are mainly performed using the TPS method (Pan et al., 2017; Mirzanamadi et al., 2018; Petkova-Slipets & Zlateva., 2018; Khasawneh et al., 2023). Accordingly, a review of studies focusing on transient approaches, specifically the TPS method, is presented.

Byzyka et al. (2021) measured the thermal properties of samples prepared with unaged and aged bitumen using the TLS method. In this study, the TLS needle was placed in the center of the sample and served as a linear heat source, as shown in Figure 2.21.

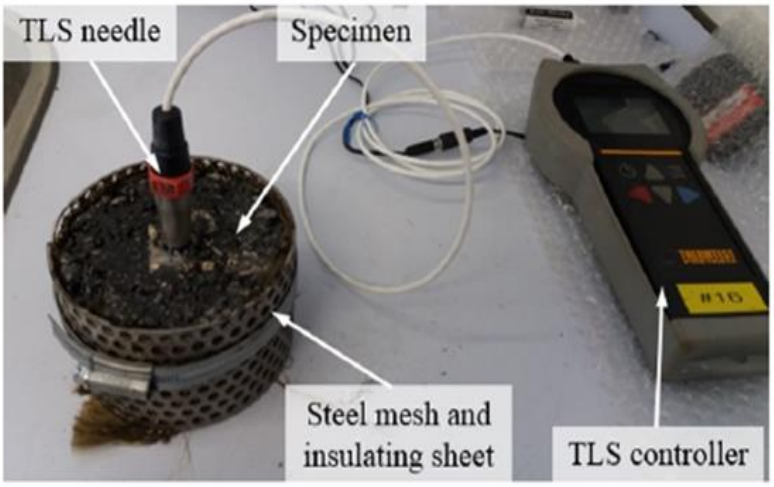


Figure 2.21 Use of the TLS method in asphalt concrete sample (Byzyka et al., 2021).

In the study by Byzyka et al. (2021), the thermocouple was used to measure the temperature differences in the sample when heat was transferred from the hot wire over a while. The sample's thermal conductivity was then determined using Equation 2.12 (Franco, 2007).

$$k = \frac{Q}{4\pi\,[T(t_2)-T(t_1)]} \ln\left(\frac{t_2}{t_1}\right) \qquad 2.12$$

In Equation 2.13, k (W/m.K) represents the thermal conductivity, t (sec) denotes time, L (m) is the distance between thermocouples, and Q (W) signifies the heating power. This study mentioned that the hot-wire method and the needle-probe method were performed similarly. In fact, the needle probe method differs from the hot wire because the probe serves as both a heating element source and a sensor.

The study of Byzyka et al. (2021) was concerned with investigating the effects of a mixture of air void content, temperature, and ageing on thermal properties. This study examined the impact of using the TLS method for measuring thermal conductivity. It was observed that the temperature contact between the needle and the surface of the asphalt mix could alter the measured values of thermal conductivity. This was explained as the disturbance of the sample by entrapped air or granite and limestone dust residues from drilling, which can affect thermal conductivity measurement. In addition, the uneven dissipation of heat from the needle during the measurement process can also influence the results.

Mirzanamadi et al. (2018) examined the impact of different design variables of asphalt concrete and the surrounding environment on thermal properties. In their study, the utilized TPS method is validated by a 2-D numerical model. This study also emphasizes three critical parameters essential for ensuring measurement reliability in the TPS method. These are the measurement time, the applied heat power, and the sensor size. Based on this statement, Table 2.3 provides recommendations based on sensor type, including heating power, measurement time, and thermal penetration depth. In general, the study emphasized that selecting these parameters mainly relies on experience and the accurate interpretation of

measurement results. In addition, the correlation between the sensor diameter, the maximum aggregate size, and the change in thermal properties was investigated by Mirzanamadi et al. (2018). The study found that there was a notable discrepancy in the measured thermal properties when the ratio of sensor diameter to maximum aggregate size was smaller than 2. Similarly, Chen et al. (2022b) also used the TPS method in their study to measure the thermal properties of asphalt mixtures. In the following, Figure 2.22 shows the experimental setup of their study.

Table 2.3 Measurement details of asphalt concrete samples using the different TPS sensor sizes (Mirzanamadi et al., 2018).

Sensor ID	Sensor Diameter (mm)	Power (mW)	Measurement Time (s)	Thermal Penetration Depth (mm)
5465	6.36	100	10	4-5
5501	12.8	200	40	8-10
8563	19.7	300	80	12-18
4922	29.2	1000	160	18-21
5599	58.8	1000	320	22-26



Figure 2.22 The test setup of TPS device (Chen et al., 2022b).

In one of the latest studies, Khasawneh et al. (2023) similarly favored the TPS method when examining the thermal properties of asphalt mixtures about aggregate gradation and Superpave volumetrics. The TPS measurements were conducted using a unidirectional experimental setup, with the sensor placed directly on the sample's surface. Additionally, a weight was applied to the TPS sensor to enhance its contact. It was found that heat transfer was strongly dependent on the contact area and air void volume. However, the study did not investigate the reliability of measurements related to the properties of the mixture in the contact zone. It focused primarily on the good contact of the sensor with the surface.

With advances in measurement technology, Petkova-Slipets & Zlateva (2018) used the MTPS method, as shown in Figure 2.23. This method is also known as the TPS method in an extended form. In this study, several advantages of the MTPS method were mentioned. First, this method has been demonstrated to provide unilateral measurements in both field and laboratory settings. Unlike the TPS method, it is no longer necessary to prepare two identical samples. It also allows short-term measurements regardless of the size and shape of the materials tested (see Figure 2.23).



Figure 2.23 Testing different samples with the MTPS (Petkova-Slipets & Zlateva, 2018).

In the studies reviewed above, it is usually emphasized that the measurement accuracy is affected by the relationship between the TPS sensor size and the aggregate size. However, due to their speed and simplicity, this has not diminished the popularity of TPS or other transient methods for heterogeneous materials. Consequently, research continues to focus on transient methods in asphalt concrete. Unlike the measurement of thermal conductivity through transient methods, the previously mentioned studies do not specifically address the measurement of specific heat capacity. Therefore, this aspect is summarized separately in the following section.

2.3.2.2 Specific Heat Capacity Measurements Using Transient Methods in Previous Studies

In 2004, Mathis Instruments Ltd. developed the MTPS method based on the advances in measurement technology (Mathis & Chandler, 2002). This approach was one of the few ways to measure the specific heat capacity of asphalt concrete (Petkova-Slipets & Zlateva, 2018). Besides the TPS method, other popular techniques include the DSC and MDSC methods. The DSC method provides quantitative and qualitative information on physical and chemical changes, as well as on heat capacity variations. In addition, the MDSC method is defined as a novel and patent-pending version of the standard DSC method that provides data on the reversible and irreversible aspects of thermal events. In one of the latest studies, Hu & Yu (2016) used the MDSC method to characterize the thermal behavior of innovative thermochromic asphalt pavements. Consequently, the mean value of specific heat capacity was measured in the range of 1475-1778 J/(kg. K) from -20 to 50 °C for black asphalt coating.

Upon reviewing previous studies, it was observed that transient methods, especially DSC and MDSC, often measure the specific heat capacity of bitumen rather than that of the asphalt mixture. This is due to the inappropriate sample size of the asphalt mixture for the transient methods. In the DSC method, the quantity of sample in the

measuring pans during sample preparation is reported to be around 10-20 mg (Zadshir et al., 2020). Thus, the DSC method is typically used to measure changes in thermal properties of bitumens (Hosseinnezhad et al., 2019; Zadshir et al., 2020; Elkashef et al., 2020). Measuring the specific heat capacity of asphalt concrete using transient methods is prone to enhancement. Therefore, studies using the above transient methods for asphalt concrete are still in progress.

2.4 Determination of Thermal Properties of Asphalt Concrete with Numerical Approaches

Using experimental methods to determine thermal properties has several disadvantages. These include requiring many samples, specialized tools, and expertise in a typical pavement engineering laboratory, etc. (Chen et al., 2015b). This situation results in the experimentally determined thermal properties of asphalt concrete being subject to inconsistencies (Mirzanamadi et al., 2018). For example, the thermal conductivity of an asphalt mixture varies over time due to changes in the air voids during service or paving operations. Therefore, repeated measurement of thermal properties in a standard pavement engineering laboratory is still challenging (Chu et al., 2020). On the other hand, numerical methods that account for the microstructure of asphalt concrete have recently gained popularity in determining thermal properties (Carotenuto, 2000; Chen et al., 2015b). Due to its efficacy and cost-effectiveness, computational modeling of multiphase materials is also advised for estimating thermal conductivity, in addition to experimental and numerical methods (Adkins & Merkley, 1990; Ren et al., 2018).

Heat transfer analysis is the initial step for numerical approaches to determine thermal properties. The asphalt concrete is frequently defined as a homogeneous material in conventional heat transfer analysis (Hai-Gui et al., 2007; Mu et al., 2020). If the asphalt concrete is densely graded and has few air voids, the model of a homogeneous structure works. Nevertheless, the internal structure of other graded mixes cannot be considered homogeneous because of the numerous interrelated

voids and inconsistent gradation. It is a fact that the components of these mixtures are randomly distributed, and thus, the internal temperature field is non-uniform and discontinuous (Mu et al., 2020; Zhao et al., 2020).

Accordingly, numerous researchers have used numerical methods like finite difference and Finite Element Method (FEM) to model the microstructure of composite materials (Carotenuto, 2000; Chen et al., 2015b; Mirzanamadi et al., 2018; Chu et al., 2020). Mu et al. (2020) identified two crucial concerns regarding the analysis of heat transmission in asphalt mixtures based on microstructure. Determining the thermophysical properties of the mix components and creating a geometric model of the asphalt mixture based on microstructure are two of these tasks. The subsequent section provides a concise overview of previous studies on ascertaining thermal properties through numerical methodologies.

2.4.1 Determination of Thermal Properties of Asphalt Concrete Using Numerical Approaches in Previous Studies

Microstructural modeling is the initial step in applying numerical methods to ascertain the thermal model of asphalt concrete. Therefore, two main approaches for three-dimensional (3D) modeling of asphalt mixtures, namely computer-aided and image-based modeling methods, are suggested (Wang et al., 2018; Chen et al., 2015b; Zhang et al., 2017). In addition, new ideas for thermal property prediction that integrate multiscale and mathematical modeling techniques are being developed (Ren et al., 2018). In this context, some related studies using these approaches are summarized below.

Chen et al. (2015b) created a multi-scale 3D asphalt concrete microstructure model, integrating it with Finite Element Analysis (FEA) for enhanced simulation. This study depicted asphalt concrete as a three-phase heterogeneous material. Then, a novel algorithm was developed to generate 3D microstructures in which the aggregates and air voids were represented by simplified polyhedrons dispersed in the asphalt binder. Moreover, the developed FEM is considered a steady heat transfer

mechanism. The top and bottom boundaries of the cubic sample were subjected to constant temperatures, as shown in Figure 2.24. Following the steady-state method's one-dimensional heat flow principle, the cubic sample's other four boundaries were thermally isolated. At the end of the study, the FEA results were verified against experimental data. In summary, the predicted effective thermal conductivity of asphalt concrete was found to be quite close to the experimental results. According to the findings, the average relative error between estimated and actual values for specimens made from crushed gravel and hornfels is 4.35% and 8.92%, respectively.

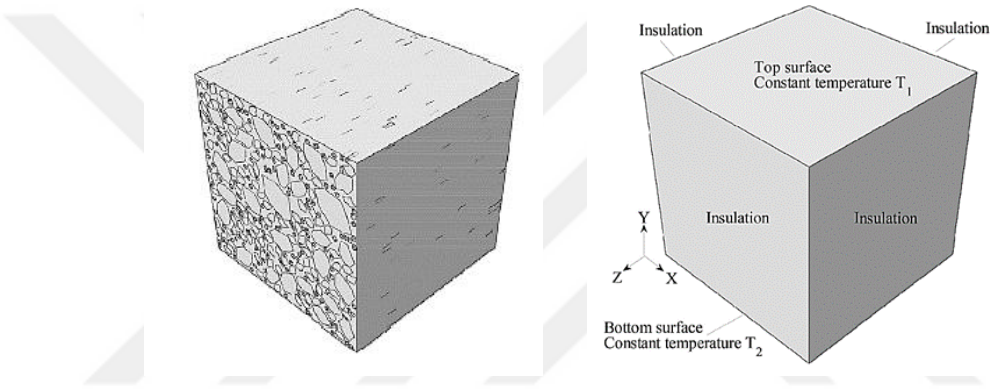


Figure 2.24 Illustration of steady heat transfer in FEA (Chen et al., 2015b)

Chen et al. (2015a) additionally investigated and applied the modification of the aggregate/inclusion generation algorithm developed by Wang et al. (1999). This algorithm generated angular coarse aggregates as polygons with predefined elongation ratios. The random aggregate microstructures were then generated using MATLAB codes, which were then integrated into ABAQUS. In the following, the scheme for generating the overall microstructure using a hierarchical multiscale approach is shown in Figure 2.25. Lastly, The FE model was employed to create three-node linear heat transmission triangle components in ABAQUS utilizing the data by Mrawira & Luca (2006). The study mentioned that if the air voids within the asphalt concrete are unevenly distributed, the thermal conductivity can diverge from the usual values, as seen from the comparison table (See Table 2.4).

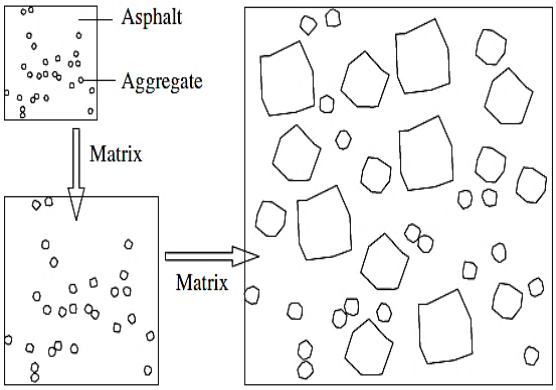


Figure 2.25 Generating the microstructure of aggregates using a hierarchical multiscale method (Chen et al., 2015a).

Table 2.4 Thermal conductivity results obtained by the studies of Chen et al. (2015a) and Mrawira & Luca (2006).

Thermal Conductivity, W/m.K			
Sample	**Sample 1 Air void content: 7.8%**	**Sample 2, Air void content: 3.8%**	**Sample 3 Air void content: 8.2%**
Based on the FE model in the study of Chen et al. (2015a)	1.51	1.70	1.57
Experimental data obtained by the study of Mrawira & Luca (2006)	1.70	2.01	1.84

Zhang et al. (2017) conducted a study on a 3D random microstructure of an asphalt mixture using a Voronoi diagram. The study found that the Voronoi diagram significantly improves the efficiency of generating a random microstructure with no overlap between polyhedral. At the end of the study, the thermal conductivity of an asphalt mixture was determined using the FE modeling of the steady heat transfer process. It is concluded that the shape and rotation angle of the dispersed phase impacted the thermal conductivity of the asphalt mixture.

Chu et al. (2020) explored the connection between volumetric percentiles of mixture components and thermal conductivity using a computerized approach. Moreover, a more straightforward solution to the problematic procedure of producing a randomly

distributed aggregate microstructure was proposed, called as the regular row-column model. It symbolized the mixture's varying character. The model structure shown in Figure 2.26. It shows a schematic representation of the 4-node square element meshes used in the FEA. Heat transfer was totally isolated from the two vertical boundaries. Consequently, it was believed that the only method of heat transfer involved in this process was conduction. The study's findings indicated that the simpler model was more beneficial in real-world scenarios since it generated results that were just as accurate as those of the more sophisticated microstructure-based models documented in the literature.

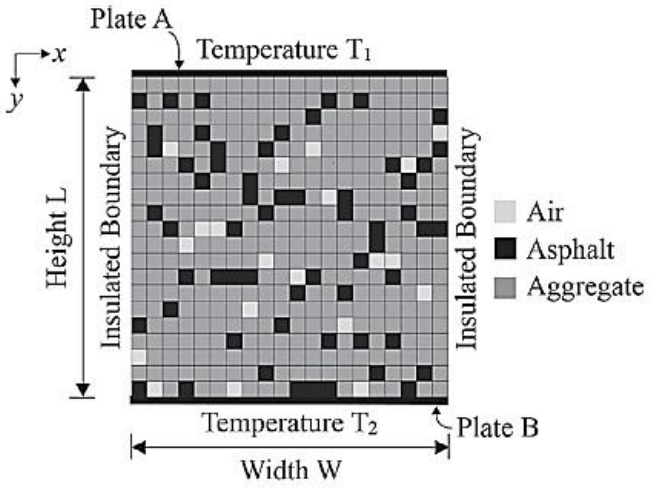


Figure 2.26 2D row-column representation of asphalt mixture (Chu et al., 2020).

Zhao et al. (2020) investigated the thermal properties of porous asphalt concrete and the internal structure of the samples using X-ray CT scanning technology. In their study, the FE simulation model of asphalt mixture was created using the mapped meshing method. Accordingly, the entire model development process is summarized in detail in Figure 2.27 below. Zhao et al. (2020) conducted a transient heat transfer analysis focusing on the thermal properties of asphalt mixtures. Due to the heterogeneous structure of porous asphalt concrete, air voids were emphasized in their study, in contrast to dense-graded asphalt concrete.

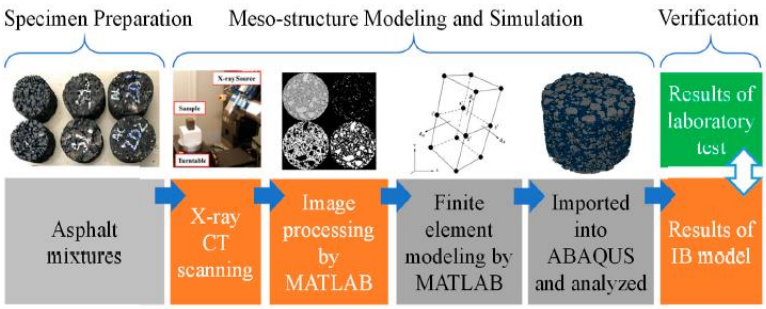


Figure 2.27 Image-based model development steps (Zhao et al. 2020).

In summary, recent advances in numerical approaches and computational methods promote inverse methods for solving problems characterized by differential equations (Telejko & Malinowski, 2004). When specific data required for direct solutions are unavailable, an inverse technique can determine them based on the temperature field within a given sample. Thus, it can be concluded that after developing a suitable material model, the inverse method can also be combined with commercially available finite element software to determine the thermal properties of asphalt concrete.

2.5 Effects of Mixture Components on Thermal Properties of Asphalt Concrete

Due to the multi-component material structure of the asphalt mixture, the thermal properties are affected by each component. There is no doubt that the thermal properties of asphalt concrete depend on factors such as the type of aggregate, the degree of compaction, the amount of water in the mix, the percentage of air voids, the viscoelasticity of the bitumen, and the addition of conductive additives (Mrawira & Luca, 2006; Côté & Konrad, 2005; Bai et al., 2015). This can be explained by the fact that the different combination of the mix components have different capacities for heat transfer, storage, and release (Cengel, 2003). Under these conditions, these capacities ultimately affect the thermal properties of asphalt concrete directly or

indirectly. Therefore, some studies have been conducted on the effects of mix components on thermal properties. This section summarizes in detail the impact of the main mixture constituents (such as aggregate, bitumen and air voids) on the thermal characteristics of asphalt concrete.

2.5.1 Effects of Aggregate on Thermal Properties of Asphalt Concrete

Aggregates are the most critical component and are constantly exposed to heat from the mixing stage to compaction, as shown in Figure 2.28 (Jamshidi et al., 2017).

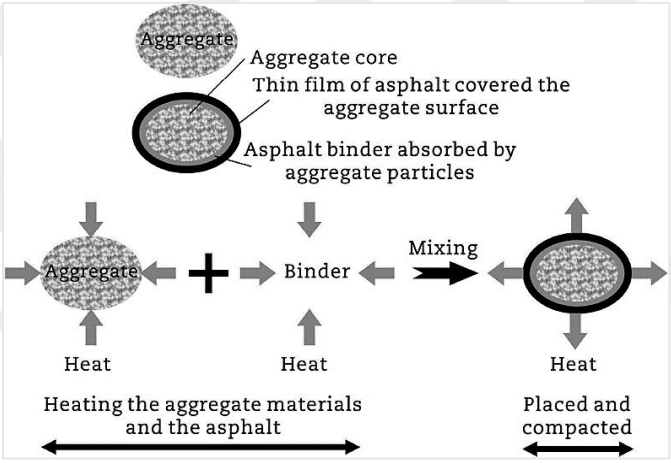


Figure 2.28 Endothermic and exothermic stages of aggregates (Jamshidi et al., 2017).

In asphalt pavements, temperature variations in the aggregates inevitably contribute to thermal stress and affect their thermal performance. Thus, it is particularly crucial to comprehend the thermal properties of aggregates to guarantee the longevity of the pavements. In this context, Stempihar et al. (2012) stated that the thermal properties of aggregates depend on the origin, mineral content, moisture content, particle size, and total density. As mentioned earlier, the thermal properties are specific to the material; therefore, the aggregate origin is expected to control these properties. Before examining how the aggregate influences the thermal properties of asphalt

concrete, the study by Tang et al. (2019) presented the results on the thermal conductivity of the aggregate itself. This should improve the understanding of its role in the mixture. The following shows the thermal conductivities of various rocks from the Sichuan Basin in Table 2.5.

Table 2.5 Thermal conductivity values of different rocks in the Sichuan Basin (Tang et al., 2019)

Type	**Thermal Conductivity (W/m.K)**
Dolomite	1.91 – 5.55
Limestone	1.74 – 4.64
Sandstone	1.74 – 5.24
Mudstone	1.69 – 3.89
Shale	1.80 – 3.14

Based on the thermal conductivity results as reported by Tang et al. (2019), the aggregates dominate the thermal properties of the asphalt mixtures. Since they have better thermal properties than the other mixture components (Côté & Konrad, 2013; Han et al., 2021). This is due to the fact that the values measured in previous studies for the thermal conductivity of bitumen and air were about 0.17 W/m.K and 0.024 W/m.K, respectively, significantly lower than those of aggregates (Côté & Konrad, 2013).

Mrawira & Luca (2006) investigated the effects of different aggregate gradations, aggregate types, and degrees of compaction on thermal properties. In their study, two aggregates, three gradations and four compaction levels were chosen. Then, the thermal conductivity was determined in the range of 1.7 to 2.1 W/m.K using the University of New Brunswick k-alpha tester. Although the study directly concluded that aggregate type most affects the thermal characteristics of asphalt concrete, neither the degree of compaction nor the effects of aggregate size distribution are

identified as statistically significant parameters due to the limited range of mix design factors. Côté & Konrad (2013) also confirmed that the thermal conductivity of asphalt mixture depends on the mineralogical origin of the aggregates. Moreover, Chen et al. (2022a) pointed out that more interlocking and contact points between aggregates can be expected when more coarse aggregates are present, which can improve heat conduction (see Figure 2.29). Additionally, changing the coarse aggregate content leads to alterations in other factors, including air void content, total aggregate content, and asphalt binder content. Inevitably, these parameters directly affect the thermal conductivity of the asphalt mixtures (Chen et al., 2022a).

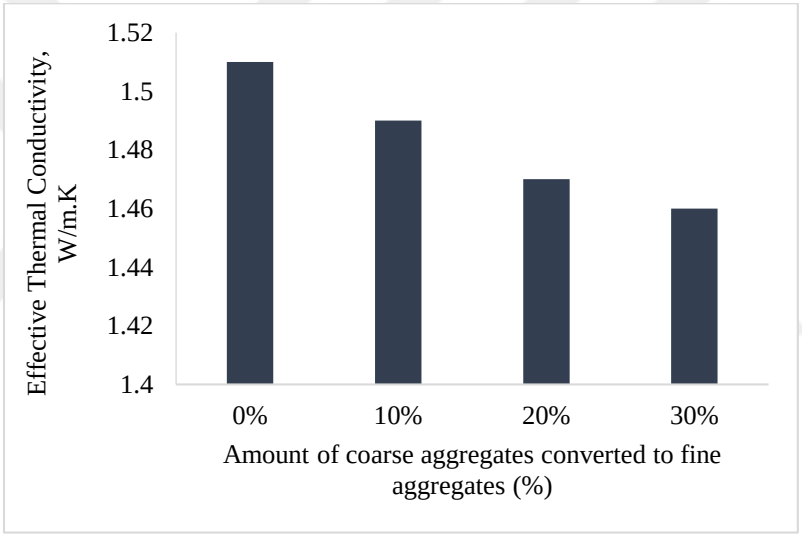


Figure 2.29 Change in thermal conductivity with coarse aggregate content (Chen et al., 2022a).

On the other hand, Mirzanamadi et al. (2018) stated that mixtures prepared with aggregates with high thermal conductivity will lead to higher thermal conductivity of mixture. Han et al. (2021) supported the study of Mirzanamadi et al. (2018) and further stated that aggregates control the asphalt mixture's thermal properties. Chen et al. (2018) also reported that smaller aggregates with a size between 2.36 and 4.75 mm have lower porosity and higher thermal conductivity than those with a size between 4.75 and 9.5 mm. Yan et al. (2019) discussed the effect of gradation (such

as dense or open graded) on the thermal conductivity of asphalt mixtures. According to their study, the dense-graded mix had a much higher thermal conductivity value than the open-graded mix. Their study also noted that aggregate size affects the thermal conductivity of the mixture. Therefore, the study concluded that mixtures containing larger aggregates exhibit higher thermal conductivity than those containing smaller aggregates.

2.5.2 Effects of Bitumen on Thermal Properties of Asphalt Concrete

In asphalt mixtures, bitumen acts as a kind of binding agent between aggregate particles (Rahman et al., 2020). In addition, bitumen is the most sensitive to temperature variations in the mix, and its influence on the thermal properties of the mixture is apparent. Therefore, this section summarizes several studies on the effects of bitumen on the thermal properties of asphalt concrete.

Côté & Konrad (2013) investigated the impact of different bitumen types on the thermal conductivity of asphalt concrete. Accordingly, Table 2.6 shows the thermal conductivity of the three different bitumen. It is obvious that the type of bitumen has little effect on the degree of heat transfer in asphalt concrete. However, the study claimed that the bitumen's presence in the mixture raised its thermal conductivity. The idea that bitumen forms heat bridges between aggregates supported this claim.

Table 2.6 Thermal conductivity of different bitumen types measured by Côté & Konrad (2013).

Bitumen Type	Air Void, %	Thermal Conductivity (W/m.K)
PG58-28	8.5	1.24
PG58-34		1.22
PG64-34		1.21

Pan et al. (2017) also studies the relationship between the different types of bitumen and the thermal conductivity of the mixtures. They reported that the percentage of bitumen in asphalt mixtures is relatively low, and hence, changing bitumen types does not significantly change the thermal properties of asphalt mixtures. Nazki et al. (2020) then investigated the rheological properties and thermal conductivity of bitumen in solving rutting problems in asphalt mixtures. They mentioned how the bitumen itself affects the thermal conductivity of asphalt mixtures and not the type of bitumen. Although 85–87% of asphalt mixtures consist of aggregate, the bitumen, which makes up 10-15% of the volume, determines the thermal conductivity as it absorbs heat and stores in the layer due to its black color. Their study concluded that the lower thermal conductivity of bitumen reduces heat transfer to deeper layers, which increases the temperature within the layer.

In short, there are very few studies on the effect of bitumen on the thermal conductivity of asphalt mixture. On the other hand, the number of research continues to increase using thermally conductive fillers. Graphite, carbon and steel fibers, etc. have recently been favored as thermally conductive additives to improve the thermal conductivity of bitumen or asphalt mixtures (Dawson et al., 2012; Zhou et al., 2012; Vo et al., 2017; Nazki et al., 2020).

2.5.3 Effects of Air Voids on Thermal Properties of Asphalt Concrete

Air voids are one of the most critical components affecting the thermal properties of asphalt concrete (Yan et al., 2019). Hassn et al. (2016a) experimentally investigated the effects of air void content on asphalt concrete. In their study, asphalt mixtures with different air void contents prepared using 60/40 penetration grade bitumen and a maximum particle size of 20 mm were examined. According to their study, asphalt concrete's volumetric heat capacity and thermal conductivity dropped to 30% and 40%, respectively, when the percentage of air void content was raised from 5% to 25%. Chen et al. (2022a) also found similar conclusions to Hassn et al. (2016a), as shown in Figure 2.30. In general, the thermal conductivity and specific heat capacity

of mixtures with high air content were reported to be lower, and this result is consistent with other previous studies (Mrawira & Luca, 2006; Pan et al., 2017; Nassiri & Nantasai, 2017; Khasawneh et al., 2023).

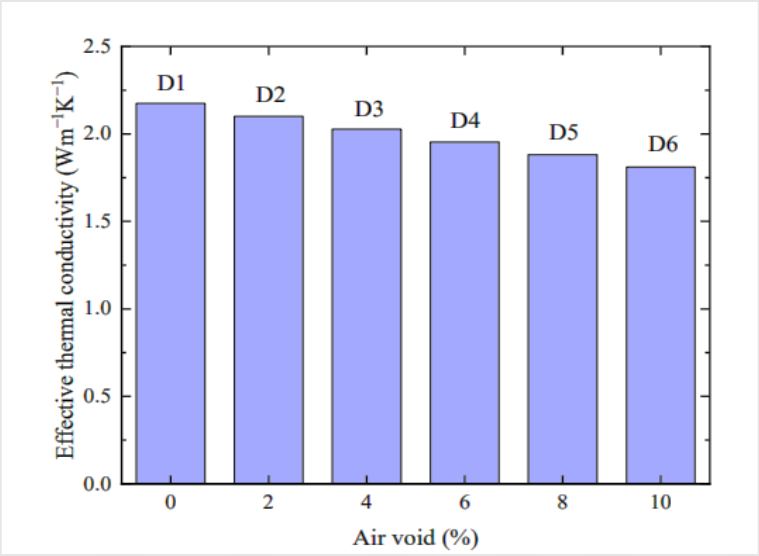


Figure 2.30 Effects of air voids on six sets of three-dimensional digital asphalt concrete specimens (Chen et al., 2022a).

Additionally, Han et al. (2021) claimed that air voids serve as a thermal barrier due to their low thermal conductivity. As the compaction effort was increased, the air voids in the mixture were reduced. This allows the bitumen to fill the VMA, resulting in a tightly packed aggregate particle. Thus, a well-compacted asphalt mixture is expected to have higher thermal conductivity (Mrawira & Luca, 2006). During the winter snowmelt, Pan et al. (2017a) researched the relationship between the air void content and the thermal properties of asphalt pavements. According to their study, melting snow water penetrated the air voids of asphalt concrete and changed its thermal conductivity. The general statement is that the thermal conductivity of water is higher than that of air. Accordingly, this study concluded that, as shown in Figure 2.31, water-saturated specimens demonstrated better thermal conductivity compared to dry samples, despite the use of different types of aggregates.

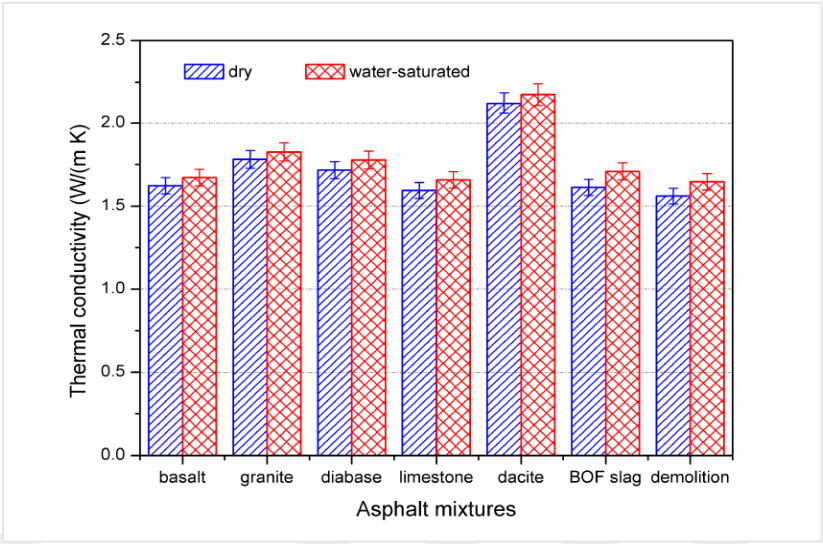


Figure 2.31 Thermal conductivity of dry and water-saturated asphalt mixtures (Pan et al., 2017).

CHAPTER 3

METHODOLOGY

3.1 Introduction

In this section, the methodology of the experimental design is described in detail. First, the matrix for selecting test materials and design is presented. Then, the physical and mechanical properties of the materials used in this study are presented. Next, the design gradations, optimum binder contents, and volumetric properties are explained in relation to the Superpave mix design method. In addition, the test setups and procedures for determining the specific heat capacity and thermal conductivity are described. Finally, the technical details of these test setups and procedures are explained in more detail.

3.1.1 Classification of Experimental Groups

This study focused on the effects of mix properties such as aggregate type, air void content, and maximum aggregate size (MAS) on the thermal properties of asphalt concrete. In this context, basalt and dolomite were selected as two aggregates commonly used in road construction. 19 mm and 12.5 mm were selected as two different maximum aggregate sizes. The mix designs were carried out using the Type 1 and Type 2 gradation limits of the Turkish General Directorate of Highways (TGDH) according to the Superpave mix design method. After finalizing the mix design with 4% air void content, samples with 2% and 6% air void content were also prepared to investigate the effects of different compaction levels in the field. In the following sections, a summary of the mix variables is shown in Figure 3.1.

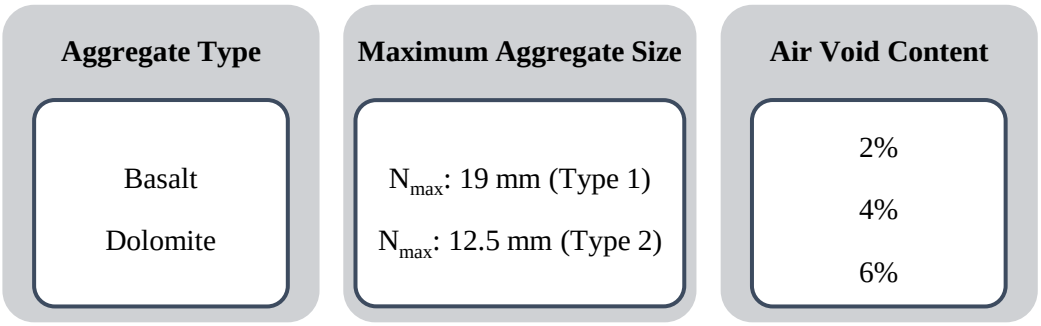


Figure 3.1 Variables in the experimental matrix.

According to this classification, a total of 12 different mix designs were carried out and five replicate samples were prepared for each combination. A total of 60 samples were used for the test program. To differentiate the samples, an abbreviated nomenclature is used for the following parts. The letters 'B' and 'D' are used for basalt and dolomite, respectively. The air void content is given after the abbreviation of the aggregate type. The abbreviation 'T1' or 'T2' refers to Type 1 or Type 2, respectively. Finally, the last part of the abbreviation stands for the sample number. The following example of this nomenclature is shown in Table 3.1.

Table 3.1 Nomenclature of the samples.

Aggregate Type	Air Void Content	Gradation Type	Sample No	Nomenclature
Basalt	2%	Type 1	01	B2T101
Dolomite	6%	Type 2	04	D6T204

3.2 Materials

This section provides a discussion on the materials utilized in the mix designs, along with the corresponding physical properties of these materials.

3.2.1 Aggregates

Two different aggregates were used in this study for the production of asphalt mixtures. The basalt and dolomite aggregates were obtained from quarries in Kayseri and Konya. The coarse (retained on the No. 4 sieve), fine (passing the No. 4 sieve), and filler (passing the No. 200 sieve) aggregates were tested for necessary properties according to TGDH specifications. The measured physical properties of the aggregates are listed in Table 3.2.

Table 3.2 Physical properties of aggregates used in this study.

Aggregate Properties		**Standards**	**Aggregate Types**	
			Basalt	**Dolomite**
Specific Gravity for Coarse Aggregate	Bulk	ASTM C127	2.663	2.781
	SSD		2.723	2.796
	Apparent		2.833	2.824
Water Absorption for Coarse Aggregate (%)			2.26	0.55
Specific Gravity for Fine Aggregate	Bulk	ASTM C128	2.693	2.742
	SSD		2.758	2.764
	Apparent		2.880	2.806
Water Absorption for Fine Aggregate (%)			2.41	0.85
Specific Gravity for Filler		ASTM D854	2.711	2.814
Los Angeles Abrasion (%)		ASTM C131	11.7	18.4

As mentioned in the literature review, the material composition directly affects the thermal properties. In particular, the mineralogical origin of aggregates can help to understand the thermal properties of asphalt mixtures since different minerals have different thermal conductivities and heat storage capacities (Robertson, 1988). For example, aggregates rich in minerals such as quartz or feldspar tend to have higher thermal conductivity than aggregates dominated by clay minerals (Clauser & Huenges, 1995). For this reason, in addition to the physical properties listed in Table 3.2, X-ray powder diffraction analysis was made to identify unknown crystalline materials. As can be seen in Figure 3.2, feldspar minerals of calcareous origin, especially anorthite, dominate the basalt, while quartz minerals make up the bulk of the dolomite.

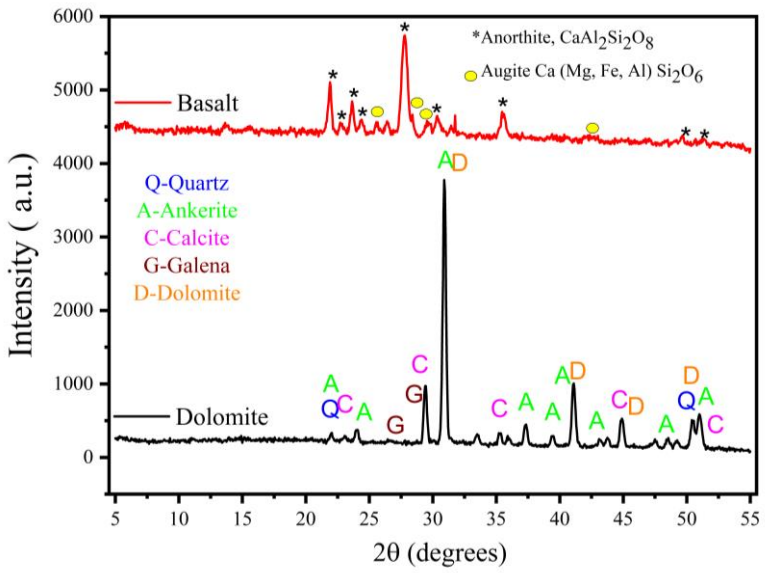


Figure 3.2 X-ray diffraction intensity vs. diffraction angle of basalt and dolomite.

3.2.2 Bitumen

A virgin binder was used with a penetration grade 50/70 to prepare the asphalt mixtures. The physical properties of the bitumen were also determined using the relevant standards and listed in Table 3.3.

Table 3.3 Bitumen properties used in this study.

Binder Properties		**Standards**
Binder Grade	Pen 50/70	
Specific Gravity G_b (gr/cm^3)	1.029	ASTM C70
Softening Point (˚C)	51	ASTM D36
Ductility (cm)	>100	ASTM D113
Penetration (25˚C, 0.1mm)	52	ASTM D5
Flash point (˚C)	338	ASTM D92
Fire point (˚C)	387	ASTM D92

3.2.2.1 Mixing and Compaction Temperature

The mixing and compaction temperatures were determined using the temperature-viscosity curve. In accordance with the AASHTO T316 standard, the viscosity of bitumen was tested at different temperatures using a rotational viscometer. The viscosity readings were recorded at 10°C intervals, starting from 120°C and continuing until the temperature reached 180°C. The temperature controller was programmed to attain the desired temperature within a time frame of 30 minutes for each individual stage. The viscosity reading was taken at the target temperature after 10 minutes of the equilibrium period. The rotational speed of the viscometer was adjusted to 20 revolutions per minute. The temperatures required for mixing and compacting the asphalt mixture to the desired viscosity were then determined, as shown in Figure 3.3. Finally, the mixing and compaction temperatures were set at 155°C and 145°C.

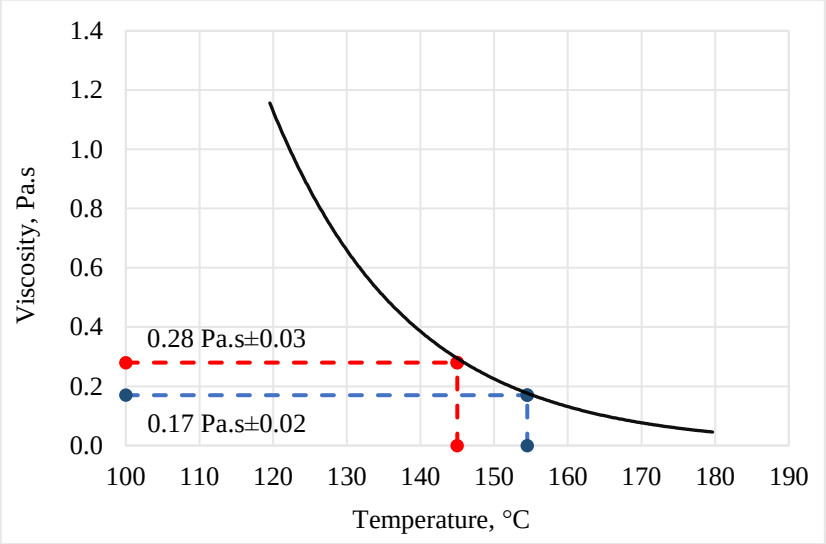


Figure 3.3 Temperature-viscosity curve of Pen 50/70 bitumen.

3.3 Superpave Mix Design

The Superior Performing Asphalt Pavement System (Superpave) was developed in 1993 as an important result of the SHRP. A practical and logical mix design method was the goal of this program. The selection of asphalt binder and aggregate was directly integrated into the design process considering traffic and climatic conditions. A gyratory compactor was proposed to achieve a laboratory density equivalent to the estimated field density at various traffic volumes. In addition, the number of gyrations was varied to simulate the expected traffic volumes. Finally, the volumetric properties in the mix design were used to select the optimum bitumen content for the design gradation. Accordingly, the Superpave mix design method was used to prepare the mix designs in this study. The Superpave mix design was prepared following the AASHTO M323 and AASHTO R35 standards. Below is a brief explanation of the basic steps required for the Superpave design process.

3.3.1 Superpave Gyratory Compactor

In this study, the Controls ICT 250 gyratory compactor shown in Figure 3.4 was used for compaction. Three parameters controlled the compaction performance of the Superpave gyratory compactor. These were the vertical pressure, the gyration angle, and the number of gyrations. According to the Superpave system, the vertical pressure was set to 600 kPa, and the gyration angle to 1.25 deg. The gyrations were performed at 30 revolutions per minute. The compactor was also equipped with molds that had a height of 300 mm and a diameter of 150 mm.



Figure 3.4 Superpave gyratory compactor.

The Superpave gyratory compactor was specifically engineered to compress asphalt mixtures to the desired density that should be attained in practical circumstances with vehicular traffic. At this point, the number of gyrations for different traffic levels should be known to continue the Superpave mix design process. In the following, Table 3.4 shows the initial, design, and maximum number of gyrations for various Design ESALs values (specified in AASHTO R35). The design ESALs value was

set at 3 to <30 million in this study. Thus, the Superpave gyratory compactor was adjusted to 100 gyrations when the samples were placed inside the compactor. A total of 60 samples were compacted with the gyratory compactor.

Table 3.4 The number of gyrations according to different design ESALs (specified in AASHTO R35).

Design ESALs (million)	**Compaction Parameters**		
	$N_{initial}$	**N_{design}**	**$N_{maximum}$**
<0.3	6	50	75
0.3 to <3	7	75	115
3 to <30	8	100	160
≥ 30	9	125	205

3.3.2 Control Points in the Selection of Aggregate Blends

The Superpave mix design method begins with the selection of aggregate type based on its availability and its ability to meet certain criteria in terms of mechanical and shape properties. Then, an appropriate binder is selected based on its Performance Grade (PG), which considers the temperature limits of the region and the traffic volume. In this study, two types of aggregates and one type of bitumen were used, whose physical properties have been already presented in Table 3.2 and Table 3.3.

It is well known that a well-designed aggregate blend directly influences the volumetric properties specified in the AASHTO Superpave volumetric design standards. Therefore, it was essential to follow some limit values when selecting trial aggregate blends. Accordingly, the gradation limits established by TGDH and

AASHTO were considered together for the wearing course. In the following, the gradation limits for the wearing course according to TGDH are listed in Table 3.5.

Table 3.5 Gradation limits according to TGDH specifications for the wearing course.

Sieve Sizes, mm	**Type -1**	**Type -2**
19	100	-
12.5	88 – 100	100
9.5	72 – 90	80 – 100
6	-	-
4.75	42 – 52	55 – 72
2	25 – 35	36 – 53
0.425	10 – 20	16 – 28
0.180	7 – 14	8 – 16
0.075	3 – 8	4 – 8

According to the specifications of TGDH, three types of gradation limits are defined for the wearing course. The upper and lower limits of Type-1 and Type-2 were selected in this study. In addition to the TGDH gradation limits, the control points and the restricted zone boundary values were also defined for NMAS of 12.5 mm and 9.5 mm according to AASHTO M323, as listed in Table 3.6. In this study, TGDH and AASHTO limits were considered together to select appropriate aggregate blends.

Table 3.6 The control points and restricted zone boundary (AASHTO M 323).

Sieve Sizes, mm	12.5 mm Nominal Size				9.5 mm Nominal Size			
	Control Points		Restricted Zone Boundary		Control Points		Restricted Zone Boundary	
	Lower	Upper	Lower	Upper	Lower	Upper	Lower	Upper
19	100	100						
12.5	90	100			100	100		
9.5	-	90			90	100		
4.75	-	-			-	90		
2.36	28	58	39.1	39.1	32	67	47.2	47.2
1.18	-	-	25.6	31.6	-	-	31.6	37.6
0.60	-	-	19.1	23.1	-	-	23.5	27.5
0.30	-	-	15.5	15.5	-	-	18.7	18.7
0.15	-	-			-	-	-	-
0.075	2	10			2	10	-	-
Nominal Maximum Aggregate Size					12.5 mm		9.5 mm	
Primary Control Sieve					2.36 mm		2.36 mm	
PCS Control Point (% Passing)					39		47	

3.3.3 Design Requirements in Volumetric Properties

The Superpave mix design method uses the volumetric properties of compacted mixtures to select the optimum bitumen content. The optimum bitumen content is defined as the point at which a minimum of voids in the mineral aggregate (VMA) is achieved. In this study, the limits of the volumetric properties for the wearing course according to TGDH are shown in Table 3.7 below. In addition to the TGDH design requirements, care was taken to ensure that the prepared samples met the specifications of AASHTO M323. In the following, the volumetric design requirements according to AASHTO are also listed Table 3.8.

Table 3.7 Volumetric design requirements according to TGDH.

Specifications, %	Type -1 & Type -2	
	Min	Max
Air Void Content (V_a)	3	5
Voids Filled with Asphalt (VFA)	65	75
Voids in the Mineral Aggregate (VMA)	14	16
Dust-to-Binder Ratio	-	1.5
Bitumen content	4	7

Table 3.8 Volumetric design requirements according to AASHTO M323.

Design ESALs[a] (Million)	Required Relative Density, Percent of Theoretical Maximum Specific Gravity			VMA, Percent Minimum			VFA Range[b], Percent	Dust-to-Binder Ratio Range[c]
				NMAS, mm				
	$N_{initial}$	N_{design}	N_{max}	19	12.5	9.5		
<0.3	≤91.5	96	≤98	13	14	15	70-80[d]	0.6-1.2
0.3 to <3	≤90.5	96	≤98	13	14	15	65-78	0.6-1.2
3 to <10	≤89	96	≤98	13	14	15	65-75[e]	0.6-1.2
10 to <30	≤89	96	≤98	13	14	15	65-75[e]	0.6-1.2
≥30	≤89	96	≤98	13	14	15	65-75[e]	0.6-1.2

[a] Design ESALs are the anticipated project traffic level expected on the design lane over a 20-year period. Regardless of the actual design life of the roadway, determine the design ESALs for 20 years.

[b] for 37.5-mm nominal maximum size mixtures, the specified lower limit of the VFA range shall be 64 percent for all design traffic levels.

[c] for 4.75-mm nominal maximum size mixtures, the dust-to-binder ratio shall be 0.9 to 2.0.

[d] for 25.0-mm nominal maximum size mixtures, the specified lower limit of the VFA range shall be 67 percent for design traffic levels < 3 million ESALs,

[e] for design traffic levels >3 million ESALs, 9.5-mm nominal maximum size mixtures, the specified VFA range shall be 73 to 76 percent and for 4.75-mm nominal maximum size mixtures shall be 75 to 78 percent

3.3.4 Sample Preparation Procedure with Superpave Gyratory

During the mix design, the aggregates and bitumen were initially kept at a mixing temperature in the oven to ensure thermal equilibrium. Next, the mixtures were thoroughly mixed at mixing temperature. Then, all loose mixtures were aged in the oven at compaction temperature for 2 hours. After the short-term aging, the mixtures were compacted with the Superpave gyratory compactor at the selected compaction temperature. Before starting the compaction process, the papers and steel plates were placed on top and bottom of the molds. In addition, the molds were heat-treated at the compaction temperature to ensure that they reached thermal equilibrium. During these processes, the AASHTO T312 was followed. When the required conditions were satisfied, the compacted samples with a diameter of 150 mm and an average height of 120 mm were produced using approximately 4900 g of aggregate. After that, the compacted samples were allowed to cool before measuring the volumetric properties. In summary, the following design parameters were preferred during the sample preparation phase, as given in Table 3.9.

Table 3.9 Selected design parameters.

Design Parameters	**Selected Parameters**
N_{des}	100 cycles
Design ESALs	3 to <30 million
Mixing Temperature	155 °C
Compacting Temperature	145 °C
Air Void Content, %	4

3.3.5 Design Gradation

The determination of the design gradation was based on factors such as the lower and upper limits, the control points, the maximum density line, and the restricted zone boundary. Specifically, the lower and upper design limits of TGDH and AASHTO specifications were considered in selecting the aggregate blends, as shown in Table 3.5 and Table 3.6. Each design gradation was kept within these limits to meet the volumetric property requirements of the Superpave mix design method. Accordingly, four mix designs were developed, each incorporating two types of aggregates, two different maximum aggregate sizes, and two design gradations (See Table 3.10 and Table 3.11). In Type 1, the gradation curves for basalt and dolomite were similar, except that the filler content was 3.4% for basalt and 4% for dolomite to meet the specification limits. On the other hand, the gradation curves for Type 2 were chosen to be identical for basalt and dolomite. In the following, the gradation curves used in this study are also shown in Figure 3.5 and Figure 3.6, respectively.

Table 3.10 Mix design classifications.

Mix Design ID	**Design 1**	**Design 2**	**Design 3**	**Design 4**
Aggregate Type	Basalt		Dolomite	
Design Gradation	Type-1	Type-2	Type-1	Type-2

Table 3.11 The design gradations used in this study.

Types	**Sieve Sizes, mm**	**19**	**12.5**	**9.5**	**4.75**	**2**	**0.425**	**0.18**	**0.075**
Type 1	Basalt	100	97	85	49	28	13	8	3.4
	Dolomite	100	97	85	49	28	13	8	4
Type 2	Basalt & Dolomite	-	100	97	72	38	16	8	4

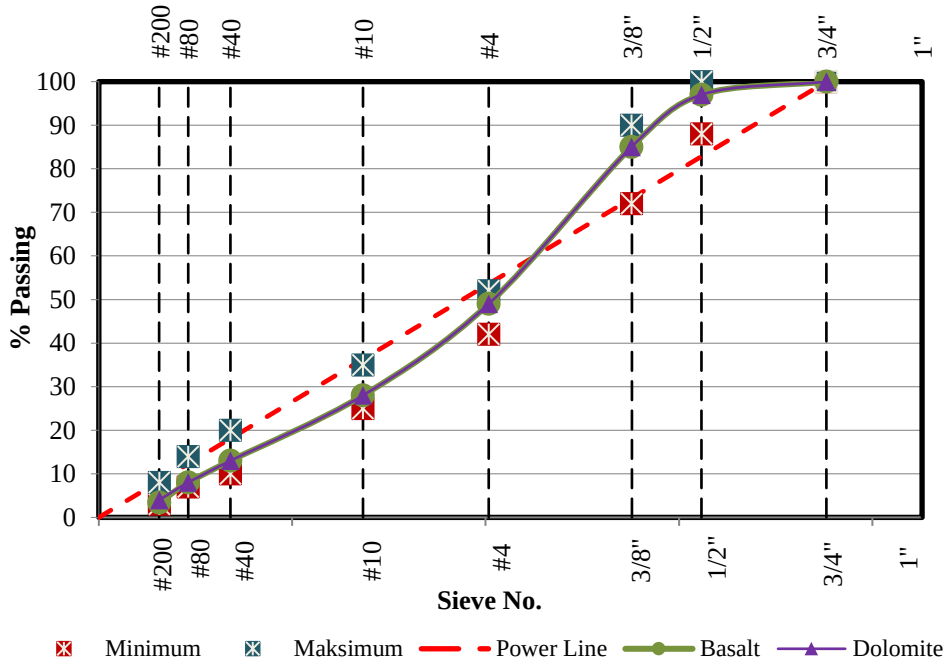


Figure 3.5 The gradation curves of aggregate blends for Type 1 basalt and dolomite.

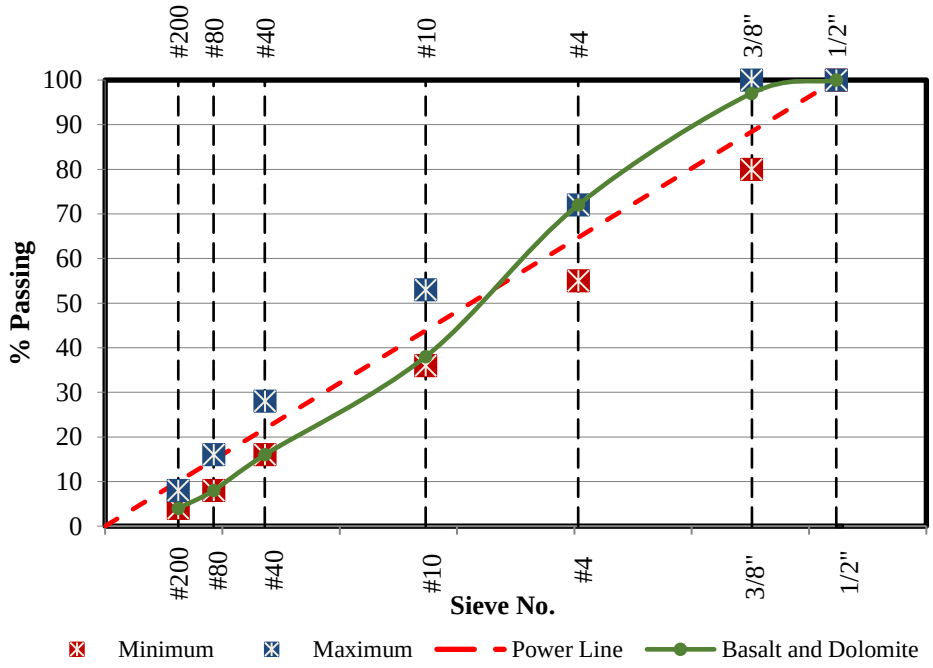


Figure 3.6 The gradation curves of aggregate blends for Type 2 basalt and dolomite.

After determining the design gradations, the bulk specific gravity (G_{sb}) of the aggregate blend was required to calculate the volumetric properties of the mixtures. The relative ratios of coarse aggregate, fine aggregate, and filler in the aggregate blends were known for each mix design. Therefore, Equation 3.1 was used to calculate the value of G_{sb} for each blend.

$$G_{sb} = \frac{P_1+P_2+P_3}{\frac{P_1}{G_1}+\frac{P_2}{G_2}+\frac{P_3}{G_3}} \quad 3.1$$

In Equation 3.1, P represents the percentage of each constituent, and G represents the bulk specific gravity of these constituents. Accordingly, Table 3.12 shows the specific bulk gravity values for each design gradation.

Table 3.12 The bulk specific gravity values of aggregate blends in mix designs.

Mixture Design Type	**Coarse Aggregate, %**	**Fine Aggregate, %**	**Filler, %**	**G_{sb}**
Design 1	51	45.6	3.4	2.678
	2.663	2.693	2.711	
Design 2	28	68	4	2.685
	2.663	2.693	2.711	
Design 3	51	45	4	2.765
	2.781	2.742	2.814	
Design 4	28	68	4	2.756
	2.781	2.742	2.814	

3.3.6 Optimum Bitumen Content of the Design Gradation

Determining the optimum bitumen content first requires a trial grading and selection of an estimated bitumen content. Then, trial mixtures were prepared in accordance with AASHTO T312. These mixtures were prepared with different bitumen contents.

These included the estimated bitumen content, the estimated content ±0.5%, and the estimated content +1%. After that, three replicate samples were produced for each bitumen content and their volumetrics were calculated according to the TGDH and AASHTO specifications. As indicated in the Superpave mix design method, design gradation is established when the volumetric property limits in the relevant standards are met; otherwise, trial gradation and bitumen selection are further attempted. In the Superpave mix design method, the optimum bitumen content is determined at 4% air voids or 96% of the theoretical maximum density at N_{des}, as shown in Figure 3.7.

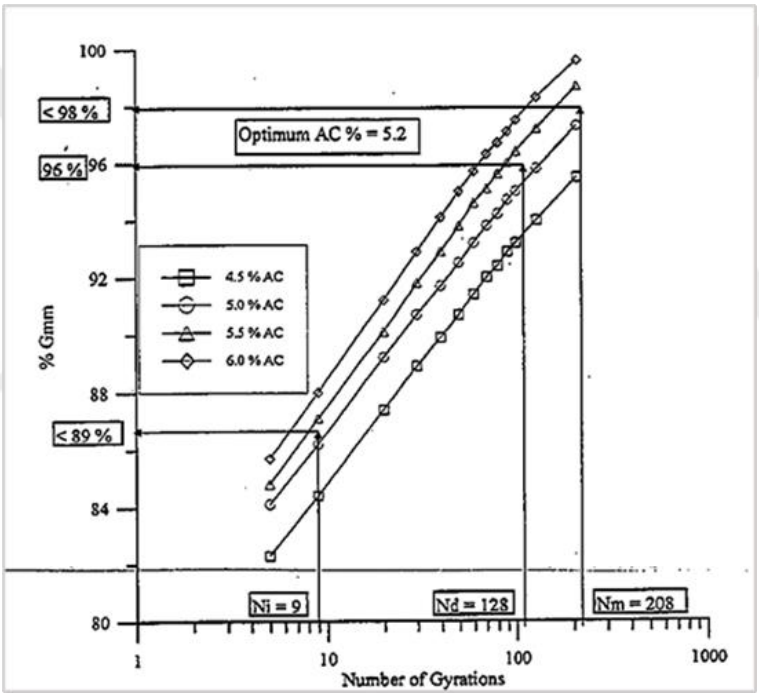


Figure 3.7 Plots for determination of optimum bitumen content (Roberts et al., 1996).

Moreover, Figure 3.8 below shows a diagram of the volumetric properties of asphalt mixtures that help determine the optimum bitumen content. In this regard, twelve compacted samples (at least three compacted samples for each bitumen content) and loose mixtures were prepared. Then, the bulk specific gravity of the compacted samples, G_{mb} (AASHTO T166, 2010), and the theoretical maximum density of the

loose mixtures, G_{mm} (AASHTO T209, 2010), were determined. After that, these densities were used to calculate the volumetric properties of asphalt mixtures. First of all, Equation 3.2 was used to calculate the air void content (V_a) of the mixtures.

$$\mathrm{Va} = \left(1 - \frac{G_{mb}}{G_{mm}}\right) \mathrm{x}100 \qquad 3.2$$

In addition to V_a, the voids in the mineral aggregates (VMA), the voids filled with asphalt (VFA), and the volume of absorbed asphalt (V_{ba}) were calculated to describe the volumetric properties of the mixtures. It is defined that VMA is the sum of the volumes of air and effective asphalt in a component diagram and can be calculated using Equation 3.3.

$$\mathrm{VMA} = \left(1 - \frac{G_{mb}(1-P_b)}{G_{sb}}\right) \qquad 3.3$$

VFA is the percentage of compacted aggregate voids filled by asphalt, and Equation 3.4 below was used to calculate the VFA.

$$\mathrm{VFA} = \frac{\mathrm{VMA}-\mathrm{Va}}{\mathrm{VMA}} \qquad 3.4$$

V_{ba} is the amount of asphalt absorbed into aggregate pores, and Equation 3.5 below was used to calculate the V_{ba}.

$$V_{ba} = \left(\frac{G_{se}-G_{sb}}{G_{se}G_{sb}}\right) G_b \times 100 \qquad 3.5$$

G_{se} represents the effective specific gravity of the aggregate, and G_b represents the specific gravity of the bitumen.

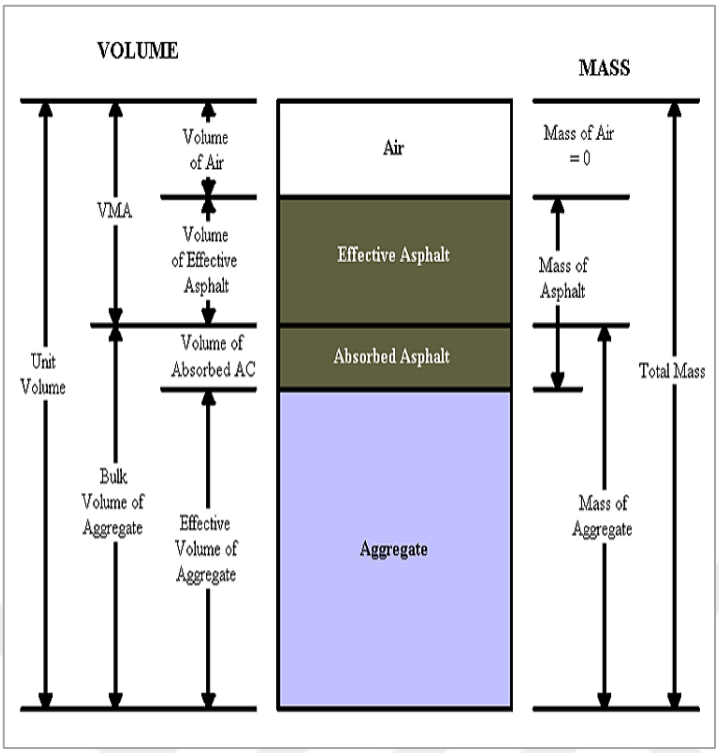


Figure 3.8 Components in volume and mass of asphalt mixtures (Coree & Hislop, 2000).

Using the above equations, the volumetric properties of mixtures with different bitumen contents were calculated, resulting in the generation of graphs. These graphs were used to determine the optimum bitumen contents of the mixtures and are shown in Appendix A. In particular, the air void and bitumen content graphs were first used to determine the optimum bitumen contents, which initially corresponded to an air content of 4%. Then, the volumetric properties corresponding to the optimum bitumen content were determined. Table 3.13 below summarizes the requirements of the relevant standards and includes the optimum bitumen contents, VMA, VFA, unit weights, and dust ratios for each mix design. It can be concluded that the volumetric properties determined met both the TGDH and AASHTO limits, so the mix design was completed for this study.

Table 3.13 Volumetric properties of each mix design in this study.

Mix Design ID	Optimum Bitumen Content, %	VMA, %	VFA, %	Density, kg/m^3	Dust to Binder Ratio
Design 1 (Basalt + Type 1)	5.5	15.9	74.5	2386	0.665
Design 3 (Dolomite + Type 1)	4.9	14.5	72.2	2487	0.927
Requirements (According to AASHTO and TGDH)	4 - 7	14 - 16	65 - 75	-	0.6 – 1.2
		Min. 14			<1.5
Design 2 (Basalt + Type 2)	6.2	15.1	74.3	2430	0.860
Design 4 (Dolomite + Type 2)	5.7	16.1	75	2452	0.805
Requirements (According to AASHTO and TGDH)	4 - 7	14 - 16	65 – 75	-	0.6 – 1.2
		Min. 15			<1.5

3.4 Volumetric Properties of the Compacted Samples

This section gives the average volumetric properties of the compacted samples used in the thermal property measurements. As mentioned above, the samples were prepared following the above mix design process. At first, design samples with 4% air void content were prepared. Subsequently, samples with two other air voids (2% and 6%) were also prepared to represent typical air voids in the field. Since the samples were used both in thermal conductivity and specific heat capacity measurements, five replicates were prepared, and their volumetric properties were measured subsequently. The volumetric properties and design parameters of all the test samples are listed in Appendix B. In Table 3.14, the average volumetric properties of the samples prepared with Design 1, Design 2, Design 3 and Design 4 are listed.

Table 3.14 Average volumetric properties of five replicate samples.

Sample ID	Volumetric Properties				
	Va,%	VMA,%	VFA,%	Density, kg/m^3	Dust to Binder Ratio
B2T1	1.9	13.9	86.1	2438.6	0.675
B4T1	4.1	15.8	74.2	2385.4	
B6T1	6.1	17.6	65.4	2335.8	
B2T2	2.0	13.24	85.2	2483.4	0.874
B4T2	4.0	15.04	73.5	2432.0	
B6T2	6.0	16.78	64.5	2382.0	
D2T1	2.0	12.8	84.1	2536.8	0.924
D4T1	4.1	14.6	72.0	2483.2	
D6T1	6.0	16.3	63.1	2433.4	
D2T2	1.9	14.2	86.8	2508.4	0.798
D4T2	4.1	16.1	74.8	2452.2	
D6T2	6.0	17.8	66.2	2402.4	

3.5 Measurement of Thermal Properties for Asphalt Concrete Samples

This section presents a number of methods for determining the specific heat capacity and thermal conductivity of asphalt concrete. Initially, the process for measuring specific heat capacity with a calorimeter is described. Then, thermal conductivity measurements using steady-state and transient methods are explained.

3.5.1 Measurement of Specific Heat Capacity in Asphalt Concrete Using a Calorimetry-Based Approach

Previous test methods are primarily intended for uniform materials. However, asphalt concrete is a multi-component material, and measuring the specific heat capacity of asphalt pavements is still challenging. (Luca & Mrawira, 2005). In the past, various attempts have been made to measure the specific heat capacity of asphalt concrete, such as the weighted average method, the drop calorimeter method, DSC, and MDSC, etc., as summarized in Section 2.3.1.2 & 2.3.2.2 (Jordan & Thomas, 1976; Wolfe et al., 1980; Johnston, 1981; Hosseinnezhad et al., 2019; Zadshir et al., 2020). Nevertheless, the current methods for determining the specific heat capacity of asphalt concrete still have significant limitations, such as edge loss, the heterogeneous nature of asphalt concrete, the size effect, etc. Accordingly, a new approach was required to determine the specific heat capacity of asphalt concrete, and a method based on calorimetry was proposed in this study. Generally, a calorimeter is a test device used to quantify the amount of heat consumed or released. Moreover, calorimetry is a design widely used in thermochemistry to determine enthalpy, heat capacity, stability, and other properties. In this context, the proposed calorimeter design of this study is described in detail below.

3.5.1.1 Sample Preparation

As indicated earlier, the samples were prepared with a diameter of 150 mm and an average height of 120 mm. However, adjustments in these original dimensions were required in order to fit into the cabinet of the specific heat capacity test setup. Initially, a 1 cm thick slice was cut from the upper and bottom parts of the sample. Then, the remaining part of the sample was divided into two identical slices, each having a maximum height of about 5 cm. It should be noted that the maximum height of the sliced samples can be varied due to the different air void contents (2%, 4%, and 6%). After obtaining the slices, a hole was drilled in the center of the samples to

attach the Resistance Temperature Detector (RTD) sensors (See Figure 3.9). During the test, these sensors were used to record the temperatures in the center of the sample. Therefore, it was necessary to seal this hole before placing the samples in the cabinet to prevent contact with water. The hole was covered with waterproof tape before starting the test. After that, the pair of samples was ready for preconditioning until their initial temperature remained constant.

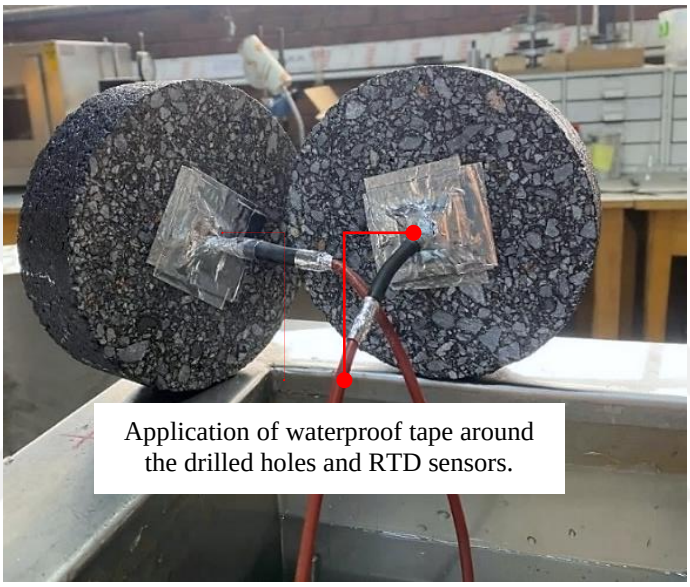


Figure 3.9 Samples with sensors attached prior to testing.

3.5.1.2 Test Setup

The test setup consisted of an insulated steel cabinet (40 x 40 x 45 cm), a plywood environmental chamber (60 x 60 x 60 cm), a preconditioning cabinet, a data acquisition system, RTD sensors, a water body, and a pair of samples. The first task in this setup was thermal insulation to minimize heat loss through the calorimeter walls as much as possible. Therefore, Izocam foam boards (λ: 0.035 W/m.°C) with a thickness of 5 cm were used to prepare the insulated cabinet and the environmental chamber. Figure 3.10 shows the Izocam foam boards, the walls of the cabinet, the environmental chamber, and the top view of the cabinet after insulation.

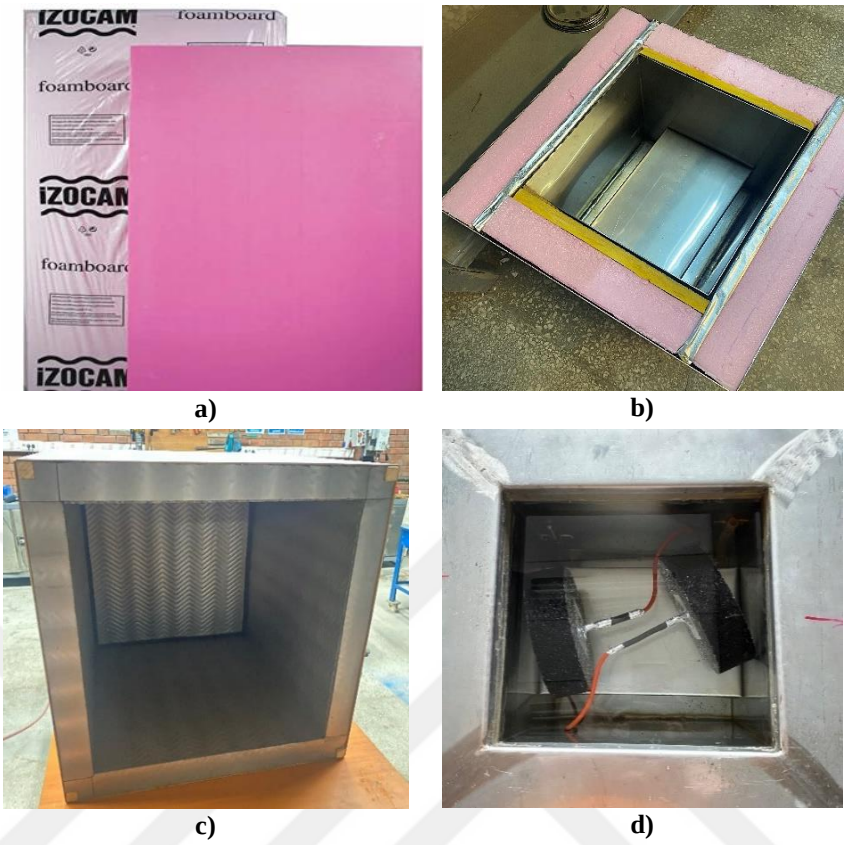


Figure 3.10 a) Izocam foam boards, b) Insulated cabinet, c) Insulated environmental chamber, d) Samples inside the insulated cabinet.

After completing the thermal insulation, the interior of the insulated cabinet was set up. Initially, a water heating resistor and a water circulation pump were placed at the bottom of the cabinet. The RTD sensors were then placed inside the cabinet to measure the temperature changes of the water in the cabinet and the samples. One of the sensors was attached to the wall of the cabinet, another was attached to the cover of the cabinet, and the other two were placed in the holes drilled in the center of the samples. A shelf was placed above the resistance of the water heater and the water circulation pump to place the samples. Once all of the equipment was in place, the distilled water was filled into the cabinet first, then the samples. Finally, the cover of the cabinet was closed, and the environmental chamber was placed on top. A detailed illustration of this setup can be seen in Figure 3.11.

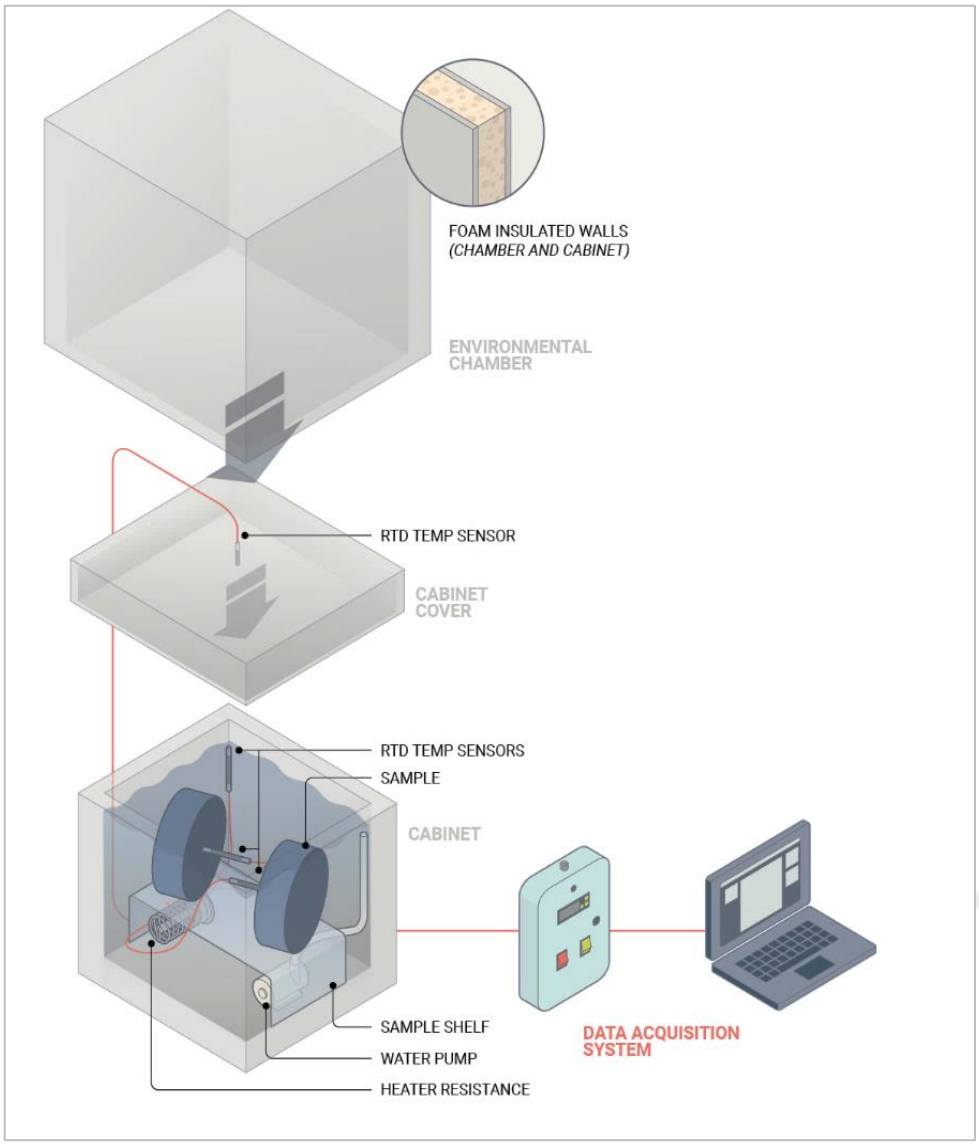


Figure 3.11 A detailed illustration of the test setup.

Figure 3.12 additionally shows all components of the setup in an overall view. The environmental chamber was designed to protect the insulated cabinet from temperature fluctuations under laboratory conditions. The insulated cabinet was then prepared for the samples to be subjected to heat transfer as in calorimetry. Prior to testing, the samples were conditioned at a constant temperature in the preconditioning cabinet. Finally, the data acquisition system recorded and monitored the temperature changes during the test.

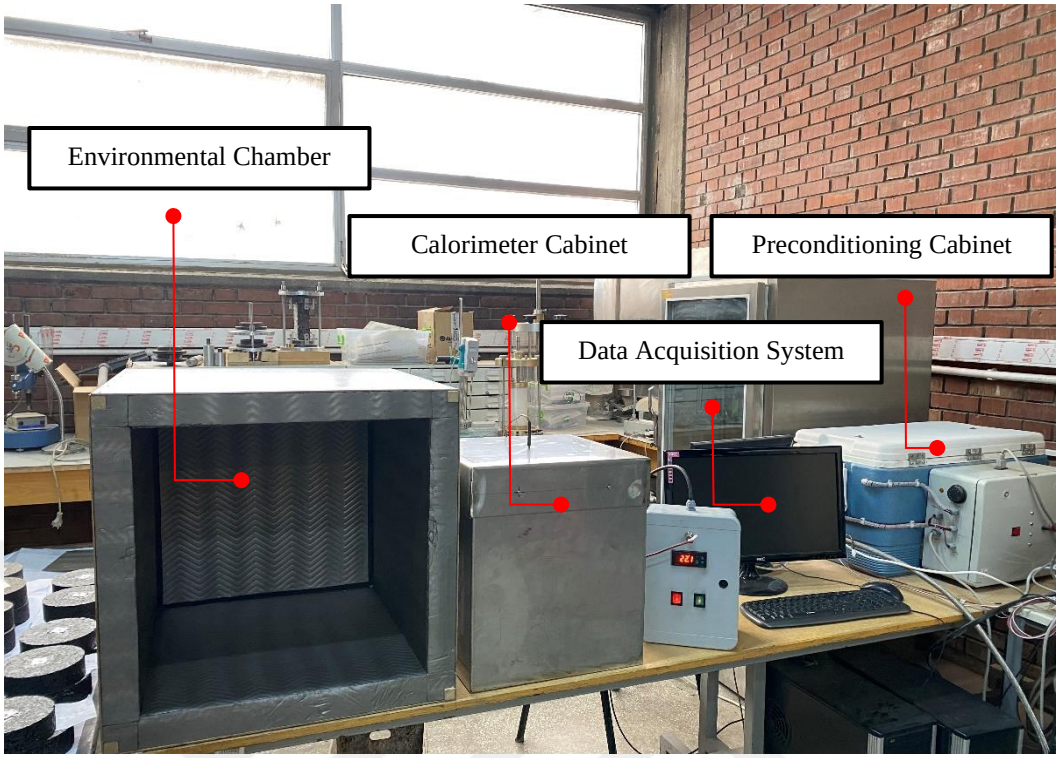


Figure 3.12 The main parts of the test setup.

3.5.1.3 Test Procedure

The proposed test for measuring specific heat capacity was based on the basic principle of calorimetry. In calorimetry, a secondary medium was needed to trigger heat transfer. In other words, heat was transferred when a system had a temperature gradient from the high to low energy areas. According to the first law of thermodynamics or energy conservation law, the difference between the total energy flowing into and out of the system during a process is the net change in the system's energy. In this regard, heat was transferred from the hot water in the insulated cabinet to the sample at a lower temperature in this setup (See Figure 3.10 & Figure 3.11). To calculate the transferred heat, some input parameters were necessary. These were the heat loss of the insulated cabinet, the masses of the sample pair and water, and the initial and final temperatures of the sample pair and water.

For calorimetry, it was assumed that the cabinet was well insulated when preparing the experimental setup. Nevertheless, the heat loss of the cabinet itself was checked. In this case, the insulated cabinet was filled with about 15 kg of distilled water and heated to about 60°C. After 60°C, the insulated cabinet was no longer heated, and the hot water's temperature change was monitored over time. According to Figure 3.13, the decrease in temperature was determined to be 1.0 °C per hour (≈0.16 °C per 10 min) in the first hour and 1.1 °C and 0.9 °C for the second and the third hours, respectively. In the test procedure, this temperature drop was necessary to calculate the pure heat energy transferred to the sample pair.

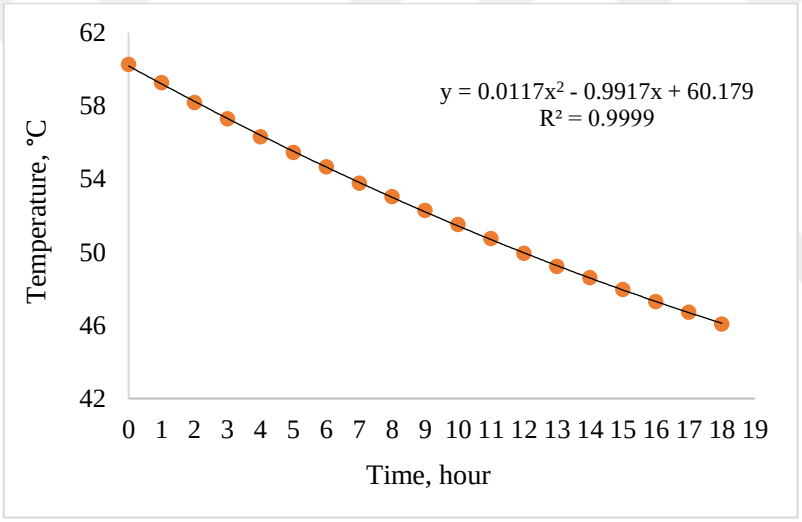


Figure 3.13 Change in temperature of water over time.

After that, some input parameters were necessary to calculate the stored and emitted heat. First, the mass of the water was taken as a constant of 15 kg, while the mass of the sample pair was measured before each test. The initial temperatures were then assigned. The sample pair was conditioned at specific temperatures. The specified temperatures of the samples were set as -2 °C, 20 °C, and 40 °C, respectively. For water, the initial temperature was set to about 50 °C. It was essential that the temperature of the sample pair and the hot water must be constant before starting the test. After the water and sample pair temperatures were constant, the sample pair was

quickly immersed in hot water, and the insulated cabinet was covered to maintain the temperature. As soon as the pair of samples was placed, heat transfer from the hot water to the sample pair began.

3.5.1.4 Details of Specific Heat Capacity Calculation

The temperature changes of the hot water and the pair of samples were monitored throughout the test. When the system reached equilibrium or heat transfer was complete, the specific heat capacity of the sample was calculated using the following equations.

$$Q_{water} - h_{loss} = Q_{sample} \quad 3.6$$

$$C_{sample} = \frac{m_w C_w (T_w - T_f)}{m_{sample}(T_f - T_{sample})} \quad 3.7$$

In Equation 3.6, Q_{water}, h_{loss}, and Q_{sample} represent the total energy (Joule) of the hot water, the heat loss of the insulated cabinet, and the total energy of the sample, respectively. In Equation 3.7, m_w (kg), C_w (J/kg.°C), and T_w (°C) are the mass, specific heat capacity, and initial temperature of the hot water and m_s (kg), T_{sample} (°C) are the mass and initial temperature of the sample, respectively. T_f (°C) is the final temperature of the system (includes the sample pair and water). Additionally, the specific heat capacity of water was assumed to be 4182 J/kg.°C during the calculations. In summary, the formulas given are valid if the energy released by the hot water and the energy absorbed by the pair of samples are equal at steady state.

3.5.2 Measurement of Thermal Conductivity in Asphalt Concrete Using a Steady-State Approach

The recommended test methods for determining the thermal conductivity of asphalt concrete are mainly divided into two as the steady-state and transient methods (as mentioned in Section 2.3). This section only deals with the steady-state method. The

steady-state methods are generally defined as more stable in terms of measurement accuracy, provided that the appropriate application conditions are met (Palacios et al., 2019). However, it is stated that there are some limitations in measuring the thermal conductivity of asphalt concrete by steady-state methods, such as the heat loss at the edges, the heterogeneous nature of asphalt concrete, the long test duration, and the size-dependent influence on the properties, etc. (Luca & Mrawira, 2005; Kuvandykova & Bateman, 2013).

Considering these limitations, a steady-state method with a heat flux meter was developed in this study. Accordingly, some relevant standards were consulted to apply this method and minimize these limitations during the study. Among these standards, ASTM C177-19 was used to understand the measurement of heat flux through the sample using the guarded-hot plate. Then, ASTM C518-21 was followed to design the test setup with a heat flux meter. Moreover, ASTM C1058-10 was used to define a proper ambient temperature. Lastly, ASTM C1045-19 was used in the calculation of thermal conductivity measurements.

3.5.2.1 Sample Preparation

The steady-state method in this study was based on the principle of Fourier's law in one dimension. This principle led to a limitation that recommends the use of flat slab samples whose thickness does not exceed 1/3 of the maximum linear dimension of the measured area (specified in ASTM C177-19). However, Superpave samples with a diameter of 150 mm were prepared in this study. The maximum heights of the samples can differ depending on the air void content (2%, 4%, and 6%). Therefore, the samples were prepared by cutting them into two slices with a diamond saw. First, about 1 cm from the top and bottom of each sample were trimmed. Then, the remaining part of the sample was divided into two slices with a maximum height not exceeding 5 cm, as shown in Figure 3.14.

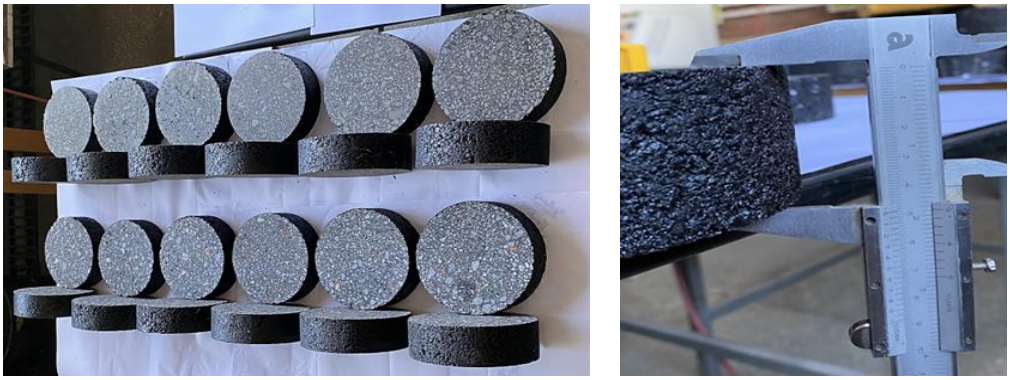


Figure 3.14 Samples used in the thermal conductivity measurements.

After cutting, the surface condition of each slice was checked. This was because the heat flux meter measured the one directional steady-state heat flow through a sample between two parallel plates. In this context, it was necessary to keep the surfaces of the slices parallel to the plates to ensure uniform thermal contact and allow efficient heat transfer. To create better plate-to-sample contact, the thermally conductive paste shown in Figure 3.15 was applied to both the top and bottom surfaces of the slices.



Figure 3.15 a) The control of the sample surface before the test and b) A thermal silicone paste.

3.5.2.2 Test Setup

This section details the test setup based on the test method described in ASTM C518-21. The heat flux meter is an essential tool in this setup because it is simple in design,

works quickly, and is suitable for various specimens. Moreover, it is stated that these sensors are ideal for building science applications, soil and geothermal heat flux studies, and any other application requiring a very low heat flux. Since it provides excellent accuracy and consistency within the expected heat flow range when adequately calibrated. As mentioned, it measures the one directional steady-state heat flow in a sample between two parallel plates. Basically, the setup includes a heat flow transducer, a hot plate, a cold plate, and a sample, as shown in Figure 3.16.

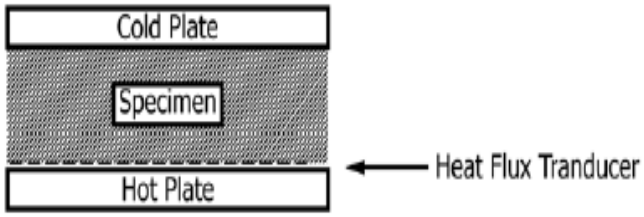


Figure 3.16 The basic test configuration (specified in ASTM C518-21).

The above configuration was modified to develop the test setup of this study. The test setup consisted of a refrigerated circulator, an insulated chamber, a DC power supply, a temperature control unit, and a data acquisition system, as shown in Figure 3.17. Then, an insulated hollow cylinder was designed and placed in the center of the insulated chamber (see details in Figure 3.18). In this configuration, the insulated chamber protected the insulated hollow cylinder from temperature fluctuations under laboratory conditions. For this purpose, 5 cm thick Izocam foam (λ: 0.035 W/m.°C) sheets were used for thermal insulation to prevent heat loss at the edges during heat transfer to the sample.

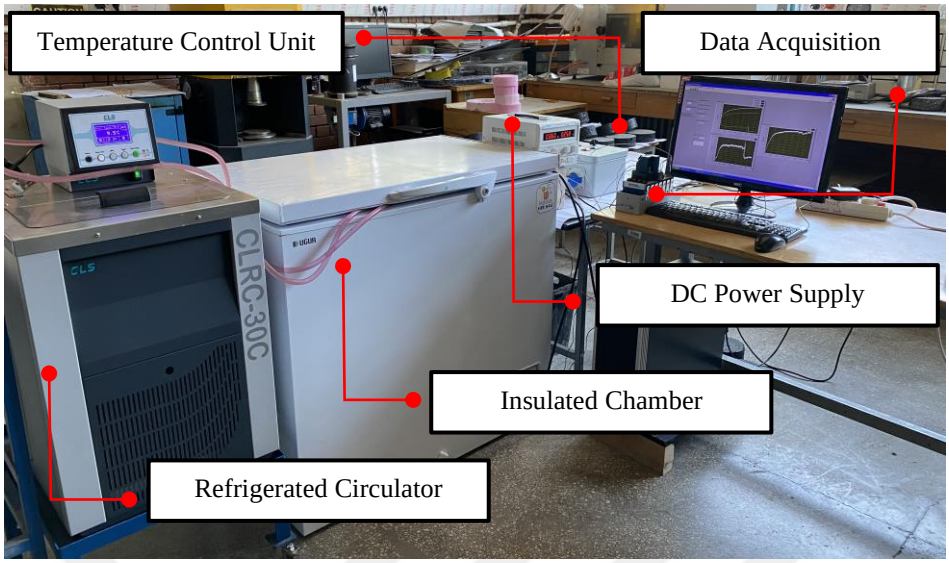


Figure 3.17 General view of the test setup.

The refrigerated circulator ensured the constant temperature on the cold plate while the constant temperature of the hot plate was controlled by the current supplied to the heating pad from the DC power supply. The temperature changes on the hot and cold plates were monitored using thermal sensors. The temperature control unit was then used to keep the ambient temperature of the insulated chamber constant and to control the operation of the air-circulating system inside the chamber. Finally, the data acquisition system adequately monitored and recorded the temperature changes and heat flux during the tests.

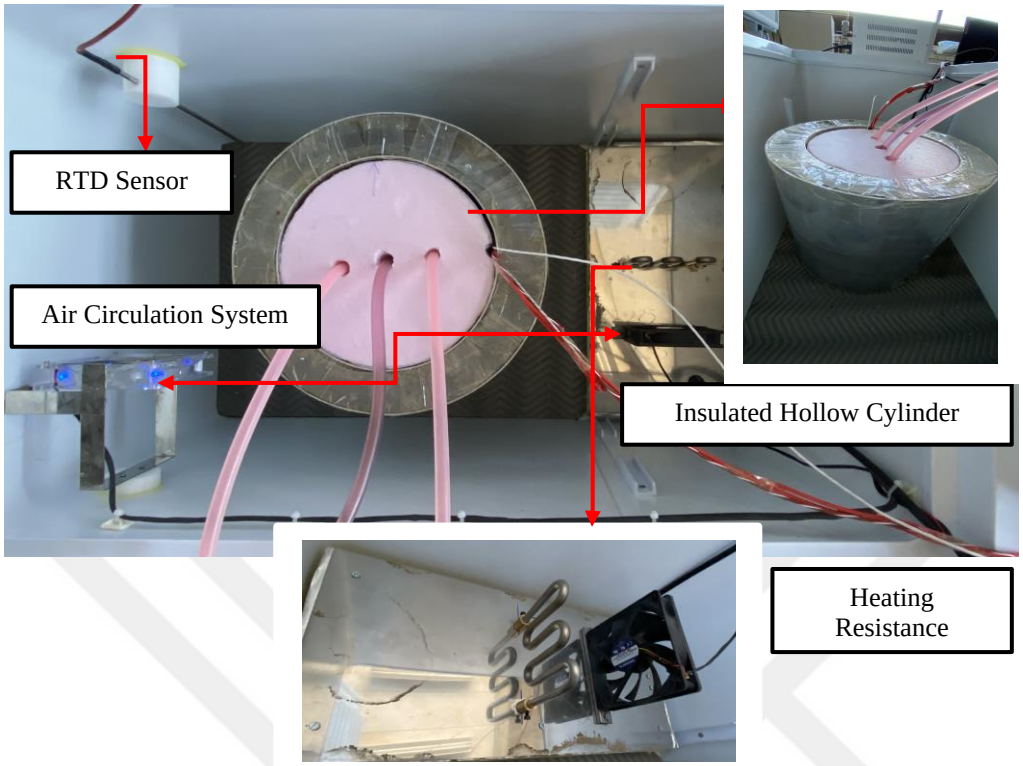


Figure 3.18 Interior design of the insulated chamber.

The interior of the insulated chamber was specially designed and adapted, as shown in Figure 3.18. The heating resistance and air circulating system were placed appropriately to maintain a constant temperature inside the chamber. An RTD sensor was attached to control the ambient temperature of the chamber. The insulated hollow cylinder was then built by interweaving two tubes with different diameters (outer diameter: 35 cm and inner diameter: 25 cm) from an aluminum plate with a height of 35 cm. The 5 cm thick space between the tubes was filled with glass wool sheets (ODE Evomineral, λ: 0.037 W/m.K) to prevent possible heat loss. Later, a silicone heating pad (diameter: 150 mm, 12 V), hot and cold plates, a sliced sample, temperature sensors, and a heat flow meter were placed in the insulated hollow cylinder (See Figure 3.19). All of these components had a fixed diameter of 15 cm. The arrangement within the insulated hollow cylinder consisted of the heating pad at the bottom, followed by the hot plate, the heat flux meter, the sample, the temperature sensor of the cold plate, and finally, the cold plate itself.

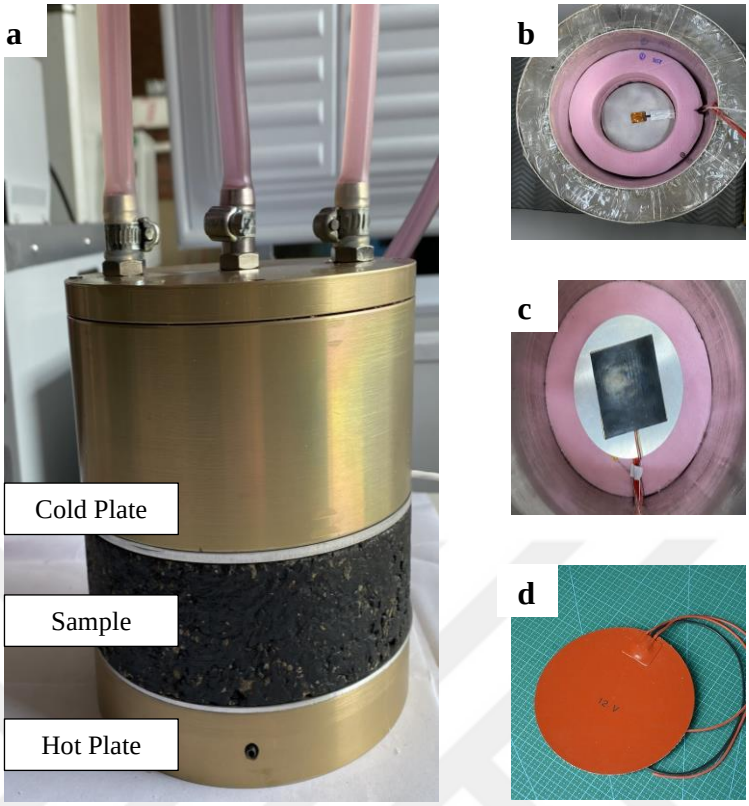


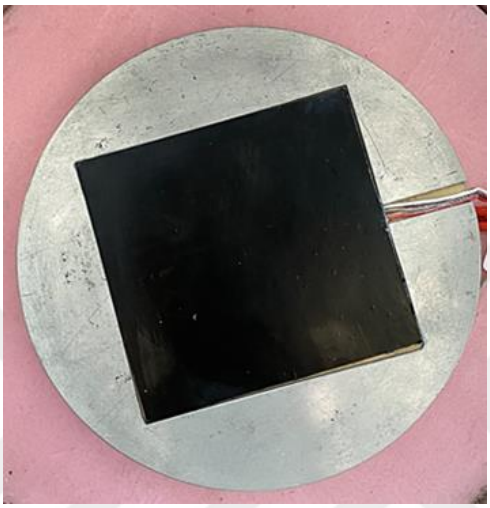
Figure 3.19 a) The assembly of interior parts in the insulated hollow cylinder, b) temperature sensor under the cold plate, c) a heat flow meter on the hot plate, and d) a silicone heating pad under the hot plate.

In this configuration, the FluxTeq Ultra-09 Plate Heat Flux Sensor (PHFS), which comes standard with a flat black coating with a known emissivity of 0.94, was used (See Figure 3.20). The FluxTeq Ultra-09 PHFS used a differential temperature thermopile to measure the movement of heat energy per unit area or heat flux through the sensor surface. It also included an integrated thermocouple that can measure the temperature during the test.

In the following, a schematic representation of the thermocouple temperature measurement location and sensing area of the Ultra-09 PHFS is shown in Figure 3.20. According to the FluxTeq reports, it is stated that the Ultra-09 PHFSs have a very high sensitivity. Additionally, the sensor manual defines the sensitivity of the PHFS used in the study as 130.37 ± 5.5 μV/(W/m^2) at 25 °C. However, it is also

noticed that if the sensor is used at a temperature other than 25 °C, it is advisable to adjust the sensitivity to account for the temperature effect, using the following Figure 3.21. Lastly, the technical characteristics of the Ultra-09 PHFS are also listed in Table 3.15.

a)



b)

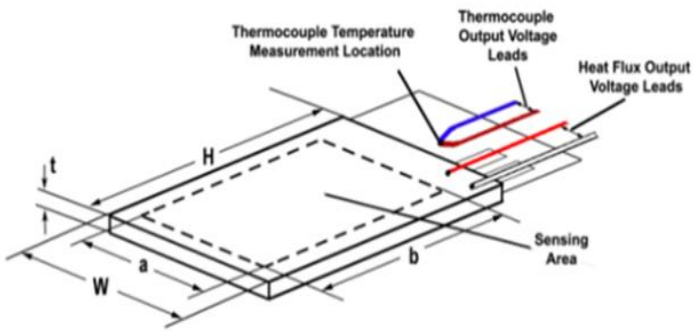


Figure 3.20 a) Heat flux sensor positioned on the hot plate and b) schematic view of the sensor.

Table 3.15 Technical specifications of the FluxTeq-Heat Flux sensor.

Sensor Type	Differential-Temperature Thermopile
Encapsulation Material	Kapton (polyimide)
Temperature Range	-20 °C to 200 °C
Sensor Surface Thermocouple	Type-T
Nominal Sensitivity	Approx. 1000 mV/(W/cm^2)
Sensing Area Dimensions	a = 6.8 cm b = 7.6 cm
Total Sensor Dimensions	W = 9.2 cm H = 8.7 cm
Sensing Area	52 cm^2
Total Sensor Area	80 cm^2
Sensor Thickness	1.5 mm
Thermal Conductivity	0.2 W/(m.K)
Absolute Thermal Resistance	1.25 K/W
Specific Thermal Resistivity	6.3 K/(kW/m^2)
Response Time	5 seconds

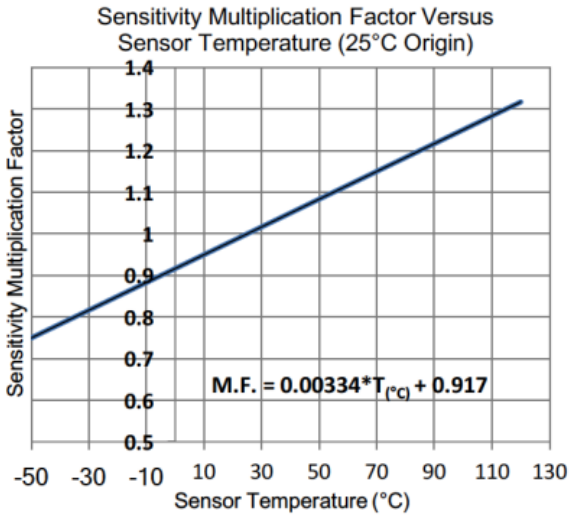


Figure 3.21 Sensitivity multiplication factor and sensor temperature chart.

Proper installation of the Ultra-09 PHFS in the insulated hollow cylinder was critical for accurate testing. Therefore, it was necessary to mount the sensor firmly on smooth and clean surfaces for optimum performance and accuracy. In this regard, applying a thin layer of thermal paste between the sensor and the measurement

surface and between the sensor and the cold plate was recommended. Thermal paste was also applied between the hot surface and the bottom of the sensor, as indicated in the heat flux meter manual, to minimize thermal contact resistance and allow for more accurate measurements.

Once all the components shown in Figure 3.19 were installed in the insulated cabinet, preventing heat loss at the edges became a significant concern. As the inner diameter of the tube and the diameter of the plates are 25 cm and 15 cm, it leaves an uninsulated gap of 5 cm. Thus, the edges of the configuration shown in Figure 3.22 were carefully wrapped with Izocam foam while placed in the insulated cabinet. This precaution was directly related to minimizing potential heat loss at the edges and ensuring one-dimensional heat transfer between the plates. When all the parts for the installation were assembled to this point, the setup was a new variation of the configuration specified in ASTM C518-21.

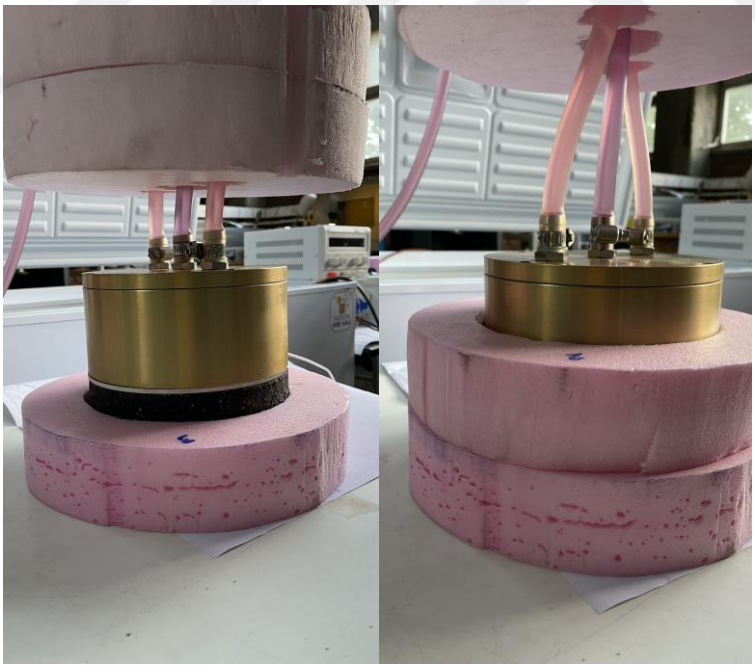


Figure 3.22 Side insulation of the hot and cold plates in the insulated hollow cylinder.

3.5.2.3 Test Procedure

As discussed above, several essential steps were performed until the test setup was ready for testing. Figure 3.23 summarizes these steps in a sequence: sample preparation, test setup assembly, pre-conditioning, setting the temperature difference, data acquisition, and steady-state phase.

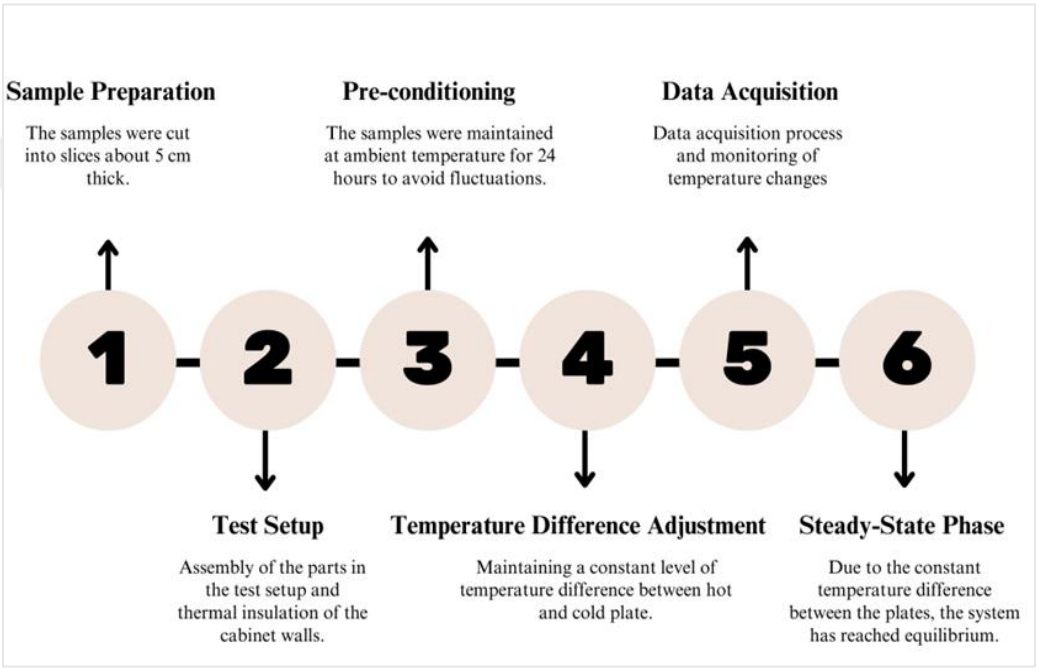


Figure 3.23 The flow diagram of the test procedure.

The test procedure was developed based on two primary principles. The first was the design of the test setup, which conformed to the Fourier heat transfer principle, and the second was that the heat flow meter was appropriately calibrated according to ASTM C177-19 and ASTM C518-21. Two crucial steps were then followed in applying the Fourier heat transfer principle: a one-dimensional heat flow and ensuring a constant temperature difference between the hot and cold plates. In this direction, the size of the sample (diameter (d): 150 mm, height (h): max. 50 mm, h/d: max. 1/3) was first adjusted to maintain the one-dimensional heat flow. The parts of

the test setup were then assembled according to the requirements of the Fourier principle. The measurement cabinets were also insulated with Izocam foam board and glass wool sheets to prevent possible heat loss through the side walls, as mentioned above. The sample was conditioned at ambient temperature for 24 hours to eliminate temperature fluctuations. In short, all these conditions were met to ensure the one-dimensional heat flow.

To ensure a constant temperature difference between the plates, the temperature was carefully controlled with the ambient temperature specified in the corresponding standard (ASTM C1058-10). Later, ASTM C518-21 also states that the test method is applied in a temperature range of 10 to 40 °C under ambient conditions. In this regard, the ambient temperature was set not to exceed the average temperature of the plates. Accordingly, the temperatures of the hot and cold plates were set to about 40 °C and 10 °C during the test, respectively. Based on the temperatures of the plates, the ambient temperature in the environmental chamber was set to about 25 °C. It can be said that these adjustments were essential for the practical application of Fourier's principle and the proper functioning of the heat flux meter.

After the required steps were fulfilled, the data acquisition system monitored the heat flux and temperature changes during the tests. While the value of the heat flux was measured with a heat flux meter, the surface temperatures of the hot and cold plates were measured with thermal sensors. Measurements were then continued until the temperature and heat flux values stabilized. At this point, evaluating the results was crucial to draw a correct conclusion. For example, the heat flux curve shown in Figure 3.24 was the expected situation for calculating thermal conductivity using a steady-state method. The most important step of the test procedure was the thermal equilibrium of the system to ensure the reliability of the obtained results. For this reason, when a sample's temperature and heat flux were measured for 8 hours, the measurement was waited for at least 8 hours to reach the first temperature value of the measurement cabinet before proceeding with the second sample. In short, it was aimed that all samples were tested under the same test conditions.

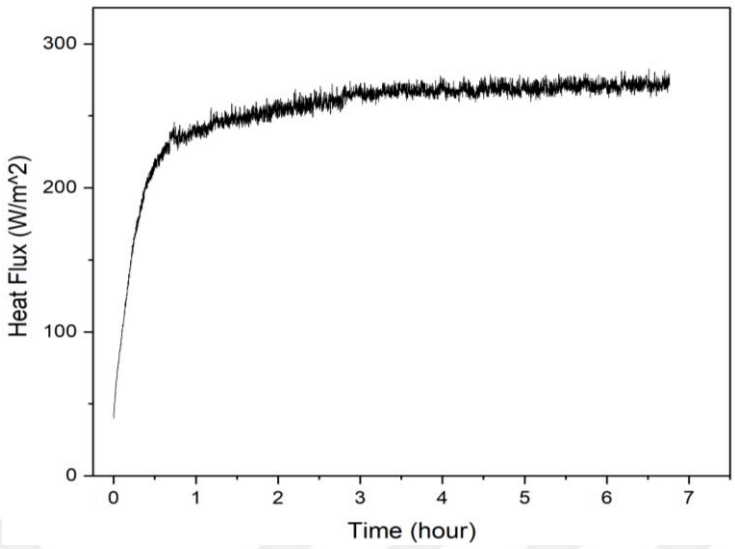


Figure 3.24 Heat flux at steady state.

3.5.2.4 Details of Thermal Conductivity Calculation

ASTM C1045-19 standard was followed to calculate the thermal conductivity using the data obtained from this setup. In other words, the Fourier equation was used to calculate the thermal conductivity when the system reached the steady state shown in Figure 3.24. According to ASTM C1045-19, Equation 3.10 is derived from Equation 3.8 and Equation 3.9. While Equation 3.8 was used to calculate the thermal resistance, R (m^2.°C/W), Equation 3.9 was used to calculate the thermal conductance, C (W/m^2.°C). The Fourier heat equation was then applied in Equation 3.10. For these equations, T_h (°C), the temperature of the hot plate; T_c (°C), the temperature of the cold plate; Q (W), the heat flux; A (m^2), the area normal to the heat flux; and L (m), the thickness of a sample, were necessary inputs and were already measured during the tests.

$$R = \frac{A(T_h - T_c)}{Q} \quad 3.8$$

$$C = \frac{Q}{A\,(T_h - T_c)} = \frac{1}{R} \quad 3.9$$

$$\lambda = \frac{QL}{A\,(T_h - T_c)} \quad 3.10$$

Additionally, it is helpful to remember that the steady-state method is based on the comparative approach. As with the calibration of the heat flux sensor, the calibration of the test setup was also required to evaluate the accuracy of the setup. In this regard, Izocam foam board (λ: 0.035 W/m.°C) and aerated concrete block (λ: 0.11 W/m.°C) were used for the calibration process. They were prepared based on the sample dimensions used in the test, as shown in Figure 3.25. Then, the thermal conductivity values of the Izocam foam board and the autoclaved aerated concrete were measured and compared with their known thermal conductivity values. Lastly, the measured results of all sliced samples are calibrated with the obtained coefficient.

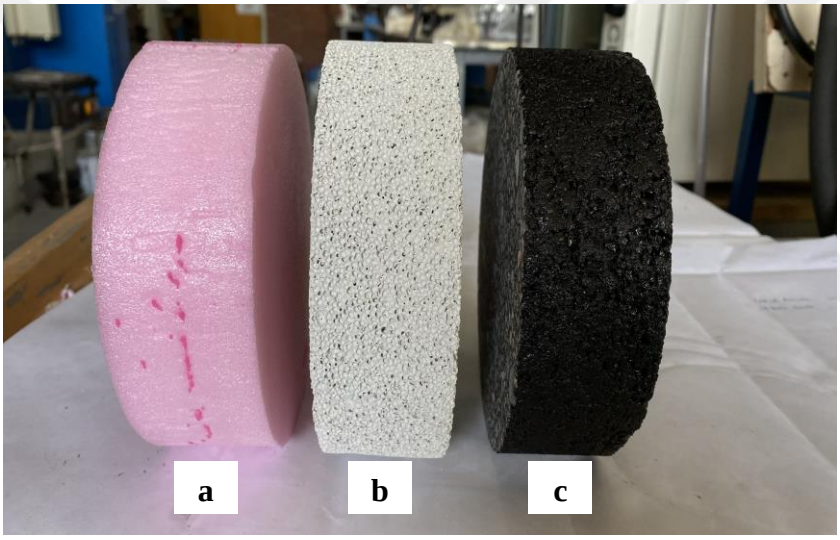


Figure 3.25 a) Izocam foam board, b) autoclaved aerated concrete, and c) asphalt concrete for the test setup calibration.

3.5.3 Measurement of Thermal Conductivity in Asphalt Concrete Using Transient Approach

This section presents the TPS method as an option to conventional steady-state methods for measuring thermal conductivity. The TPS method is generally used to measure temperature change over time and provides faster results. The method is described below, including the steps for measuring the thermal conductivity of asphalt concrete using the Hot Disk TPS 2500S test device.

3.5.3.1 Hot Disk TPS 2500S

The Hot Disk TPS 2500S instrument, available in the Department of Materials Science and Nanotechnology at TOBB University, was used to perform the measurements (See Figure 3.26). The Hot Disk Thermal Constant Analyzer can generally measure the thermal properties of a wide range of materials with thermal conductivities from 0.03 W/m.K to 500 W/m.K for bulk isotropic materials. In addition, a more comprehensive range of thermal conductivities from 0.005 W/m.K to 1800 W/m.K can be measured with Hot Disk's other measurement modules. This instrument can operate over a wide temperature range from very low temperatures up to 1000°C (specified in Hot Disk TPS 2500S Test Manual).

The main component of this device is the TPS sensor shown in Figure 3.26, which consists of a double spiral of thin nickel immersed in the nanofluid and surrounded by suitable housing. Nickel foil is used because of its high-temperature resistance coefficient. The electrically conductive pattern is placed between two thin insulating layers by lamination. In addition, the device offers a wide range of options for selecting sensors. Depending on the application, sensors with different diameters and materials, such as Kapton, Teflon, and Mica insulation, can be used. Moreover, these sensors contain a thin heater as a heat source and a temperature sensor. In this regard, thermal conductivity measurement depends directly on the effective use of these sensors.

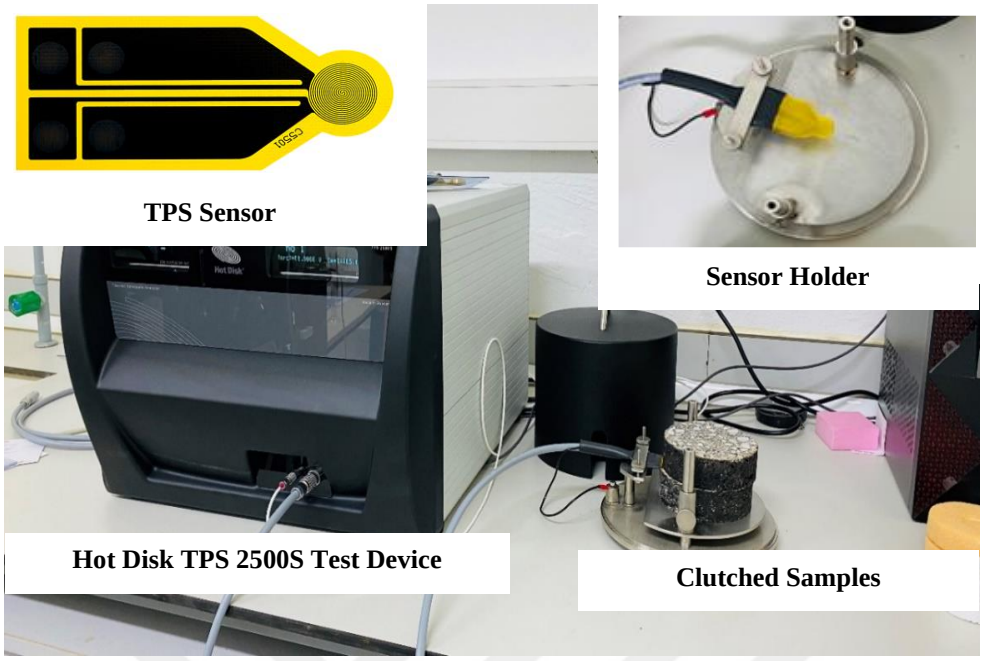


Figure 3.26 Hot Disk TPS 2500S Test Device and parts.

3.5.3.2 Sample Preparation

The theory underlying the TPS method assumes that the sensor is in a material of infinite size. Therefore, to obtain accurate results on thermal properties, it is advantageous if the thickness of the sample is equal to or greater than the radius of the TPS sensor. In this context, one way to determine the appropriate sample size is to use the probing depth, as shown in Figure 3.27.

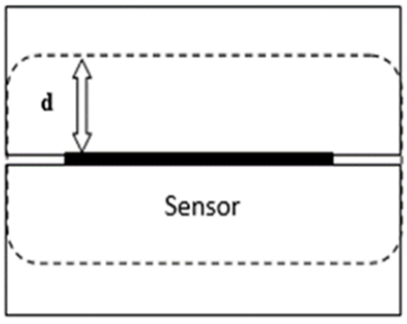


Figure 3.27 Schematic view of the TPS sensor and probing depth from the side.

In this study, the TPS sensor was positioned between the plain surfaces of two identical samples. Therefore, the Superpave samples were cored to a diameter of 100 mm and then cut into three equal slices: upper, center, and bottom. There were also certain size constraints for the sensor holder housing, as shown in Figure 3.28. Each slice was made with a thickness of 25 mm ± 0.1 mm, and a sensor with a diameter of 12.8 mm (sensor ID: 5501) was used. The thickness of the sample used in the study was more significant than the diameter of the sensor, which was consistent with the measurement theory. Then, the positions of the TPS sensor were determined. First, the sensor was positioned between the center and bottom slices, then between the center and upper slices, as shown in Figure 3.28. Ultimately, it became possible to measure the thermal conductivity of a sample suitable for the sensor holder instead of the thermal conductivity of the entire Superpave sample.

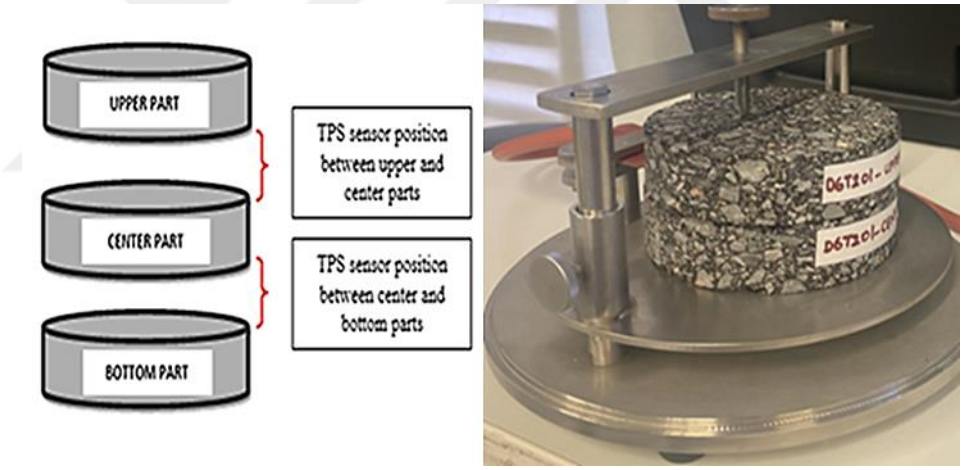


Figure 3.28 The measurement areas of the TPS sensor and the placement of two identical samples in the sensor holder.

3.5.3.3 Test Procedure

The TPS measurements were performed on the plane surface on which the sensor was laid. The first step in the test procedure was to select a suitable TPS sensor, as indicated in the previous section. Because it was found that there is a relationship

between the sensor size and the reliability of the test results, since asphalt concrete is a multiphase material, the sensor may not be in contact with the entire aggregate and mastic, which means that the thermal property results may not accurately reflect the thermal conductivity of the entire sample. Accordingly, the following equivalencies can be used to decide the largest viable sensor for a given sample. In the provided equivalencies, the sensor radius is indicated as r (mm), the sample thickness as h (mm), and the sample diameter as D (mm).

$$\text{Sample thickness: } r \leq h \leq 2r \tag{3.11}$$

$$\text{Sample diameter: } 4r \leq D \leq 6r \tag{3.12}$$

Accordingly, a Kapton insulated sensor with the sensor ID: 5501 (Diameter: 12.8 mm) was available in the laboratory and used in this study. This sensor was also used in previous studies to determine the thermal conductivity of asphalt concrete (Mirzanamadi et al., 2018). According to Mirzanamadi et al. (2018), significant deviations in measured thermal properties can be eliminated when the sensor diameter to maximum aggregate size ratio is greater than 2. Therefore, this study was aware that using a sensor with a diameter of 12.8 mm (sensor ID: 5501) for samples with a NMAS of 19 mm (Type 1) could affect measurement consistency. To solve this problem, several measurements were made on four different zones of the surface of the sliced samples, testing each zone three times, as shown in Figure 3.29. This approach was also applied to samples with a MAS of 12.5 mm. Then, a waiting period of at least 20 minutes was established between each measurement to ensure adequate cooling.

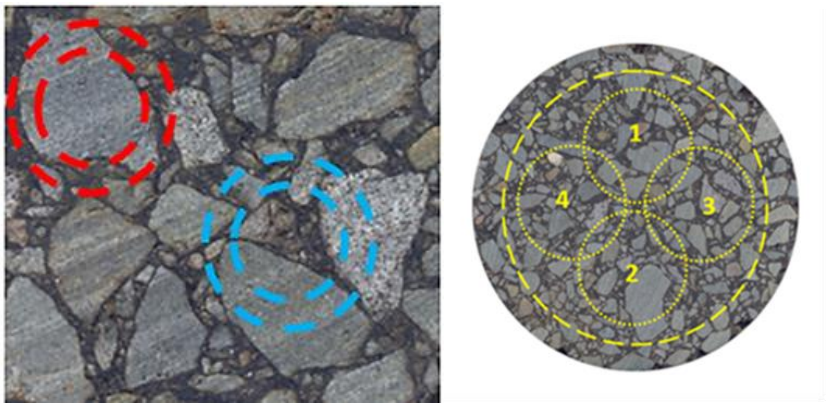


Figure 3.29 Contact zones on the plane surface of the sample.

After that, the measurement time and the heating power are adjusted to obtain reliable results and select appropriate contact zones. According to the instruction manual, the measurement time depends on the thermal diffusivity of the sample, the possibility of probing depth, and the size of the TPS sensor. In the following, Equation 3.13 is used to determine the probing depth.

$$d_p = 2\sqrt{\alpha t} \tag{3.13}$$

In Equation 3.13, d_p (mm) is the probing depth, α (mm^2/sec) is the thermal diffusivity, and t (sec) is the measurement time. Also, it is stated that the probing depth should be in the range of sensor radius, r (mm) to sensor diameter, 2r. With a given sensor size and a sample large enough to allow a 2r probing depth, Equation 3.14 can be written as follows. The maximum measurement time can also be calculated using the thermal diffusivity in Equation 3.15.

$$2r = 2\sqrt{\alpha . t_{max}} \tag{3.14}$$

$$T_{max} = \frac{r^2}{\alpha} \tag{3.15}$$

In addition to the measurement time, the heating power must also be determined. Generally, heating power refers to the constant energy supplied to the sensor throughout the measurement process. The purpose is to supply a suitable total

temperature increase. It should be noted that the thermal conductivity of the material will affect how much power should be used. As an example, Table 3.16 provides a summary of these parameters for various materials from the Hot Disk Thermal Constant Analyzer Instruction Manual, 2016.

Table 3.16 Summary of the experimental parameters for different materials.

	Aluminum Alloy	Dense Ceramic	Stainless Steel	Ceramic Material	Plastic	Low Conducting Material
Thermal Conductivity, W/m.K	166	40	14.2	1.45	0.19	0.028
Thermal Diffusivity, mm^2/s	68.5	11.4	3.74	0.96	0.11	0.75
Specific Heat, $MJ/m^3.K$	2.42	3.5	3.8	1.51	1.73	0.037
Rec. Temp. Increase, K	0.3	0.5	1.0	1.5	2.5	5.0
Disk Radius, mm	14.65	6.394	6.394	6.394	6.394	14.65
Sample (mm/mm)*	30/90	30/70	20/60	15/50	10/40	30/90
Measurement Time, s	5	20	10	40	160	160
Heating Power, W	2	2 to 5	2	1.5	0.6	0.1
*The first number denotes the thickness of the sample pieces, and the second number gives the equivalent diameter.						

Accordingly, the appropriate measurement time and heating power for the basalt and dolomite samples were set at 40 s and 200 mW and 20 s and 250 mW, respectively, based on the behavior of the residual graphs obtained during the test. The choice of measurement time and heating power in this study was also consistent with the results of the study by Mirzanamadi et al. (2018). Table 2.3 also summarizes the heating power and measurement time depending on the sensor ID and application depth for the asphalt concrete samples.

Finally, the residual graph was a helpful indicator in decision-making, as it showed the deviation between observed and predicted values in a fitted model. An ideal residual graph should have a random and consistent scatter around a horizontal line, as shown in Figure 3.30. As mentioned above, measurement time and heating power were controlled to keep the thermal penetration depth within the sample thickness based on this graph. In summary, the test procedure was based on the correct selection of sensor type, measurement time, and heating power. It can be concluded that these parameters directly affect the reliability of the measurement and should be controlled during the measurements.

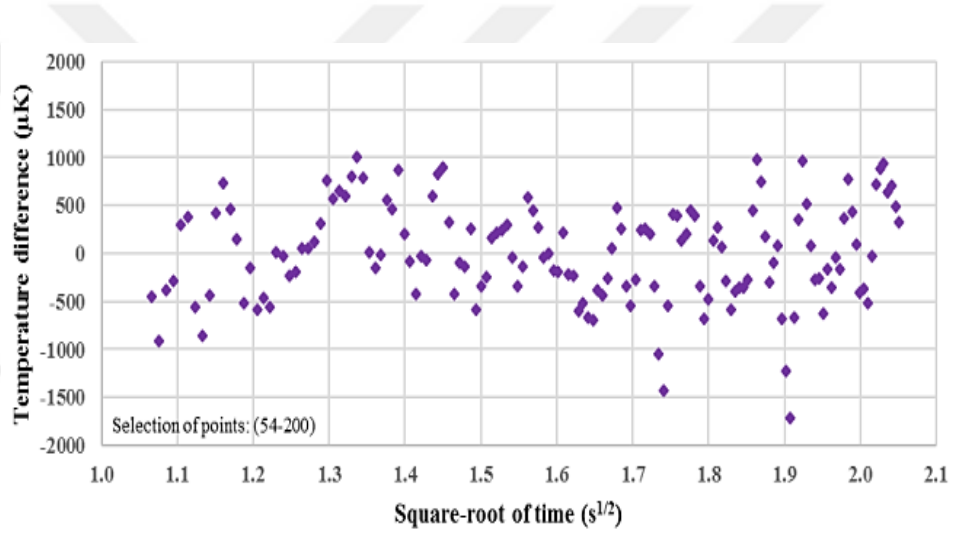


Figure 3.30 Example of a scatter plot taken during a thermal conductivity measurement (Gunasekara et al., 2019).

3.5.3.4 Thermal Conductivity Determination in the Hot Disk Constant Analyzer

The essential point in the calculations was the working principle of the TPS sensor. As mentioned earlier, the TPS sensor works simultaneously as a continuous planar heat source and a temperature sensor. In other words, it supplies energy to the sample through the sensor and simultaneously measures the temperature rise through the electrical resistance of the sensor. Thus, the rise in temperature can be calculated

using Fourier's law of heat conduction. In this way, Equation 3.16 can be used for the calculation.

$$\Delta T(\tau) = \frac{Q}{\pi^{1.5} rk} D(\tau) \quad 3.16$$

In Equation 3.16, Q (W) is the heat output of the sensor, k (W/m.°C) is the sample's thermal conductivity, r (m) is the radius of the sensor, and D is a dimensionless time function of τ and given in the following equation. In Equation 3.17, α (m^2/sec) is the thermal diffusivity of the sample, and t (sec) is the measurement time.

$$\tau = \frac{\sqrt{\alpha t}}{r} \quad 3.17$$

The Hot Disk Constant Analyzer software integrates the equations above to calculate the sample's thermal conductivity, provided the correct sensor, heating power, and measurement time are selected. As observed from the results, the impact of microstructural features in the contact zones on thermal conductivity is further examined in the following section.

3.6 Investigation of Microstructural Properties of Asphalt Concrete Samples

It is widely acknowledged that asphalt concrete's mechanical performance is directly impacted by its internal structure (Masad et al., 1999; Wang et al., 2018; Liang et al., 2021). After completing the measurements using the TPS method, this study also proposes that the properties of the internal structure can affect the thermal performance of asphalt concrete. This is because heat conduction through an asphalt concrete sample can be significantly affected by variables such as aggregate size, aggregate distribution, presence of moisture, etc. (Zhao et al., 2020; Liu et al., 2023). Moreover, understanding the relationship between the internal structure of asphalt concrete and thermal conductivity is critical to pavement design, construction, and performance evaluation since it helps identify materials that are most durable and thermally efficient in a variety of applications. This relationship has been studied in

the literature using various experimental methods, including image processing, microstructure analysis, and thermal testing (Moon & Falchetto, 2015; Concha et al., 2020). In this section, instead of examining the internal structural properties of the entire sample, the focus is on the microstructural properties in the contact zone of the TPS sensor. Therefore, this study involves using image processing to analyze the microstructural features of the cropped area on the sample surface, where thermal conductivity measurements are conducted using the TPS sensor. A brief overview of the image processing technique used is given below.

3.6.1 Image Processing-Based Analysis of Aggregate Distribution

The distribution of aggregates plays a crucial role in shaping the internal structure of asphalt concrete (Onifade, 2013). In particular, their distribution on the plane surface may cause variations in the TPS measurements due to the working principle of the TPS sensor. Therefore, an attempt was made to study the distribution of aggregates on the surface of asphalt concrete samples using a digital imaging method. iPas software, a free program developed by the University of Wisconsin-Madison and Michigan State University, was used in this study.

iPas is an effective tool for processing two-dimensional (2D) cross-sectional images and determining the microstructural properties of the contact zone on the sample surface. In particular, the number of contact points, total contact length, total aggregate area, orientation, and segregation are determined using this tool. The software used in this study has two main functions: Image processing and image analysis. The steps required from image acquisition to image analysis are shown in Figure 3.31 (Coenen et al., 2012).

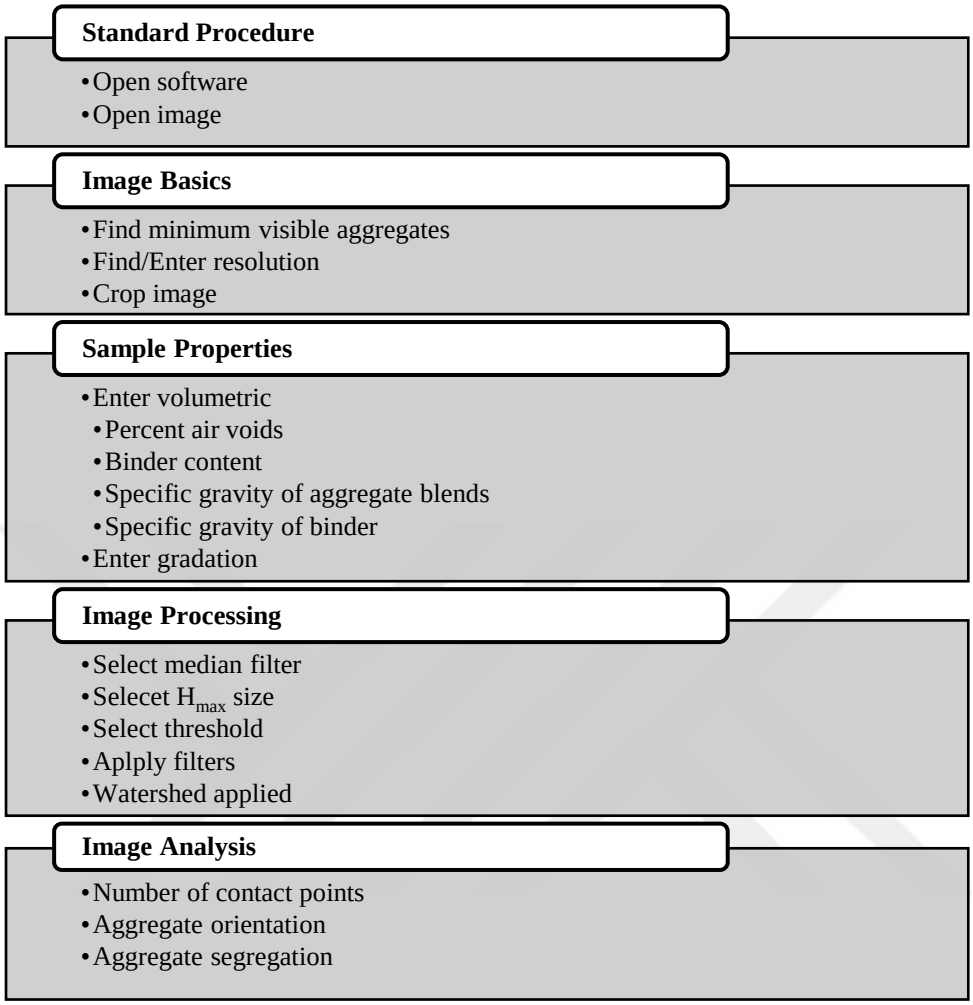


Figure 3.31 Steps of image processing (Coenen et al., 2012).

It should be remembered that three slices were taken from a Superpave sample for the TPS measurements (see Figure 3.28). Therefore, image processing was required for these surfaces on which the TPS sensor was laid. In this regard, cross-sectional images of the upper and bottom surfaces of the slices were acquired using a standard flatbed scanner with a resolution of 600 dpi. After that, the scanned original cross-sectional images captured in RGB color map were first loaded into the iPas software, and then the resolution of the images was defined. Next, the surface of the cored sample, having a diameter of 10 cm, was cropped into a rectangle, as shown in Figure 3.32.

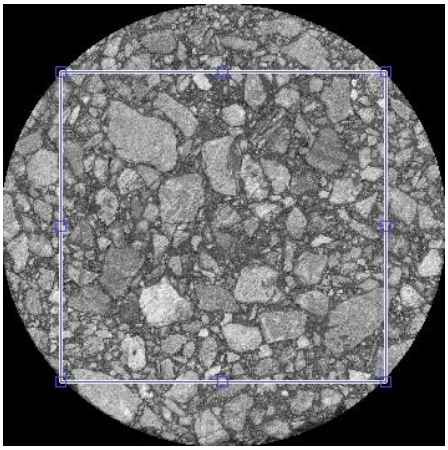


Figure 3.32 Rectangular area extracted from the sample surface.

The software required the input of a known aggregate gradation in order to compare it to the gradation derived from the image. The sample properties such as percent air void content, binder content, specific gravity of aggregate blends and bitumen were then defined. The software utilized this information to determine the volumetric percentage of the aggregate (P_{sv}). The P_{sv} was assigned to calculate the planar two-dimensional percentage of the aggregate area. Moreover, it was important to establish the surface distance threshold (SDT). The selection of SDT was based on the technique presented by Coenen et al. (2012). Based on previous studies, the inclusion criterion for aggregates was limited to those larger than 1.18 mm. In addition, the proximity of aggregate particles was considered as contact if the distance between the particles was 0.2 mm or less. Image filters in a sequence of the median filter, H_{max} filter, watershed transform, and thresholding were applied to the images to reduce noise, smooth color variations in the aggregate regions, separate the aggregates, and convert the grayscale image into a binary image to define the aggregates. In summary, the image processing process described in this study was carried out in the order shown in Figure 3.33.

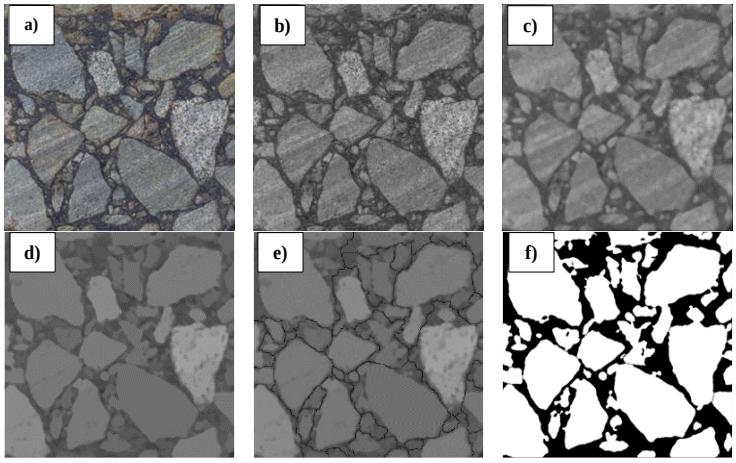


Figure 3.33 Image processing steps: (a) Original image, (b) Grayscale image, (c) Median filtered, (d) H_{max} filtered, (e) After watershed transform, (f) After thresholding.

After the processing stage, the microstructural properties of the rectangular area on the sample surface was evaluated using three indicators, aggregate contact points, orientation, and segregation. As illustrated in Figure 3.34, this analysis effectively determined the total surface area of aggregates in the contact zone and their contact points within the cross-section.

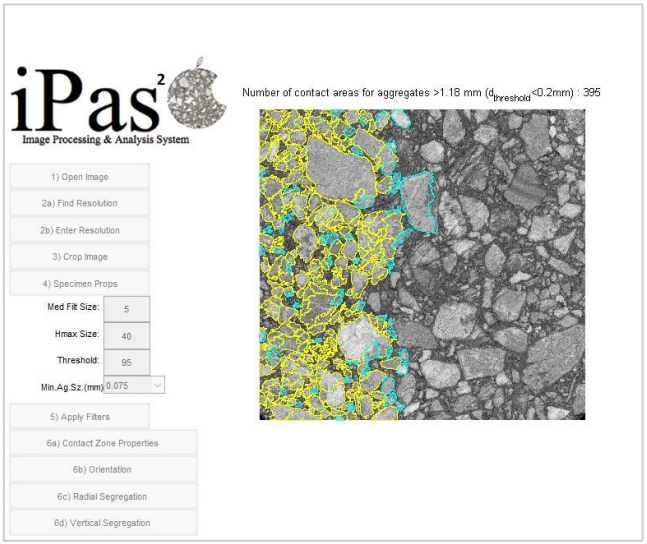


Figure 3.34 Detection of aggregate distribution in iPas image analysis.

CHAPTER 4

RESULTS AND DISCUSSIONS

In this section, details regarding the experimental plan used to measure the thermal properties of asphalt concrete samples are presented. Initially, the measurement of specific heat capacity is introduced using a calorimeter-based test setup, and then the measurement of thermal conductivity using steady-state and transient methods is discussed in detail. An abbreviated terminology is proposed to ensure clarity and distinction among the test samples. The aggregate type is denoted by 'B' for basalt and 'D' for dolomite, succeeded by the air void content. The abbreviations 'T1' and 'T2' represent the maximum aggregate sizes (MAS) of 19 mm and 12.5 mm, respectively. For example, basalt samples with 2% air void content and Type 1 and Type 2 gradations are named B2T1 and B2T2, respectively, while dolomite samples with the same air void content are named D2T1 and D2T2.

4.1 Evaluation of Specific Heat Capacity Results Using the Calorimetry-Based Test Method

This section presents the results of specific heat capacity measurements conducted on different asphalt concrete samples. Then, it comprehensively examines the influence of parameters such as optimum bitumen content, aggregate type, air void content, and maximum aggregate size on the specific heat capacity. The change in specific heat capacity due to the different conditioning temperatures is also discussed. In this section, the average specific heat capacities of two identical slices are used to evaluate the repeatability and reliability of the proposed experimental method. Thus, significant care was given to ensure that the two identical slices of the

samples had similar weights so that the absorbed energies by the replicate samples were nearly equal (details given in Appendix C). During the sample preparation phase, the average mass ratio between the slices was achieved around 1.015 ± 0.02.

4.1.1 Effect of Optimum Bitumen Content on Specific Heat Capacity

This section discusses the effect of optimum bitumen content on the specific heat capacity. Table 4.1 lists the average specific heat capacities of the samples with four different optimum bitumen contents. It can be observed that as the optimum bitumen content increases, the specific heat capacity of the samples decreases when the air void contents are unchanged in the mixtures. Previous studies have claimed that bitumen has no significant influence on the thermal properties of the mixture due to its relatively low proportion in the mix (Pan et al., 2017). On the other hand, it is reported that bitumen has a significant role in determining the specific heat capacity of the asphalt mixtures. Since bitumen acts as a thermal bridge interconnecting the aggregates, it establishes a continuous heat conduction pathway around them. However, increasing the optimum bitumen content for the same volume of asphalt mixtures reduces the volume of aggregates, thereby decreasing the specific heat capacity of the mixture.

Table 4.1 Optimum bitumen contents of the design mixtures and the average specific heat capacities of the compacted samples.

Mix Design ID	Optimum Bitumen Content, %	Sample ID	Air Void Content, %	Average Specific Heat Capacity, J/kg. °C at 20 °C
Desing 1: Basalt + Type 1	5.5	B4T1	4 %	1027.8
Design 2: Basalt + Type 2	6.2	B4T2		968.4
Design 3: Dolomite + Type 1	4.9	D4T1		1056.1
Design 4: Dolomite + Type 2	5.7	D4T2		1025.2

4.1.2 Effect of Aggregate Type on Specific Heat Capacity

This section first presents the mineralogical origin of basalt and dolomite aggregates. Then, it evaluates the effect of the aggregate type on the specific heat capacity. In this study, the X-ray powder diffraction analysis shows that while dolomite comprises quartz minerals, basalt is rich of calcareous feldspar minerals, especially anorthite (see Section 3.2.1 & Figure 3.2). Thus, due to the difference in the mineralogical origin of the aggregates, the aggregate type is expected to affect the specific heat capacity of asphalt concrete. The specific heat capacities of the samples prepared by basalt and dolomite with three air void contents, two maximum aggregate sizes, and three conditioning temperatures are shown in Figure 4.1 through Figure 4.6, respectively. It can be seen that the dolomite samples generally have a higher specific heat capacity than the basalt samples, regardless of the effects of the other experimental parameters. This is because dolomite has a high specific heat capacity due to its high percent of quartz minerals and bulk specific gravity (See Section 3.2.1).

It can be generally expected that the specific heat capacity of asphalt mixtures is mainly dominated by aggregate thermal properties. However, small variations can occur due to changes in the air void content, as observed from the samples compacted to 6% air voids. For example, the basalt samples with 6% air voids have a slightly higher specific heat capacity than those produced with dolomite for both MAS 19 mm and 12.5 mm, as seen in Figure 4.3 and Figure 4.6. Each mix component affects the total mass of the asphalt mixture and, thus, the bulk specific gravity of the sample. Since the specific heat capacity is a thermal property related to the mass of the material, the difference in the bulk specific gravity of the asphalt mixture also affects the specific heat capacity of the asphalt concrete sample (Waples & Waples, 2004; Cengel, 2003).

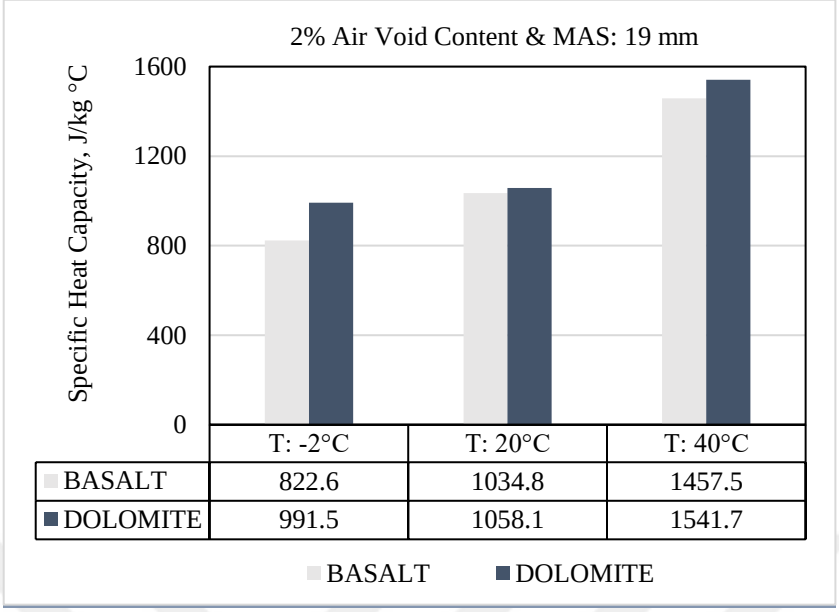


Figure 4.1 Specific heat capacity of basalt and dolomite samples with 2% air voids, maximum aggregate size of 19 mm, and varying initial temperatures.

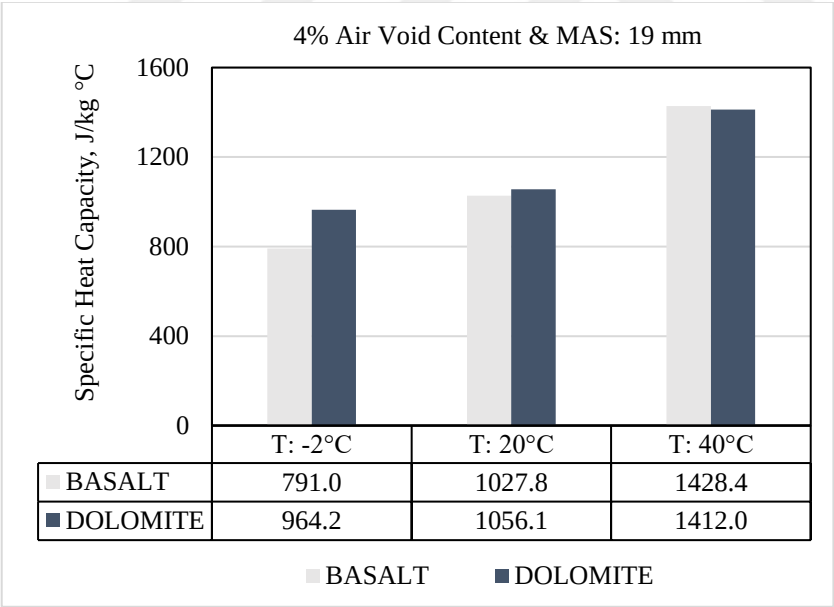


Figure 4.2 Specific heat capacity of basalt and dolomite samples with 4% air voids, maximum aggregate size of 19 mm, and varying initial temperatures.

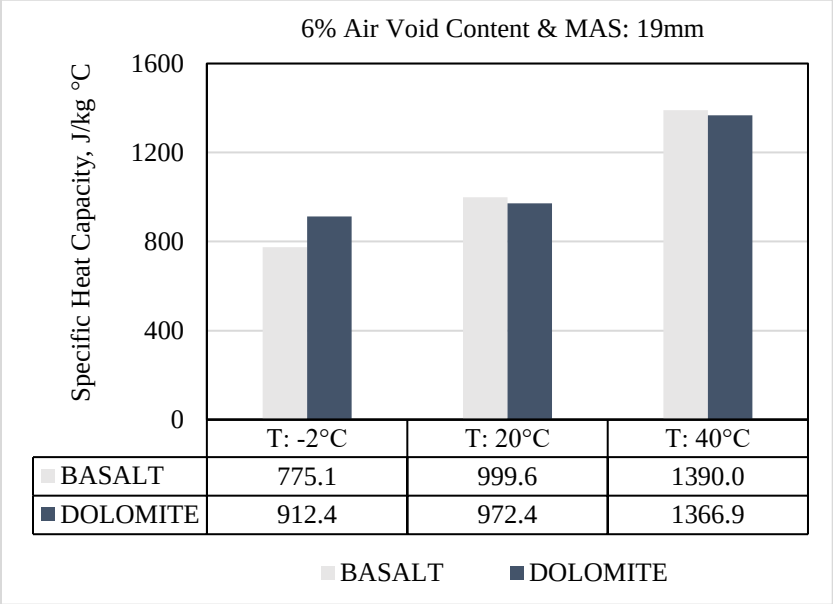


Figure 4.3 Specific heat capacity of basalt and dolomite samples with 6% air voids, maximum aggregate size of 19 mm, and varying initial temperatures.

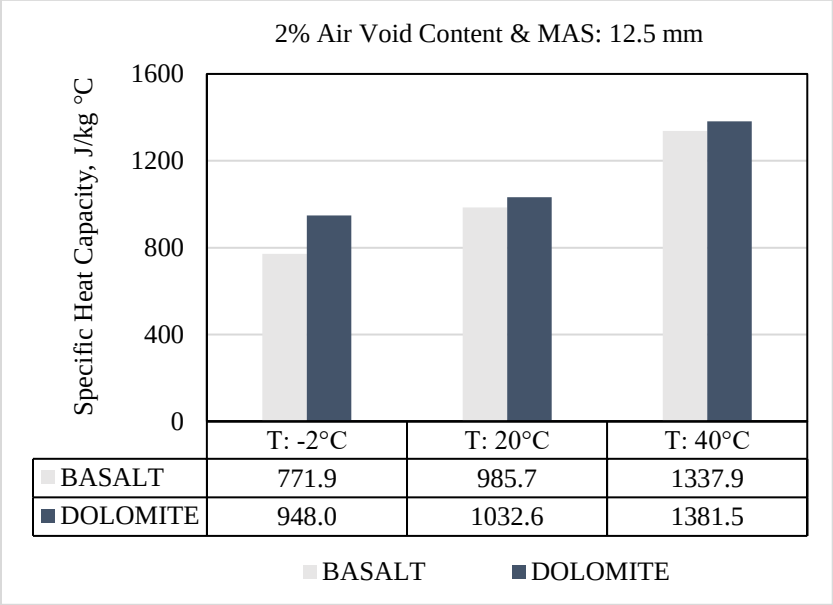


Figure 4.4 Specific heat capacity of basalt and dolomite samples with 2% air voids, maximum aggregate size of 12.5 mm, and varying initial temperatures.

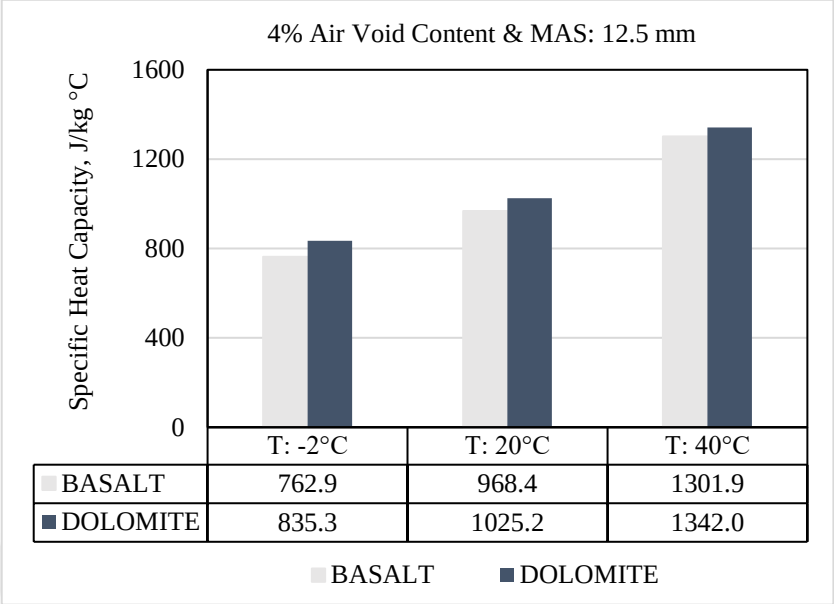


Figure 4.5 Specific heat capacity of basalt and dolomite samples with 4% air voids, maximum aggregate size of 12.5 mm, and varying initial temperatures.

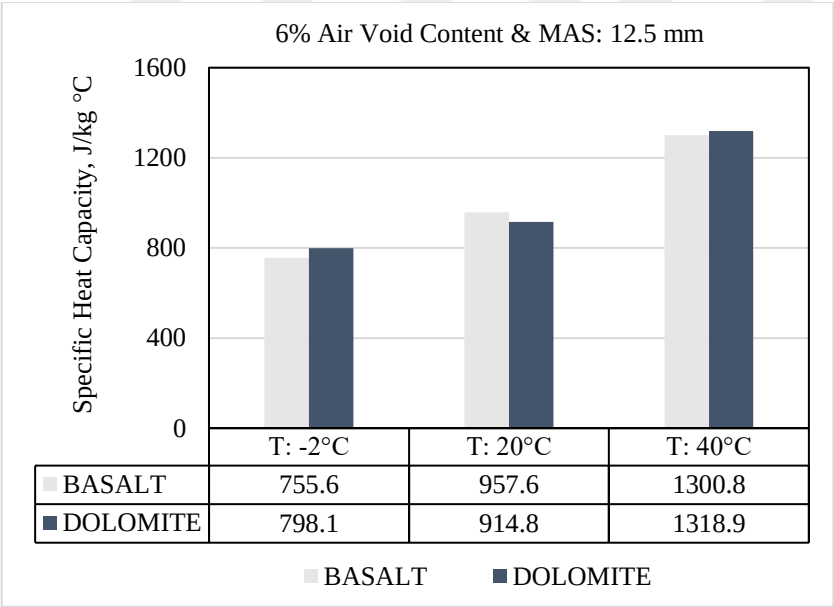


Figure 4.6 Specific heat capacity of basalt and dolomite samples with 6% air voids, maximum aggregate size of 12.5 mm, and varying initial temperatures.

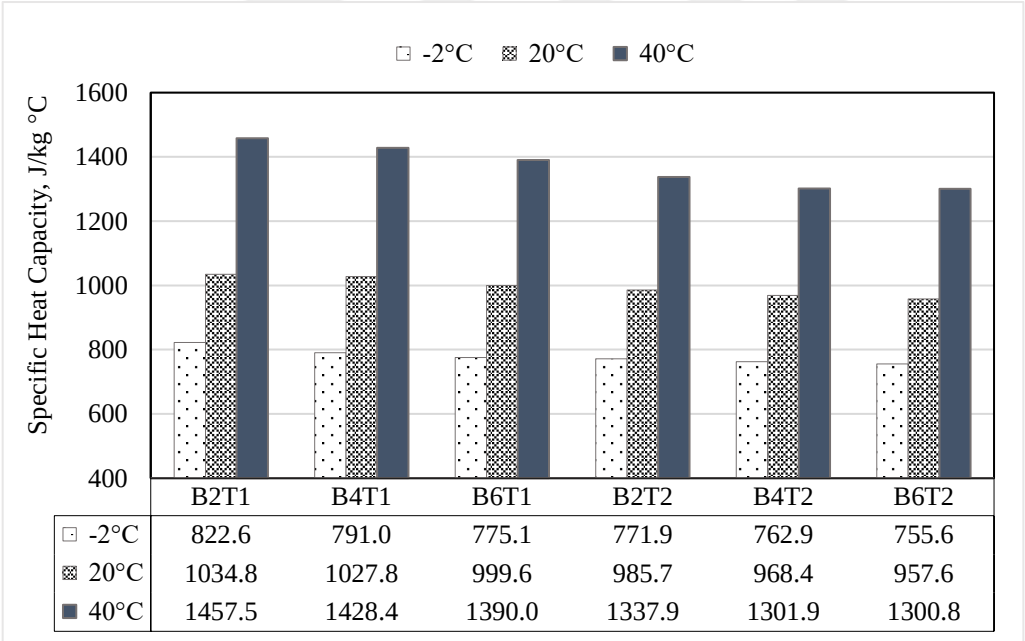
4.1.3 Effect of Air Void Content on Specific Heat Capacity

Air voids are one of the critical design parameters in the asphalt mixture and are affected by the degree of compaction during asphalt paving. Moreover, an optimum air void content is suggested to maintain the durability and performance of the asphalt concrete pavements. In addition to their impacts on mechanical properties, air voids also affect the thermal properties of asphalt pavements. It should be emphasized that the air void contents of the tested samples used in this study deviate slightly from the target values of 2%, 4%, and 6% due to cutting during the sample preparation stage. The measured actual air void contents are given in Table 4.2, and details are provided in Appendix C.

Table 4.2 Measured air void contents of the sliced samples.

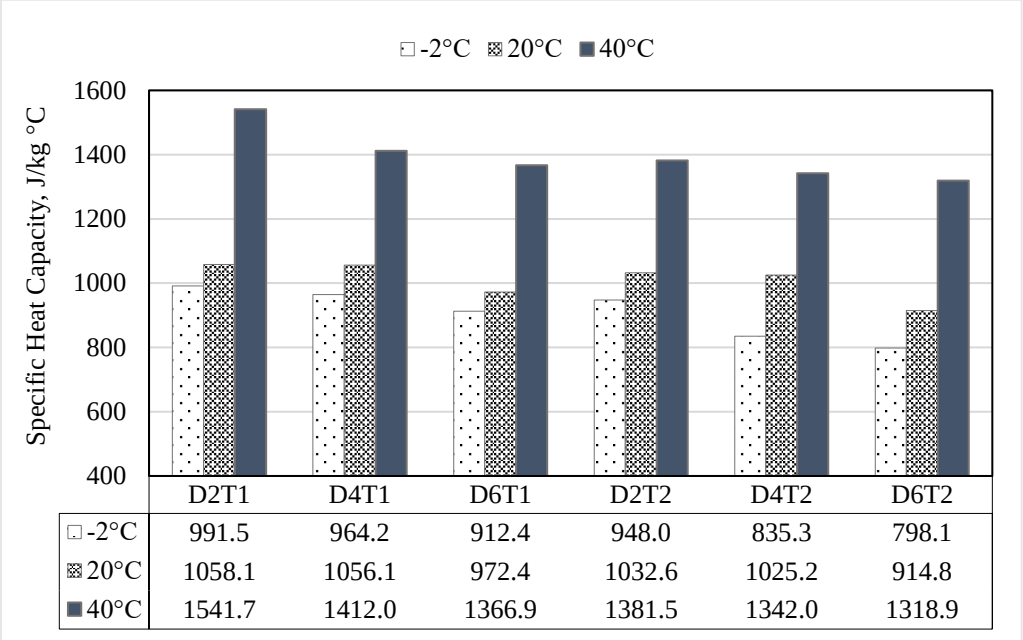
Target Air Voids (%)	**2**	**4**	**6**	**2**	**4**	**6**
Basalt, Sample ID	**B2T1**	**B4T1**	**B6T1**	**B2T2**	**B4T2**	**B6T2**
Air Void Content of Slice 1, %	1.3	2.6	4.8	1.1	3.4	5.0
Air Void Content of Slice 2, %	1.0	2.7	4.9	0.9	2.9	5.3
Average Air Void Content, %	1.2	2.7	4.8	1.0	3.2	5.1
Dolomite, Sample ID	**D2T1**	**D4T1**	**D6T1**	**D2T2**	**D4T2**	**D6T2**
Air Void Content of Slice 1, %	2.3	3.2	5.0	1.4	3.2	5.3
Air Void Content of Slice 2, %	0.8	3.8	5.3	0.8	2.8	4.8
Average Air Void Content, %	1.5	3.5	5.1	1.1	3.0	5.1

The specific heat capacities of the samples with different air void contents are shown in Figure 4.7 and Figure 4.8, respectively. The figures show that the specific heat capacities of the samples decrease with the increase in air void content. This trend does not change regardless of the aggregate type, maximum aggregate size, and conditioning temperature. However, it should be noted that this trend is particularly pronounced for the dolomite samples. The decrease in specific heat capacity with increasing air void can be attributed to the fact that the specific heat capacity of air ($\lambda_{air} \approx 0.024$ W/m.°C) is significantly lower than that of solid components, hence resulting in decrease in the mixture's specific heat capacity (Côté et al., 2013). It should also be remembered that an increase in the air voids will lower the bulk specific gravity, which in turn, decreases the specific heat capacity of the compacted samples (See Table 4.3).



	B2T1	B4T1	B6T1	B2T2	B4T2	B6T2
-2°C	822.6	791.0	775.1	771.9	762.9	755.6
20°C	1034.8	1027.8	999.6	985.7	968.4	957.6
40°C	1457.5	1428.4	1390.0	1337.9	1301.9	1300.8

Figure 4.7 Average specific heat capacities of basalt samples at three air void contents and conditioning temperatures.



	D2T1	D4T1	D6T1	D2T2	D4T2	D6T2
-2°C	991.5	964.2	912.4	948.0	835.3	798.1
20°C	1058.1	1056.1	972.4	1032.6	1025.2	914.8
40°C	1541.7	1412.0	1366.9	1381.5	1342.0	1318.9

Figure 4.8 Average specific heat capacities of dolomite samples at three air void contents and conditioning temperatures.

4.1.4 Effect of Maximum Aggregate Size on Specific Heat Capacity

It is known that not only the changes in the maximum aggregate size but also the mixture constituents affect the bulk specific gravity. When analyzing the effect of maximum aggregate size, it must be evaluated together with the other mixture properties such as bulk density and air voids. In the following, Table 4.3 shows the average specific heat capacities of the samples produced with Type 1 (MAS: 19 mm) and Type 2 (MAS: 12.5 mm) gradations at different conditioning temperatures and the average bulk specific gravities. It can be seen that the samples prepared with Type 1 gradation have a significantly higher specific heat capacity. Moreover, the bulk specific gravity of samples with Type 1 gradation, especially those prepared with dolomite, is consistently higher than that of samples with Type 2 gradation.

Table 4.3 Comparison of specific heat capacities according to maximum aggregate sizes.

Sample ID	Average Bulk Specific Gravity, G_{mb}	Average Specific Heat Capacity, J/kg.°C at -2°C	Average Specific Heat Capacity, J/kg.°C at 20°C	Average Specific Heat Capacity, J/kg.°C at 40°C
B2T1	2.457	822.6	1034.8	1457.5
B2T2	2.507	771.9	985.7	1337.9
B4T1	2.420	791.0	1027.8	1428.4
B4T2	2.453	762.9	968.4	1301.9
B6T1	2.367	775.1	999.6	1390.0
B6T2	2.403	755.6	957.6	1300.8
D2T1	2.550	991.5	1058.1	1541.7
D2T2	2.528	948.0	1032.6	1381.5
D4T1	2.499	964.2	1056.1	1412.0
D4T2	2.480	835.3	1025.2	1342.0
D6T1	2.457	912.4	972.4	1366.9
D6T2	2.427	798.1	914.8	1318.9

The results show that a high specific heat capacity associated with a high bulk specific gravity is validated for the samples prepared with dolomite but not for those prepared with basalt. On the other hand, the specific heat capacity of samples prepared with basalt and Type 1 gradation is higher than those prepared with Type 2. This discrepancy in the results may be due to the varying water absorption

capacities of basalt and dolomite aggregates, affecting the binder absorption (See Table 3.2).

The parameters discussed in this section, including optimum bitumen content, air void content, aggregate type, and maximum aggregate size, directly influence the bulk specific gravity and the specific heat capacity of the mixtures. In addition to these factors, temperature is another controlling parameter for specific heat capacity, which is discussed in the next section.

4.1.5 Effect of Conditioning Temperature on Specific Heat Capacity

The temperature difference is the driving force for the heat transfer in the calorimetry-based test method, as mentioned in Section 3.5.1.3. Three different conditioning temperatures of -2°C, 20°C, and 40°C were chosen to obtain three temperature gradients between the hot water (50°C) and the samples. Later, the temperature change in the samples was monitored during the heat transfer from the surface resting on the hot plate to the surface resting on the cold plate. The changes in the temperature with time are plotted between Figure 4.9 through Figure 4.12 for the samples with 4% air voids, Type 1 and Type 2 gradations of basalt and dolomite aggregates, respectively (B4T1 & B4T2 and D4T1 & D4T2). The temperature-time curves for the other samples with 2% and 6% air voids are given in Appendix D.

It can be observed that the conditioning temperature significantly affects the specific heat capacity of the asphalt mixture despite the differences in aggregate type, air void content, and maximum aggregate size. It can also be seen that the specific heat capacity of the samples increases with increasing conditioning temperature, as listed in Table 4.3. This result can be attributed to the fact that when a substance absorbs heat energy, the kinetic energy of its particles increases, and thus, the temperature increases (Kreith & Bohn, 2001). The results show that the samples conditioned at 40°C yield the highest specific heat capacity among the initial conditioning temperatures tested in the experimental program. Figure 4.9 through Figure 4.12 not only shows the temperature change in the samples over time but also provides details

about their thermal behavior. To calculate the rate of change in temperature, polynomial equations are fitted to the portion the temperature-time curves after the thermal equilibrium is reached in each sample. The fitted equations are embedded into the figures and used to determine the slope of the temperature-time curves.

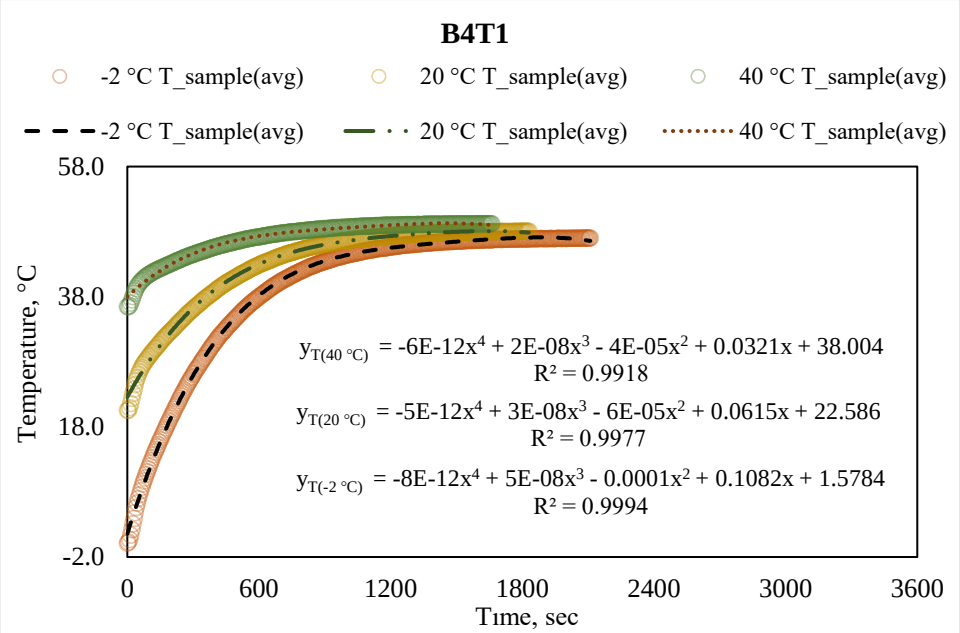


Figure 4.9 Temperature and time curves for B4T1 under three different conditioning temperatures.

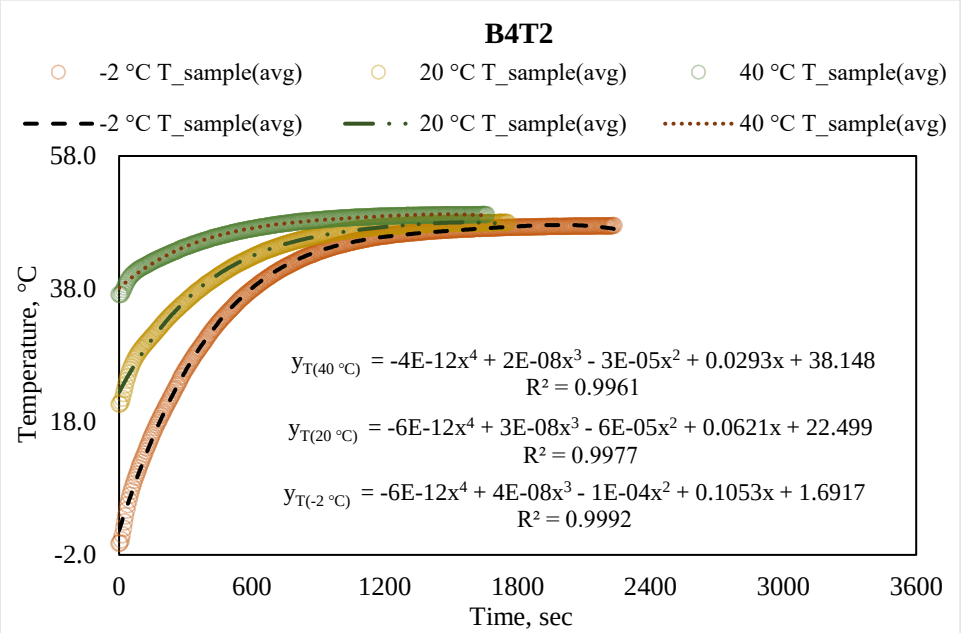


Figure 4.10 Temperature and time curves for B4T2 under three different conditioning temperatures.

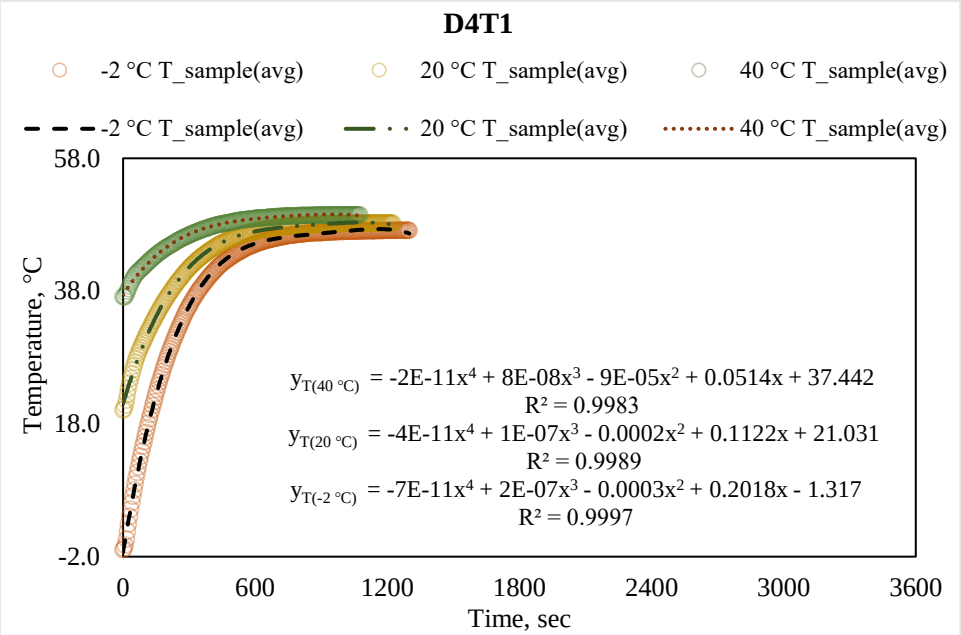


Figure 4.11 Temperature and time curves for D4T1 under three different conditioning temperatures.

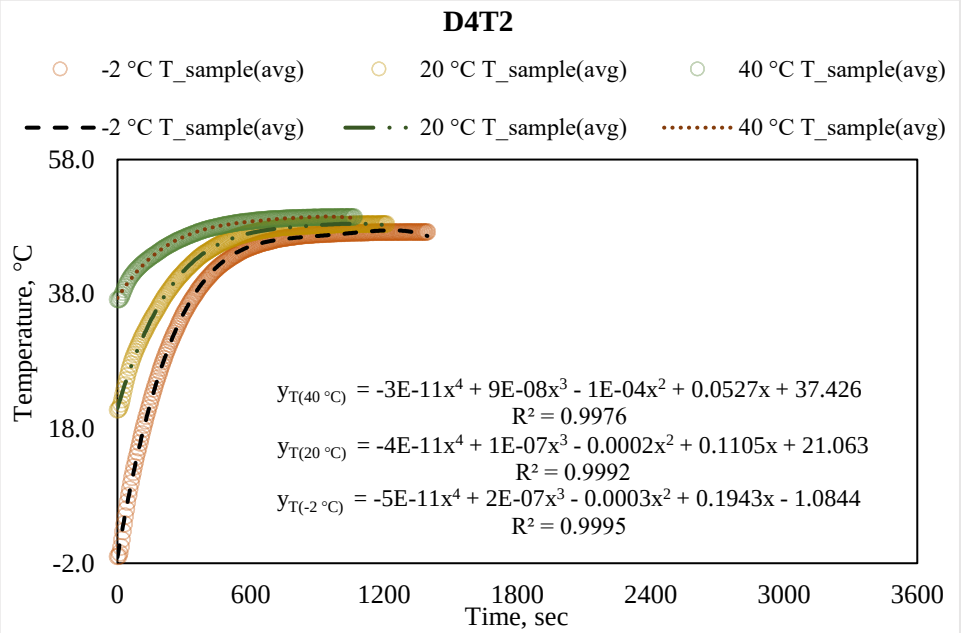


Figure 4.12 Temperature and time curves for D4T2 under three different conditioning temperatures.

Before determining the slope of temperature-time curves, the trends for basalt and dolomite samples were carefully evaluated. It can be seen that the trends for B4T1 and B4T2 basalt samples in Figure 4.9 and Figure 4.10 are quite similar, so as for the D4T1 and D4T2 dolomite samples in Figure 4.11 and Figure 4.12. However, when a cross-comparison is made between basalt and dolomite samples (B4T1 and D4T1 in Figure 4.9 and Figure 4.11), it appears that the time-dependent temperature sensitivity is quite different. Moreover, the samples prepared with dolomite are more sensitive to temperature changes than those prepared with basalt, as they reach a steady state condition faster. For instance, while it takes about 2000 seconds to reach equilibrium for the basalt samples, it takes only 1200 seconds for the dolomite samples, as can be observed from Figure 4.13 and Figure 4.14 plotted for 2% air voids. The data given in Appendix D show that this trend remains the same for the other samples.

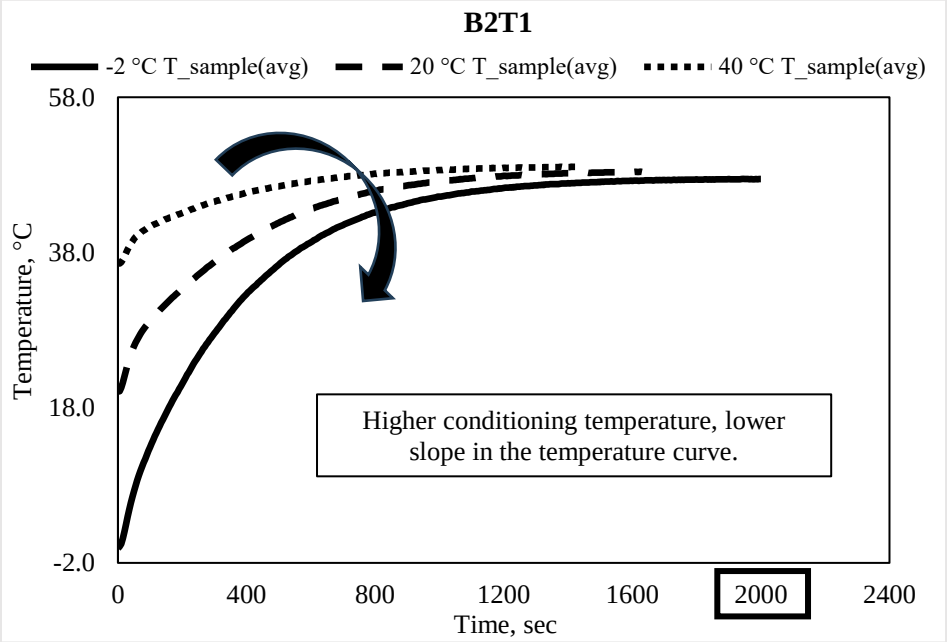


Figure 4.13 Temperature behavior characteristic of B2T1 at three conditioning temperatures.

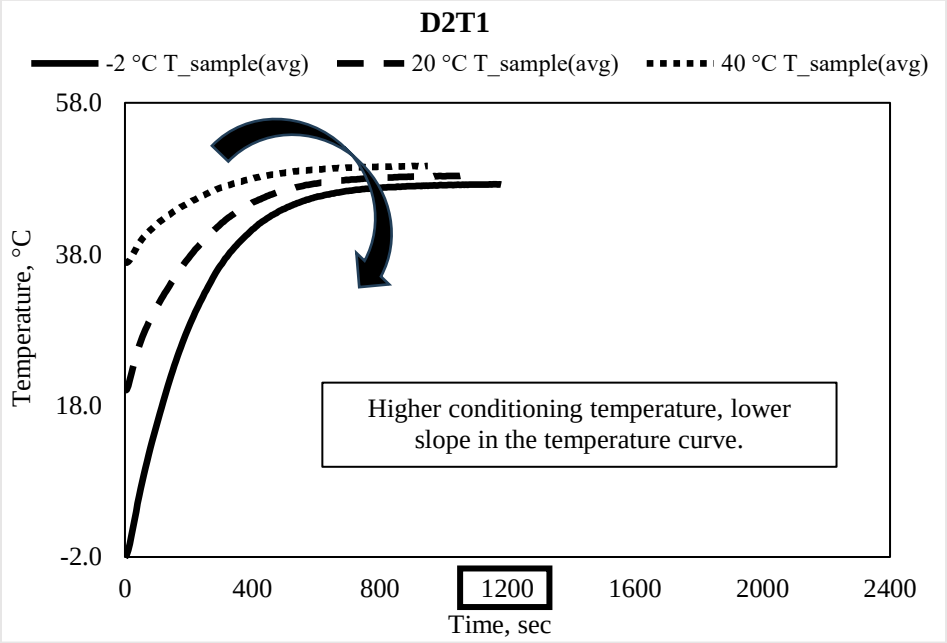


Figure 4.14 Temperature behavior characteristic of D2T1 at three conditioning temperatures.

Table 4.4 through Table 4.6 present the temperature gradients of the samples for both basalt and dolomite aggregates at conditioning temperatures of -2°C, 20°C, and 40°C, respectively. It can be noticed that the samples conditioned at 40°C have the smallest temperature gradient, regardless of the aggregate type, air void content, and maximum aggregate size (See Table 4.6). Therefore, it can be stated that the higher the conditioning temperatures are, the lower the slope of temperature-time curves is in the calorimeter-based test method.

In Table 4.4, it is seen that the temperature gradient of the samples prepared basalt decreases from 0.087 to 0.072 for Type 1 and from 0.085 to 0.065 for Type 2 with increasing air void content. For the samples prepared with dolomite, the temperature gradient decreases from 0.104 to 0.094 for Type 1 and from 0.110 to 0.100 for Type 2 with increasing air void content. This outcome is also consistent for both aggregates subjected to the conditioning temperature of 20°C, as shown in Table 4.5. However, in the samples conditioned at 40°C, it is found that the temperature gradients are quite close to each other even at different air void contents, as can be seen in Table 4.6.

Despite the differences in air void content, maximum aggregate size, and conditioning temperature, the comparison of all temperature gradients shows the significant effect of aggregate type on specific heat capacity. Accordingly, the samples prepared with dolomite have a higher temperature gradient than those prepared with basalt. Finally, evaluating the relationship between the maximum aggregate size and the temperature gradient at three conditioning temperatures reveals that some samples exhibit a high-temperature gradient for Type 1 in both aggregates. However, this does not provide sufficient evidence to support a generalization due to the deviations in the results.

Table 4.4 The temperature gradients of the samples prepared with basalt and dolomite at a conditioning temperature of -2°C.

Initial Conditioning Temperature, -2°C						
BASALT	**B2T1**	**B4T1**	**B6T1**	**B2T2**	**B4T2**	**B6T2**
Temperature at t=0 sec.	1.5	1.6	2.9	3.5	1.7	3.6
Temperature at t=400 sec.	36.4	31.9	31.8	37.4	30.2	29.6
Temperature Gradient	0.087	0.076	0.072	0.085	0.071	0.065
DOLOMITE	**D2T1**	**D4T1**	**D6T1**	**D2T2**	**D4T2**	**D6T2**
Temperature at t=0 sec.	-3.03	-1.32	-1.73	-1.79	-1.08	-2.62
Temperature at t=400 sec.	38.44	42.41	35.97	42.06	40.16	37.48
Temperature Gradient	0.104	0.109	0.094	0.110	0.103	0.100

Table 4.5 The temperature gradients of the samples prepared with basalt and dolomite at a conditioning temperature of 20°C.

Initial Conditioning Temperature, 20°C						
BASALT	**B2T1**	**B4T1**	**B6T1**	**B2T2**	**B4T2**	**B6T2**
Temperature at t=0 sec.	22.124	22.586	23.096	22.06	22.499	22.361
Temperature at t=400 sec.	39.2536	39.378	38.6624	40.124	39.5054	37.993
Temperature Gradient	0.043	0.042	0.039	0.045	0.043	0.039
DOLOMITE	**D2T1**	**D4T1**	**D6T1**	**D2T2**	**D4T2**	**D6T2**
Temperature at t=0 sec.	20.463	21.031	21.018	19.462	21.063	22.02
Temperature at t=400 sec.	48.623	39.287	38.874	37.854	38.639	49.468
Temperature Gradient	0.070	0.046	0.045	0.046	0.044	0.069

Table 4.6 The temperature gradients of the samples prepared with basalt and dolomite at a conditioning temperature of 40°C.

Initial Conditioning Temperature, 40°C						
BASALT	**B2T1**	**B4T1**	**B6T1**	**B2T2**	**B4T2**	**B6T2**
Temperature at t=0 sec.	37.698	38.004	37.966	37.656	38.148	38.025
Temperature at t=400 sec.	46.202	45.5704	45.198	46.72	46.2456	45.6682
Temperature Gradient	0.021	0.019	0.018	0.023	0.020	0.019
DOLOMITE	**D2T1**	**D4T1**	**D6T1**	**D2T2**	**D4T2**	**D6T2**
Temperature at t=0 sec.	36.909	37.442	36.927	37.257	37.426	37.178
Temperature at t=400 sec.	49.765	48.21	49.503	47.065	47.498	47.626
Temperature Gradient	0.032	0.027	0.031	0.025	0.025	0.026

4.2 Evaluation of Thermal Conductivity Results Using the Transient Plane Source Method

This section presents the results of the thermal conductivity measurements with the Hot Disk TPS 2500S to evaluate the effects of mixture properties. As stated in Section 3.5.3.2, the TPS sensor is positioned between the center and bottom slices to measure the bottom part's thermal conductivity and between the upper and center slices for the upper part's thermal conductivity. Therefore, there are two results produced for each sample: one for the upper part and one for the bottom part. The average thermal conductivity of the bottom and upper parts represents the overall thermal conductivity of the entire sample.

In the TPS measurements, at least four readings were taken for each part to eliminate the variations in the readings. Accordingly, at the end of the measurements, 101

readings were taken for the upper part and 76 readings for the bottom part of the samples. The difference in the number of readings was due to the repeated measurements to compensate for the effect of high variance. In this study, an analysis of variance (ANOVA) was also performed to evaluate the significance of the mix properties. Accordingly, Table 4.7 shows the significance level of the aggregate type, the air void content, and the maximum aggregate size for the thermal conductivities of the upper and bottom parts of the samples.

Table 4.7 According to the ANOVA results, the mix components effects.

Parts	Source	Sum of Squares	Degrees of Freedom	Mean Square	F-ratio	P-value	Partial Eta Squared
Upper Part	Air Void (%)	0.124	2	0.062	9.571	0.000	0.166
	Maximum Aggregate Size	0.113	1	0.113	17.426	0.000	0.154
	Aggregate Type	38.526	1	38.526	5956.4	0.000	0.984
	Total	261.917	101				
	Adjusted R^2= 0.984						
Bottom Part	Air Void (%)	0.060	2	0.030	8.481	0.000	0.193
	Maximum Aggregate Size	0.034	1	0.034	9.564	0.003	0.119
	Aggregate Type	32.114	1	32.114	9021.8	0.000	0.992
	Total	197.866	76				
	Adjusted R^2 = 0.992						

It can be seen that the thermal conductivity is affected by all the mix design parameters, i.e., air void content, maximum aggregate size, and aggregate type. In particular, the significance level of aggregate type leads to the highest impact on thermal conductivity. It is believed that the localized measurements performed using the TPS sensor is responsible for this result, as elaborated in the following sections.

4.2.1 Effect of Aggregate Type on Thermal Conductivity

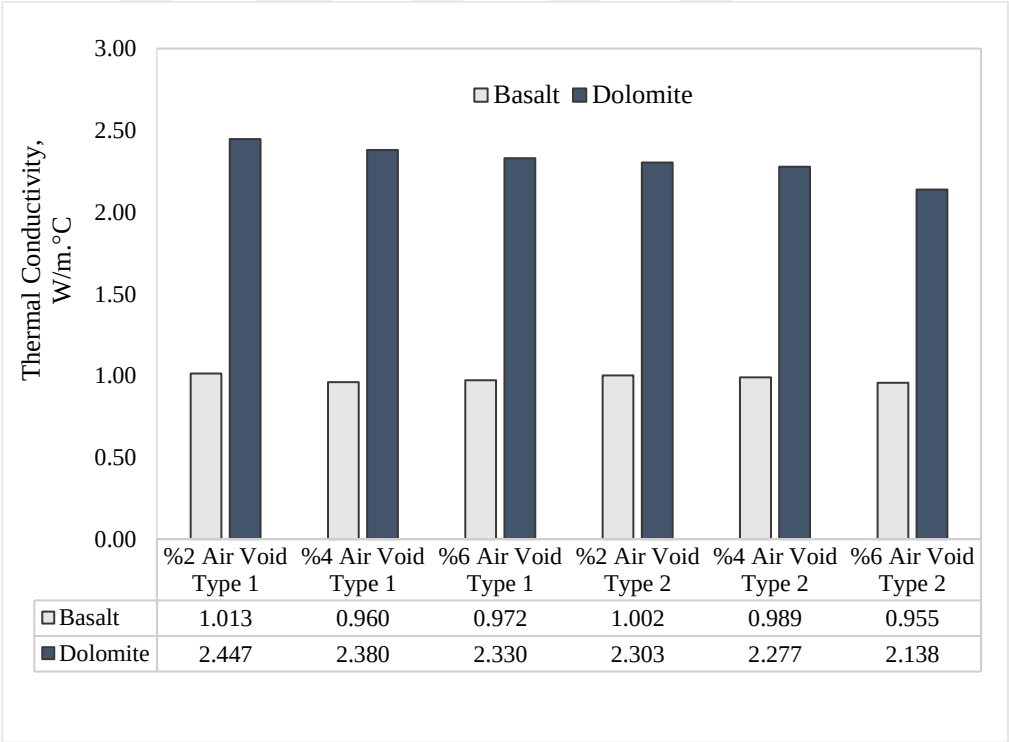
Due to the high volumetric proportion of aggregate in the asphalt mixture, there is a high representation of aggregate particles in the contact zone of the TPS sensor. Thus, in this study, the aggregates dominated the thermal conductivity of asphalt mixtures, not only because of their higher thermal conductivity but also because of their high proportion in the mixtures (Mrawira & Luca, 2006; Côté et al., 2013; Hassn et al., 2017). In other words, this study concluded that the thermal conductivity of the asphalt mixture is close to the thermal conductivity of the aggregate. To confirm this conclusion, this study aimed to measure the thermal conductivity of aggregates. For this purpose, almost two identical slices were cut from each aggregate particle, and the TPS sensor was placed between these slices, as shown in Figure 4.15.



Figure 4.15 Preparation of the aggregate particle for the TPS measurements in this study.

Considering the sensor radius and aggregate diameter, a kapton-insulated sensor with a sensor ID of 7577 (radius: 2.001 mm) was used in the measurements. In the test phase, a heating power of 50 mW for basalt and 75 mW for dolomite was applied for

10 seconds using the ideal residual graph mentioned in Section 3.5.3.3. As a result, the thermal conductivity of basalt and dolomite were obtained as 1.41 ± 0.2 W/m.°C and 3.98 ± 0.2 W/m.°C, respectively. It can be stated that the thermal conductivity of the asphalt mixtures prepared with basalt and dolomite is highly correlated with the thermal conductivity of basalt and dolomite aggregates. Accordingly, Figure 4.16 clearly shows that the average thermal conductivities of the samples prepared with dolomite are almost twice those of basalt samples regardless of the variations in air void contents (produced at 2%, 4%, and 6%) and maximum aggregate sizes (Type 1: 19 mm and Type 2: 12.5 mm). Based on the differences in the thermal conductivity of basalt and dolomite aggregates, it is evident that the aggregate type plays a crucial role in the thermal conductivity of the asphalt mixture.



	%2 Air Void Type 1	%4 Air Void Type 1	%6 Air Void Type 1	%2 Air Void Type 2	%4 Air Void Type 2	%6 Air Void Type 2
Basalt	1.013	0.960	0.972	1.002	0.989	0.955
Dolomite	2.447	2.380	2.330	2.303	2.277	2.138

Figure 4.16 Thermal conductivity values of the samples prepared with basalt and dolomite aggregates.

4.2.2 Effect of Air Void Content on Thermal Conductivity

The relationship between the thermal conductivity and the measured air void content is explained in this section. The air void contents of the asphalt mixtures, which were initially 2%, 4%, and 6%, changed due to coring and cutting processes (See Section 3.5.3.2). Thus, each slice's bulk specific gravity (G_{mb}) and air void content were determined again and presented in Table 4.8 and Table 4.9. These tables show that the air void contents differ significantly from the intended initial values and must be considered when analyzing the thermal conductivities below.

Initially, Table 4.8 shows the average thermal conductivities of the upper part, the bottom part, and the entire samples prepared with basalt. According to Table 4.8, the average thermal conductivities of the samples vary between 1.033 and 0.950 W/m.°C, and a slight decrease in thermal conductivity is generally observed with increasing air void content. Then, Table 4.9 shows the average thermal conductivities of the samples prepared with dolomite, which vary between 2.494 and 2.101 W/m.°C. The results show that the thermal conductivity of the samples prepared with dolomite decreases significantly with increasing air void content compared to the basalt samples. This decreasing tendency can also be seen in the upper and bottom parts of the samples of both aggregates.

The generally accepted view in previous studies is that more air voids in asphalt mixtures lower their thermal conductivity because air conducts heat poorly (Hassn et al., 2016b). On the other hand, although the thermal conductivity tends to decrease with increasing air void content in this study, the thermal conductivities are still close (See Table 4.8 and Table 4.9). The main reason for this finding is that only a small part of the mixture's air voids are in contact with the TPS sensor. Therefore, to observe the air's negative effect more clearly on thermal conductivity in the TPS measurement, the mixture must have a higher air void content than what was used in this study. This would increase the amount of air in the contact zone.

Table 4.8 The bulk specific gravity, air void content, and thermal conductivity results of the basalt samples.

Sample ID	Slices	Bulk Specific Gravity, G_{mb}	Measured Air Void Content, %	Upper Part-Average Thermal Conductivity, W/m.°C	Bottom Part-Average Thermal Conductivity, W/m.°C	Total Sample-Average Thermal Conductivity, W/m.°C
B2T1	Bottom	2.482	0.2	1.033	0.994	1.013
	Center	2.490	0.0			
	Upper	2.479	0.3			
B4T1	Bottom	2.456	1.2	0.959	0.961	0.960
	Centre	2.468	0.8			
	Upper	2.435	2.1			
B6T1	Bottom	2.412	3.0	0.960	0.984	0.972
	Centre	2.438	2.0			
	Upper	2.401	3.5			
B2T2	Bottom	2.534	0.0	1.004	0.999	1.002
	Centre	2.537	0.0			
	Upper	2.520	0.5			
B4T2	Bottom	2.514	0.8	0.973	1.006	0.989
	Centre	2.514	0.8			
	Upper	2.469	2.5			
B6T2	Bottom	2.464	2.7	0.950	0.961	0.955
	Centre	2.471	2.4			
	Upper	2.424	4.3			

In addition to the effect of air void content on thermal conductivity, this section also provides the relationship between bulk specific gravity and thermal conductivity. As is known, the presence of air directly affects the bulk specific gravity of the asphalt mixtures. Therefore, the effect of bulk specific gravity on thermal conductivity cannot be studied alone. Accordingly, Table 4.8 and Table 4.9 show that the center slice of the samples has the highest bulk specific gravity because it contains the slightest air. Thus, the average thermal conductivity in the bottom part of the samples is slightly higher than in the upper part due to the lower air void and higher bulk specific gravity.

Table 4.9 The bulk specific gravity, air void content, and thermal conductivity results of the dolomite samples.

Sample ID	Slices	Bulk Specific Gravity, G_{mb}	Measured Air Void Content, %	Upper Part-Average Thermal Conductivity, W/m.°C	Bottom Part-Average Thermal Conductivity, W/m.°C	Total Sample-Average Thermal Conductivity, W/m.°C
D2T1	Bottom	2.575	0.6	2.399	2.494	2.447
	Centre	2.587	0.1			
	Upper	2.554	1.4			
D4T1	Bottom	2.538	2.0	2.346	2.414	2.380
	Centre	2.562	1.1			
	Upper	2.522	2.6			
D6T1	Bottom	2.492	3.8	2.288	2.371	2.330
	Centre	2.531	2.3			
	Upper	2.456	5.2			
D2T2	Bottom	2.540	0.6	2.242	2.364	2.303
	Centre	2.550	0.2			
	Upper	2.522	1.3			
D4T2	Bottom	2.513	1.7	2.224	2.331	2.277
	Centre	2.533	0.9			
	Upper	2.493	2.5			
D6T2	Bottom	2.457	3.9	2.101	2.175	2.138
	Centre	2.484	2.8			
	Upper	2.393	6.4			

Lastly, Figure 4.17 and Figure 4.18 show the relationship between air void content and thermal conductivities of all the data collected graphically. These figures represent the regression results using confidence and prediction ranges. In brief, the following curves show that the thermal conductivity of dolomite samples decreases more pronounced with an increasing air void content in the TPS method.

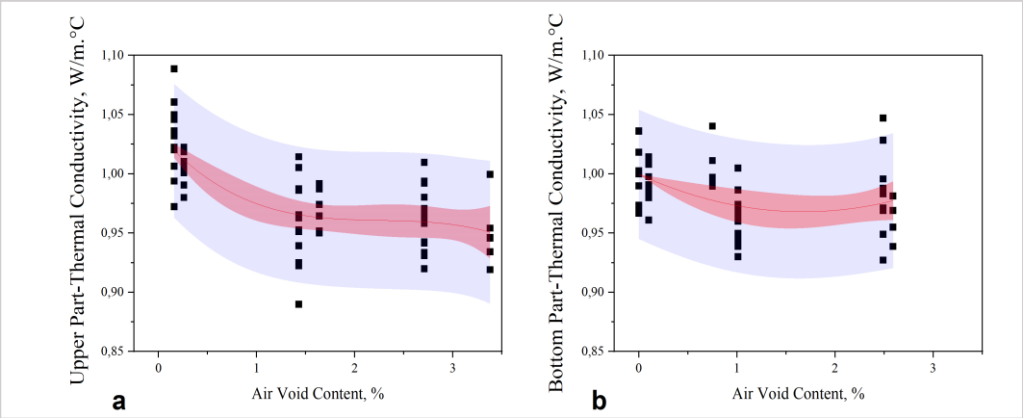


Figure 4.17 Distribution of thermal conductivity in the upper part (a) and bottom part (b) of the sliced samples prepared with basalt.

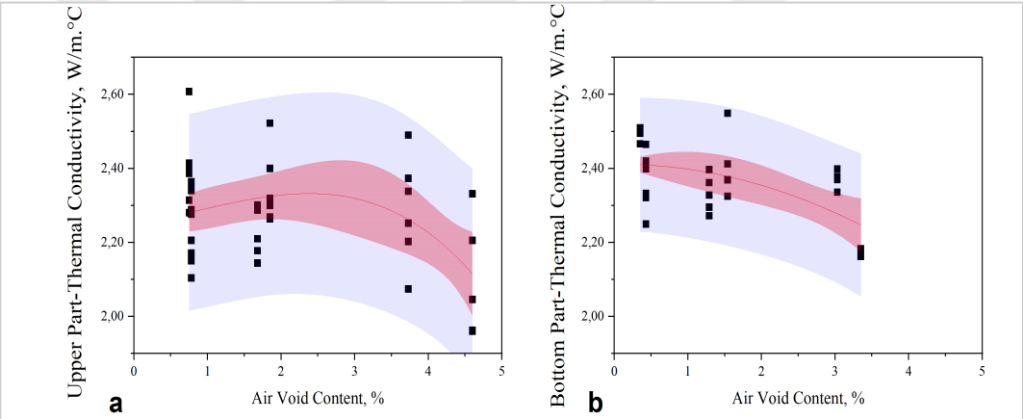


Figure 4.18 Distribution of thermal conductivity in the upper part (a) and bottom part (b) of the sliced samples prepared with dolomite.

4.2.3 Effect of Volumetric Properties on Thermal Conductivity

This section evaluates the relationship between the volumetric properties of the mix designs and the average thermal conductivity of the samples. In the TPS method, this relationship cannot be meaningful due to the measurement approach of the TPS method. However, since these properties are assumed to be partly represented in the contact zone, their effects on thermal conductivity can be discussed briefly. Accordingly, the volumetric properties of the mix designs and the average thermal

conductivities of the samples are presented in Table 4.10. It is seen that the average thermal conductivity of the samples tends to decrease with increasing VMA and V_a. In other words, the thermal conductivity is inversely proportional to VMA and V_a, even if the aggregate type and the maximum aggregate sizes differ. Also, it is observed that samples with a high VFA generally have higher average thermal conductivity. This can be attributed to the presence of bitumen because it increases the thermal conductivity of the asphalt mixtures compared to unbonded aggregate blends (Côté et al., 2013). Apart from these properties, the density of asphalt mixtures also controls the thermal conductivity of the samples.

Table 4.10 The average thermal conductivity results of the samples with their volumetric properties.

Sample ID	**Average Thermal Conductivity, W/m.°C**	**Optimum Bitumen Content, %**	**Va, %**	**VMA, %**	**VFA, %**	**Density (kg/m^3)**
B2T1	1.013	5.5	1.95	13.9	86.0	2439
B4T1	0.960		4.10	15.8	74.1	2385
B6T1	0.972		6.11	17.6	65.3	2335
B2T2	1.002	6.2	1.90	13.2	85.6	2485
B4T2	0.989		3.96	15.0	73.6	2433
B6T2	0.955		6.03	16.9	64.2	2380
D2T1	2.447	4.9	2.02	12.8	84.2	2537
D4T1	2.380		3.91	14.5	73.0	2488
D6T1	2.330		5.92	16.3	63.5	2436
D2T2	2.303	5.7	1.81	14.1	87.2	2510
D4T2	2.277		3.97	16.0	75.2	2455
D6T2	2.138		6.17	17.9	65.6	2398

As seen in Figure 4.19 and Figure 4.20, the density of asphalt mixtures changes depending on air void content, aggregate type, and maximum aggregate size. As the density of asphalt mixtures changes, the thermal conductivity of the samples also changes. The following figures show that the sample's thermal conductivity decreases as the mixture density decreases with increasing air void content.

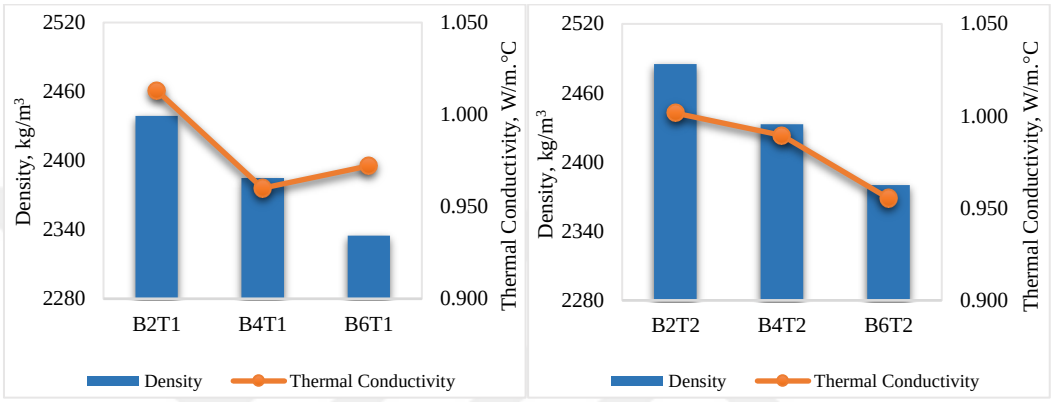


Figure 4.19 The relationship between the average thermal conductivities of the entire samples and the density of the mixtures prepared with basalt and Type 1 and Type 2 gradations.

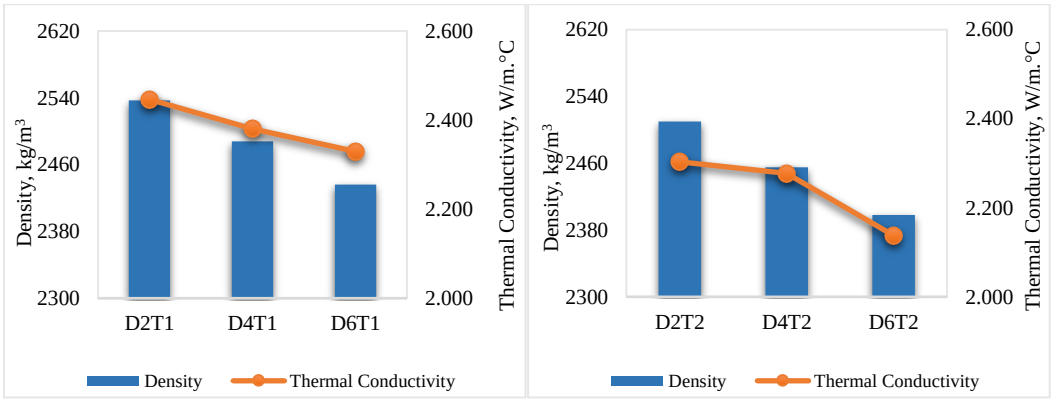


Figure 4.20 The relationship between the average thermal conductivities of the entire samples and the density of the mixtures prepared with dolomite and Type 1 and Type 2 gradations.

4.2.4 Effect of Maximum Aggregate Size on Thermal Conductivity

In the TPS method, the maximum aggregate size affects the area of the aggregate particles distributed over the contact zone. It is stated in previous studies that the change in maximum aggregate size does not make a significant difference in the results of thermal conductivity measurements using the TPS method (Mirzanamadi et al., 2018; Khasawneh et al., 2023). However, this study claims that the maximum aggregate size significantly affects the thermal conductivity when not evaluated alone. As is known, the maximum aggregate size affects the asphalt mix's aggregate gradation, thus, its air void content and optimum bitumen content. When the mix's aggregate gradation, air void content, and optimum bitumen content change, the distribution of the aggregate particles naturally changes in the contact zone. As the effect of air void content was discussed in the previous section, this section evaluates the effect of maximum aggregate size on thermal conductivity together with the mix's aggregate gradation and optimum bitumen content.

The changes in thermal conductivity of the basalt and dolomite samples produced with two different maximum aggregate sizes (Type 1: 19 mm and Type 2: 12.5 mm) are shown in Figure 4.21 and Figure 4.22. The optimum bitumen contents of the asphalt mixtures are already given above in Table 4.10. In the Type 1 gradations, the asphalt mixtures' optimum bitumen contents are low. In contrast, the mixtures' optimum bitumen contents with the Type 2 gradations are high. As a result, the thermal conductivity in Figure 4.21 is low for the basalt samples at the high optimum bitumen and the Type 2 gradation. An example from Table 4.10: B2T1 (λavg: 1.013 W/m.°C) has a slightly higher thermal conductivity than B2T2 (λavg: 1.002 W/m.°C). Another result is the difference in thermal conductivity of dolomite samples depending on the change in maximum aggregate size, which can be seen in Figure 4.22. In summary, Figure 4.22 shows that the thermal conductivity of the dolomite samples at the low optimum bitumen content and the Type 1 gradation is slightly higher than those prepared with the high optimum bitumen content and the

Type 2 gradation. An example from Table 4.10: D2T1 (λavg: 2.447 W/m.°C) has a higher thermal conductivity than D2T2 (λavg: 2.303 W/m.°C).

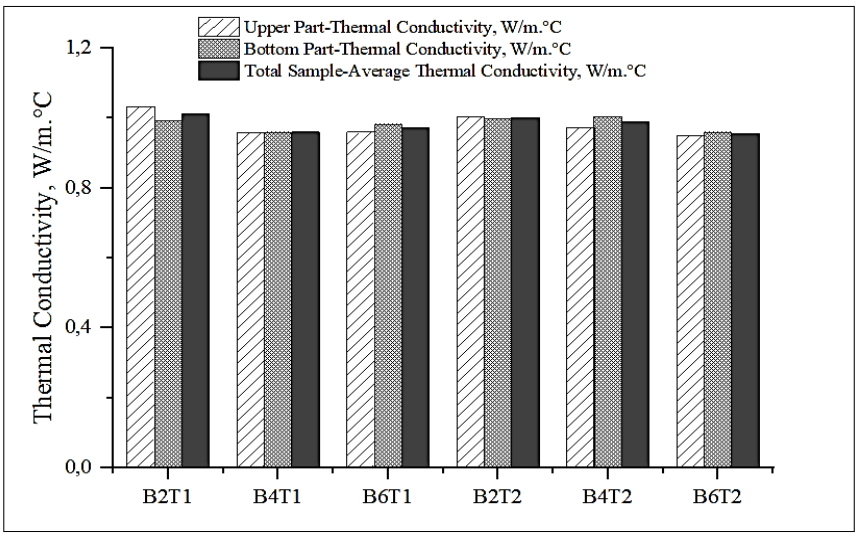


Figure 4.21 Change in thermal conductivity of basalt samples at different air void contents and maximum aggregate sizes.

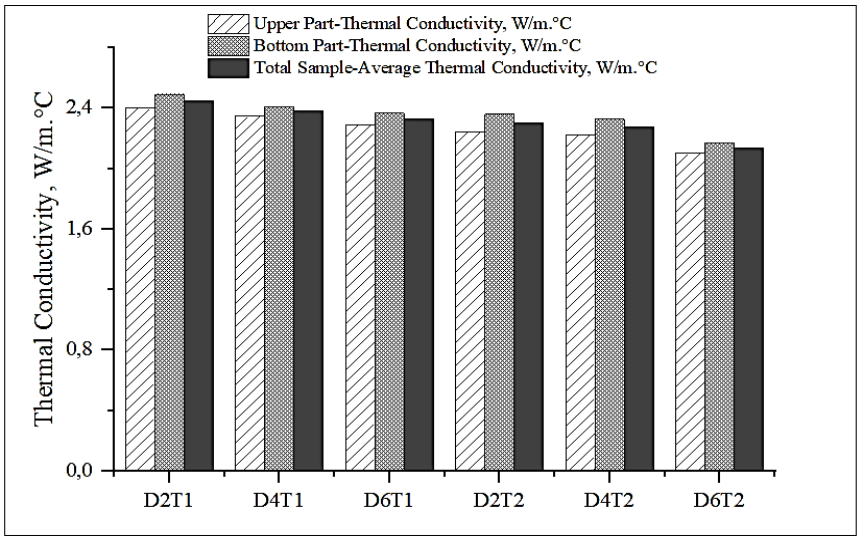


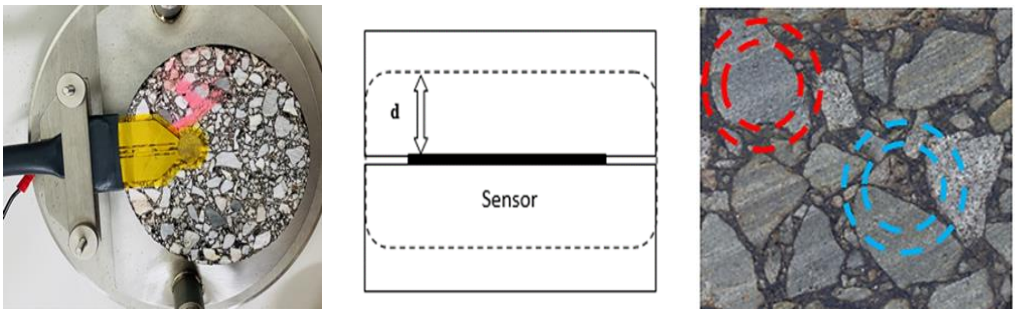
Figure 4.22 Change in thermal conductivity of dolomite samples at different air void contents and maximum aggregate sizes.

The results of this section mostly show that the Type 1 gradation, which requires less optimum bitumen content, leads to higher thermal conductivity in the TPS method. This is because the bituminous area that decreases between the aggregates due to the large aggregate size allows the TPS sensor to take measurements mainly on the aggregate. To explain it differently, if the optimum bitumen content is increased, the presence of bitumen between the aggregate particles deviates the heat intensity. Thus, it slows the heat transfer of the TPS sensor. Therefore, this section emphasizes that the high optimum bitumen content can cause a decrease in thermal conductivity. In summary, the effect of maximum aggregate size on thermal conductivity in the TPS method is mainly associated with the distribution of aggregate particles and bitumen in the contact zone. To support this result, the following section provides the microstructural properties of the contact zone using image analysis.

4.2.5 Effect of Microstructural Properties of the Contact Zone on Thermal Conductivity

The effects of aggregate type, air void content, and maximum aggregate size on thermal conductivity are substantial, especially when these parameters are adequately represented in the contact zone. In particular, the size, shape, and distribution of aggregate particles in the contact zone control the thermal conductivity of the asphalt concrete samples. This study supports this assertion by determining the microstructural properties of the contact zone through image analysis. This study examines two crucial microstructural aspects: the contact points of the aggregate particles and the total surface area of aggregate particles within the contact zone. These key features are crucial in determining the nature of the measurement surface. Figure 4.23 illustrates how these features influence thermal conductivity. It includes the TPS sensor on the sample surface, the measuring depth, and two distinct contact zones. In the first zone, the sensor is directly placed on the aggregate, whereas in the second zone, it is located at the interface between the aggregate and the bitumen. Due to the microstructural differences in these zones, the

thermal conductivity measured may not accurately reflect the overall thermal conductivity of the entire asphalt concrete sample.



a) b) c)

Figure 4.23 a) Top view of the TPS sensor, b) Schematic view of TPS sensor from the side, and c) TPS sensor contact zones on the section surface.

In this study, the microstructural properties of the samples are determined using the iPas software program. Initially, the image analysis is performed on two interface surfaces of both the bottom and upper parts of the samples. Then, the contact zone properties, orientation, and segregation in the vertical and radial directions are determined. According to the results, the variation in the thermal conductivity of the samples is examined concerning the contact properties and orientation outputs. Table 4.11 shows the total aggregate area, and the number of contact points of the samples made from basalt, and Table 4.12 displays the same microstructural properties for the samples made from dolomite.

An important outcome from these tables is that as the air void content of the samples increases, the total aggregate surface area, number of contact points, and their thermal conductivity generally tend to decrease. This also means the air void content is appropriately represented in the contact zone. Additionally, the samples with Type 1 gradation have a larger total aggregate surface area than those with Type 2 for both aggregates, as seen in Table 4.11 and Table 4.12. For both aggregates, the number of contact points is lower for a maximum aggregate size (MAS) of 19 mm compared to a MAS of 12.5 mm. When the MAS is large in the cross-section, fewer contact

points are possibly detected during the image analysis, resulting in a smaller number of contact points. Therefore, the samples using Type 1 gradation generally show higher thermal conductivity values for both aggregates. On the other hand, a greater number of contact points reflects a higher proportion of smaller particles within the cross-section. It also enhances the chance for the TPS sensor to assess thermal conductivity in areas that contain aggregates, bitumen, and air voids. Thus, the samples using Type 2 gradation typically show lower thermal conductivity values for both aggregates. Based on these findings, the maximum aggregate size is also adequately represented in the contact zone.

Table 4.11 The microstructural properties of the samples prepared with basalt.

Sample ID	Section	Average Number of Contact Points	Average Total Aggregate Surface Area (mm^2)	Average Thermal Conductivity, W/m.°C
B2T1	Bottom	252	3547	0.994
	Upper	356	3684	1.033
B4T1	Bottom	310	3620	0.961
	Upper	250	3296	0.959
B6T1	Bottom	250	3544	0.984
	Upper	231	3270	0.960
B2T2	Bottom	323	3038	0.999
	Upper	374	3229	1.004
B4T2	Bottom	348	3259	1.006
	Upper	359	3021	0.973
B6T2	Bottom	301	2767	0.961
	Upper	282	2867	0.950

Table 4.12 The microstructural properties of the samples prepared with dolomite.

Sample ID	Section	Average Number of Contact Points	Average Total Aggregate Surface Area (mm^2)	Average Thermal Conductivity, W/m.°C
D2T1	Bottom	514	3780	2.494
	Upper	426	3468	2.399
D4T1	Bottom	415	3418	2.414
	Upper	352	3430	2.346
D6T1	Bottom	402	3504	2.371
	Upper	330	3276	2.288
D2T2	Bottom	595	3407	2.364
	Upper	590	3421	2.242
D4T2	Bottom	530	3223	2.331
	Upper	518	3314	2.224
D6T2	Bottom	586	3311	2.175
	Upper	493	3079	2.101

Figure 4.24 and Figure 4.25 also graphically show the change in average thermal conductivity results with the average total aggregate surface area on the upper and bottom surfaces. The abbreviations 'B' and 'U' in these figures denote the bottom and upper parts, respectively. These figures indicate that samples with a larger aggregate surface area exhibit higher thermal conductivity. It means that the heat in the contact zone is mainly transferred by the aggregate particles rather than the other components. Consequently, in the TPS method, the aggregate particles predominantly determine the thermal conductivity of the samples.

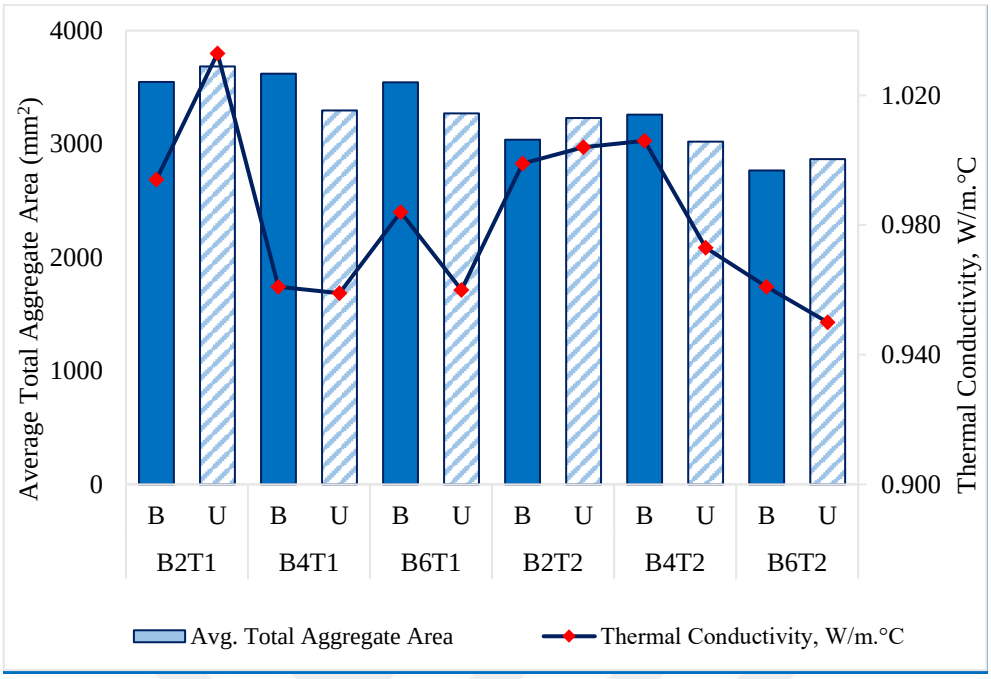


Figure 4.24 Relationship between thermal conductivity values and total aggregate area values of the samples prepared with basalt.

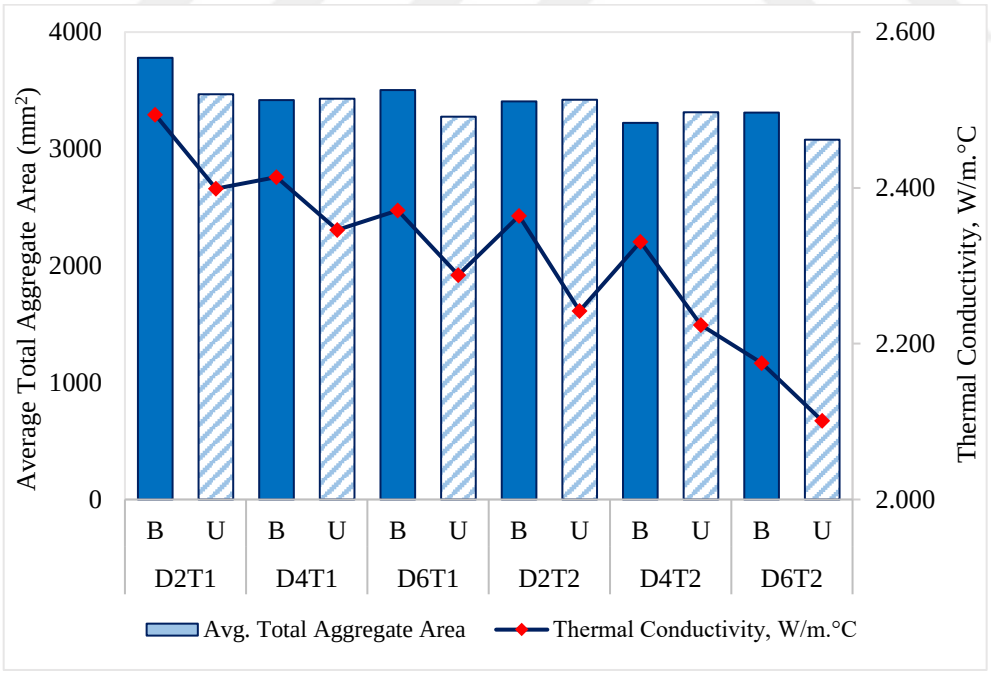


Figure 4.25 Relationship between thermal conductivity values and total aggregate area values of the samples prepared with dolomite.

4.3 Evaluation of Thermal Conductivity Results Using the Developed Steady-State Test Method

This section presents the results of thermal conductivity measurements obtained using the developed steady-state test setup in the laboratory. Before actual measurements on the asphalt concrete samples were taken, the test setup was calibrated to assess the reliability and accuracy of the proposed test setup. Thus, the initial measurements were conducted on materials with known thermal conductivities, namely Izocam foam board and autoclaved aerated concrete. During these calibration measurements, particular attention was paid to maintaining constant sample thickness and the temperatures of the hot and cold plates, as detailed in Table 4.13.

Table 4.13 Calibration coefficient of the test setup based on thermal conductivity results from Izocam Foam Board and Autoclaved Aerated Concrete samples.

Izocam Foam Board		
Actual Thermal Conductivity Value, W/m.°C	Measured Thermal Conductivity Value, W/m °C	Calibration Coefficient
0.035	0.038	**0.92**
Hot Plate Temperature at Steady-State: 47.2°C Cold Plate Temperature at Steady-State: 10.9°C Sample Thickness: 50 mm		
Autoclaved Aerated Concrete		
Actual Thermal Conductivity Value, W/m.°C	Measured Thermal Conductivity Value, W/m.°C	Calibration Coefficient
0.110	0.090	**1.22**
Hot Plate Temperature at Steady-State: 47.2°C Cold Plate Temperature at Steady-State: 10.8°C Sample Thickness: 50 mm		
Calibration Coefficient of Test Setup: 1.07 ± 0.15		

The calibration coefficients, the ratio between the actual and measured thermal conductivities, are calculated for each material. Subsequently, the calibration coefficient for the developed steady-state test setup is determined as the average of these individual coefficients. This average is 1.07, with an allowable variation of ± 0.15, as given in Table 4.13. Accordingly, the thermal conductivity of each asphalt concrete sample is determined by multiplying its measured thermal conductivity by the calibration coefficient.

In the developed steady-state test setup, thermal conductivity measurements were conducted on two replicates of the sample prepared from each mixture. It is important to note that each replicate is divided into two parts, as mentioned in Section 3.5.2.1. Therefore, four samples per mixture were tested to account for variations. To differentiate between the sliced samples, the terminology of the sample includes slice numbers designated as 01 and 02 for the first and second slices, respectively (e.g., B2T1-01 or B2T1-02).

As described in Section 3.5.2.3, temperature and heat flux changes were monitored until the temperature difference between the hot and cold plates stabilized. Based on this approach, the minimization of standard deviations between the measured thermal conductivities in this test setup indicates that the system has reached a steady state. In this study, the system consistently reached equilibrium within approximately 3 hours for all samples. Subsequently, average and calibrated thermal conductivities are determined at steady state and are presented in the tables below. Table 4.14 and Table 4.15 display the average thermal conductivity results of the samples prepared with basalt. Detailed information about the basalt samples, including their thicknesses, air void contents, temperature differences, and heat flux values, is provided in Appendix E. The thermal conductivities of the 24 sliced samples made with basalt were measured over a narrow range, from the lowest at 0.383 W/m.°C to the highest at 0.491 W/m.°C, regardless of variations in air voids and maximum aggregate sizes. Consequently, the calibrated thermal conductivities were calculated to be between 0.410 ± 0.15 and 0.526 ± 0.15 W/m.°C.

Table 4.14 Thermal conductivity results of the samples prepared with basalt (Replicate No: 1).

Sample ID Replicate No.1	Standard Deviation	Average Thermal Conductivity, W/m.°C	
		Measured	Calibrated
B2T1-01	0.005	0.422	0.452 ± 0.15
B2T1-02	0.005	0.415	0.444 ± 0.15
B4T1-01	0.007	0.455	0.487 ± 0.15
B4T1-02	0.005	0.425	0.454 ± 0.15
B6T1-01	0.008	0.427	0.457 ± 0.15
B6T1-02	0.006	0.425	0.455 ± 0.15
B2T2-01	0.006	0.432	0.462 ± 0.15
B2T2-02	0.007	0.427	0.457 ± 0.15
B4T2-01	0.007	0.440	0.471 ± 0.15
B4T2-02	0.006	0.434	0.464 ± 0.15
B6T2-01	0.006	0.456	0.488 ± 0.15
B6T2-02	0.005	0.441	0.472 ± 0.15

Table 4.15 Thermal conductivity results of the samples prepared with basalt (Replicate No: 2).

Sample ID Replicate No.2	Standard Deviation	Average Thermal Conductivity, W/m.°C	
		Measured	Calibrated
B2T1-01	0.006	0.422	0.452 ± 0.15
B2T1-02	0.009	0.433	0.463 ± 0.15
B4T1-01	0.006	0.437	0.467 ± 0.15
B4T1-02	0.008	0.428	0.458 ± 0.15
B6T1-01	0.012	0.491	0.526 ± 0.15
B6T1-02	0.005	0.406	0.434 ± 0.15
B2T2-01	0.006	0.417	0.446 ± 0.15
B2T2-02	0.006	0.383	0.410 ± 0.15
B4T2-01	0.008	0.416	0.445 ± 0.15
B4T2-02	0.006	0.408	0.436 ± 0.15
B6T2-01	0.005	0.451	0.483 ± 0.15
B6T2-02	0.005	0.395	0.423 ± 0.15

Following the thermal conductivity results for the basalt samples, Table 4.16 and Table 4.17 present the average and calibrated thermal conductivities of the samples prepared with dolomite. Similarly, detailed information about the dolomite samples, including their thicknesses, air void contents, temperature differences, and heat flux values, is provided in Appendix E. Upon analyzing the thermal conductivities of the 24 sliced samples made with dolomite, the measured values were found to range

from the lowest at 0.556 W/m.°C to the highest at 0.801 W/m.°C, regardless of differences in air voids and maximum aggregate sizes. As a result, the calibrated thermal conductivities were calculated to be between 0.594 ± 0.15 and 0.857 ± 0.15 W/m.°C.

Table 4.16 Thermal conductivity results of the samples prepared with dolomite (Replicate No: 1).

Sample ID Replicate No.1	**Standard Deviation**	**Average Thermal Conductivity, W/m.°C**	
		Measured	**Calibrated**
D2T1-01	0.007	0.556	0.594 ± 0.15
D2T1-02	0.007	0.566	0.606 ± 0.15
D4T1-01	0.006	0.579	0.619 ± 0.15
D4T1-02	0.008	0.649	0.694 ± 0.15
D6T1-01	0.012	0.608	0.651 ± 0.15
D6T1-02	0.009	0.644	0.689 ± 0.15
D2T2-01	0.008	0.558	0.597 ± 0.15
D2T2-02	0.011	0.614	0.657 ± 0.15
D4T2-01	0.009	0.707	0.757 ± 0.15
D4T2-02	0.016	0.655	0.701 ± 0.15
D6T2-01	0.009	0.695	0.744 ± 0.15
D6T2-02	0.007	0.668	0.715 ± 0.15

Table 4.17 Thermal conductivity results of the samples prepared with dolomite (Replicate No: 2).

Sample ID Replicate No.2	Standard Deviation	Average Thermal Conductivity, W/m.°C	
		Measured	Calibrated
D2T1-01	0.008	0.677	0.724 ± 0.15
D2T1-02	0.011	0.628	0.672 ± 0.15
D4T1-01	0.010	0.729	0.781 ± 0.15
D4T1-02	0.013	0.586	0.627 ± 0.15
D6T1-01	0.009	0.678	0.726 ± 0.15
D6T1-02	0.009	0.698	0.746 ± 0.15
D2T2-01	0.013	0.707	0.756 ± 0.15
D2T2-02	0.015	0.739	0.791 ± 0.15
D4T2-01	0.016	0.801	0.857 ± 0.15
D4T2-02	0.010	0.696	0.745 ± 0.15
D6T2-01	0.008	0.669	0.716 ± 0.15
D6T2-02	0.011	0.705	0.755 ± 0.15

4.3.1 Effect of Mix Properties on Thermal Conductivity

Based on the results presented in the previous section, this section explores the effects of mix properties on the thermal conductivity. It is first noticed that the relationship between differences in air void content and thermal conductivity is

variable. When comparing the thermal conductivities of B2T1-01 and B6T1-01 in replicate 1, they are observed to be almost the same (see Table 4.14). The thermal conductivity of B6T1-01 in replicate 2 is higher than that of B2T1-01 (see Table 4.15). Despite the increased air void content, there is almost no difference in the thermal conductivities of D2T1-01 and D6T1-01 in replicate 2, similar to those prepared with basalt (see Table 4.17). These results can be attributed to two main factors. Firstly, the samples were prepared with three air void contents that are relatively close to each other, representing the typical air void content of pavements in the field. Secondly, this experimental setup measured varying heat flux through the sample depth. For these reasons, the volumetric proportion of air throughout the sample depth is critical. Since there are no significant differences in air void content between the samples, the volumetric contribution of air to the total sample depth becomes relatively smaller. Hence, based on this method it is not possible to establish a strong correlation between thermal conductivities and air void contents.

It can also be observed that the thermal conductivity of samples produced with dolomite does not exhibit a relationship with the maximum aggregate size. For instance, the thermal conductivities of D4T1-02 and D4T2-02 in replicate 1 demonstrate a trend: the smaller the maximum aggregate size, the higher the thermal conductivity (see Table 4.16). However, the thermal conductivities of D6T1-01 and D6T2-01 in replicate 2 exhibit the opposite trend (see Table 4.17). Similarly, the effect of maximum aggregate size on thermal conductivity does not follow a linear pattern for the samples produced with basalt (See Table 4.14 and Table 4.15). The primary reason for this outcome is that, while the maximum aggregate sizes differ, the volumetric proportions of the aggregates in the mixtures do not vary significantly enough to cause a noticeable difference in the thermal conductivity results. Another factor is that the heat flux in the steady-state test method is unevenly distributed among the components of the mixture, particularly at the interfaces where aggregates and other components meet, as noted by Han et al. (2021).

In contrast to the effects of air void content and maximum aggregate size on thermal conductivity, it is determined that the type of aggregate significantly influences

thermal conductivities in the developed steady-state test setup. In this section, the analysis of variance (ANOVA) using the thermal conductivities of all samples (comprising a total of 48 samples produced from basalt and dolomite) is also presented to support the above discussions (see Table 4.18). The analysis confirms that the aggregate type is the most significant parameter. The analysis indicates that changes in air void content and maximum aggregate size do not significantly affect thermal conductivity. For the developed steady-state method, this outcome is primarily related to the volumetric representation of the mix components within the sample depth. Specifically, the uneven distribution of mix components at various depths causes fluctuations in the heat flux as measured by the heat flux meter. Consequently, this results in the effects of air void content and maximum aggregate size on thermal conductivity appearing less significant.

Table 4.18 The relationship between mix components and thermal conductivity in the steady state using ANOVA analysis.

Part	Source	Sum of Squares	Degrees of Freedom	Mean Square	F-ratio	P-value	Partial Eta Squared
All sliced samples	Air Void Content	0.082	30	0.003	1.474	0.215	0.747
	Maximum Aggregate Size	0.001	1	0.001	0.412	0.531	0.027
	Aggregate Type	0.110	1	0.110	59.208	0.000	0.798
	Total	17.092	48				
	Adjusted R^2= 0.897						

4.3.2 Relationship Between Heat Flux and Temperature Difference

In the developed steady-state test setup, heat flux was directly measured using the heat flux meter. However, fluctuations in heat flux occurred due to various factors such as changes in current or voltage, temperature differences, the nature of the sample surfaces, and the heterogeneous structure of the samples. As expected, these

fluctuations impacted the performance of the heat flux meter and the recorded heat fluxes. Consequently, the collected data set was processed using OriginPro 2023b (Learning Edition) software to enhance the presentation of the results. Then, curves of heat flux and thermal conductivity versus temperature differences were plotted and are presented below.

Since the behaviors of the heat flux and thermal conductivity curves did not vary significantly, only the first replications of the basalt and dolomite mixtures prepared with 4% air void content are presented in Figure 4.26 through Figure 4.33. All figures illustrate the heat flux and thermal conductivity change until the system reaches equilibrium. It is also seen that the maximum temperature difference at the time of equilibrium is about 28°C, as detailed in Appendix E. The heat flux and thermal conductivity curves of all mixtures are also available in Appendix F. It is observed that the heat flux and thermal conductivity curves exhibit similar behavior regardless of the differences in mix properties. This indicates that an increasing temperature difference causes an increase in both thermal conductivity and heat flux. This is expected, as heat flux is directly proportional to the temperature gradient and the material's thermal conductivity according to Fourier's law of heat conduction. Therefore, the sample's thermal conductivity increases at a constant depth and steady state with increasing heat flux.

Figure 4.26 through Figure 4.29 pertain to basalt samples with 4% air void contents and two different maximum aggregate sizes (B4T1-01, B4T1-02, B4T2-01, and B4T2-02). These figures show that the heat flux varies between 200 and 300 W/m², regardless of the difference in maximum aggregate size. Figure 4.30 through Figure 4.33 correspond to samples prepared with dolomite, featuring 4% air void contents and two maximum aggregate sizes (D4T1-01, D4T1-02, D4T2-01, and D4T2-02). These figures indicate that the heat flux ranges between 300 and 400 W/m², regardless of the difference in maximum aggregate size. Additionally, the heat fluxes for all samples can be found in Appendix E. The heat fluxes and, consequently, the thermal conductivities of samples prepared with dolomite are higher than those prepared with basalt, as illustrated graphically.

On the other hand, it is noticed that heat fluxes differed even between two nearly identical slices of the same Superpave sample. For example, while the heat flux of B6T1-01 is determined as 307.68 W/m^2, the heat flux of B6T1-02 is measured as 263.62 W/m^2. Like the basalt samples, the heat flux of D4T1-01 is obtained as 398.18 W/m^2, whereas the heat flux of D4T1-02 is 337.20 W/m^2. This variation directly results from the heat flux varying across the sample depth due to the high sensitivity of the heat flux meter. To give details, it can be attributed to the differences in the thermal conductivity of the mix components, the thermal resistance of the interfaces in the mix, and the different saturation states, etc.

The study also highlights the importance of various internal structural properties of sliced samples, including the varying distribution of aggregate particles along the sample depth, the volumetric percentage of mix components, and the interface between two components. When these properties vary within the asphalt concrete sample, this naturally leads to deviations, such as those observed in the heat fluxes and thermal conductivities. Therefore, these properties should be determined to discuss the macroscopic thermal performance of asphalt concrete. However, in this study, the defined internal structural properties of the samples could not be determined using the three-dimensional imaging technique due to the lack of an X-ray tomography device. However, claiming that only the internal structural features influence the heat flux deviations in the developed steady-state test setup would be inaccurate. It should be emphasized that stabilizing the experimental setup is also crucial to eliminate the deviations in the measured heat flux values under different conditions. In this context, the following section discusses the basic requirements that must be considered for the consistency of the developed steady-state test method.

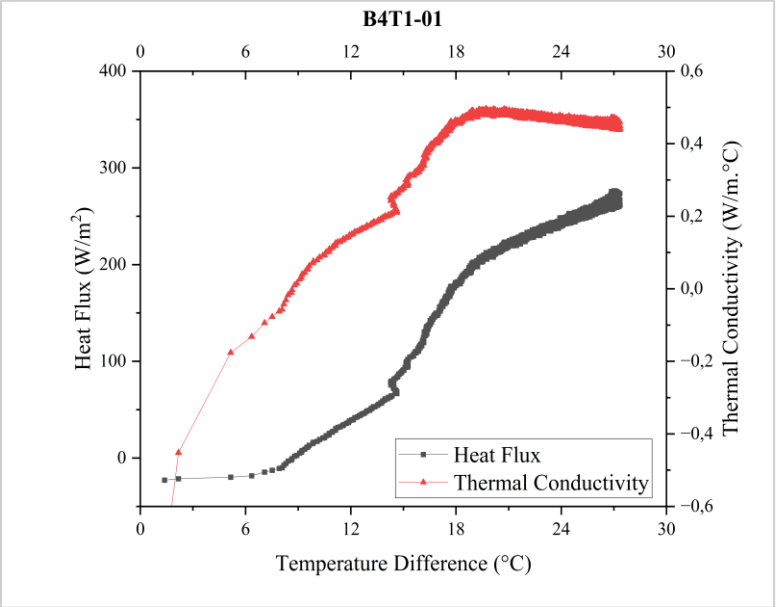


Figure 4.26 The change in heat flux and thermal conductivity values of the first slice of B4T1.

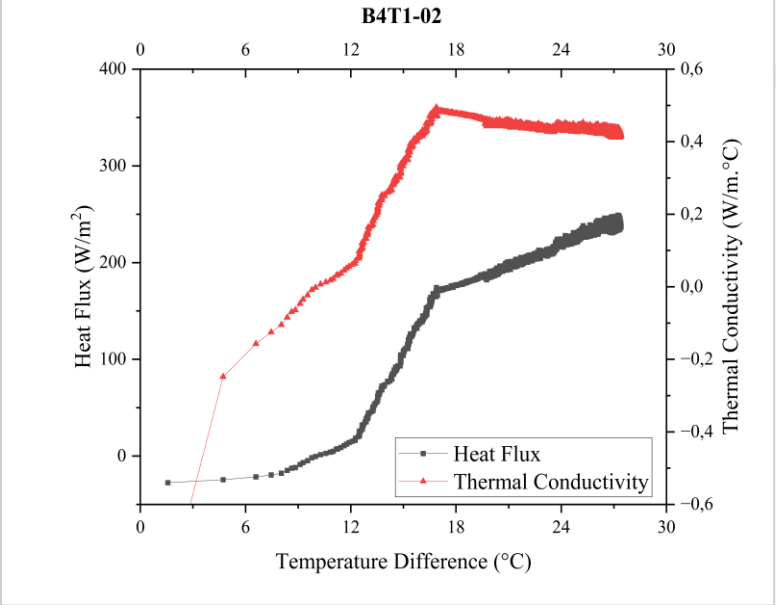


Figure 4.27 The change in heat flux and thermal conductivity values of the second slice of B4T1.

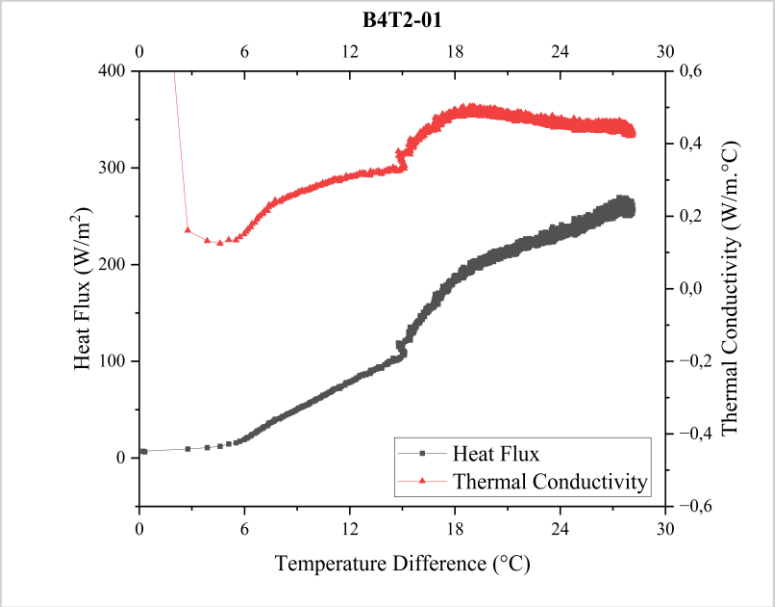


Figure 4.28 The change in heat flux and thermal conductivity values of the first slice of B4T2.

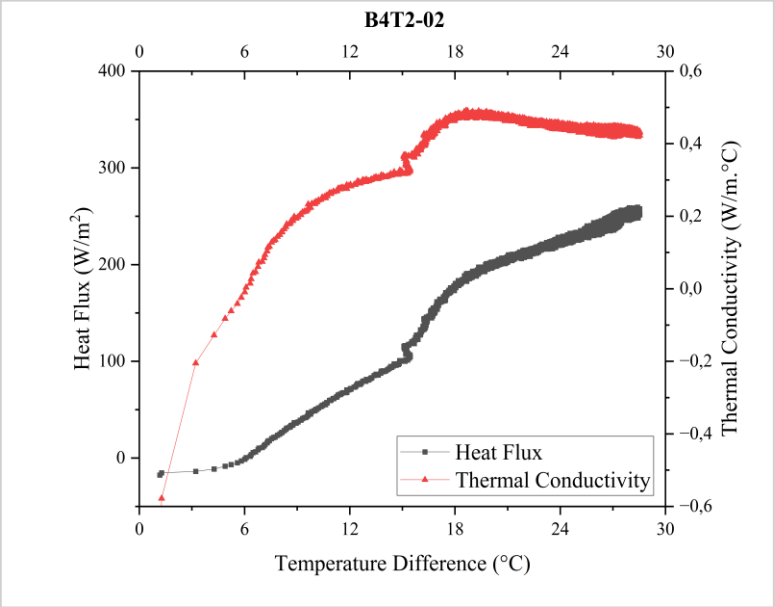


Figure 4.29 The change in heat flux and thermal conductivity values of the second slice of B4T2.

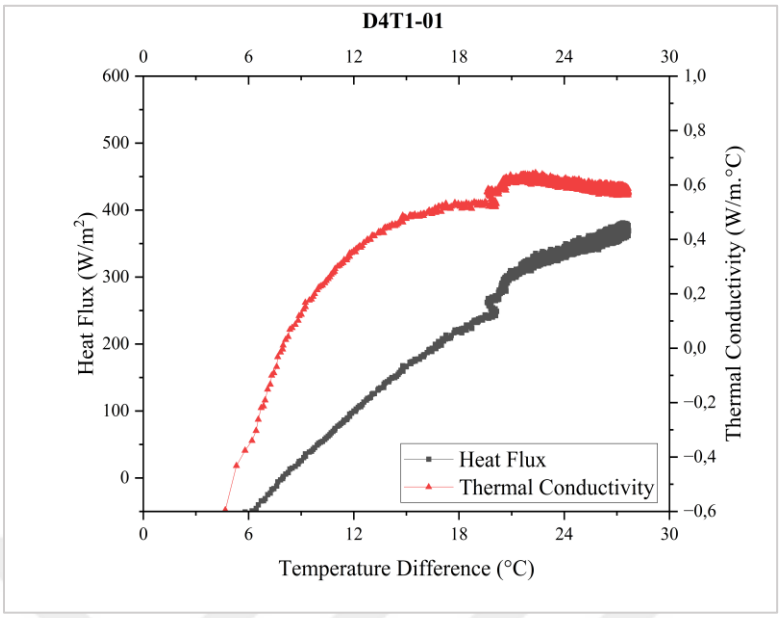


Figure 4.30 The change in heat flux and thermal conductivity values of the first slice of D4T1.

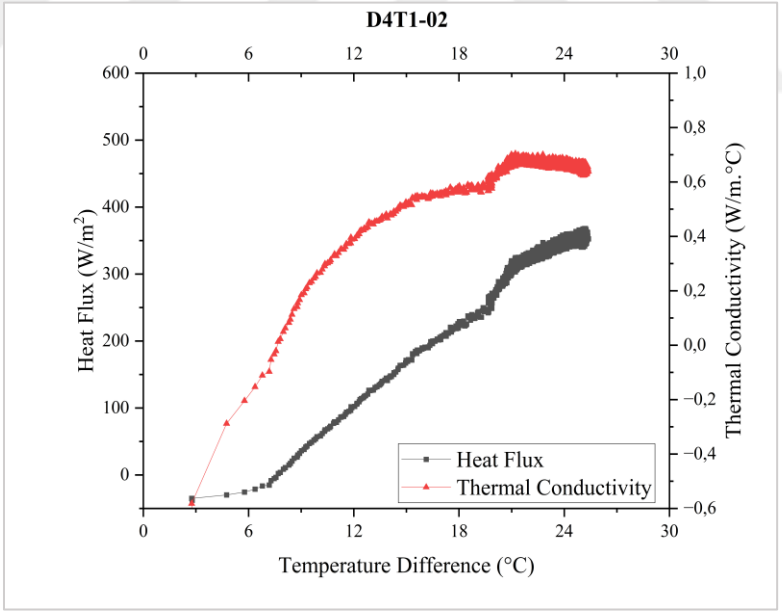


Figure 4.31 The change in heat flux and thermal conductivity values of the second slice of D4T1.

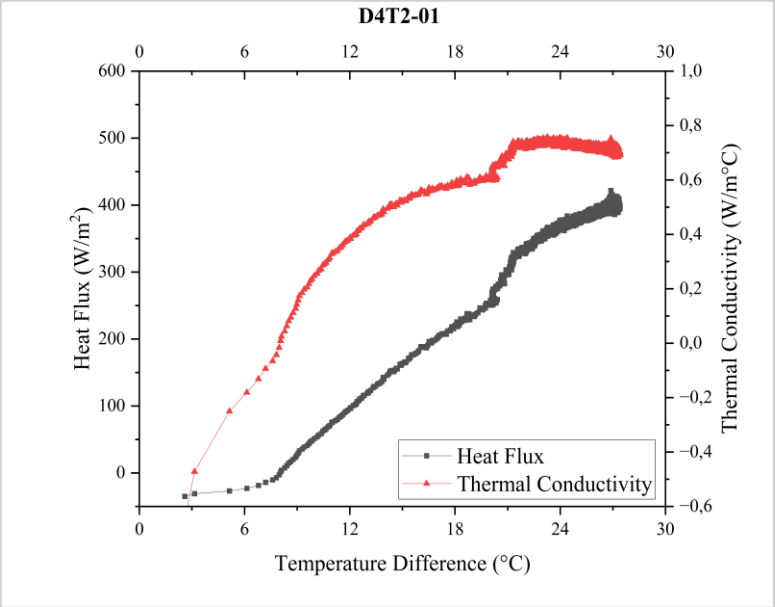


Figure 4.32 The change in heat flux and thermal conductivity values of the first slice of D4T2.

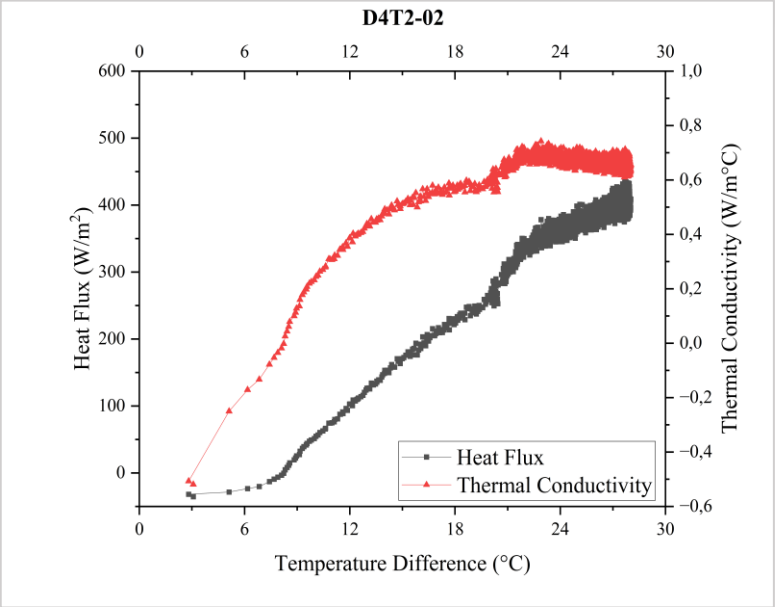


Figure 4.33 The change in heat flux and thermal conductivity values of the second slice of D4T2.

4.3.3 Parameters to Enhance the Reliability of the Developed Steady-State Test Setup

This study developed a reliable test method that minimizes potential deviations in heat flow, ensuring accurate thermal conductivity measurements in asphalt mixtures. Therefore, this section summarizes the key parameters necessary for implementing such a test method. ASTM C177-19 and ASTM C518-21 specify that the steady-state test method includes various components and procedures beyond its principal steps. In addition, measuring the thermal conductivity of asphalt concrete samples is complex due to their heterogeneous structure. Consequently, developing the steady-state test setup for this study was challenging. In this study, the primary purpose of the test design was to overcome the limitations identified in ASTM C177-19 and ASTM C518-21. Specifically, ensuring one-dimensional heat transfer in the asphalt concrete sample was foremost during the development of the proposed test method. Given the lack of a standard procedure for determining the thermal conductivity of asphalt mixtures, the parameters outlined in this section are critical for developing both a standardized test procedure and a reliable test method. Accordingly, some fundamental parameters are listed below:

- Initial temperature of hot and cold plates,
- Initial temperature of the asphalt concrete samples,
- Initial temperature of the test cabinet,
- Ambient temperature in the laboratory,
- Conditioning temperature of the test chamber and sample,
- Surface smoothness of the samples,
- Required sample thickness (as specified in ASTM C177-19),
- Test duration,

- Application and non-application of thermal paste on the measurement surfaces,
- Current and voltage fluctuations transferred to the hot and cold plates,
- Lateral heat losses from the test cabinet,
- Thermal insulation condition of the experimental setup,

The most critical among the above parameters is undoubtedly the temperature factor. Changes in temperature within the experimental setup, sample, and environmental conditions can cause significant differences in measurement results, as they directly impact the sensitivity of the heat flux meter. Besides the temperature factor, the other listed parameters are vital for stabilizing the heat flux meter and, thus, the experimental setup. In summary, test results become comparable when these parameters remain constant for each test.

4.4 Comparison of Steady-State and Transient Methods

This section compares the steady-state and transient methods used in this study. As presented in Table 4.19, the test duration is the most apparent difference between the methods. Accordingly, the TPS method had the shortest test duration. Another difference between the test methods is the sample size. In the steady-state methods, the sample size was determined by the limit specified in ASTM C177-19. However, in the TPS method, care was taken to make two identical samples that could fit in the sensor holder. Another critical difference is that steady-state methods monitored heat transfer throughout the sample depth. In contrast, in the TPS method, it was observed through the measurement depth of the TPS sensor.

In the calorimeter-based test method, temperature changes were monitored using RTD sensors placed in a hole at the center of the sample. The specific heat capacity was then calculated based on the sample's mass and the temperature difference. In the TPS method, the thermal conductivity measurement was confined to the diameter

of the TPS sensor and measured directly using the TPS sensor. Conversely, in the developed steady-state method, the measurement was limited to the sensing area of the heat flux meter. Like the TPS method, thermal conductivity was directly measured using the heat flux meter. Lastly, it is essential to note that the developed steady-state test setup was significantly more complex than the other methods, owing to its extensive test equipment and the complexity of the test procedures.

In addition to the differences mentioned above, Table 4.19 also details the mix properties that influence the measurement results. When measuring specific heat capacity and thermal conductivity using the calorimetry-based test method and the TPS method, these properties are significantly influenced by the aggregate type, air void content, and maximum aggregate size. However, in the developed steady-state method, only the aggregate type significantly affects the thermal conductivity, while air void content and maximum aggregate size seem less significant. A key conclusion of this study is that the impact of mixture properties on thermal conductivity varies depending on the measurement methods used. To clarify the effect of differences in measurement methods on thermal conductivity, this section also compares the thermal conductivities measured with the developed steady-state and TPS methods, as presented in Table 4.20.

Table 4.19 Comparison of test setups prepared based on selected test methods.

Parameters	**Steady-State Method**		**Transient Method**
	Calorimeter-Based Test Setup	**Developed Steady-State Test Setup**	**Hot Disk TPS 2500S Test Device**
Thermal Conductivity	×	✓	✓
Specific Heat Capacity	✓	×	×
Sample Material	Asphalt Concrete		
Sensor Type	Resistance Temperature Detector (RTD) sensors	FluxTeq Ultra-09 Plate Heat Flux Sensor (PHFS) Total Sensor Dimensions: width: 9.2 cm, height: 8.7 cm	TPS Sensor ID: 5501, a sensor with a diameter of 12.8 mm
Test Duration	approx. 30 minutes	approx. 3 hours	approx. 5-10 seconds
Sample Size	Diameter: 15 cm, Thickness: ± 5 cm Two identical sliced samples	Diameter: 15 cm, Thickness: ± 5 cm Two identical sliced samples	Diameter: 10 cm, Thickness: ± 2.5 cm Three identical cored and sliced samples
Heat Transfer	Through the sample depth	Through the sample depth	Through the probing depth
Effect of Aggregate Type	✓	✓	✓
Effect of Air Void Content	✓	Not exactly	✓
Effect of Maximum Aggregate Size	✓	Not exactly	✓
Effect of Initial Temperature of the Samples	✓	✓	✓
Effect of Ambient Temperature	✓	✓	✓
Complexity Level of The Test Setup	Medium	High	Low

Table 4.20 shows that samples from the same components exhibit different thermal conductivities due to varied measurement methods. It indicates that the thermal conductivities determined by the TPS method are higher than those determined by the developed steady-state method. This result stems from the microstructural properties of the contact zone. When the TPS measurement is conducted on a contact zone with a high proportion of aggregate particles, the sample's thermal conductivity approaches that of the aggregate, known for its high thermal conductivity. Besides the aggregate type, properties like air void content and maximum aggregate size also influence thermal properties, as they alter the microstructural properties of the contact zone.

Table 4.20 Comparison of thermal conductivity results taken from the Hot Disk TPS 2500S test device and the developed steady-state test setup.

Tests	**Hot Disk TPS 2500S Test Device Results**	**Developed Steady-State Test Setup Results**
Sample ID	**Total Sample-Average Thermal Conductivity, W/m.°C**	**Total Sample-Average Thermal Conductivity, W/m.°C**
B2T1	1.013	0.419
B4T1	0.960	0.440
B6T1	0.972	0.426
B2T2	1.002	0.429
B4T2	0.989	0.437
B6T2	0.955	0.448
D2T1	2.447	0.561
D4T1	2.380	0.614
D6T1	2.330	0.626
D2T2	2.303	0.586
D4T2	2.277	0.681
D6T2	2.138	0.681

The TPS method limits the measurement area by the sensor's contact zone and probing depth. As a result, asphalt concrete samples are not tested throughout their depth, making it challenging to assert that the measured thermal conductivities represent the whole sample. Therefore, whether the TPS method is suitable for determining the thermal properties of heterogeneous materials like asphalt concrete remains debatable.

In contrast to the measurement approach of the TPS method, heat is transferred along the sample depth in the developed steady-state test method. Thus, deviations in heat fluxes and thermal conductivities are expected to be experienced due to the uneven distribution of the main constituents throughout the sample depth. In particular, the thermal conductivity of the aggregate is the highest among the other mix components, and the heat flux density between the adjacent aggregates is more intense. As a result, only the aggregate significantly affects the thermal conductivity of the samples when tested under steady-state conditions. However, the irregular distribution of the aggregate particles leads to deviations in the heat fluxes within the mixtures. Hence, these fluctuations lead to variations and reduce the heat flux density of the mixture. Therefore, it is believed that the thermal conductivities measured with the developed steady-state method are lower; yet seem to be more realistic than the measurements made with the TPS method. This indicates the importance of selecting an appropriate test method to measure the thermal properties of asphalt concrete if reliable measurements are demanded.

CHAPTER 5

CONCLUSION AND RECOMMENDATION

5.1 Conclusion

In this study, several methods for measuring the thermal properties of asphalt concrete are proposed. The study has two main objectives: The first is to develop a suitable and applicable test setup for measuring the thermal properties of asphalt concrete. The second is to evaluate the mixture properties that influence these properties and to compare the measurement methods in terms of reliability and accuracy. In this context, the results of specific heat capacity and thermal conductivity determined by the steady-state method are discussed, taking into account the effects of mixture constituents. The thermal conductivity values measured with the TPS method, and the effects of the mixture components are also evaluated. Finally, the two methods used are compared based on the test results. In the following sections, the results of the individual tests are comprehensively evaluated.

The following conclusions can be drawn from the measurement of specific heat capacity using the calorimetry-based test setup:

1. The results of the calorimetric test setup show that the specific heat capacity of asphalt concrete is directly related to the heat storage capacity of the individual mixture components. In addition, denser mixtures, which have more mass per unit volume, have a higher heat storage capacity. From this, it can be concluded that each mixture component that influences the density of the asphalt mixture also influences its specific heat capacity. Accordingly, it can be stated that high air void content not only reduces the specific gravity as it causes a loose structure but also diminishes the specific heat capacity.

2. The mineralogical origin of the aggregate has a direct effect on the specific heat capacity of the asphalt mixture. The X-ray powder diffraction analysis performed shows that dolomite contains more quartz minerals. As described in the literature, quartz has a higher specific heat capacity than the mixture due to its dense mineral structure. Therefore, the specific heat capacities of asphalt mixtures produced from dolomite are expected to be higher than those of basalt.
3. The specific heat capacity of air is significantly lower than that of solid components of asphalt mixtures, including bitumen and aggregates ($\lambda_{air} \approx$ 0.024 W/m.°C, reported by Côté et al., 2013). Therefore, if there are more air voids in the mixture, the percentage of material with a lower specific heat capacity is higher, and thus the overall specific heat capacity of asphalt mixtures decreases.
4. The specific heat capacity of bitumen is higher than that of air, but lower than that of aggregates in the asphalt mixture ($\lambda_{bitumen} \approx 0.17$ W/m.°C). In addition, bitumen is an important component instead of air, as it acts as a thermal bridge between the aggregates during heat transfer. However, if the air void content in the mixture remains constant, as in this study, the specific heat capacity of the mixture decreases when the optimum bitumen content increases, as bitumen has a lower specific heat capacity compared to the aggregates.
5. The relationship between maximum aggregate size and specific heat capacity of mixtures should be carefully investigated. The results show that the dolomite samples produced with coarse gradation (MAS: 19 mm) have a significantly higher specific heat capacity and also a higher specific gravity compared to basalt samples. This may be due to the different water absorption capacities of basalt and dolomite aggregates and, thus the percentage of binder absorption.
6. The results of the calorimetry-based test method show that the conditioning temperature of the samples has a significant influence on the specific heat

capacity. The conditioning temperature has a direct effect on the temperature difference, which is defined as the driving force in the heat transfer mechanism. The test results show that the specific heat capacity of the samples increases significantly with increasing conditioning temperature. This is to be expected since a higher initial temperature leads to greater kinetic energy required to increase the temperature of the sample by 1°C.

7. Based on the time-temperature curves obtained from the calorimetry-based test setup, it can be concluded that the samples produced with dolomite react more sensitively to temperature changes than the basalt samples. This is because the samples made with dolomite reach equilibrium more quickly than those made with basalt. This result also reflects the thermal behavior of the aggregate and, thus the thermal behavior of the asphalt concrete samples. This finding is particularly important for solving critical thermally induced problems such as rutting and cracking at low temperatures during the service life of the pavement.
8. In conclusion, the calorimetry-based test setup developed in this study performs well in measuring the specific heat capacity of asphalt concrete as the results produced for asphalt concrete are within the ranges of specific heat capacity reported in the literature.

The results obtained with the TPS method for measuring the thermal conductivity of samples lead to the following conclusions:

1. In the TPS measurements, the type of aggregate has the greatest influence on the thermal conductivity of asphalt concrete, which is confirmed by the ANOVA analysis. In this study, the thermal conductivities of the two aggregates are measured individually to illustrate this effect. The results show that the thermal conductivity of dolomite is higher than that of basalt, and this correlation also applies to the mixtures. The test results show that the average thermal conductivities of the samples made with dolomite are almost twice as high as those made with basalt, regardless of the variations in air void content and maximum particle sizes.

2. Based on the results of the TPS measurements, there is a clear trend towards a decrease in thermal conductivity with increasing air void content. This is because air voids have the lowest thermal conductivity among the mix constituents in the contact zone, which hinders heat transfer between the aggregates and reduces the overall thermal conductivity.
3. Considering the relationship between the average thermal conductivities obtained from the TPS measurement and the volumetric parameters of the mixtures, the thermal conductivities are inversely proportional to VMA and V_a, even if the type of aggregates and the maximum size of the aggregates are different. On the other hand, it can be seen that the average thermal conductivities are generally high for samples with high VFA. This is because the voids are filled with bitumen, which has a higher thermal conductivity than air voids.
4. The density of the asphalt mixture is defined as a key parameter to evaluate the average thermal conductivities of the samples in the TPS measurements. As already mentioned in the results of the calorimetry-based test method, the density is directly related to the components of the asphalt mixture and the degree of compaction. The higher the density of the samples, the higher the thermal conductivity, as the aggregate structure of the asphalt mixture is improved.
5. The maximum aggregate size has a direct influence on the optimum bitumen content, the air void content, the degree of compaction, and thus the density of asphalt mixtures. In this study, it was found that asphalt mixtures with larger maximum aggregate sizes generally have a higher thermal conductivity. This result can also be linked to the optimum bitumen content. This is because the average thermal conductivity of the samples produced with coarse gradation (MAS: 19 mm) remains slightly higher than that of the samples produced with fine gradation (MAS: 12.5 mm) due to their lower optimum bitumen content, especially for the samples produced with dolomite. However, this can also be attributed to the fact that the probability

of the TPS sensor coming into contact with other components, such as bitumen and air, decreases as the maximum aggregate size increases. In other words, as the proportion of coarse aggregate increases, the TPS sensor encounters aggregate with high thermal conductivity at the contact points and takes measurements, thereby increasing the thermal conductivity of the mixture.

6. In the TPS method, it is not only the mixture components but also the parameters associated with the test procedures, such as heating power, test duration, and sensor sizes used, that are decisive for the reliability and accuracy of the results. The selection and application of these parameters are at least as important for the results as the effect of the mixture components. It should be noted that these parameters are even more critical for heterogeneous structures, as the deviation in these parameters is relatively small for homogeneous materials. This is because the contact area of the TPS sensor with different components simultaneously leads to variations in the thermal resistance of the TPS sensor.
7. With the TPS measurements, the correct interpretation of the results also depends heavily on the microstructural properties of the contact zone. In particular, the distribution and total area of the mixture components (air voids, bitumen, and aggregates) in the contact zone are very important. In this context, image analysis with iPas software is preferred to determine the microstructural properties and to understand their impact on the thermal properties.
8. The result of the image analysis shows that the distribution of the aggregates, the number of contact points, and the total area of the aggregate have a considerable influence on the thermal conductivity of asphalt mixtures. As the aggregate has a higher thermal conductivity than the mixtures, the samples with a larger area of aggregate in the cross-sections also tend to have a higher thermal conductivity, which facilitates heat transfer within the sample. It was also found that an increase in the number of contact points

indicates a higher percentage of finer aggregates distributed on the measured surface. If the TPS sensor comes into contact with bitumen, aggregates, and/or air voids at the same time, the heat transfer is interrupted, and thus the thermal conductivity of the mixture is reduced.

9. In addition to the microstructural properties of the aggregate particles on the contact zone, it should also be noted that the uneven distribution of air voids on the contact zone leads to a weakening of the heat flow between the components and, thus to deviations in the measurement reliability of the TPS sensor. On the one hand, this result can be seen as a limitation of the sensor-based measurement approach in the TPS method. On the other hand, the TPS sensor can interact directly with the mixture components via the contact zone, so that the effects of these components on the thermal conductivity can be recorded. However, it should be noted that the thermal conductivity is not measured for the entire sample thickness but is only effective for the contact zone on which the sensor measures and the probing depth into which it penetrates. Therefore, the applicability of the TPS method for asphalt concrete is controversial.

Finally, the following conclusions are drawn based on the results of the developed steady-state test setup:

1. The results of the developed steady-state test setup show that the effect of aggregate type on thermal conductivity is quite significant. The ANOVA analysis also confirms that the type of aggregate is the only parameter that influences the thermal conductivity of asphalt concrete samples.
2. The air void contents of 2%, 4%, and 6% originally determined in the production of asphalt mixtures changed due to the cutting process used in the sample preparation process. In fact, the difference in air void content was significantly reduced to less than 1% between some of the test samples. As a result, the influence of air voids was not clearly established in the statistical analyses due to the small variation in air voids and appears to be an insignificant variable for thermal conductivity. However, this result

contradicts the existing literature as the reported values were measured using the TPS method for samples prepared with large air void variations. It should be emphasized that the TPS method measures the thermal properties only at the contact zone, where small variations in the mixture constituents become important, whereas the steady-state methods measure the properties over the entire sample volume. As the volume fractions of the mix constituents become smaller, their relative influence on the thermal properties becomes insignificant. Since the aggregates have the highest volume fraction in the mix, their influence on the thermal properties is stronger than that of air voids and bitumen, which comprises around 3% to 6% of the mix volume.

3. Similar to the effect of air voids, a change in maximum aggregate size does not lead to a change in thermal conductivity when measured under steady-state conditions. However, the effect of maximum aggregate size on thermal conductivity has not been clearly explained in the literature based on the steady-state measurement methods. The reason for this is the difficulty in controlling the transition of heat flux through the sample thickness, the lack of measurement accuracy, and the significant heat losses between the components of the test setup.
4. Once the heat transfer between the hot and cold plates has reached a steady-state condition, the thermal conductivity can be calculated directly from the heat flux measured by the heat flux sensor. However, it should be emphasized that the reliability of the measurements is highly dependent on how well the sensor and the test setup are calibrated together before the actual measurements begin.
5. Based on the relationship between heat flux/thermal conductivity and temperature difference, the increase in the temperature gradient between the hot and cold plate leads to an increase in the rate of heat flux regardless of the differences in the mix constituents. According to Fourier's law of heat conduction, the heat flux is directly proportional to the temperature gradient and the thermal conductivity of the material. It is, therefore, to be expected

that the thermal conductivity of the sample will increase as the heat flux through the thickness of the sample increases.

6. The results of the data analysis showed that the stability of the experimental setup and the accuracy of the measurements of heat flux, temperature, and specimen thickness are important factors influencing the reliability of the measured thermal properties, especially under state-state conditions. During the tests, it was found that the variability of the measured heat flux and, thus thermal conductivity is mainly due to current/voltage fluctuations, changes in ambient temperature, stability of the power source used to generate current, inappropriate sample thickness, poor contact between the sample and the hot/cold plates, insufficient insulation and test duration, and unstable environmental conditions, etc.
7. To compare the two methods used in this study, it is obvious that the TPS method has a shorter test duration than the steady-state method. Besides, the test setup for the TPS method is less complicated than the developed steady-state test setup. Another difference is that the specimen dimension varies, while a larger specimen can be used in the steady-state method, a much smaller specimen must be used because of the size requirements of the TPS method.
8. The results of this study indicate that the TPS method is not suitable for measuring the thermal conductivity of heterogeneous materials, such as asphalt mixtures, because the TPS sensor only measures the thermal conductivity around the contact zone and not through the entire sample. It can be concluded that the results of the developed steady-state test method can better represent the thermal conductivity of the asphalt concrete samples given the variations in the mix constituents.

5.2 Recommendations For Future Studies

The following recommendations for further studies are derived from the results of this study:

- The measurement methods used in this study and the potential effects of mixture properties on thermal properties provide valuable information for identifying and solving future thermal-related problems.
- The findings from the experimental methods developed in this study can be used as key inputs to create estimation models based on the thermal performance of asphalt concrete pavements. In particular, modeling the heat flux and thermal conductivity at the interface between each component is critical and recommended if the internal structural properties of the mixture are defined throughout the sample depth.
- The study emphasizes that the internal structural properties of the mixture influence the thermal conductivity, especially when measured under steady-state conditions. Because it is costly, X-ray tomography imaging could not be used to model the internal structure of asphalt concrete samples. The development of a suitable experimental setup to measure the microstructural properties will be helpful to better understand the mechanism of heat transfer in asphalt concrete.

REFERENCE

AASHTO M323-07. (2010). Superpave Volumetric Mix Design. In *Standard Specifications for Transportation Materials and Methods of Sampling and Testing (Part 1A Specifications)*, Thirtieth Edition. AASHTO, Washington D.C.

AASHTO R35-09. (2010). Superpave Volumetric Design for Hot Mix Asphalt (HMA). In *Standard Specifications for Transportation Materials and Methods of Sampling and Testing (Part 1A Specifications),* Thirtieth Edition. AASHTO, Washington D.C.

AASHTO T100-06. (2010). Specific Gravity of Soils. In *Standard Specifications for Transportation Materials and Methods of Sampling and Testing (Part 1A Specifications)*, Thirtieth Edition. AASHTO, Washington D.C.

AASHTO T166-10. (2010). Bulk Specific Gravity of Compacted Hot Mix Asphalt (HMA) Using Saturated Surface-Dry Specimens. In *Standard Specifications for Transportation Materials and Methods of Sampling and Testing (Part 1A Specifications)*, Thirtieth Edition. AASHTO, Washington D.C.

AASHTO T209-10. (2010). Theoretical Maximum Specific Gravity and Density of Hot Mix Asphalt (HMA). In *Standard Specifications for Transportation Materials and Methods of Sampling and Testing (Part 1A Specifications)*, Thirtieth Edition. AASHTO, Washington D.C.

AASHTO T316-10. (2010). Viscosity Determination of Asphalt Binder Using Rotational Viscometer. In *Standard Specifications for Transportation Materials and Methods of Sampling and Testing (Part 1A Specifications)*, Thirtieth Edition. AASHTO, Washington D.C.

AASHTO T84-10. (2010). Specific Gravity and Absorption of Fine Aggregate. In *Standard Specifications for Transportation Materials and Methods of Sampling and Testing (Part 1A Specifications)*, Thirtieth Edition. AASHTO, Washington D.C.

AASHTO T85-10. (2010). Specific Gravity and Absorption of Coarse Aggregate. In *Standard Specifications for Transportation Materials and Methods of Sampling and Testing (Part 1A Specifications)*, Thirtieth Edition. AASHTO, Washington D.C.

AASHTO T96-02. (2010). Resistance to Degradation of Small-Size Coarse Aggregate by Abrasion and Impact in the Los Angeles Machine. In *Standard Specifications for Transportation Materials and Methods of Sampling and Testing (Part 1A Specifications)*, Thirtieth Edition. AASHTO, Washington D.C.

Abbas, F. A., & Alhamdo, M. H. (2023). Enhancing the thermal conductivity of hot-mix asphalt. *Results in Engineering, 17*, 100827.

Adkins, D. F., & Merkley, G. P. (1990). Mathematical Model of Temperature Changes in Concrete Pavements. *Journal of Transportation Engineering*, *116*(3), 349–358.

Aletba, S.R.O., Hassan, N.A., Jaya, R.P., Aminudin, E., Mahmud, M.Z.H., Mohamed, A., Hussein, A.A. (2021). Thermal performance of cooling strategies for asphalt pavement: A state-of-the-art review. *Journal of Traffic and Transportation Engineering*, *8*(3), 356–373.

Andolfsson, T. (2013). *Analyses of thermal conductivity from mineral composition and analyses by use of Thermal Conductivity Scanner : a study of thermal properties of Scanian rock types* (Dissertations in Geology at Lund University).

Annaratone, D. (2010). Engineering Heat Transfer. In Springer eBooks. https://doi.org/10.1007/978-3-642-03932-4.

Assael, M. J., Karagiannidis, L., Malamataris, N., & Wakeham, W. A. (1998). The Transient Hot-Wire Technique: A Numerical Approach. *International Journal of Thermophysics*, *19*(2), 379-389.

ASTM C1045-19. (2019). *Standard Practice for Calculating Thermal Transmission Properties Under Steady-State Conditions*. ASTM International, West Conshohocken, PA.

ASTM C1058-10. (2015). *Standard Practice for Selecting Temperatures for Evaluating and Reporting Thermal Properties of Thermal Insulation.* ASTM International, West Conshohocken, PA.

ASTM C177-19. (2023). *Standard Test Method for Steady-State Heat Flux Measurements and Thermal Transmission Properties by Means of the Guarded-Hot-Plate Apparatus*. ASTM International, West Conshohocken, PA.

ASTM C518-21. (2021). *Standard Test Method for Steady-State Thermal Transmission Properties by Means of the Heat Flow Meter Apparatus*. ASTM International, West Conshohocken, PA.

ASTM D2493-16. (2017). *Standard Practice for Viscosity-Temperature Chart for Asphalt Binders*. ASTM International, West Conshohocken, PA.

ASTM D5334-22. (2022). *Standard Test Method for Determination of Thermal Conductivity of Soil and Rock by Thermal Needle Probe Procedure*. ASTM International, West Conshohocken, PA.

ASTM D5930-17. (2017). *Standard Test Method for Thermal Conductivity of Plastics by Means of a Transient Line-Source Technique*. ASTM International, West Conshohocken, PA.

ASTM D7984-21. (2021). *Standard Test Method for Measurement of Thermal Effusivity of Fabrics Using a Modified Transient Plane Source (MTPS) Instrument*. ASTM International, West Conshohocken, PA.

ASTM E473-16. (2019). *Standard Terminology Relating to Thermal Analysis and Rheology.* ASTM International, West Conshohocken, PA.

Ayasrah, U. B., Tashman, L., AlOmari, A., & Asi, I. (2023). Development of a Temperature Prediction Model for Flexible Pavement Structures. *Case Studies in Construction Materials*, *18*, e01697.

Bai, B. C., Park, D. W., Vo, H. V., Dessouky, S., & Im, J. S. (2015). Thermal Properties of Asphalt Mixtures Modified with Conductive Fillers. *Journal of Nanomaterials*, *2015*.

Basheer Sheeba, J., & Krishnan Rohini, A. (2014). Structural and Thermal Analysis of Asphalt Solar Collector Using Finite Element Method. *Journal of Energy*, *2014*, 1–9. https://doi.org/10.1155/2014/602087.

Bateman, R., Harris, A., Lee, L., Howle, C. R., & Ackermann, S. L. (2016). Application of the Modified Transient Plane Source Technique for Early Detection of Liquid Explosives. *Chemical, Biological, Radiological, Nuclear, and Explosives (CBRNE) Sensing XVII*, *9824*, 98-112.

Boháč, V. (2017, May). Thermal properties of materials and their characterization by classic and transient methods. *11th International Conference on Measurement*, pp. 53-62.

Bouguerra, A., Aït-Mokhtar, A., Amiri, O., & Diop, M. B. (2001). Measurement of thermal conductivity, thermal diffusivity and heat capacity of highly porous building materials using transient plane source technique. *International Communications in Heat and Mass Transfer*, *28*(8), 1065-1078.

Bulatović, V., & Malešev, M. Properties of building materials at elevated temperatures. *Fire Safety in Buildings*, *44*.

Byzyka, J., Rahman, M., & Chamberlain, D. A. (2021). A Laboratory İnvestigation on Thermal Properties of Virgin and Aged Asphalt Mixture. *Construction and Building Materials, 305*, 124757.

Calkins, M., 2012. *The Sustainable Sites Handbook: A Complete Guide to the Principles, Strategies, and Best Practices for Sustainable Landscapes*. John Wiley & Sons, Hoboken, New Jersey, USA.

Carlson, J. D., Bhardwaj, R., Phelan, P. E., Kaloush, K. E., & Golden, J. S. (2010). Determining Thermal Conductivity of Paving Materials Using Cylindrical Sample Geometry. *Journal of materials in civil engineering*, *22*(2), 186-195.

Carotenuto, G. B. A. (2000). The Effective Thermal Conductivity of Packed Beds of Spheres for A Finite Contact Area. *Numerical Heat Transfer: Part A: Applications*, *37*(4), 343-357.

Cengel, Y. A. (2003). *Heat Transfer: A Practical Approach*. McGraw-Hill Science, New York.

Ceylan, H., Coree, B., & Gopalakrishnan, K. (2009). Evaluation of The Mechanistic-Empirical Pavement Design Guide For İmplementation in Iowa. *The Baltic Journal of Road and Bridge Engineering*, *4*(1), 5-12.

Chen, G. (2005). *Nanoscale Energy Transport and Conversion: A Parallel Treatment of Electrons, Molecules, Phonons, And Photons*. Oxford University Press.

Chen, J., Chen, X., Dan, H., & Zhang, L. (2022a). Combined prediction method for thermal conductivity of asphalt concrete based on meso-structure and renormalization technology. *Applied Sciences*, *12*(2), 857.

Chen, J., Wang, H., & Li, L. (2015a). Determination of effective thermal conductivity of asphalt concrete with random aggregate microstructure. *Journal of Materials in Civil Engineering*, *27*(12), 04015045.

Chen, J., Wang, H., & Xie, P. (2019). Pavement temperature prediction: Theoretical models and critical affecting factors. *Applied Thermal Engineering, 158*, 113755.

Chen, J., Zhang, M., Wang, H., & Li, L. (2015b). Evaluation of thermal conductivity of asphalt concrete with heterogeneous microstructure. *Applied Thermal Engineering*, *84*, 368-374.

Chen, X., Wang, H., Jiang, B., & Venkiteela, G. (2022b). Evaluation of microwave heating for potential applications in hot in-place recycling of asphalt pavement. *Transportation Research Record*, *2676*(9), 256-268.

Chiarelli, A., Dawson, A. R., & Garcia, A. (2017). Field evaluation of the effects of air convection in energy harvesting asphalt pavements. *Sustainable Energy Technologies and Assessments, 21*, 50-58.

Chu, L., He, L., & Fwa, T. F. (2020). Determination of thermal conductivity of asphalt paving mixtures using finite element method. *Construction and Building Materials*, *243*, 118250.

Clauser, C., & Huenges, E. (1995). Thermal conductivity of rocks and minerals. *Rock physics and phase relations: a handbook of physical constants*, *3*, 105-126.

Concha, J. L., & Norambuena-Contreras, J. (2020). Thermophysical properties and heating performance of self-healing asphalt mixture with fibres and its application as a solar collector. *Applied Thermal Engineering*, *178*, 115632.

Coree, B., & Hislop, W. P. (2000). *A laboratory investigation into the effects of aggregate-related factors of critical VMA in asphalt paving mixtures* (No. IDOT TR-415). Iowa State University. Center for Transportation Research and Education.

Corlew, J. S. (1968). *Methods for calculating temperature profiles of hot-mix asphalt concrete as related to the construction of asphalt pavements* (1960-1969-Mines Theses & Dissertations).

Côté, J., & Konrad, J. M. (2005). Thermal conductivity of base-course materials. *Canadian Geotechnical Journal*, *42*(1), 61-78.

Côté, J., Grosjean, V., & Konrad, J. M. (2013). Thermal conductivity of bitumen concrete. *Canadian Journal of Civil Engineering*, *40*(2), 172-180.

Danley, R. L. (2002). New heat flux DSC measurement technique. *Thermochimica acta*, *395*(1-2), 201-208.

Dawson, A. R., Dehdezi, P. K., Hall, M. R., Wang, J., & Isola, R. (2012). Enhancing thermal properties of asphalt materials for heat storage and transfer applications. *Road Materials and Pavement Design, 13*(4), 784-803.

Dos Santos, W. N., & Gregório, R. (2003). Numerical and experimental determination of the minimum and maximum measuring times for the hot wire parallel technique. *Cerâmica*, *49*, 29-35.

Elkashef, M., Elwardany, M. D., Liang, Y., Jones, D., Harvey, J., Bolton, N. D., & Planche, J. P. (2020). Effect of using rejuvenators on the chemical, thermal, and rheological properties of asphalt binders. Energy & Fuels, 34(2), 2152-2159.

Elkholy, A., Sadek, H., & Kempers, R. (2019). An improved transient plane source technique and methodology for measuring the thermal properties of anisotropic materials. *International Journal of Thermal Sciences*, *135*, 362-374.

Franco, A. (2007). An apparatus for the routine measurement of thermal conductivity of materials for building application based on a transient hot-wire method. *Applied Thermal Engineering*, *27*(14-15), 2495-2504.

Gao, L., Wang, Z., Xie, J., Liu, Y., & Jia, S. (2019). Simulation of the cooling effect of porous asphalt pavement with different air voids. *Applied Sciences*, *9*(18), 3659.

García, A., Norambuena-Contreras, J., & Partl, M. N. (2013). Experimental evaluation of dense asphalt concrete properties for induction heating purposes. *Construction and Building Materials*, *46*, 48-54.

Gill, P. S., Sauerbrunn, S. R., & Reading, M. (1993). Modulated differential scanning calorimetry. *Journal of thermal analysis*, *40*, 931-939.

Gist, R. L. (1971). Thermal conductivity of hot-mix asphalt concrete by the transient line source method. *1970-1979-Mines Theses & Dissertations*.

Gong, X., Liu, Q., Lv, Y., Chen, S., Wu, S., & Ying, H. (2023). A Systematic Review on The Strategies of Reducing Asphalt Pavement Temperature. Case Studies in Construction Materials, e01852.

Grossegger, D., & Garcia, A. (2019). Influence of the thermal expansion of bitumen on asphalt self-healing. *Applied Thermal Engineering*, *156*, 23-33.

Gunasekara, S. N., Ignatowicz, M., Chiu, J. N., & Martin, V. (2019). Thermal conductivity measurement of erythritol, xylitol, and their blends for phase change material design: a methodological study. *International Journal of Energy Research, 43*(5), 1785-1801.

Gustafsson, S. E. (1991). Transient plane source techniques for thermal conductivity and thermal diffusivity measurements of solid materials. Review of scientific instruments, 62(3), 797-804.

Hai-Gui, K., Yuan-Xun, Z., Ying-Chun, C., & Yan, L. I. U. (2007). Regression analysis of actual measurement of temperature field distribution rules of asphalt pavement. *China Journal of Highway and Transport*, *20*(6), 13.

Han, D., Liu, G., Zhao, Y., Pan, Y., & Yang, T. (2021). Research on thermal properties and heat transfer of asphalt mixture based on 3D random reconstruction technique. *Construction and Building Materials*, *270*, 121393.

Harris, A., Kazachenko, S., Bateman, R., Nickerson, J., & Emanuel, M. (2014). Measuring the thermal conductivity of heat transfer fluids via the modified transient plane source (MTPS). *Journal of Thermal Analysis and Calorimetry, 116*, 1309-1314.

Hassn, A. A. (2017). *Effect of air voids on pavement thermal properties* (Doctoral dissertation, University of Nottingham).

Hassn, A., Aboufoul, M., Wu, Y., Dawson, A., & Garcia, A. (2016a). Effect of air voids content on thermal properties of asphalt mixtures. *Construction and Building Materials, 115*, 327-335.

Hassn, A., Chiarelli, A., Dawson, A., & Garcia, A. (2016b). Thermal properties of asphalt pavements under dry and wet conditions. *Materials & Design, 91*, 432-439.

Hermansson, Å. (2001). Mathematical model for calculation of pavement temperatures: comparison of calculated and measured temperatures. *Transportation Research Record, 1764*(1), 180-188.

Highter, W.H., and Wall, D.J. 1984. Thermal properties of some asphaltic concrete mixes. In Asphalt mixtures and performance. Transportation Research Record 968, Transportation Research Board, Washington, D.C. pp. 38–45.

Hosseinnezhad, S., Zadshir, M., Yu, X., Yin, H., Sharma, B. K., & Fini, E. (2019). Differential effects of ultraviolet radiation and oxidative aging on bio-modified binders. *Fuel*, *251*, 45-56.

Hu, J., & Yu, X. (2016). Innovative thermochromic asphalt coating: characterisation and thermal performance. *Road Materials and Pavement Design*, *17*(1), 187-202.

Hu, J., Wanasekara, N., & Yu, X. (2014). Thermal properties of thermochromic asphalt binders by modulated differential scanning calorimetry. *Transportation Research Record*, *2444*(1), 142-150.

Hwang, Y. J., Ahn, Y. C., Shin, H. S., Lee, C. G., Kim, G. T., Park, H. S., & Lee, J. K. (2006). Investigation on characteristics of thermal conductivity enhancement of nanofluids. *Current Applied Physics*, *6*(6), 1068-1071.

Isa, I. A. A., & Jodeh, S. W. (2001). Thermal properties of automotive polymers III—Thermal characteristics and flammability of fire retardant polymers. *Materials Research Innovations*, *4*(2-3), 135-143.

Islam, M. R., & Tarefder, R. A. (2014). Determining thermal properties of asphalt concrete using field data and laboratory testing. *Construction and Building Materials*, *67*, 297-306.

ISO 22007-2 Plastics-Determination of thermal conductivity and thermal diffusivity-Part 2: Transient plane heat source (hot disc) method

Jamshidi, A., Kurumisawa, K., Nawa, T., Mao, J., & Li, B. (2017). Characterization of effects of thermal property of aggregate on the carbon footprint of asphalt industries in China. *Journal of traffic and transportation engineering (English edition)*, *4*(2), 118-130.

Jbeili, M., & Zhang, J. (2021). The generalized periodic boundary condition for microscopic simulations of heat transfer in heterogeneous materials. *International Journal of Heat and Mass Transfer*, *173*, 121200.

Jiao, W., Sha, A., Liu, Z., Li, W., Jiang, W., Qin, W., & Hu, Y. (2020). Study on thermal properties of steel slag asphalt concrete for snow-melting pavement. *Journal of Cleaner Production, 277*, 123574.

Johnston, G. H. (1981). Permafrost: engineering design and construction. *(No Title)*.

Jordan, P. G., & Thomas, M. E. (1976). Prediction of cooling curves for hot-mix paving materials by a computer program. *Publication of: Transport and road research laboratory*, (TRRL Lab Rpt LR 729 Monograph).

Kandhal, P. S., Parker, F., & Mallick, R. B. (1997). Aggregate tests for hot-mix asphalt: state of the practice.

Khadrawi, A. F., Al-Shyyab, A., & Abo-Qudais, S. A. (2012). Transient thermal behavior of hot–mix asphalt pavement. *Applied Mechanics and Materials*, *110*, 400-407.

Khasawneh, M. A., Sawalha, A. A., Aljarrah, M. T., & Alsheyab, M. A. (2023). Effect of aggregate gradation and asphalt mix volumetrics on the thermal properties of asphalt concrete. *Case Studies in Construction Materials*, *18*, e01725.

Kim, D., Lee, S., & Yang, I. (2021). Verification of thermal conductivity measurements using guarded hot plate and heat flow meter methods. *Journal of the Korean Physical Society*, *78*(12), 1196-1202.

Kothandaraman, C. P. (2006). *Fundamentals Of Heat and Mass Transfer* (3rd ed.).New Age International Publishers, New Delphi.

Kreith, F. & Bohn, M.S. (2001). *Principles of Heat Transfer.* 6th ed. Pacific Grove, CA: Brooks/Cole.

Krupa, P., & Malinaric, S. (2014). Using the transient plane source method for measuring thermal parameters of electroceramics. *International Journal of Mechanical and Mechatronics Engineering*, *8*(5), 735-740.

Ksaibati, K., & Kasperick, T. (2015). Calibration of the mechanistic-empirical pavement design guide for local paved roads in Wyoming.

Kuvandykova, D., & Bateman, R. (2013). A new transient method to measure thermal conductivity of asphalt. Thermal Conductivity 31.

Kuvandykova, D., & St-Laurent, R. (2010). Application of the modified transient plane source technique in testing the thermal conductivity of concrete. C-Therm Technol, 18, 1-7.

Li, Y., Li, W., Han, T., Zheng, X., Li, J., Li, B., ... & Qiu, C. W. (2021). Transforming heat transfer with thermal metamaterials and devices. *Nature Reviews Materials*, *6*(6), 488-507.

Li, Y., Shi, C., Liu, J., Liu, E., Shao, J., Chen, Z., ... & Hu, X. (2013). Improving the accuracy of the transient plane source method by correcting probe heat capacity and resistance influences. *Measurement Science and Technology*, *25*(1), 015006.

Liang, B., Lan, F., Shi, K., Qian, G., Liu, Z., & Zheng, J. (2021). Review on the self-healing of asphalt materials: Mechanism, affecting factors, assessments and improvements. *Construction and Building Materials*, *266*, 120453.

Lienhard, IV, J. H. and Lienhard, V, J. H. (2019). *A Heat Transfer Textbook, 5th Edition, Dover Publications, Mineola, NY.*

Liu, D., Zhang, H., Liu, Z., Liu, D., He, D., & Yu, T. (2023). The heat flux evolution of porous asphalt mixture based on meso-structure and its influence on heat transfer property. *Thermal Science and Engineering Progress*, *43*, 102020.

Liu, P. S., & Chen, G. F. (2014). Chapter Ten-Characterization Methods: Physical Properties. *Porous Materials*, 122-125.

Log, T., & Gustafsson, S. E. (1995). Transient plane source (TPS) technique for measuring thermal transport properties of building materials. *Fire and materials*, *19*(1), 43-49.

Luca, J., & Mrawira, D. (2005). New measurement of thermal properties of superpave asphalt concrete. *Journal of materials in civil engineering*, *17*(1), 72-79.

Mahan, J. R. (2002). *Radiation Heat Transfer: A Statistical Approach*. John Wiley & Sons, New York.

Mamlouk, M. S., Witczak, M. W., Kaloush, K. E., & Hasan, N. (2005). Determination of thermal properties of asphalt mixtures.

Marcus, S. M., & Blaine, R. L. (1994). Thermal conductivity of polymers, glasses and ceramics by modulated DSC. *Thermochimica Acta*, *243*(2), 231-239.

Martínez-Ibáñez, V., Garrido, M. E., Signes, C. H., & Tomás, R. (2021, August). Determination of thermal conductivity variation through Modified Transient Plane Source (MTPS), and its relationship with porosity variation on thermally treated Prada limestone. In *IOP Conference Series: Earth and Environmental Science* (Vol. 833, No. 1, p. 012026). IOP Publishing.

Masad, E., Muhunthan, B., Shashidhar, N., & Harman, T. (1999). Internal structure characterization of asphalt concrete using image analysis. *Journal of Computing in Civil Engineering, 13*(2), 88-95.

Masson, J. F., Polomark, G. M., & Collins, P. (2002). Time-dependent microstructure of bitumen and its fractions by modulated differential scanning calorimetry. *Energy & Fuels*, *16*(2), 470-476.

Mehling, H., & Cabeza, L. F. (2008). Heat and cold storage with PCM. *Heat and mass transfer*, 11-55.

Min, S., Blumm, J., & Lindemann, A. (2007). A new laser flash system for measurement of the thermophysical properties. *Thermochimica Acta*, *455*(1-2), 46-49.

Minhoto, M. J., Pais, J. C., Pereira, P. A., & Picado-Santos, L. G. (2005). Predicting asphalt pavement temperature with a three-dimensional finite element method. *Transportation Research Record*, *1919*(1), 96-110.

Mirzanamadi, R., Johansson, P., & Grammatikos, S. A. (2018). Thermal properties of asphalt concrete: A numerical and experimental study. *Construction and Building Materials*, *158*, 774-785.

Moon, K. H., & Falchetto, A. C. (2015). Microstructural investigation of hot mix asphalt (HMA) mixtures using digital image processing (DIP). *KSCE Journal of Civil Engineering, 19*, 1727-1737.

Mrawira, D. M., & Luca, J. (2002). Thermal properties and transient temperature response of full-depth asphalt pavements. *Transportation Research Record, 1809*(1), 160-171.

Mrawira, D. M., & Luca, J. (2006). Effect of aggregate type, gradation, and compaction level on thermal properties of hot-mix asphalts. *Canadian Journal of Civil Engineering*, *33*(11), 1410-1417.

Mu, K., Chen, J., Mu, Q., Garg, A., Gao, Z., & Li, Y. (2020). Development of a microstructure-based numerical approach for analyzing heat transfer within the asphalt mixture. *Construction and Building Materials*, *260*, 119890.

Nagasaka, Y., & Nagashima, A. (1981). Absolute measurement of the thermal conductivity of electrically conducting liquids by the transient hot-wire method. *Journal of Physics E: Scientific Instruments*, *14*(12), 1435.

Nassiri, S., & Nantasai, B. (2017). Thermal conductivity of pervious concrete for various porosities. *ACI Materials Journal, 114*(2), 265.

Nazki, M. A., Chopra, T., & Chandrappa, A. K. (2020). Rheological properties and thermal conductivity of bitumen binders modified with graphene. *Construction and Building Materials*, *238*, 117693.

Onifade, I. (2013). *Internal structure characterization of asphalt concrete using x-ray computed tomography* (Master dissertation, Royal Institute of Technology (KTH), Stockholm).

Palacios, A., Cong, L., Navarro, M. E., Ding, Y., & Barreneche, C. (2019). Thermal conductivity measurement techniques for characterizing thermal energy storage materials–A review. *Renewable and Sustainable Energy Reviews*, *108*, 32-52.

Pan, P., Wu, S., Hu, X., Liu, G., & Li, B. (2017). Effect of material composition and environmental condition on thermal characteristics of conductive asphalt concrete. *Materials, 10*(3), 218.

Parker, W. J., Jenkins, R. J., Butler, C. P., & Abbott, G. L. (1961). Flash method of determining thermal diffusivity, heat capacity, and thermal conductivity. *Journal of applied physics*, *32*(9), 1679-1684.

Petkova-Slipets, R., & Zlateva, P. (2018). Thermal properties of a new pavement material for using in road construction. *Civil and Environmental Engineering*, *14*(2), 99-104.

Philipp, A., Eichinger, J. F., Aydin, R. C., Georgiadis, A., Cyron, C. J., & Retsch, M. (2020). The accuracy of laser flash analysis explored by finite element method and numerical fitting. *Heat and Mass Transfer*, *56*, 811-823.

Qin, Y., Zhang, X., Tan, K., & Wang, J. (2022). A review on the influencing factors of pavement surface temperature. *Environmental Science and Pollution Research*, *29*(45), 67659-67674.

Rahman, M. T., Mohajerani, A., & Giustozzi, F. (2020). Recycling of waste materials for asphalt concrete and bitumen: A review. *Materials*, *13*(7), 1495.

Ren, Z., Wang, H., Zhang, L., & Chen, C. (2018). Computational analysis of thermal conductivity of asphalt mixture based on a multiscale mathematical model. *Journal of Engineering Mechanics*, *144*(8), 04018064.

Richter, C., Viljoen, H. J., & Van Rensburg, N. F. J. (2003). Effective thermal conductivity estimates of particulate mixtures. *Journal of applied physics*, *93*(5), 2663-2670.

Risk, W. P., Rettner, C. T., & Raoux, S. (2009). Thermal conductivities and phase transition temperatures of various phase-change materials measured by the 3ω method. *Applied Physics Letters*, *94*(10).

Roberts, F. L., Kandhal, P. S., Brown, E. R., Lee, D. Y., & Kennedy, T. W. (1996). *Hot mix asphalt materials, mixture design and construction*.

Robertson, E. C. (1988). Thermal Properties of Rocks: U.S. Geol. Survey, Open-File Report. 88-441, 96 p.

Schärli, U., & Rybach, L. (2001). Determination of specific heat capacity on rock fragments. *Geothermics, 30*(1), 93-110.

Shamsaei, M., Carter, A., & Vaillancourt, M. (2022). A review on the heat transfer in asphalt pavements and urban heat island mitigation methods. *Construction and Building Materials*, *359*, 129350.

Shi, C., Yu, H., Qian, G., Li, X., Zhu, X., Yao, D., & Zhang, C. (2023). Research on the characteristics of asphalt mixture gradation curve based on Weibull distribution. *Construction and Building Materials*, *366*, 130151.

Shi, X., Rew, Y., Ivers, E., Shon, C. S., Stenger, E. M., & Park, P. (2019). Effects of thermally modified asphalt concrete on pavement temperature. *International Journal of Pavement Engineering*, *20*(6), 669-681.

Solaimanian, M., & Kennedy, T. W. (1993). Predicting maximum pavement surface temperature using maximum air temperature and hourly solar radiation. *Transportation Research Record*, 1-1.

Stempihar, J. J., Pourshams-Manzouri, T., Kaloush, K. E., & Rodezno, M. C. (2012). Porous asphalt pavement temperature effects for urban heat island analysis. *Transportation Research Record*, *2293*(1), 123-130.

Sun, Y., Wu, S., Liu, Q., Zeng, W., Chen, Z., Ye, Q., & Pan, P. (2017). Self-healing performance of asphalt mixtures through heating fibers or aggregate. *Construction and Building Materials*, *150*, 673-680.

Tan, S., Fwa, T., Chuai, C., and Low, B. 1997. Determination of thermal properties of pavement materials and unbound aggregates by transient heat conduction. *Journal of Testing and Evaluation*, ASTM, 25(1): 15–22.

Tan, S., Low, B., and Fwa, T. (1992). Determination of thermal conductivity and diffusivity by transient heating of a thin slab. *Building and Environment, 27*(1): 71–76.

Tang, B., Zhu, C., Xu, M., Chen, T., & Hu, S. (2019). Thermal conductivity of sedimentary rocks in the Sichuan basin, Southwest China. *Energy Exploration & Exploitation*, *37*(2), 691-720.

Tang, N., Wu, S. P., Chen, M. Y., Pan, P., & Sun, C. J. (2014). Effect mechanism of mixing on improving conductivity of asphalt solar collector. International *Journal of Heat and Mass Transfer, 75*, 650-655.

Telejko, T., & Malinowski, Z. (2004). Application of an inverse solution to the thermal conductivity identification using the finite element method. *Journal of Materials Processing Technology*, *146*(2), 145-155.

Timm, D. H., Voller, V. R., Lee, E. B., & Harvey, J. (2001). Calcool: A multi-layer asphalt pavement cooling tool for temperature prediction during construction. *International Journal of Pavement Engineering*, *2*(3), 169-185.

Tiskatine, R., Bougdour, N., Idoum, A., Bazgaou, A., Oaddi, R., Ihlal, A., & Aharoune, A. (2023). Experimental investigation on rock thermal properties under the influence of temperature. *Thermochimica Acta*, *720*, 179424.

Tritt, T. M. (Ed.). (2005). Thermal conductivity: theory, properties, and applications.

Vo, H. V., Park, D. W., Seo, W. J., & Yoo, B. S. (2017). Evaluation of asphalt mixture modified with graphite and carbon fibers for winter adaptation: Thermal conductivity improvement. *Journal of Materials in Civil Engineering*, *29*(1), 04016176.

Wang, H., Wang, C., You, Z., Yang, X., & Huang, Z. (2018). Characterising the asphalt concrete fracture performance from X-ray CT Imaging and finite element modelling. *International Journal of Pavement Engineering*, *19*(3), 307-318.

Wang, Z. M., Kwan, A. K. H., & Chan, H. C. (1999). Mesoscopic study of concrete I: generation of random aggregate structure and finite element mesh. *Computers & structures*, *70*(5), 533-544.

Waples, D. W., & Waples, J. S. (2004). A review and evaluation of specific heat capacities of rocks, minerals, and subsurface fluids. Part 1: Minerals and nonporous rocks. *Natural resources research*, *13*, 97-122.

Weisstein, E. W. (2014). Radiation. *Eric Weisstein's World of Physics. Wolfram Research. Retrieved*, *11*.

Wolfe, R. K., Heath, G. L., & Colony, D. C. (1980). University of Toledo Time-Temperature Model Laboratory and Field Validation. Report No. FHWA/0H-80/006, Ohio Department of Transportation, April 1980.

Wu, H., Liu, Z., Yang, Y., & Bai, S. (2016). Characterizing thermal impacts of pavement materials on urban heat island (UHI) effect. *DEStech Transactions on Engineering and Technology*.

Xu, Q., & Solaimanian, M. (2008). Measurement and evaluation of asphalt concrete thermal expansion and contraction. *Journal of Testing and Evaluation, 36*(2), 507.

Xu, Q., & Solaimanian, M. (2010). Modeling temperature distribution and thermal property of asphalt concrete for laboratory testing applications. *Construction and Building Materials, 24*(4), 487-497.

Yan, X., Chen, L., You, Q., & Fu, Q. (2019). Experimental analysis of thermal conductivity of semi-rigid base asphalt pavement. *Road Materials and Pavement Design*, *20*(5), 1215-1227.

Yang, D., Karimi, H. R., & Aliha, M. R. M. (2021). Comparison of testing method effects on cracking resistance of asphalt concrete mixtures. *Applied Sciences*, *11*(11), 5094.

Yu, H., Shi, C., Qian, G., & Gong, X. (2021). Experimental study on thermophysical properties of HMA during compaction. *International Journal of Pavement Engineering*, *22*(8), 1064-1075.

Zadshir, M., Ploger, D., Yu, X., Sangiorgi, C., & Yin, H. (2020). Chemical, thermophysical, rheological, and microscopic characterization of rubber modified asphalt binder exposed to UV radiation. *Road Materials and Pavement Design*, *21*(sup1), S123-S139.

Zarr, R. R. (2010). Uncertainty Analysis of Thermal Transmission Properties Determined by ASTM C 177. *J. Testing and Evaluation*.

Zhang, L., Wang, H., & Ren, Z. (2017). Computational analysis of thermal conductivity of asphalt mixture using virtually generated three-dimensional microstructure. *Journal of Materials in Civil Engineering*, *29*(12), 04017234.

Zhao, D., Qian, X., Gu, X., Jajja, S. A., & Yang, R. (2016). Measurement techniques for thermal conductivity and interfacial thermal conductance of bulk and thin film materials. *Journal of Electronic Packaging*, *138*(4), 040802.

Zhao, Y., Jiang, J., Dai, Y., Zhou, L., & Ni, F. (2020). Thermal property evaluation of porous asphalt concrete based on heterogeneous meso-structure finite element simulation. *Applied Sciences*, *10*(5), 1671.

Zheng, Q., Kaur, S., Dames, C., & Prasher, R. S. (2020). Analysis and improvement of the hot disk transient plane source method for low thermal conductivity materials. *International Journal of Heat and Mass Transfer, 151*, 119331.

Zhong, Y., & Geng, L. (2009). Thermal stresses of asphalt pavement under dependence of material characteristics on reference temperature. *Mechanics of Time-Dependent Materials, 13*, 81-91.

Zhou, X., Wang, S., & Zhou, C. (2012). Thermal conduction and insulation modification in asphalt-based composites. *Journal of Materials Science & Technology*, *28*(3), 285-288.

Zlateva, P., & Petkova-Slipets, R. (2015). Comparative Analysis of The Thermal Conductivity Coefficients of Environmentally Friendly Building Materials. *Acta Technica Corviniensis-Bulletin of Engineering, 8*(3), 25.

APPENDICES

A. Optimum Bitumen Content and Volumetric Properties

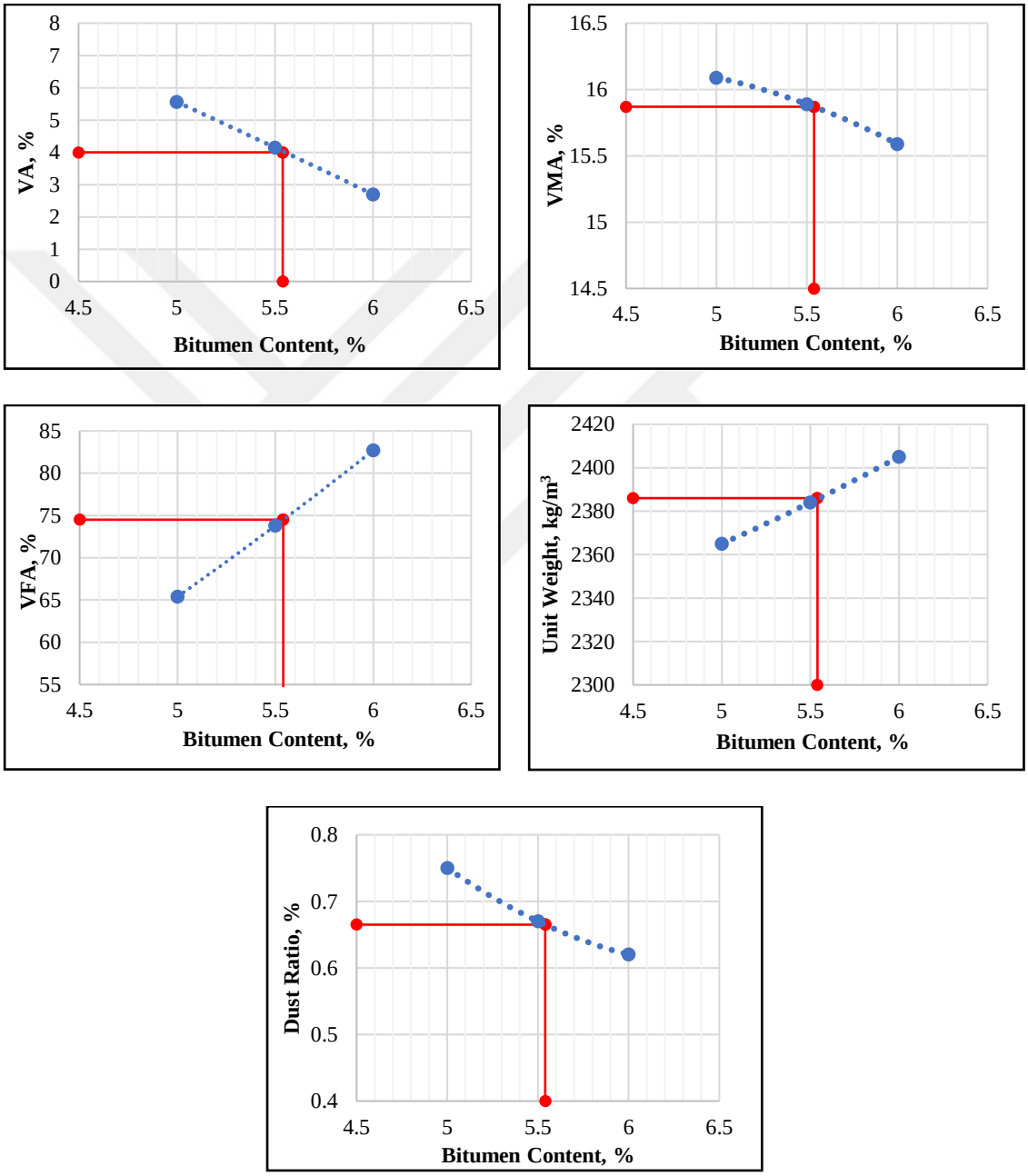


Figure A. 1 Optimum bitumen content and volumetric properties for Mix Design 1.

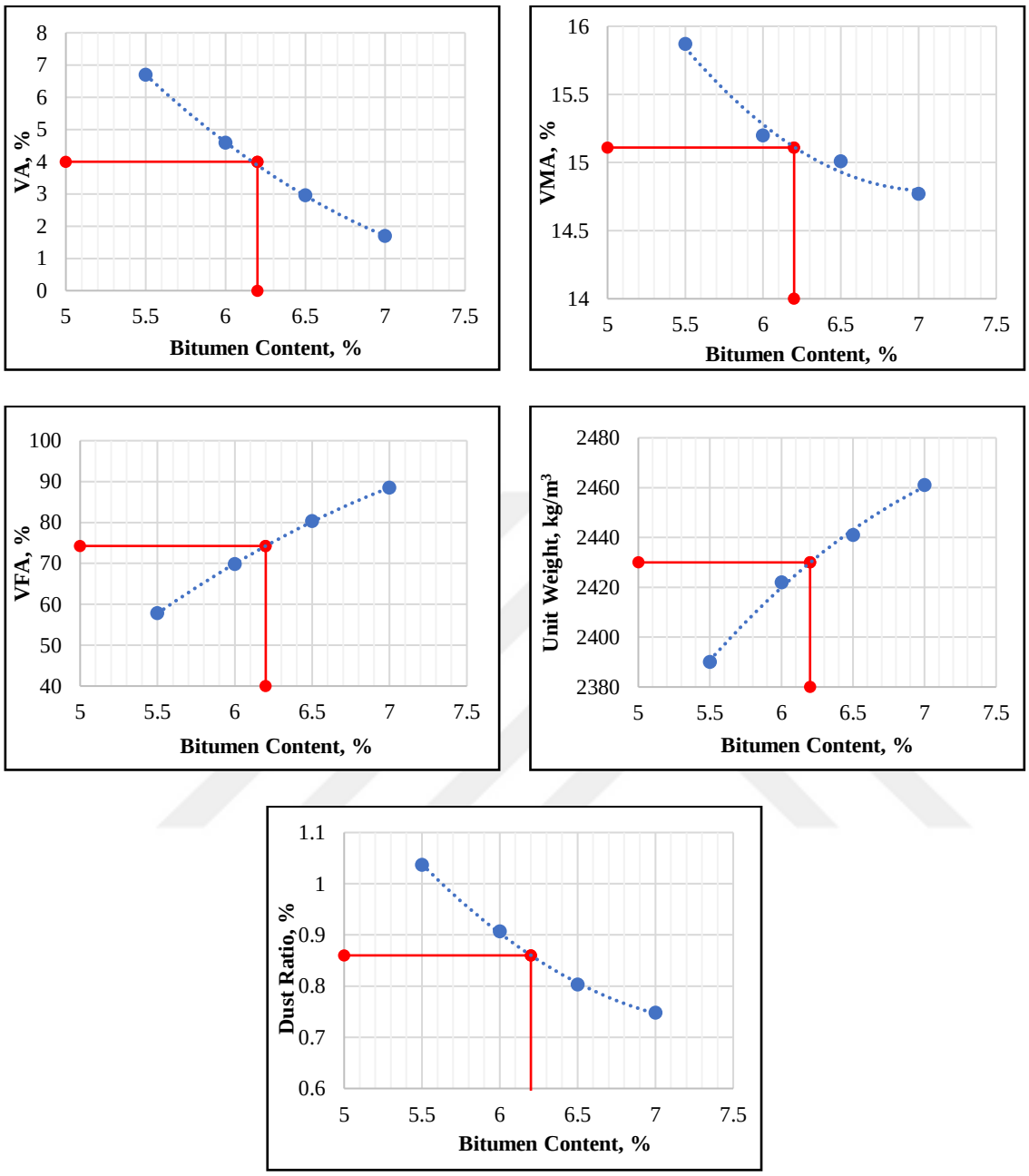


Figure A. 2 Optimum bitumen content and volumetric properties for Mix Design 2.

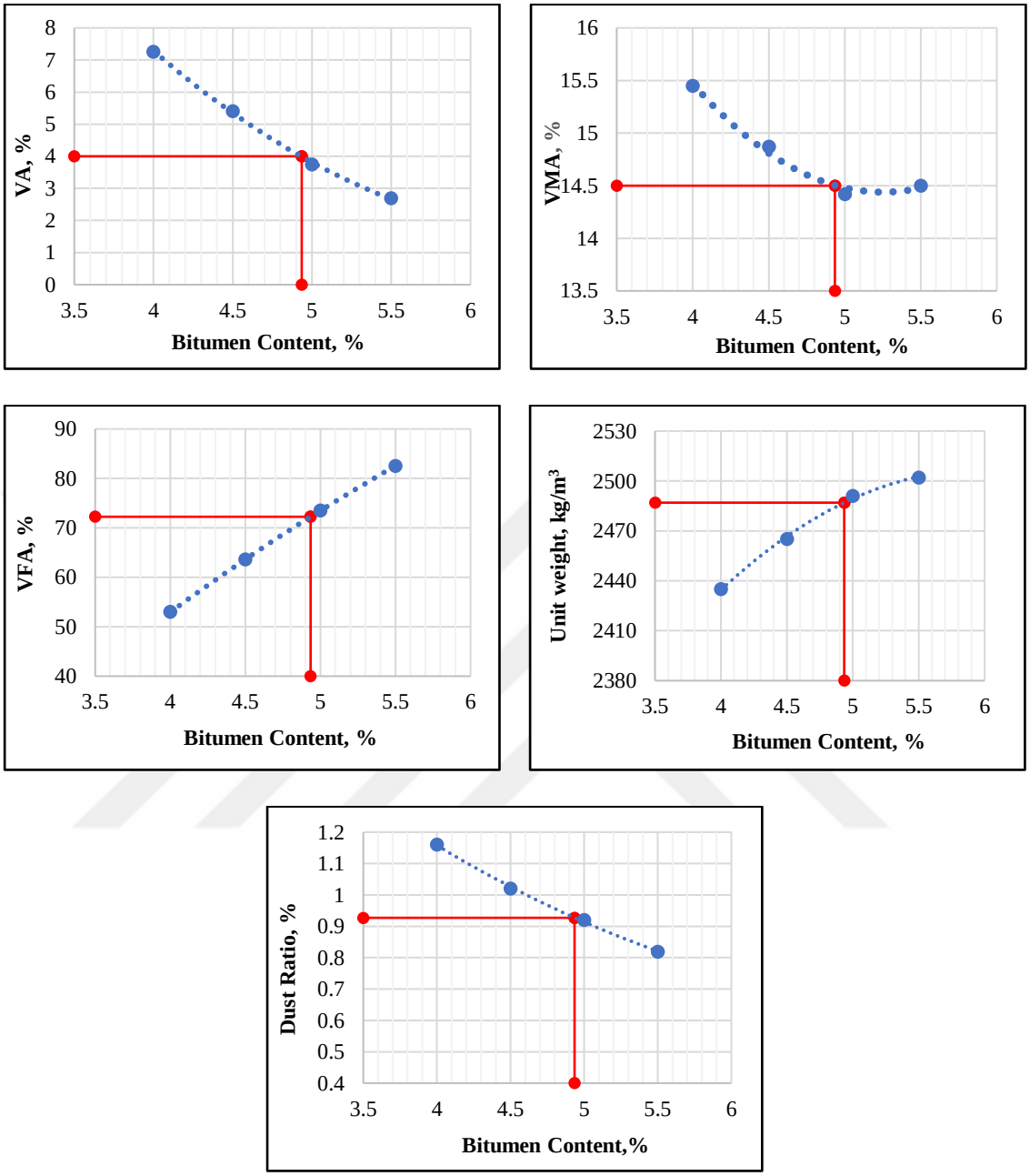


Figure A. 3 Optimum bitumen content and volumetric properties for Mix Design 3.

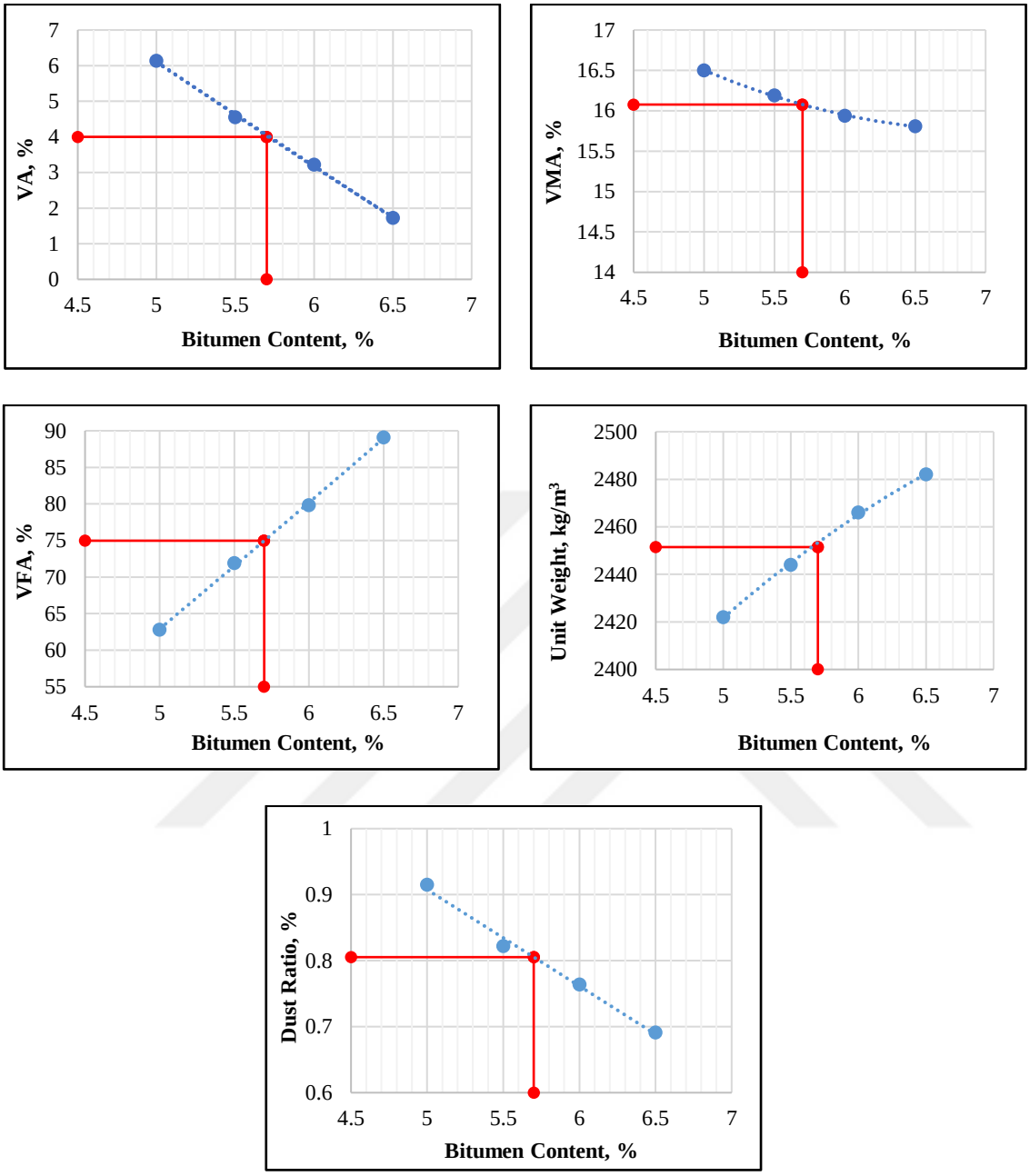


Figure A. 4 Optimum bitumen content and volumetric properties for Mix Design 4.

B. Volumetric Properties of Mix Designs

Table B. 1 Volumetric properties of Mix Design 1 with different air void contents and MAS: 19 mm.

Target Air Void Content	Sample ID	Volumetric Properties			
		Va,%	VMA,%	VFA,%	Density, kg/m^3
2%	**B2T101**	1.95	13.95	86.04	2439
	B2T102	2	13.99	85.72	2437
	B2T103	1.84	13.85	86.75	2441
	B2T104	2.01	14.01	85.63	2437
	B2T105	1.92	13.93	86.18	2439
4%	**B4T101**	4.10	15.83	74.1	2385
	B4T102	4.10	15.8	74.1	2385
	B4T103	4.12	15.9	74	2384
	B4T104	4.22	15.9	73.5	2382
	B4T105	3.85	15.6	75.3	2391
6%	**B6T101**	6.11	17.60	65.30	2335
	B6T102	6.13	17.62	65.21	2335
	B6T103	6.04	17.54	65.55	2337
	B6T104	6.12	17.61	65.23	2335
	B6T105	6.04	17.54	65.58	2337
Optimum Binder Content: 5.5% Theoretical Maximum Specific Gravity (G_{mm}): 2.487 Dust Ratio: 0.675 Bulk Specific Gravity of Aggregate Blend (G_{sb}): 2.678					

Table B. 2 Volumetric properties of Mix Design 2 with different air void contents and MAS: 12.5 mm.

Target Air Void Content	Sample ID	Volumetric Properties			
		Va,%	VMA,%	VFA,%	Density, kg/m^3
2%	**B2T201**	1.90	13.19	85.6	2485
	B2T202	1.97	13.25	85.1	2483
	B2T203	1.93	13.22	85.4	2484
	B2T204	2.02	13.30	84.8	2482
	B2T205	1.97	13.25	85.2	2483
4%	**B4T201**	3.96	15.01	73.6	2433
	B4T202	4.14	15.17	72.7	2428
	B4T203	3.87	14.94	74.1	2435
	B4T104	4.03	15.07	73.3	2431
	B4T205	3.95	15.01	73.7	2433
6%	**B6T201**	6.03	16.85	64.2	2380
	B6T202	6.09	16.90	64	2379
	B6T203	5.91	16.74	64.7	2383
	B6T204	5.86	16.69	64.9	2385
	B6T205	5.90	16.74	64.7	2383

Optimum Binder Content: 6.2%

Theoretical Maximum Specific Gravity (G_{mm}): 2.533

Dust Ratio: 0.874

Bulk Specific Gravity of Aggregate Blend (G_{sb}): 2.685

Table B. 3 Volumetric properties of Mix Design 3 with different air void contents and MAS: 19 mm.

Target Air Void Content	Sample ID	Volumetric Properties			
		Va,%	VMA,%	VFA,%	Density, kg/m^3
2%	**D2T101**	2.02	12.8	84.2	2537
	D2T102	2.11	12.8	83.6	2535
	D2T103	2.12	12.9	83.5	2535
	D2T104	1.85	12.6	85.4	2542
	D2T105	2.09	12.8	83.7	2535
4%	**D4T101**	3.91	14.45	73	2488
	D4T102	4.13	14.65	71.8	2483
	D4T103	4.17	14.7	71.6	2481
	D4T104	4.14	14.7	71.7	2482
	D4T105	4.14	14.7	71.8	2482
6%	**D6T101**	5.92	16.25	63.5	2436
	D6T102	5.91	16.23	63.6	2437
	D6T103	6.15	16.45	62.6	2430
	D6T104	6.08	16.39	62.9	2432
	D6T105	6.07	16.37	63	2432

Optimum Binder Content: 4.9%

Theoretical Maximum Specific Gravity (G_{mm}): 2.590

Dust Ratio: 0.924

Bulk Specific Gravity of Aggregate Blend (G_{sb}): 2.765

Table B. 4 Volumetric properties of Mix Design 4 with different air void contents and MAS: 12.5 mm.

Target Air Void Content	**Sample ID**	**Volumetric Properties**			
		Va,%	**VMA,%**	**VFA,%**	**Density, kg/m^3**
2%	**D2T201**	1.81	14.13	87.2	2510
	D2T202	1.85	14.16	86.9	2509
	D2T203	1.93	14.23	86.5	2507
	D2T204	1.87	14.17	86.8	2508
	D2T205	1.88	14.19	86.8	2508
4%	**D4T201**	3.97	16.01	75.2	2455
	D4T202	4.04	16.08	74.9	2453
	D4T203	4.05	16.09	74.8	2452
	D4T204	4.11	16.14	74.5	2451
	D4T205	4.14	16.16	74.4	2450
6%	**D6T201**	6.17	17.94	65.6	2398
	D6T202	5.93	17.73	66.6	2405
	D6T203	6.15	17.92	65.7	2399
	D6T204	5.97	17.76	66.4	2403
	D6T205	5.85	17.66	66.9	2407
Optimum Binder Content: 5.7% Theoretical Maximum Specific Gravity (G_{mm}): 2.556 Dust Ratio: 0.798 Bulk Specific Gravity of Aggregate Blend (G_{sb}): 2.756					

C. Sliced Samples Properties for The Calorimetry-Based Test Setup

Table C. 1 For the calorimetry-based test setup, the physical properties of the sliced samples prepared with basalt.

Sample ID	A, mass of sample in air (g)	B, mass of SSD sample in air (g)	C, mass of sample in water (g)	Bulk Specific Gravity, G_{mb}	Average Bulk Specific Gravity of the Slices, G_{mb}	Theoretical maximum specific gravity, G_{mm}	Air Void Content, %	Average Air Void Content of Two Slices, %
B2T1-01	1826.8	1827.6	1083.1	2.454	2.457	2.487	1.3	1.2
B2T1-02	1950.8	1951.8	1159.1	2.461			1.0	
B4T1-01	1895.5	1897.7	1115.0	2.422	2.420		2.6	2.7
B4T1-02	1875.1	1876.4	1101.2	2.419			2.7	
B6T1-01	2015.1	2017.1	1166.2	2.368	2.367		4.8	4.8
B6T1-02	1753.7	1756.6	1015.4	2.366			4.9	
B2T2-01	1770.5	1771.9	1064.9	2.504	2.507	2.533	1.1	1.0
B2T2-02	1919.6	1920.5	1155.4	2.509			0.9	
B4T2-01	1876.8	1878.1	1110.8	2.446	2.453		3.4	3.2
B4T2-02	1893.5	1894.9	1125.3	2.460			2.9	
B6T2-01	2006.9	2008.7	1175.0	2.407	2.403		5.0	5.1
B6T2-02	1882.0	1884.0	1099.5	2.399			5.3	

Table C. 2 For the calorimetry-based test setup, the physical properties of the sliced samples prepared with dolomite.

Sample ID	A, mass of sample in air (g)	B, mass of SSD sample in air (g)	C, mass of sample in water (g)	Bulk Specific Gravity, G_{mb}	Average Bulk Specific Gravity of the Slices, G_{mb}	Theoretical maximum specific gravity, G_{mm}	Air Void Content, %	Average Air Void Content of Two Slices, %
D2T1-01	1752.2	1753.3	1061.0	2.531	2.550	2.590	2.3	1.5
D2T1-02	1892.8	1893.9	1157.1	2.569			0.8	
D4T1-01	1935.0	1936.5	1164.7	2.507	2.499		3.2	3.5
D4T1-02	1822.2	1823.7	1092.2	2.491			3.8	
D6T1-01	1796.6	1798.9	1068.9	2.461	2.457		5.0	5.1
D6T1-02	1825.8	1827.5	1083.0	2.452			5.3	
D2T2-01	1829.5	1830.3	1104.3	2.520	2.528	2.556	1.4	1.1
D2T2-02	1892.1	1893.0	1146.7	2.535			0.8	
D4T2-01	1782.6	1783.6	1063.4	2.475	2.480		3.2	3.0
D4T2-02	1858.0	1859.0	1111.1	2.484			2.8	
D6T2-01	1800.9	1802.2	1058.0	2.420	2.427		5.3	5.1
D6T2-02	1993.5	1994.8	1175.5	2.433			4.8	

D. Temperature & Time Curves Obtained in the Developed Steady State Method

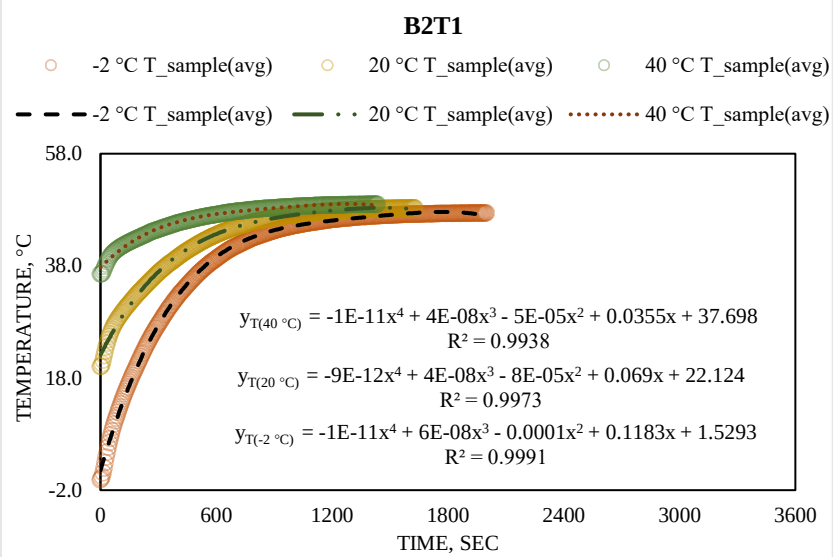


Figure D. 1 The temperature & time curves of B2T1 under three different conditioning temperatures.

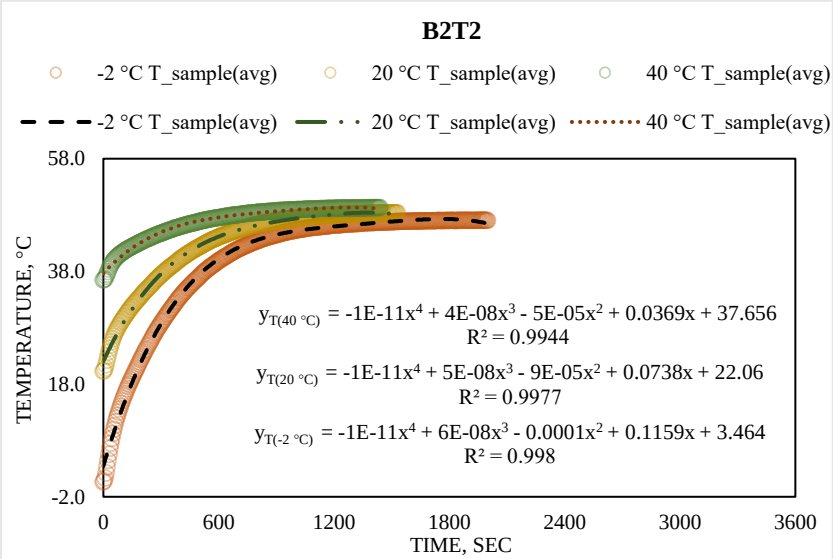


Figure D. 2 The temperature & time curves of B2T2 under three different conditioning temperatures.

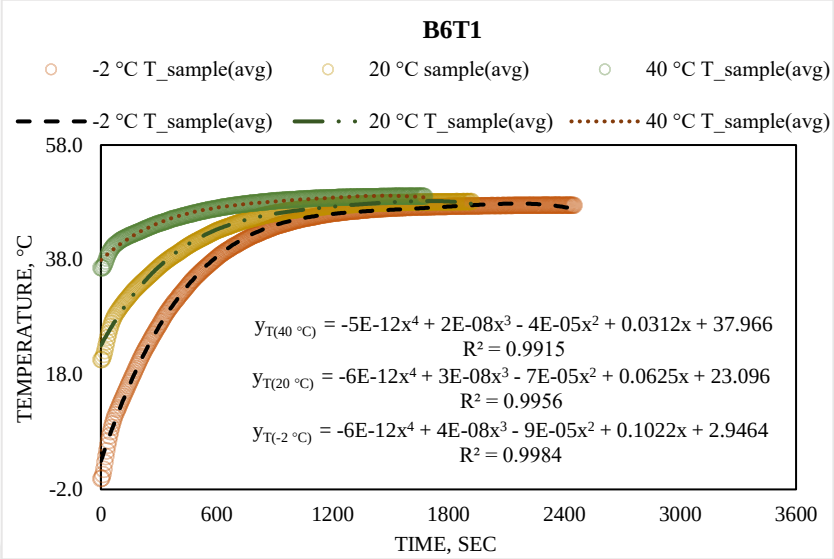


Figure D. 3 The temperature & time curves of B6T1 under three different conditioning temperatures.

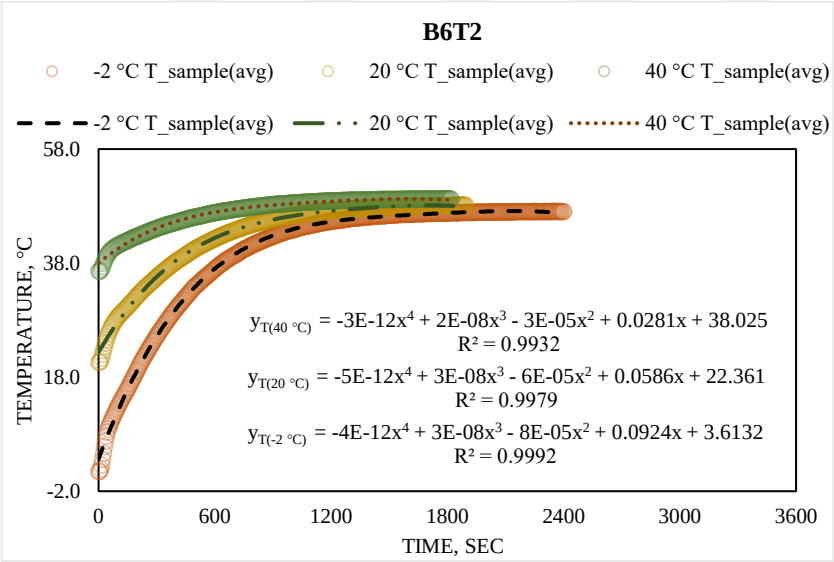


Figure D. 4 The temperature & time curves of B6T2 under three different conditioning temperatures.

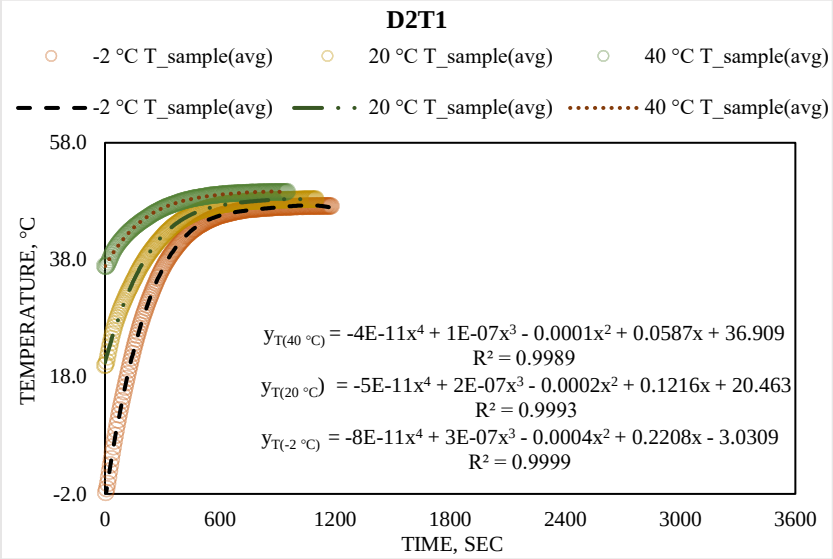


Figure D. 5 The temperature & time curves of D2T1 under three different conditioning temperatures.

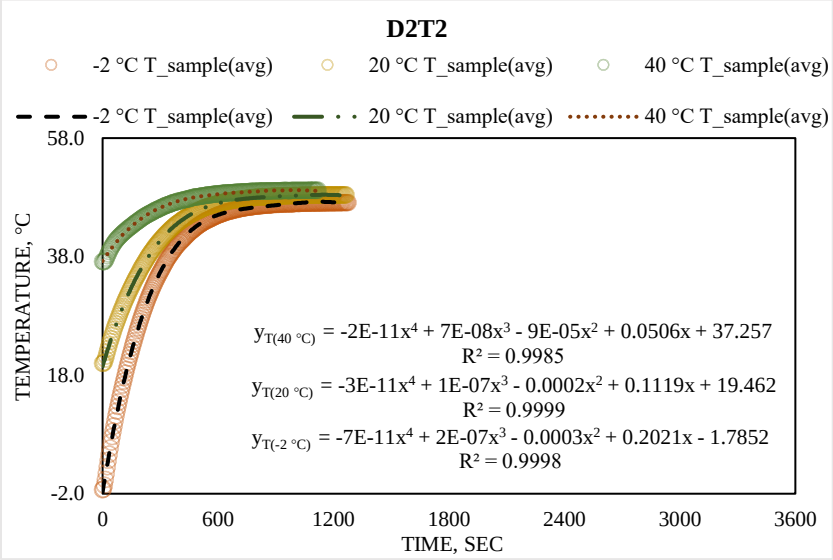


Figure D. 6 The temperature & time curves of D2T2 under three different conditioning temperatures.

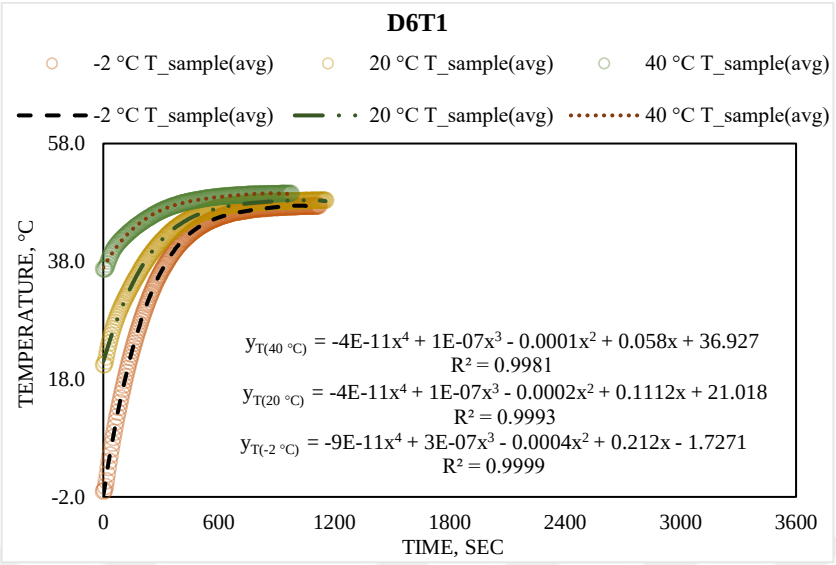


Figure D. 7 The temperature & time curves of D6T1 under three different conditioning temperatures.

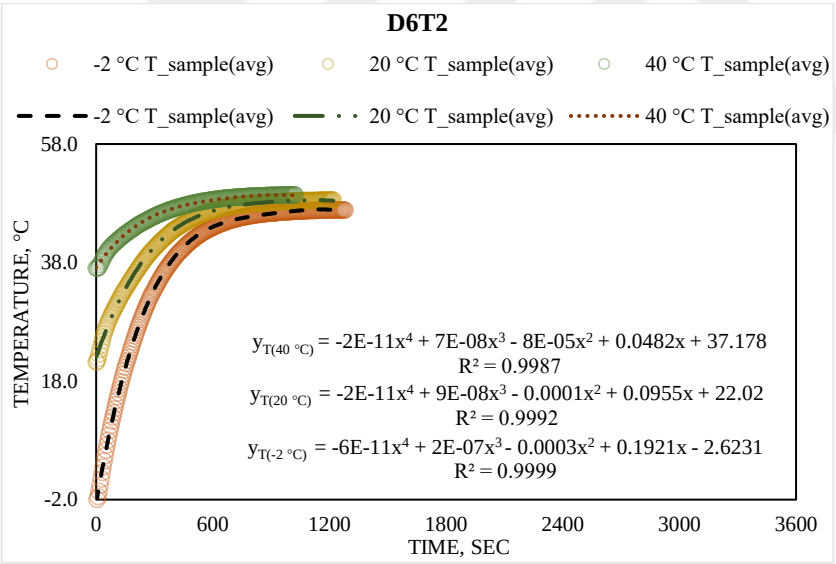


Figure D. 8 The temperature & time curves of D6T2 under three different conditioning temperatures.

E. Thermal Conductivity and Heat Flux Values in The Developed Steady-State Method

Table E. 1 For the developed steady-state test setup, all thermal conductivity results and properties of the slices prepared with basalt (Replicate No.1).

Sample ID	Average height of the slice, mm	Measured Air void, %	Bulk Specific Gravity, G_{mb}	Hot Plate Temperature at Steady-State, °C	Cold Plate Temperature at Steady-State, °C	Temperature Difference, °C	Measured Thermal Conductivity Value, W/m.°C	Calibrated Thermal Conductivity Value, W/m.°C	Heat Flux, W/m^2
B2T1-01	43	1.1	2.459	39.4	12.7	26.8	0.422	0.452 ± 0.15	262.72
B2T1-02	46	0.8	2.467	40.4	12.3	28.1	0.415	0.444 ± 0.15	250.04
B4T1-01	46	3.2	2.408	39.4	12.5	26.9	0.455	0.487 ± 0.15	266.54
B4T1-02	48	2.5	2.426	39.0	12.3	26.6	0.425	0.454 ± 0.15	239.36
B6T1-01	48	4.9	2.366	40.0	12.2	27.8	0.427	0.457 ± 0.15	247.32
B6T1-02	48	4.7	2.369	41.5	12.3	29.2	0.425	0.455 ± 0.15	254.23
B2T2-01	43	0.9	2.510	38.3	12.7	25.6	0.432	0.462 ± 0.15	253.57
B2T2-02	48	1.3	2.501	39.9	12.4	27.5	0.427	0.457 ± 0.15	243.12
B4T2-01	47	3.3	2.450	40.2	12.2	28.0	0.440	0.471 ± 0.15	258.42
B4T2-02	48	2.6	2.467	41.1	12.7	28.4	0.434	0.464 ± 0.15	245.58
B6T2-01	48	5.4	2.396	41.1	12.2	28.9	0.456	0.488 ± 0.15	266.51
B6T2-02	48	4.6	2.416	40.7	12.2	28.5	0.441	0.472 ± 0.15	261.16

Table E. 2 For the developed steady-state test setup, all thermal conductivity results and properties of the slices prepared with basalt (Replicate No.2).

Sample ID	Average height of the slice, mm	Measured Air void, %	Bulk Specific Gravity, G_{mb}	Hot Plate Temperature at Steady-State, °C	Cold Plate Temperature at Steady-State, °C	Temperature Difference, °C	Measured Thermal Conductivity Value, W/m.°C	Calibrated Thermal Conductivity Value, W/m.°C	Heat Flux, W/m^2
B2T1-01	44	1.4	2.451	42.6	13.8	28.9	0.422	0.452 ± 0.15	275.21
B2T1-02	50	0.8	2.466	43.4	12.6	30.8	0.433	0.463 ± 0.15	263.66
B4T1-01	48	3.1	2.411	43.4	12.6	30.7	0.437	0.467 ± 0.15	279.55
B4T1-02	49	2.8	2.417	43.9	12.7	31.2	0.428	0.458 ± 0.15	271.51
B6T1-01	51	4.7	2.370	44.7	12.5	32.3	0.491	0.526 ± 0.15	307.68
B6T1-02	47	5.2	2.358	43.1	12.4	30.7	0.406	0.434 ± 0.15	263.62
B2T2-01	47	1.2	2.502	43.2	12.6	30.5	0.417	0.446 ± 0.15	268.64
B2T2-02	45	0.9	2.510	42.5	12.8	29.6	0.383	0.410 ± 0.15	250.82
B4T2-01	46	3.0	2.456	43.0	12.4	30.6	0.416	0.445 ± 0.15	274.31
B4T2-02	47	2.9	2.460	42.6	12.5	30.1	0.408	0.436 ± 0.15	257.63
B6T2-01	51	5.2	2.402	44.1	12.5	31.6	0.451	0.483 ± 0.15	278.08
B6T2-02	47	4.7	2.413	43.8	13.2	30.7	0.395	0.423 ± 0.15	253.52

Table E. 3 For the developed steady-state test setup, all thermal conductivity results and properties of the slices prepared with dolomite (Replicate No.1).

Sample ID	Average height of the slice, mm	Measured Air void, %	Bulk Specific Gravity, G_{mb}	Hot Plate Temperature at Steady-State, °C	Cold Plate Temperature at Steady-State, °C	Temperature Difference, °C	Measured Thermal Conductivity Value, W/m.°C	Calibrated Thermal Conductivity Value, W/m.°C	Heat Flux, W/m^2
D2T1-01	42	2.6	2.523	41.7	14.4	27.3	0.556	0.594 ± 0.15	360.24
D2T1-02	44	0.7	2.572	41.0	14.3	26.7	0.566	0.606 ± 0.15	342.45
D4T1-01	43	3.5	2.498	41.4	14.2	27.2	0.579	0.619 ± 0.15	368.44
D4T1-02	46	3.3	2.505	40.1	15.0	25.1	0.649	0.694 ± 0.15	354.18
D6T1-01	46	6.0	2.433	41.8	14.6	27.1	0.608	0.651 ± 0.15	359.82
D6T1-02	45	5.0	2.461	40.2	14.4	25.8	0.644	0.689 ± 0.15	374.30
D2T2-01	42	1.1	2.528	42.3	14.1	28.2	0.558	0.597 ± 0.15	377.60
D2T2-02	45	1.1	2.529	40.6	14.0	26.6	0.614	0.657 ± 0.15	363.09
D4T2-01	48	3.6	2.465	40.6	13.5	27.1	0.707	0.757 ± 0.15	398.95
D4T2-02	45	3.1	2.478	41.7	14.1	27.6	0.655	0.701 ± 0.15	404.29
D6T2-01	48	6.0	2.403	42.0	13.4	28.6	0.695	0.744 ± 0.15	413.47
D6T2-02	48	5.0	2.429	40.3	13.4	26.9	0.668	0.715 ± 0.15	370.95

Table E. 4 For the developed steady-state test setup, all thermal conductivity results and properties of the slices prepared with dolomite (Replicate No.2).

Sample ID	Average height of the slice, mm	Measured Air void, %	Bulk Specific Gravity, G_{mb}	Hot Plate Temperature at Steady-State, °C	Cold Plate Temperature at Steady-State, °C	Temperature Difference, °C	Measured Thermal Conductivity Value, W/m.°C	Calibrated Thermal Conductivity Value, W/m.°C	Heat Flux, W/m^2
D2T1-01	46	1.7	2.546	40.0	13.4	26.6	0.677	0.724 ± 0.15	393.10
D2T1-02	42	0.5	2.578	40.8	14.2	26.6	0.628	0.672 ± 0.15	397.00
D4T1-01	45	3.4	2.501	38.0	13.6	24.4	0.729	0.781 ± 0.15	398.18
D4T1-02	45	3.5	2.501	39.5	13.8	25.7	0.586	0.627 ± 0.15	337.20
D6T1-01	45	5.5	2.448	40.8	13.3	27.5	0.678	0.726 ± 0.15	415.28
D6T1-02	48	5.4	2.451	39.1	13.4	25.7	0.698	0.746 ± 0.15	372.19
D2T2-01	45	1.5	2.519	39.4	13.2	26.3	0.707	0.756 ± 0.15	414.63
D2T2-02	46	0.6	2.542	39.6	13.4	26.2	0.739	0.791 ± 0.15	422.52
D4T2-01	47	3.4	2.469	39.4	13.3	26.1	0.801	0.857 ± 0.15	439.42
D4T2-02	47	3.4	2.469	38.3	13.4	24.8	0.696	0.745 ± 0.15	369.81
D6T2-01	48	5.3	2.421	40.2	13.3	27.0	0.669	0.716 ± 0.15	374.74
D6T2-02	48	5.0	2.429	38.8	13.4	25.4	0.705	0.755 ± 0.15	373.17

F. Heat Flux and Thermal Conductivity & Temperature Difference Curves

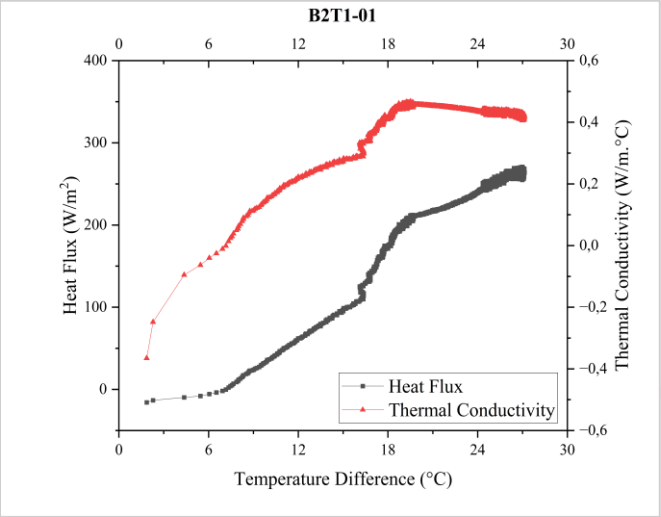


Figure F. 1 The change in heat flux and thermal conductivity values of first slice made with basalt, 2% air void content and Type 1 gradation.

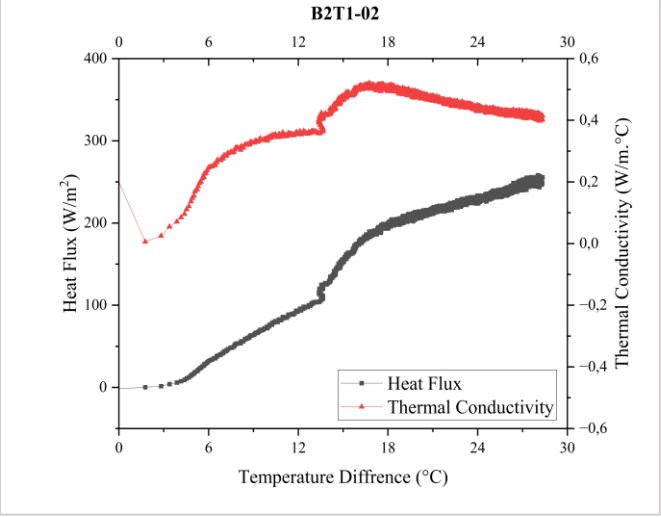


Figure F. 2 The change in heat flux and thermal conductivity values of second slice made with basalt, 2% air void content and Type 1 gradation.

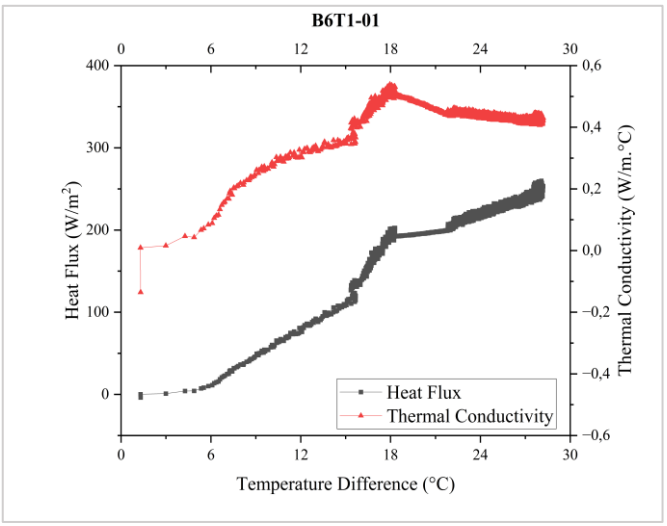


Figure F. 3 The change in heat flux and thermal conductivity values of first slice made with basalt, 6% air void content and Type 1 gradation.

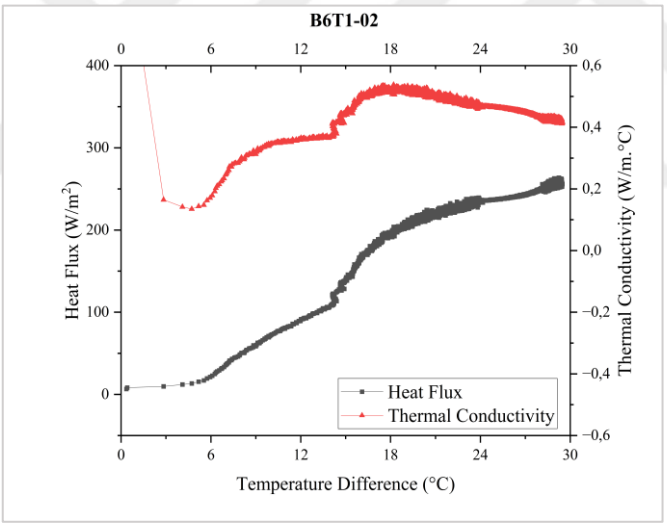


Figure F. 4 The change in heat flux and thermal conductivity values of second slice made with basalt, 6% air void content and Type 1 gradation.

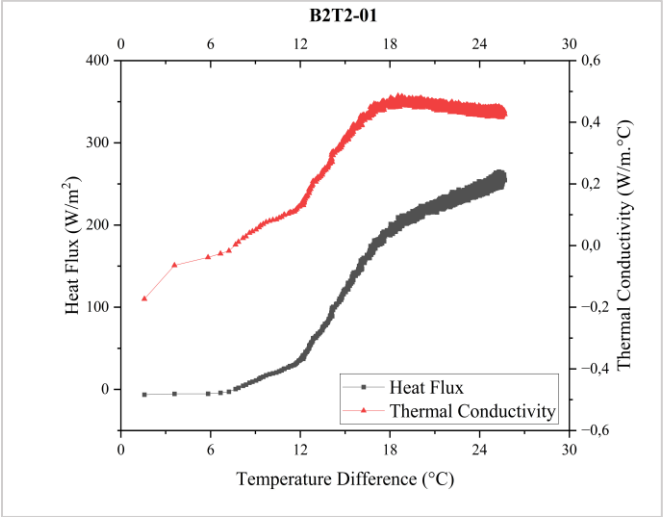


Figure F. 5 The change in heat flux and thermal conductivity values of first slice made with basalt, 2% air void content and Type 2 gradation.

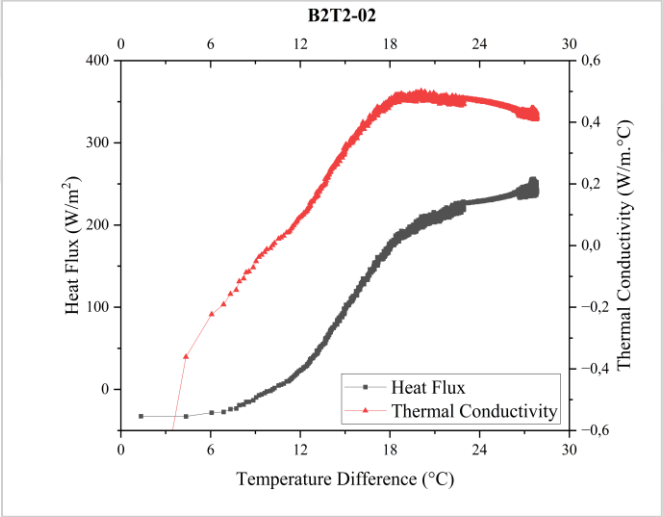


Figure F. 6 The change in heat flux and thermal conductivity values of second slice made with basalt, 2% air void content and Type 2 gradation.

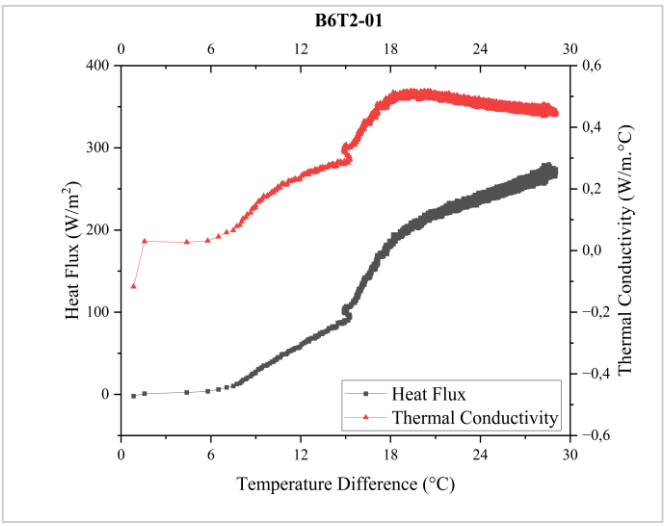


Figure F. 7 The change in heat flux and thermal conductivity values of first slice made with basalt, 6% air void content and Type 2 gradation.

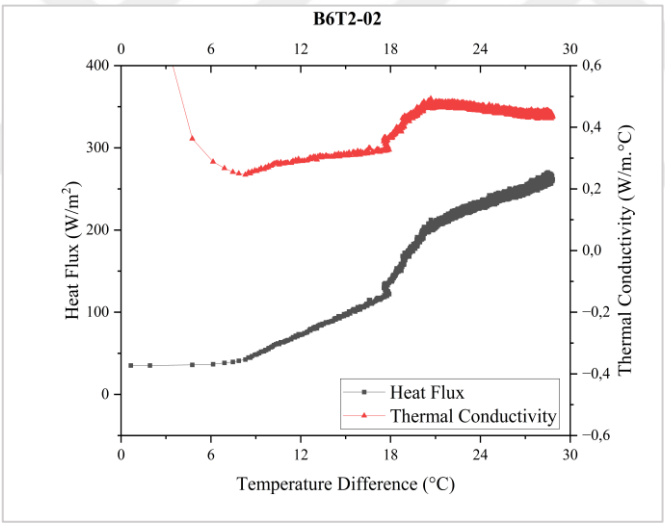


Figure F. 8 The change in heat flux and thermal conductivity values of second slice made with basalt, 6% air void content and Type 2 gradation.

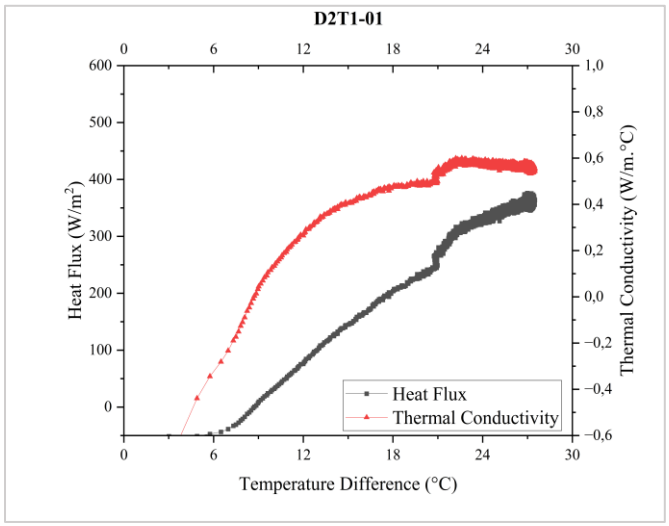


Figure F. 9 The change in heat flux and thermal conductivity values of first slice made with dolomite, 2% air void content and Type 1 gradation.

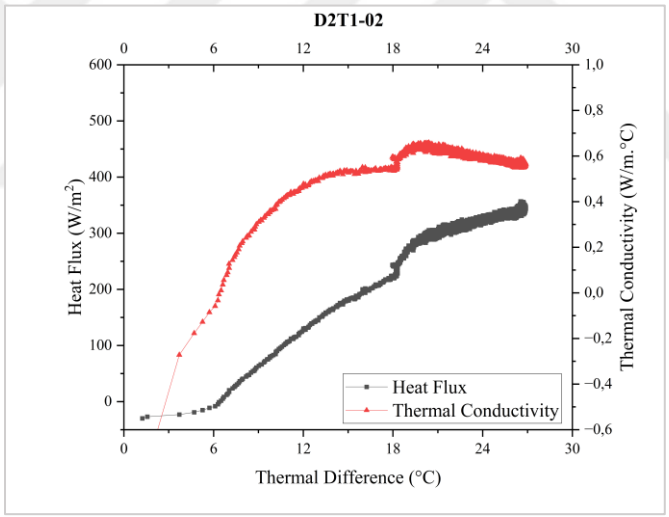


Figure F. 10 The change in heat flux and thermal conductivity values of second slice made with dolomite, 2% air void content and Type 1 gradation.

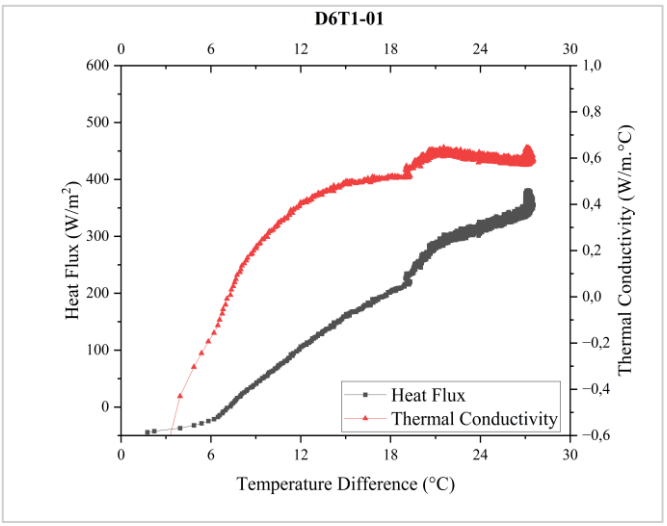


Figure F. 11 The change in heat flux and thermal conductivity values of first slice made with dolomite, 6% air void content and Type 1 gradation.

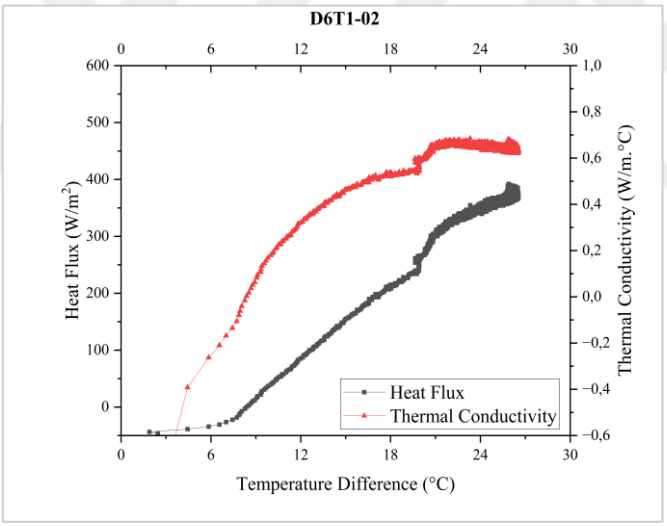


Figure F. 12 The change in heat flux and thermal conductivity values of second slice made with dolomite, 6% air void content and Type 1 gradation.

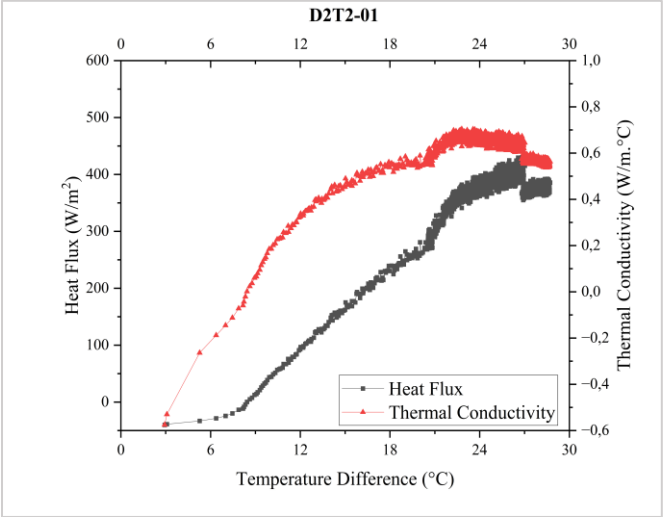


Figure F. 13 The change in heat flux and thermal conductivity values of first slice made with dolomite, 2% air void content and Type 2 gradation.

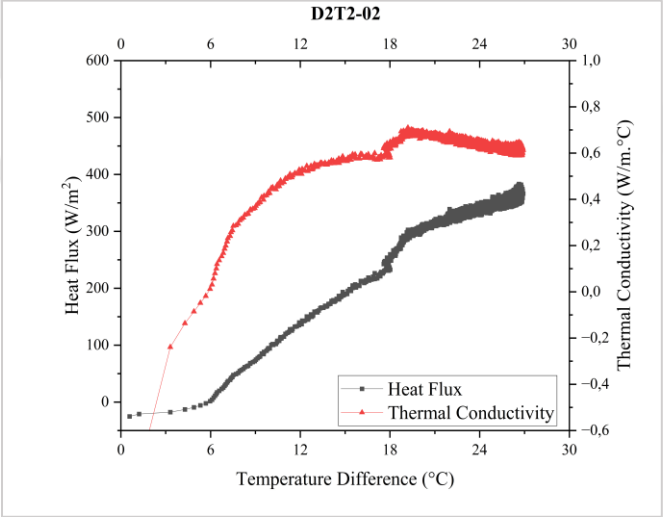


Figure F. 14 The change in heat flux and thermal conductivity values of second slice made with dolomite, 2% air void content and Type 2 gradation.

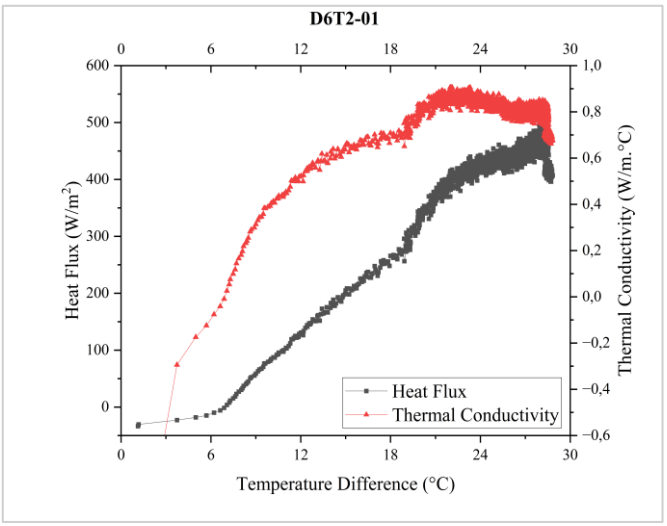


Figure F. 15 The change in heat flux and thermal conductivity values of first slice made with dolomite, 6% air void content and Type 2 gradation.

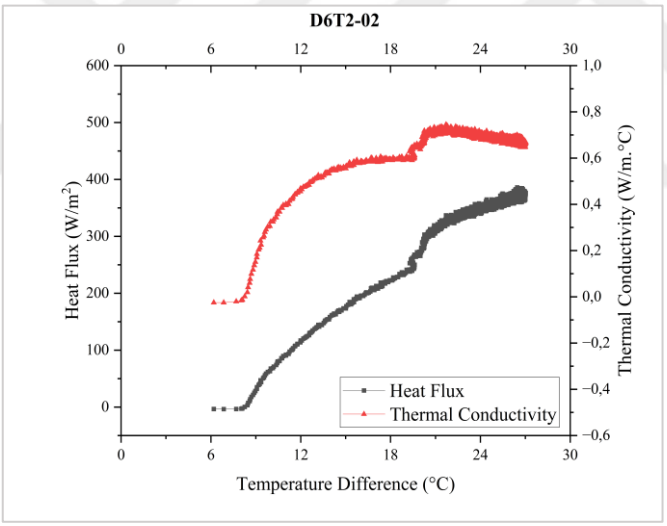


Figure F. 16 The change in heat flux and thermal conductivity values of second slice made with dolomite, 6% air void content and Type 2 gradation.

CURRICULUM VITAE

Surname, Name: Demirtürk, Duygu

EDUCATION

Degree	Institution	Year of Graduation
MS	Gazi University Civil Engineering	2017
BS	Atılım University Civil Engineering	2013
High School	Ümitköy Anatolian High School, Ankara	2007

FOREIGN LANGUAGES

Advanced English

PUBLICATIONS

1. Demirtürk, D., Öztürk, H. I., & Güler, M. (2023). Using Calorimetry-Based Method for Measuring Specific Heat Capacity of Asphalt Concrete. *Proceedings of 3rd International Civil Engineering and Architecture Congress (ICEARC'23)*, 2031-2040.
2. Demirtürk, D. (2021). Sürdürülebilir Ulaşımda Sera Gazi Etkisini Azaltmaya Yönelik Çalışmalar. *Mühendislik Bilimleri ve Tasarım Dergisi*, *9*(4), 1080-1092. https://doi.org/10.21923/jesd.932385.
3. Tunc, G., Demirtürk, D., (2016). Susuz Beton ve Türkiye Gerçeği. *Hazır Beton*, *134,* 69-82.
4. Tunc, G., Demirtürk, D., (2015). Habitat Structures on the Moon. *Yapı Dergisi*, 134-140.